Transcriptome analyses across tissues in the liver fluke *Fasciola hepatica* - from gene expression to drug target characterization

Svenja Franziska Gramberg

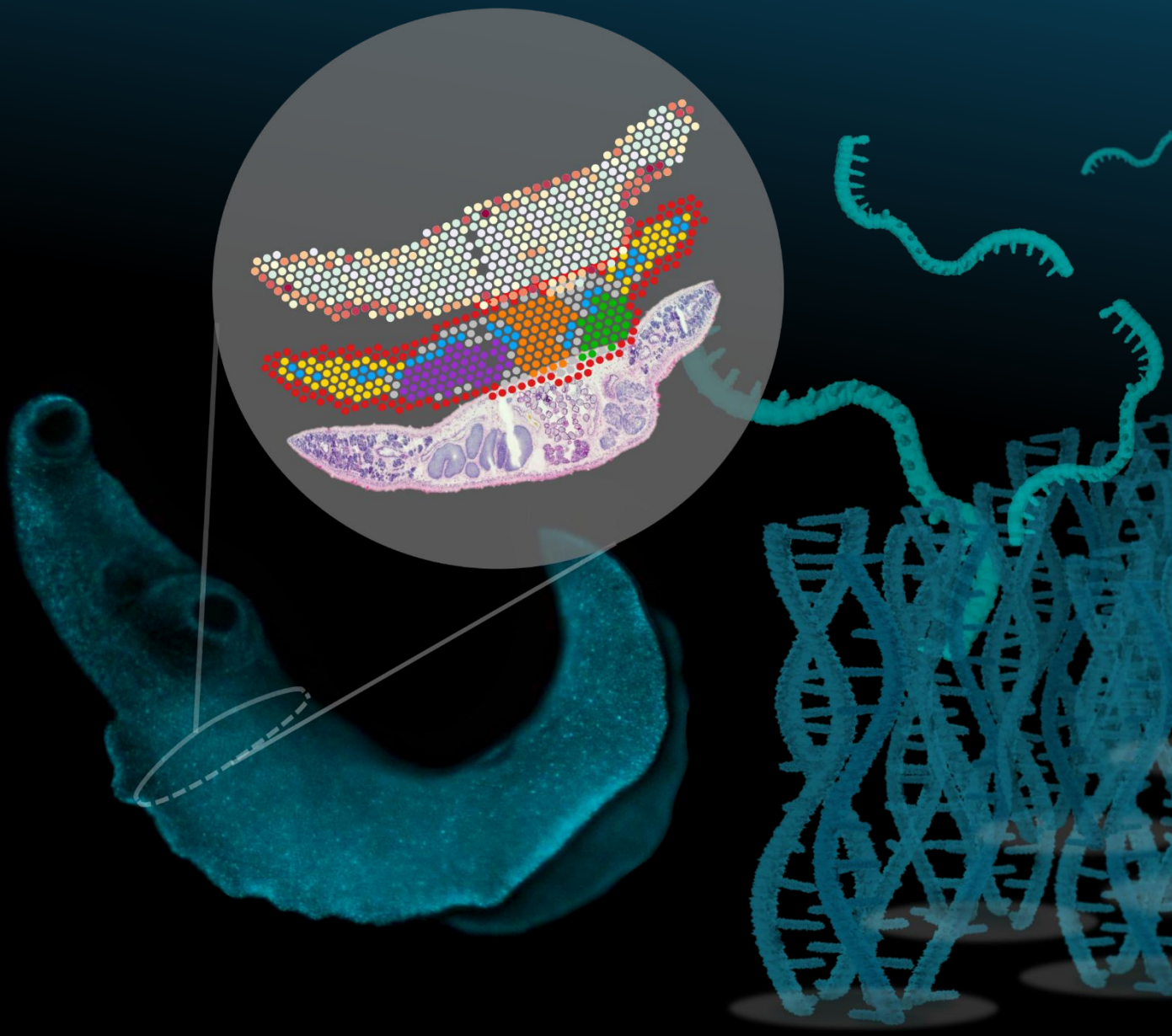

Inaugural-Dissertation zur Erlangung des Grades eines

Dr. med. vet.

beim Fachbereich Veterinärmedizin der Justus-Liebig-Universität Gießen

Aus dem Institut für Parasitologie, Justus-Liebig-Universität Gießen

Betreuerin: PD Dr. Simone Häberlein

Transcriptome analyses across tissues in the liver fluke *Fasciola hepatica* – from gene expression to drug target characterization

INAUGURAL-DISSERTATION

zur Erlangung des Grades eines

Dr. med. vet.

beim Fachbereich Veterinärmedizin

der Justus-Liebig-Universität Gießen

eingereicht von

Svenja Franziska Gramberg

Tierärztin aus Germersheim

Gießen 2025

Mit Genehmigung des Fachbereichs Veterinärmedizin der Justus-Liebig-Universität Gießen

Dekan: Prof. Dr. Dr. Stefan Arnhold

Gutachter: PD Dr. Simone Häberlein
Prof. Sascha Knauf, PhD

Tag der Disputation: 21.08.2025

CONTRIBUTIONS

A. Publications

Parts of this work have been published in/ Teile dieser Arbeit wurden bereits veröffentlicht:

Gramberg, S., Puckelwaldt, O., Schmitt, T., Lu, Z., & Haeberlein, S. (2024). Spatial transcriptomics of a parasitic flatworm provides a molecular map of drug targets and drug resistance genes. *Nature Communications*, 15(1):8918, https://doi.org/10.1038/s41467-024-53215-3. Corresponding preprint at *bioRxiv*: https://doi.org/10.1101/2023.12.11.571084.

Please note/ Hinweis:

Previously published content (text passages, illustrations) will be appropriately referenced throughout this document, citing the above-mentioned publication. Text passages are referenced paragraph-by-paragraph, illustrations in the respective figure legends. Co-author contributions are consistent with the information provided in the publication and are indicated again in relevant methods sections./ Vorab publizierte Inhalte (Textpassagen, Abbildungen) werden im Folgenden an allen relevanten Stellen unter Angabe der o.g. Publikation gekennzeichnet. Bei Textpassagen wird dies absatzweise vorgenommen. Bei Abbildungen in der Abbildungslegende. Der Beitrag der Co-Autoren entspricht den Angaben in der Publikation und wird in den relevanten Methodenkapiteln nochmals entsprechend ausgewiesen.

Further publications:

Luh, D.; Heiles, S.; **Gramberg, S**.; Haeberlein, S. & Spengler, B. (2024). Glycolipidomics of liver flukes and host tissues during fascioliasis: Insights from mass spectrometry imaging. *ACS Infectious Diseases*, 10(12), pp. 4233–4245. https://doi.org/10.1021/acsinfecdis.4c00551.

Puckelwaldt, O., **Gramberg, S.**, Ajmera, S., Koepke, J., Samakovlis, C., & Haeberlein, S. (2024). Single-cell transcriptomics identifies a p21-activated kinase important for survival of the zoonotic parasite *Fasciola hepatica*. *bioRxiv*. https://doi.org/10.1101/2024.03.26.586785.

Sprague, D.J.; Park, S.K.; **Gramberg, S.**; Bauer, L.; Rohr, C.M.; Chulkov, E.G.; Smith, E.; Scampavia, L.; Spicer, T.P.; Haeberlein, S. & Marchant, J.S. (2024). Target-based discovery of a broad-spectrum flukicide. *Nature Structural & Molecular Biology,* 31(9), pp. 1386–1393. https://doi.org/10.1038/s41594-024-01298-3 .

B. Conferences

This work has been presented at the following conferences:

Joint Parasitology Spring Meeting 2025, 11.-14. March 2025, Wuerzburg, Germany.
Poster: **Gramberg, S.**; Bauer, L., Tegni Sontia, P.; Puckelwaldt, O. & Haeberlein, S. HNF4 as a key regulator of gut biology in the liver fluke *F. hepatica*. (This contribution was awarded the 3rd prize for the best poster presentation.)

16th GGL Annual Conference 2023, 20.-21. September 2023, Giessen, Germany.
Talk: **Gramberg, S.**; Puckelwaldt, O., Schmitt, T., Lu, Z.; & Haeberlein, S. Cutting-edge technologies in parasite research – How to create a molecular map of the liver fluke *Fasciola hepatica.* (This talk was awarded the prize for the best oral presentation.)

Molecular Helminthology Meeting 2023, 26.-29. June 2023, Madison, Wisconsin, US.
Talk: **Gramberg, S.**; Puckelwaldt, O., Schmitt, T. & Haeberlein, S. Spatial transcriptomics of parasites - A molecular map of the liver fluke *Fasciola hepatica.*

Tagung der DVG-Fachgruppe Parasitologie und parasitäre Krankheiten 2023, 15.-17. May 2023, Munich, Germany.
Talk: **Gramberg, S.**; Puckelwaldt, O., Schmitt, T. & Haeberlein, S. Spatial transcriptomics of parasites - A molecular map of the liver fluke *Fasciola hepatica.*

30th Annual meeting of the German Society for Parasitology 2023, 15.-17. March 2023, Giessen, Germany.
Talk: **Gramberg, S**.; Puckelwaldt, O.; Schmitt T. & Haeberlein, S. Spatial transcriptomics of parasites - 2D transcriptome analyses of tissues in the liver fluke *Fasciola hepatica.*

15th GGL Annual Conference 2022, 14.-15. September 2022, Giessen, Germany.
Poster: **Gramberg, S.**; Puckelwaldt, O. & Haeberlein, S. Spatial transcriptomics of parasites - 2D transcriptome analyses of tissues in the liver fluke *Fasciola hepatica.*

14th GGL Annual Conference 2021, 29.-30. September 2021, Giessen, Germany.
Talk: **Gramberg, S.**; Puckelwaldt, O. & Haeberlein, S. 2D transcriptome analyses of tissues in the liver fluke *Fasciola hepatica.*

ABSTRACT

Fasciolosis is a food-borne trematode infection caused by the liver fluke *Fasciola hepatica* and related species. The disease affects human and animal health worldwide and causes considerable economic losses in the global livestock industry. The limited number of therapeutic options and the increasing resistance to anthelminthics complicate disease control and highlight the need for novel anthelmintics or a vaccine. The development of new anthelmintic strategies, however, requires a deeper understanding of fluke biology, particularly regarding organ function and organ-specific gene expression.

Technological advancements in transcriptomics technologies have opened up new avenues to study the transcriptional landscape of multicellular parasites. Spatial transcriptomics (ST) enables the visualization of the entire transcriptome of a tissue section in 2D, while preserving the original morphological context. By applying the Visium Spatial Gene Expression Solution (10x Genomics) to adult *F. hepatica*, over 9,000 genes were captured and eight different tissues were characterized, including the intestine, integument, and reproductive organs. Gene expression profiles and marker genes were identified for each tissue and subsequently validated through *in situ* hybridization. In addition, a Gene Ontology (GO) enrichment analysis was performed, revealing characteristic biological processes and molecular functions associated with each tissue. The gene expression map further uncovered the tissue-specific expression of drug targets (β-tubulins), vaccine candidates (Ly6 proteins) as well as drug resistance genes (ABC transporters, glutathione S-transferases), indicating tissue-specific biological functions. Finally, the spatial expression data was combined with a database of bioactive molecules, which identified genes in the tegument and intestine that showed homology to targets of approved drugs and drugs in clinical trials. This approach led to the identification of a tegumental protein kinase C beta, for which small-molecule targeting resulted in parasite death.

The further course of the work focussed on the parasite's intestine, a tissue that, like the tegument, is vital for parasite survival. The transcription factor hepatocyte nuclear factor 4 (HNF4) is a highly conserved regulator of metabolic homeostasis and cellular differentiation of endodermal organs such as the liver, gut, and pancreas. However, its role in liver fluke biology was unknown. Using the spatial transcriptome and *in situ* hybridization, *hnf4* expression was localized in the parasite's gastrodermis. Functional studies utilizing RNA interference (RNAi) and RNA sequencing in immature parasites revealed that HNF4 was essential for the maintenance of gut-associated gene expression, particularly genes encoding proteases such as cathepsins and legumain. RNAi-mediated knockdown of *hnf4* expression led to a significant reduction in worm viability *in vitro* and caused structural disruption of the intestine. Treatment with a commercial small-molecule inhibitor of HNF4, BI6015, had similar effects, although the

transcriptomics data indicated that the inhibitor was not HNF4-specific. Further research on the molecular mechanisms by which HNF4 regulates gut biology may identify key pathways essential for parasite survival.

Overall, this work provides the first spatial transcriptome of a parasitic flatworm and demonstrates how spatial transcriptomics can advance the understanding of multicellular parasites. The identification of tissue-specific transcripts proofed to be a valuable tool for both basic research and the discovery of new drug targets.

ZUSAMMENFASSUNG

Die Fasziolose ist eine durch Lebensmittel übertragene Trematodeninfektion, die durch den Leberegel *Fasciola hepatica* und verwandte Arten verursacht wird. Die Erkrankung beeinträchtigt die Gesundheit von Menschen und Tieren weltweit und verursacht erhebliche wirtschaftliche Verluste in der globalen Viehwirtschaft. Die begrenzte Auswahl therapeutischer Möglichkeiten und die zunehmende Resistenz gegen Anthelminthika erschweren die Bekämpfung und verdeutlichen den dringenden Bedarf nach neuen Bekämpfungsstrategien. Die Entwicklung neuer Anthelminthika oder eines Impfstoffes erfordert jedoch ein vertieftes Verständnis der Biologie des Egels, insbesondere hinsichtlich der Organfunktionen und der organspezifischen Genexpression.

Technologische Fortschritte in der Transkriptomanalyse eröffnen heute neue Möglichkeiten, um Einblicke in die Genexpressionslandschaft multizellulärer Parasiten zu gewinnen. So erlaubt die räumliche Transkriptomik (Spatial Transcriptomics, ST) die Visualisierung des gesamten Transkriptoms von Gewebeschnitten in 2D unter Bewahrung der ursprünglichen Gewebearchitektur. Durch die Anwendung der Visium Spatial Gene Expression Solution (10x Genomics) auf adulte *F. hepatica* konnten in dieser Arbeit über 9.000 Gene erfasst und acht verschiedene Gewebe charakterisiert werden, darunter Darm, Tegument und Fortpflanzungsorgane. Durch einer differentielle Genexpressionsanalyse wurden zudem für jedes dieser Gewebe Genexpressionsprofile und Markergene identifiziert und anschließend mittels *in situ* Hybridisierung validiert. Darüber hinaus ergab eine Gene Ontology (GO) Analyse charakteristische biologische Prozesse und molekulare Funktionen, die mit jedem Gewebecluster assoziiert waren. Weiterhin ermöglichte die Genexpressionskarte die Identifizierung gewebespezifischer Expressionsmuster von Medikamentenzielen (β-Tubuline), Impfstoffkandidaten (Ly6-Proteine) sowie potenziellen Resistenzgenen (ABC-Transporter, Glutathion-S-Transferasen) und lieferte damit wertvolle Hinweise auf ihre gewebespezifischen biologischen Funktionen. In Verbindung mit einer Datenbank bioaktiver Moleküle wurden schließlich in Tegument und Darm Gene identifiziert, die Homologien zu Zielen bereits

zugelassenen bzw. in klinischen Studien befindlichen Medikamenten aufweisen. Auf diese Weise wurde eine Protein Kinase C Beta und ein niedermolekularer Inhibitor identifiziert, dessen Einsatz zum Tod des Parasiten geführt hat.

Der zweite Teil der Arbeit konzentriert sich auf den Parasitendarm, einem Gewebe, das wie auch das Tegument für das Überleben des Leberegels essenziell ist. Der Transkriptionsfaktor Hepatocyte Nuclear Factor 4 (HNF4) ist ein hochkonservierter Regulator der metabolischen Homöostase und der zellulären Differenzierung endodermaler Organe wie der Leber, dem Darm und der Bauchspeicheldrüse. Seine Rolle für die Biologie des Leberegels war jedoch unbekannt. Mithilfe des räumlichen Transkriptoms sowie der *in situ* Hybridisierung konnten *hnf4*-Transkripte im Darmepithel des Parasiten lokalisiert werden. Funktionelle Studien unter Verwendung von RNA-Interferenz (RNAi) und RNA-Sequenzierung in immaturen Parasiten zeigten zudem, dass HNF4 essenziell für die Aufrechterhaltung der Expression darmassoziierter Gene ist, insbesondere für Gene, die Proteasen wie Cathepsine und Legumain kodieren. Eine RNAi-induzierte Unterdrückung der *hnf4* Expression führte *in vitro* zu einer erheblichen Verringerung der Vitalität der Würmer und verursachte strukturelle Schäden im Darm. Die Behandlung mit einem kommerziellen niedermolekularen HNF4-Inhibitor, BI6015, hatte ähnliche Auswirkungen wie die RNAi, jedoch zeigte die Transkriptomanalyse, dass der Inhibitor vermutlich nicht HNF4-spezifisch war. Weitere Untersuchungen der molekularen Mechanismen, durch die HNF4 die Darmbiologie reguliert, könnten neue Schlüsselfunktionen aufdecken, die für das Überleben des Parasiten entscheidend sind.

Zusammengefasst, liefert diese Arbeit das erste räumliche Transkriptom eines parasitären Plattwurms und zeigt, wie Spatial Transcriptomics das Verständnis von multizellulären Parasiten verbessern kann. Die Identifizierung gewebespezifischer Transkripte erwies sich als ein wertvolles Instrument sowohl für die Grundlagenforschung als auch für Entdeckung von neuen Wirkstoffzielen.

TABLE OF CONTENTS

LIST OF ABBREVIATIONS

aa	Amino acid
ABAM	Antibiotic-Antimycotic
ABC	ATP-binding cassette (transporter)
ABZ	Albendazole
AFA	Acidified formaldehyde alcohol
ANOVA	Analysis of variance
AP	Alkaline phosphatase
(d)ATP	(Deoxy-)Adenosine triphosphate
BCIP	5-Bromo-4-chloro-3-indolyl phosphate
BLAST	Basic Local Alignment Search Tool
bp	Base pairs
BSA	Bovine serum albumin
B&W	Black & white
BZ	Benzimidazole
Cat#	Catalogue number
cDNA	Complementary DNA
CISH	Chromogenic *in situ* hybridization
CLSM	Confocal laser scanning microscope/microscopy
CS	Chicken serum
(d)CTP	(Deoxy-)Cytosine triphosphate
DBD	DNA-binding domain
DEGs	Differentially expressed genes
DEPC	Diethylpyrocarbonate
DGE	Differential gene expression
dH2O	Deionized water
ddH2O	Ultrapure/ MilliQ water
ΔG	Gibbs free energy
DIG	Digoxygenin
DMSO	Dimethyl sulfoxide
DNA	Desoxyribonucleic acid
DR	Direct repeat
dsRNA	Double-stranded RNA
DTT	Dithiothreitol
EDTA	Ethylenediaminetetraacetic acid
EdU	5-Ethynyl-2'-deoxyuridine
EGTA	Ethylene glycol-bis(β-aminoethyl ether)-N,N,N′,N′-tetraacetic acid
eprs	Glutamyl-prolyl-tRNA synthetase
ES	Excretory/secretory
EtOH	Ethanol
FA	Formic acid-containing fixing solution
FABP	Fatty acid-binding protein
FC	Fold change
FF	Fresh frozen
FFPE	Formalin-fixed paraffin embedded
FISH	Fluorescence *in situ* hybridization
FOX	Forkhead box

gDNA	Genomic DNA
GO	Gene ontology
GOI	Gene of interest
GPCR	G-protein coupled receptor
GST	Glutathione S-transferase
(d)GTP	(Deoxy-)Guanosine triphosphate
H&E	Hematoxylin & eosin
HEPES	4-(2-hydroxyethyl)-1-piperazineethanesulfonic acid
HNF4	Hepatocyte nuclear factor 4
Hoechst 33342	2'-[4-ethoxyphenyl]-5-[4-methyl-1-piperazinyl]-2,5'-bi-1H-benzimidazole trihydrochloride trihydrate
HSP	Heat shock protein
IPP	Inorganic pyrophosphatase
ISH	*In situ* hybridization
ISS	*In situ* sequencing
KD	Knockdown
LB	Lysogeny broth
LBD	Ligand-binding domain
LCM	Laser capture microdissection
Log2FC	binary logarithm of the fold-change
Ly6	Lymphocyte antigen 6
MAB-T	Maleic acid buffer + Tween 20
MEIOB	Meiosis specific with OB-fold
MeOH	Methanol
mRNA	Messenger RNA
MUSCLE	Multiple sequence comparison by log-expectation
NA	Not available/ applicable
NA solution	Nitric acid-containing fixing solution
NBT	Nitro blue tetrazolium
NCBI	National Center for Biotechnology Information
NEJ	Newly excysted juvenile
NGS	Next generation sequencing
No.	Number
NR	Nuclear receptor
NTD	Neglected tropical disease
(d)NTP	(Deoxy-)Ribonucleoside triphosphate
O.C.T.	Optimal cutting temperature
PAMP	Pathogen-associated molecular pattern
PBS	Phosphate-buffered saline
PBSTx	Phosphate-buffered saline + Triton X-100
PC	Principal component
PCA	Principal component analysis
PCR	Polymerase chain reaction
PCR H_2O	Doubly distilled water
PGRP	Peptidoglycan recognition protein
p.i.	*post infectionem*
PKC	Protein kinase C
POD	Horseradish peroxidase
PRR	Pattern recognition receptor

QC	Quality check
qRT-PCR	Quantitative real-time polymerase chain reaction
RE	Responsive element
RIN	RNA-integrity number
RNA	Ribonucleic acid
RNAi	RNA interference
RNase	Ribonuclease
(sc)RNAseq	(single-cell) RNA sequencing
ROI	Region of interest
rRNA	Ribosomal RNA
RT	Reverse transcription
RXR	Retinoid-X receptor
SEM	Standard error of the mean
SD	Standard deviation
siRNA	Small interfering RNA
SSC	Saline-sodium citrate
SMART	Simple Modular Architecture Research Tool
SR	Steroid receptor
ST	Spatial Transcriptomics
TAE	TRIS-acetate-EDTA buffer
TCBZ	Triclabendazole
TE	TRIS-EDTA buffer
TEM	Transmission electron microscopy
TF	Transcription factor
T_m	Melting temperature
TO	Tissue optimization
TRIS	Tris(hydroxymethyl)aminomethane
TSS	Transcriptional start site
(d)TTP	(Deoxy-)Thymine triphosphate
UMAP	Uniform Manifold Approximation and Projection
UMI	Unique molecular identifier
UTP	Uridine triphosphate
WBPS	WormBase ParaSite
WHO	World Health Organization

LIST OF FIGURES

LIST OF TABLES

1. INTRODUCTION

1.1 Liver flukes

Liver flukes of the genus *Fasciola* are parasitic flatworms (phylum: Platyhelminthes, subphylum Neodermata) of the class Trematoda. There are two major species, *F. hepatica* and *F. gigantica* that are obligate parasites of global importance as causative agents of fasciolosis, a disease affecting both animals and humans [1].

1.1.1 Epidemiology

1.1.1.1 Global distribution and impact on human health

Fasciolosis has one of the widest distributions of all worm infections and can be found on every continent except Antarctica [2] (Fig. 1). While *F. hepatica* occurs predominantly in temperate zones, *F. gigantica* is mainly found in the tropical regions of Africa and Asia. However, both species can also occur side by side and even hybridize [3]. In Germany, *F. hepatica* prevalences are highest in Schleswig-Holstein and the north of Lower Saxony as well as in the southern part of Bavaria [4].

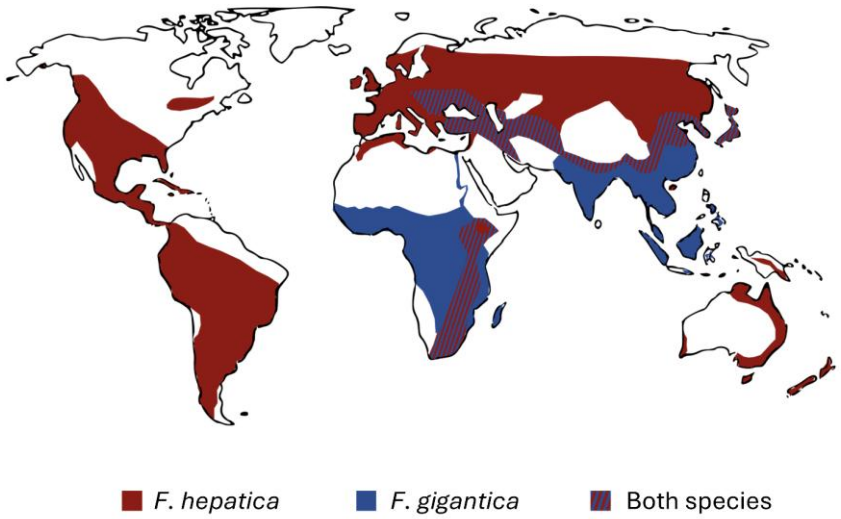

Figure 1 Geographical distribution of *Fasciola* species.
Recolored figure based on Torgerson and Claxton (1999) [5].

Human fasciolosis has received increased attention over the past three decades and was finally included in the list of neglected tropical disease (NTD) by the World Health Organization (WHO) in 2010 [6]. NTDs are a diverse group of diseases that are mainly prevalent among poor communities in tropical areas but have significant medical, social, and economic implications. In this sense, fasciolosis most commonly affects populations in the Andean countries (Peru, Bolivia, Ecuador), Egypt, Iran and Vietnam [7]. Exact infection numbers are not known. Estimates range from 2.4 million [8] to 17 million [9] infected people worldwide, with about 91 million people at risk [10].

1.1.1.2 Life cycle

The liver fluke cycle is heteroxenous and involves two host species: a snail intermediate host (for *F. hepatica*: Lymnaeidae, e.g. *Galba truncatula*), and a mammalian definitive host (Fig. 2) [7]. Liver flukes are not very host-specific and can infect a wide range of mammalian species, including humans [7]. In Europe, however, *F. hepatica* has received most attention as a parasite of domestic ruminants such as cattle, goats and sheep [11],[12]. Small ruminants are particularly susceptible to *F. hepatica* infection and do not generate significant resistance to reinfection [12],[13]. As a result, young and adult animals are equally affected. Cattle are less susceptible and tend to develop chronic forms of the disease. Fasciolosis has also been reported in non-ruminants, including horses and pigs, although both species have a much higher natural resistance compared to ruminants [14],[15]. Various wild animals such as deer, hares, coypus, camelids, kangaroos, as well as laboratory animal species (mice, rats, hamsters, rabbits) can also become infected (Fig. 2). Some of these species are regarded as important reservoir hosts [1],[7].

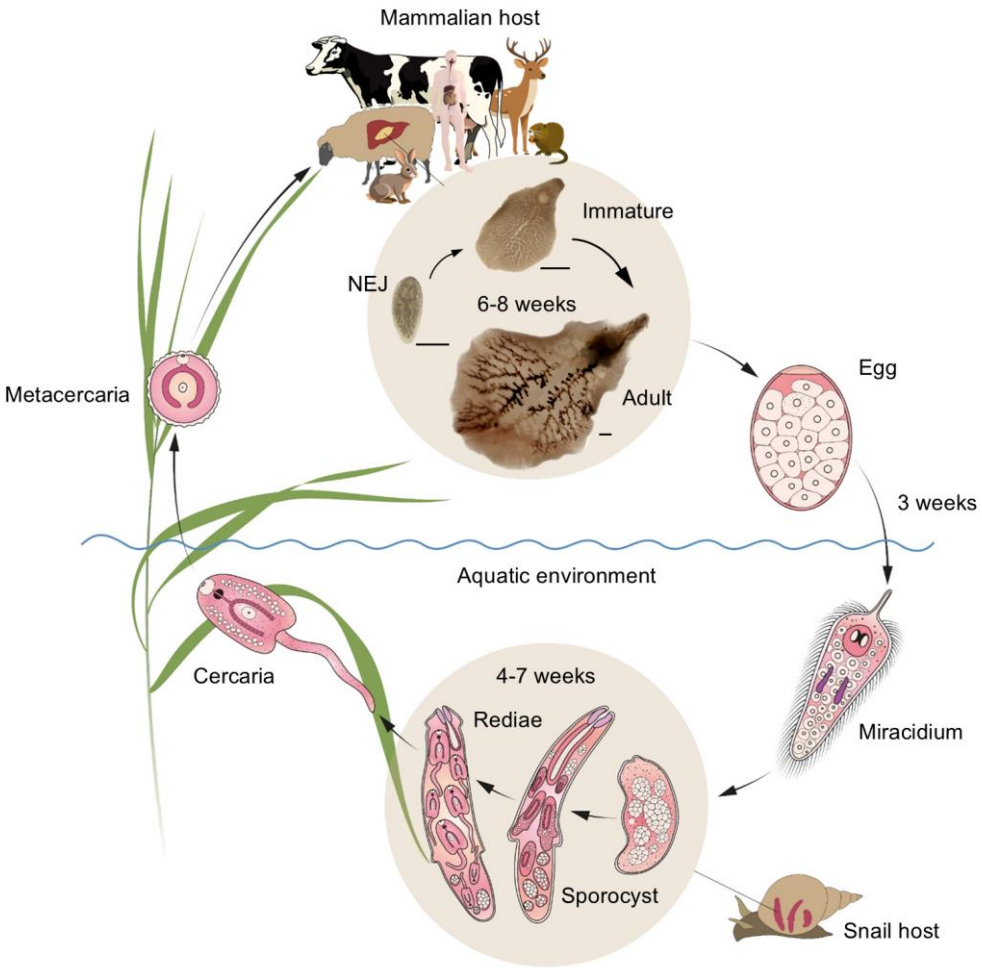

Figure 2 The life cycle of *Fasciola hepatica.*
Stages and development times under optimal conditions are indicated. Scale: NEJ = 0.1 mm, Immature and Adult = 1 mm. Credits: [Aldona]/Adobe Stock (cycle, modified) [16], [nicolasprimola]/Adobe Stock (human, modified) [17], [FineSilhouettes]/Adobe Stock (cow) [18], [pic0bird]/Adobe Stock (coypu) [19], [Pvect02]/Adobe Stock (deer) [20], [MohammadMonirul]/Adobe Stock (rabbit) [21].

Liver fluke-infected mammals excrete non-embryonated eggs with their feces. In the environment, a larva, the so-called miracidium, develops inside the egg. Embryogenesis is largely depending on humidity and temperature and takes about three weeks under optimal conditions [22]. Upon hatching, the short-lived miracidium actively moves in moist surroundings searching for a suitable snail host. Once a host is found, the miracidium penetrates the snail's skin and transforms into a sporocyst [23]. Through asexual reproduction, the sporocyst produces multiple rediae, within which cercariae are formed. Thereby, a single miracidium can give rise to 500 – 3,200 cercariae [24]. Under optimal conditions, this development takes 4-7 weeks [25]. After the cercariae have been released from the snail, they swim until they have found a suitable substrate to attach and encyst. In this encysted form, the metacercariae can survive for months or even years in a moist and temperate environment until they are consumed by a mammal together with plant material or, more rarely, with water [25]. Within the mammal's intestine, juvenile worms (newly-excysted juveniles (NEJ)) hatch from ingested metacercariae and subsequently penetrate the intestinal wall to migrate through the body cavity towards the liver [26],[27]. There, they penetrate the liver capsule and feed on the liver parenchyma until they reach sexual maturity after 6-8 weeks, depending on host species [27],[28]. The migratory stage, which is not yet sexually mature, is called immature liver fluke in the following and is thereby distinguished from juvenile liver flukes that have been excysted and cultivated *in vitro*. Adult parasites reside in the bile ducts, where they produce 4,000 - 50,000 eggs per day, which are excreted with the feces via the bile [29]. Within the definitive host, adult liver flukes can survive for several months or even years [30].

1.1.2 Anatomy of adult liver flukes

Adult *F. hepatica* are large multicellular parasites that can reach up to 3 cm body length [31]. They are dorso-ventrally flattened, leaf-like in shape and equipped with two muscular suckers (Fig. 3) [32]. The fluke's body surface is covered by a syncytial tegument of mesenchymal origin (neodermis), which is a common characteristic of many parasitic Platyhelminthes (Neodermata) [33]. In the case of the liver fluke, the tegument is covered with numerous spines [34]. Platyhelminthes do not have a body cavity (no coelom), but a mesodermal parenchyma in which the internal organs are embedded [35]. The worm's digestive tract begins at the oral sucker, which is connected to the two widely branched caeca via a muscular pharynx and a short esophagus [32]. As the intestine ends blindly, indigestible components are regurgitated through the mouth opening [36]. In addition, there is an excretory system, embedded in the parenchyma, consisting of protonephridia (flame cells) and a network of excretory ducts that culminate in the excretory bladder at the posterior end of the worm [32]. The central nervous system includes a pair of cerebral ganglia located around the pharynx, along with nerve cords extending to the posterior of the body [37]. The peripheral nervous system comprises plexuses

of nerve cells and fibers located beneath the tegument, in the oral and ventral suckers and in association with the various reproductive organs and ducts [32].

As hermaphrodites, liver flukes possess both male and female reproductive organs, which occupy a large proportion of the adult fluke's body (Fig. 3 & Fig. 4). The following details of their arrangement is based on the description by Hanna et al. [38], who visualized the reproductive organs by carmine staining of whole flukes. There are two testes that occupy the medial proportion of the worm's posterior body. A vas deferens runs forward from each testis towards the seminal vesicle, which is located in front of the abdominal sucker in the cirrus sac. From there, the ejaculatory duct, associated with the prostate gland, passes through the protrusible cirrus, and opens at the common genital pore. There is a single, branched ovary, which is significantly smaller than the two testes and located anterior of them, most commonly on the left when viewed from ventral [39]. Liver fluke eggs are composite eggs, consisting of an oocyte and multiple vitelline cells that originate in the vitellarium [40]. The vitellarium is composed of multiple vitelline follicles, which fill up the posterior and lateral margins of the worm. A duct collecting vitelline cells runs along both sides of the worm and joins with the duct from the opposite side to form the vitelline reservoir. The common vitelline duct runs forward to connect with the oviduct and opens into the ootype, where the eggs are formed. The ootype is surrounded by the Mehlis' gland, whose secretions take part in the egg formation process [41]. Eggs are then passed to the proximal uterus, where fertilization takes place before the eggshell is completely hardened. The uterus forms multiple loops and runs towards the genital pore, where it opens adjacent to the ejaculatory duct.

In NEJs, the somatic organs are already present in their basic structure, but underly developmental remodeling and growth during maturation [32]. Reproductive organs, however, newly develop during liver migration from a hourglass-shaped genital rudiment [41]. In the 4-week-old immature worms derived from rats, as used in this study, these developmental processes were largely complete, with the basic organ structure resembling that of adult liver flukes. However, gametogenesis had not yet begun and the reproductive organs were still significantly smaller than those in adult worms.

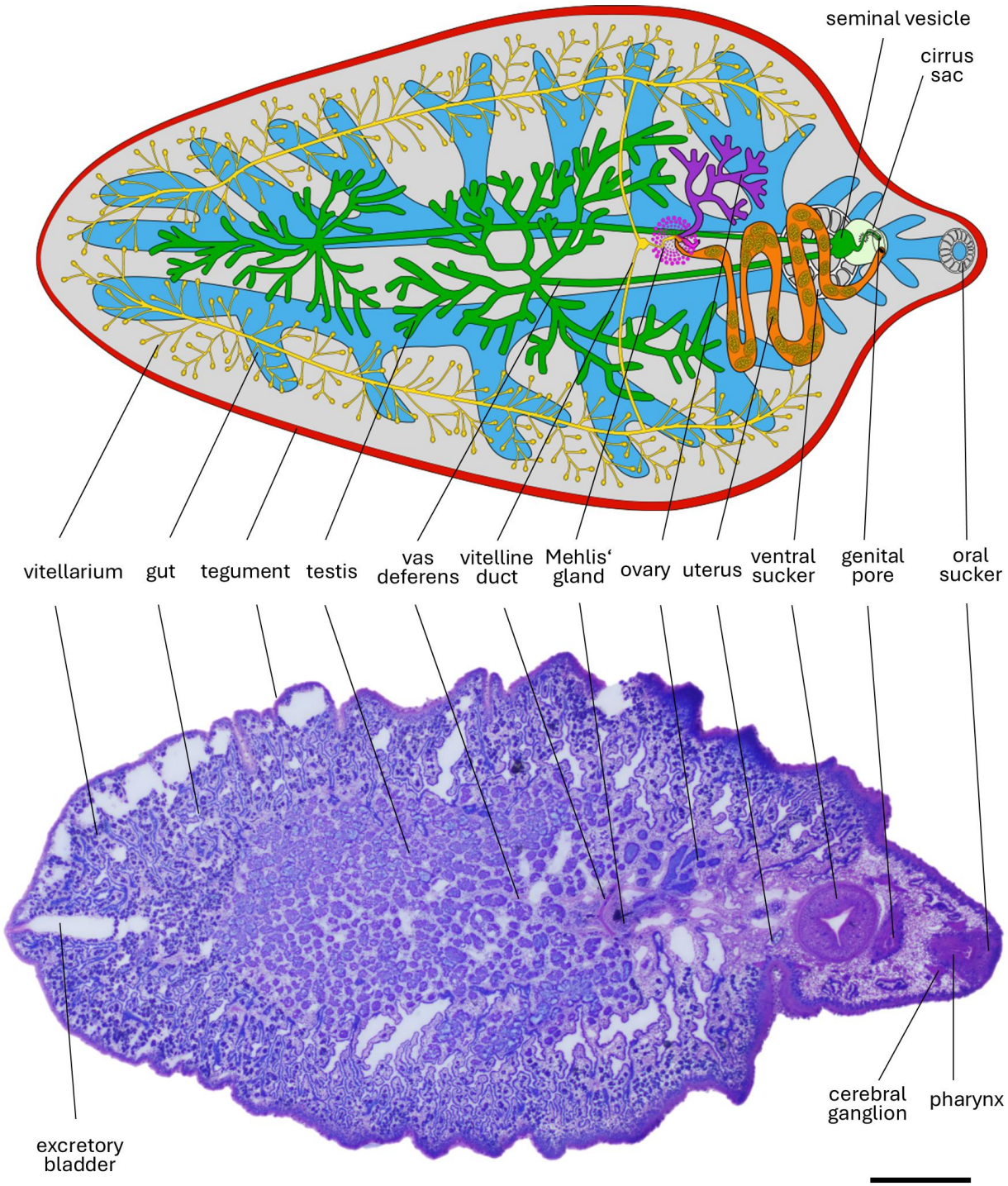

Figure 3 Anatomy of adult *F. hepatica.*
Scheme and horizontal tissue section showing anatomical features of adult *F. hepatica*. Ventral view (ovary on the left). The scheme does not include the nervous and excretory systems. Scheme created in Inkscape based on [Kazakova Maryia]/Adobe Stock [42].The histology shows a small adult specimen obtained from the rat bile duct 12 weeks post infection, which just reached sexual maturity and only had few eggs in the uterus. Diff Quick staining. Scale = 1 mm.

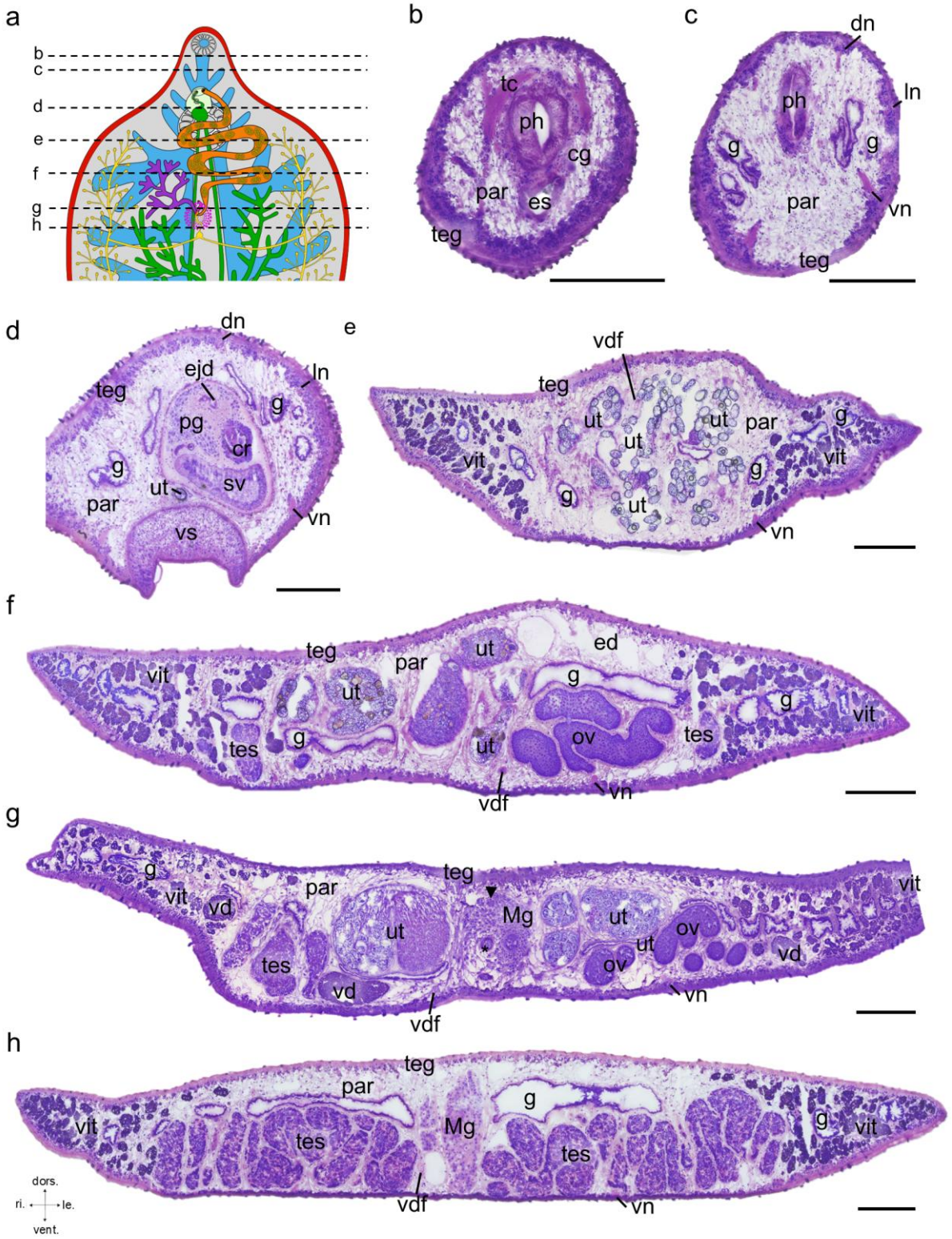

Figure 4 Histology of adult *F. hepatica*.
(**a**) Anatomic scheme, showing sectioning planes of transversal tissue sections shown in (b-h). Scheme created in Inkscape based on [Kazakova Maryia]/Adobe Stock [42]. (**b-h**) Transversal tissue sections of *F. hepatica* (Diff Quick staining). Scale = 0.5 mm. Section orientation is indicated at the bottom. dors.: dorsal, vent: ventral, ri.: right, le.: left. cg: cerebral ganglion, cr: cirrus, dn: dorsal nerve cord, ed: excretory duct, ejd: ejaculatory duct, es: esophagus, g: gut, ln: lateral nerve cord, Mg: Mehli's gland, ov: ovary, par: parenchyma, pg: prostate gland, ph: pharynx, sv: seminal vesicle, tc: transverse commissure, teg: tegument, tes: testis, ut: uterus, vd: vitelline duct, vdf: vas deferens, vit: vitellarium, vn: ventral nerve cord, vs: ventral sucker, arrow head marks Laurer's channel, asterisk marks the ootype.

1.1.3 Pathology and clinical aspects

Fasciolosis can be divided in two phases, which are closely linked to the development of liver flukes in the definitive host: (1) the acute parenchymal phase, during which immature flukes migrate through the liver parenchyma, and (2) the chronic biliary phase, when adult flukes reside in the bile ducts [43]. In natural infections, continuous reinfection and asynchronous development of parasites can prevent a clear separation of the two phases [44]. In addition, clinical signs and pathology are influenced by a variety of co-factors such as the infective dose, parasite strain, host species, age, nutritional status, and overall health [12],[43].

1.1.3.1 Pathology

In the migratory phase, liver damage is not only caused by the mechanical movement and feeding activity of the flukes, but also by their excretory/secretory products, which contain tissue-digesting and immunosuppressive enzymes [12],[43]. When the juvenile flukes migrate through the liver, they leave behind tortuous tracts filled with destroyed liver tissue and blood, which can be seen as red or yellowish streaks and foci on the liver surface (Fig. 5b) [12],[43],[44]. In response to infection and cellular damage, inflammatory cells, including numerous eosinophils and macrophages, infiltrate the migratory ducts and surrounding perivascular spaces [12],[43]. This initiates resorption, regeneration and repair processes, which extend into the chronic phase of the disease. Granulation tissue is formed around necrotic tracts, which will be replaced by connective tissue in the further course [12],[43]. Portal inflammation can lead to vascular thrombosis, resulting in focal infarctions (Fig. 5c) [12]. In addition, the proliferation of connective tissue is stimulated. This inflammatory fibrosis is macroscopically characterized by an enhanced lobular pattern in the liver (Fig. 5c, e) [12].

In the biliary phase, the constant mechanical irritation caused by the fluke's spines and suckers, together with its excretory products, leads to chronic inflammation of the bile ducts (cholangitis) [12],[43]. As a result, the bile duct epithelium proliferates and thickens (hyperplasia). Cholangitis further leads to the proliferation of granulation tissue and subsequent fibrosis or even calcification of the bile ducts, both of the latter being most prominent in cattle [12],[44]. As a result, the bile ducts appear enlarged and whitish (Fig. 5e). Accumulations of liver flukes and bile can lead to a segmental dilations [12],[44]. Inside the bile ducts, dark brown debris and small concretions are often found along with the parasites [43],[44]. The chronic infection causes an increased risk of biliary obstruction, either by the flukes themselves combined with epithelial hyperplasia or by the formation of concrements [7],[43].

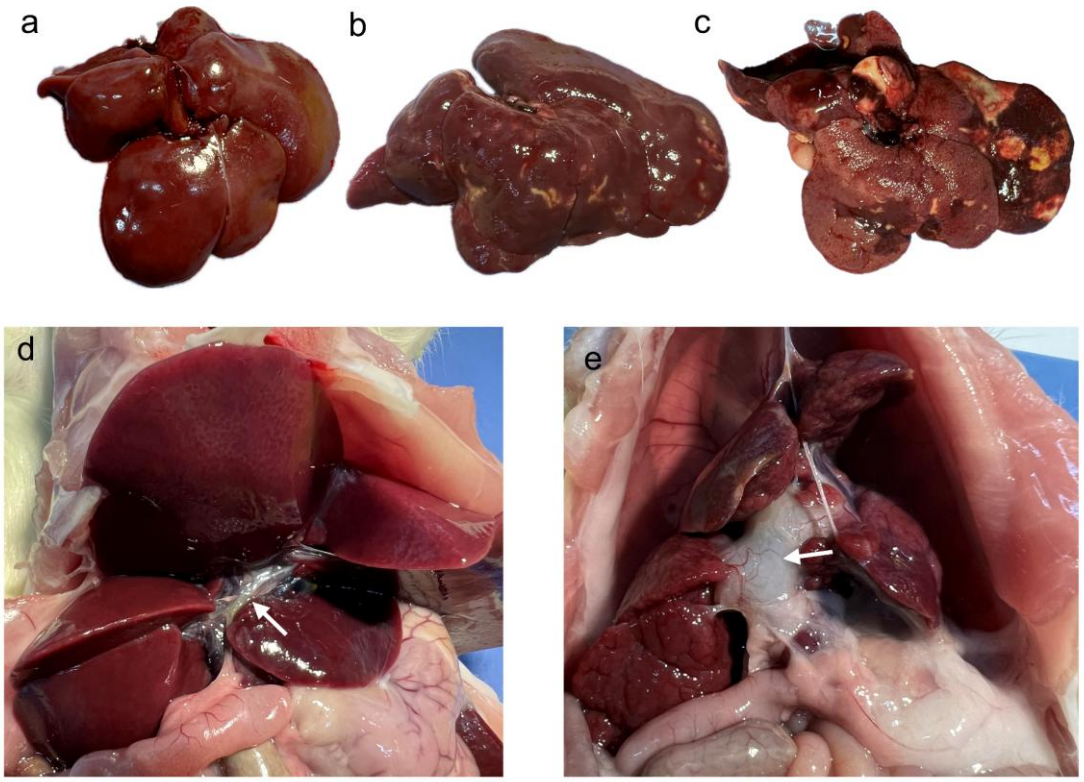

Figure 5 Gross pathology of fasciolosis in the rat.
(**a-c**) Images of isolated rat livers without infection (a), as well as four weeks (b) and 12 weeks (c) after experimental *F. hepatica* infection. (**b**) Liver showing yellowish migratory tracts. (**c**) Liver with large areas of necrosis (yellow) and an enhanced lobulation pattern. Please note that this is a severe presentation. In some animals, almost no macroscopic lesions were seen in the liver, even though adult parasites were found in the bile duct. Others only showed enhanced lobulation without necrosis. (**d, e**) Rat liver *in situ*. The median lobe is lifted to reveal the common bile duct (white arrow). (**d**) Non-infected rat. (**e**) Rat 12 weeks after *F. hepatica* infection. Please note the massive enlargement of the bile duct (arrow).

1.1.3.2 Clinical disease in animals and humans

In heavy infections of susceptible hosts, such as sheep and goats or young bovines, sudden deaths may occur in the acute phase [12],[43] In more protracted courses, the animals show lethargy, anorexia, abdominal pain and pale mucous membranes as signs of hemorrhagic anemia. Blood chemistry and hematology can show elevated liver enzyme levels (AST, GGT) and eosinophilia [12],[45]. These forms of acute fasciolosis can be serious and death of up to 25% of a flock is possible [43],[46]. However, the most common form of fasciolosis is chronic and subclinical, especially in cattle. Chronic disease can be accompanied by weight loss, anemia and subcutaneous edema due to hypoalbuminemia [12],[43]. But even in subclinical cases, reduced weight gains, milk yields, wool quality and fertility are causing economic losses (1.1.4).

The clinical picture in humans is also very heterogeneous: The infection can be asymptomatic but can also cause severe disease. Symptoms in the acute phase include fever, pain in the upper right abdomen, other gastrointestinal symptoms (anorexia, nausea, diarrhea), as well as urticaria and respiratory symptoms as a result of immunopathology triggered by the

inflammation. Jaundice occurs only occasionally. Hematology often shows strong eosinophilia. In the chronic phase, possible symptoms due to biliary obstruction include abdominal pain, fatty food intolerance, nausea and jaundice. Ectopic liver infections in a variety of different organs have also been reported. [7],[43].

1.1.3.3 The rat as model host for *F. hepatica*

Various laboratory animals, including mice, rats, guinea pigs, and rabbits, have been utilized as model hosts in liver fluke research [47]. The development time in experimental models such as rats and mice is shorter than in large animals, which leads to an accelerated disease process [43]. For instance, in mice, the first flukes reach maturity after 35 days post-infection, while in rats, this occurs after about 6 weeks [28]. The recovery rate of flukes from livers of rats infected with 20–30 metacercariae varies between 5-30% [47]–[50]. The pathology of fasciolosis in rats mirrors that observed in other animal species. Due to the smaller size of the rat liver and bile ducts, and the lack of a gallbladder, however, adult flukes predominantly accumulate in the extrahepatic common bile duct near the liver hilus (Fig. 5e) [43],[47]. Clinically affected animals usually exhibit few symptoms, with only a mild depression, marked by roughened fur and slightly increased secretions from the Harderian gland. However, sudden deaths may occur during the subacute stage of infection (approximately 5-10 weeks post-infection), sometimes accompanied by pulmonary hemorrhages, which are believed to result from ectopic immature liver flukes (own observations).

1.1.4 Economic impact

Financial losses due to fasciolosis in the livestock industry are mainly caused by reduced weight gain, milk yield, wool production and fertility, as well as increased treatment costs [51]. The first global estimate of the economic impact of fasciolosis was provided by Boray in 1985 [52], who suggested annual costs of approximately 2 billion US dollars. A more frequently cited second estimate from 1994 proposes that the annual losses are higher, at around 3.2 billion US dollars [53],[54]. However, according to Spithill et al. [54], this number was extrapolated based on data from Indonesia and therefore only applies to tropical fasciolosis caused by *F. gigantica* in Africa and Asia. It is therefore unlikely that this estimate accurately reflects the actual global losses caused by both *Fasciola* species. Updated numbers on global importance are lacking and probably difficult to determine. To get a more realistic idea of the economic burden of fasciolosis, studies from individual regions or countries should be consulted.

For example, in a quite recent study, Charlier et al estimated the costs caused by *F. hepatica* infections of ruminants in 16 European countries, Tunesia and Israel at a total of € 634.5 million per year, with Germany incurring costs of about € 57.6 million [55]. Ninety percent of the estimated German costs were due to production losses and 10% were attributed to treatment costs. Estimates from an earlier report by Fanke et al. on the costs of *F. hepatica* infections in

the German dairy cow population alone were above the estimations for the same population by Charlier et al. (€ 42 million/year vs. € 27.3 million/year), which is due to a different calculation approach and different presumptions [55],[56]. In countries where pasture access in general and sheep production in particular play a greater role than in Germany, such as the UK and Ireland, the total economic impact of fasciolosis is even higher (Charlier et al: IRL: € 99.7 million/ year UK: € 110.6 million/ year). These numbers are comparable to the costs of other epizootic and zoonotic animal diseases in Europe, some of which are being systematically combated [5]. For example, the estimated costs of the blue tongue virus outbreak in Germany between 2006-2018 were maximal with € 66.8 million in 2008 [57]. This illustrates the continuing high economic impact of liver fluke infections.

1.1.5 Diagnostics

The most common diagnostic method for liver fluke infections is the coproscopic detection of eggs using the sedimentation technique [12]. The eggs are oval, 130-150 µm long, with a thin and smooth shell interrupted by an operculum and own a golden yellow color and granulated contents. A limitation of this method is its relatively low sensitivity. In addition, this technique only allows to detect patent infections with adult worms [12], [58]. In humans, it has been further found that flukes may not mature properly and have low egg production [59]. Alternatively, copro-antigen ELISAs are available, which provide higher sensitivity and can even deliver positive result before the start of egg shedding [12]. Serological detection of antibodies in bulk tank milk samples is frequently used for herd diagnostics in dairy cows. This method is quite sensitive and able to detect prepatent infections but has the disadvantage that antibody titers can be detectable for several months after infection [12],[13]. It is therefore not suited to monitor the success of treatments. In humans, serological detection can be carried out using blood samples [59].

1.1.6 Treatment and Control

1.1.6.1 Current control and treatment of fasciolosis

Several different compounds have been shown to be effective against liver fluke infections [60]. In Germany, five compounds (albendazole, clorsulon, closantel, oxyclozanide, triclabendazole) are approved as drugs for cattle and sheep [61]. However, only triclabendazole (TCBZ) in the recommended dosage (10-12 mg/kg) is effective against the immature stages from one week after infection (Tab. 1) [60],[62]. Others, such as albendazole (ABZ) and oxyclozanide, do not show sufficient efficacy until 10-12 weeks after infection [60],[63]. Treatment can be difficult on dairy farms, as several drugs, including TCBZ, may not be used in milk-producing animals or only with withdrawal times [61]. For the treatment of human fasciolosis, TCBZ is the drug of choice recommended by the WHO [64], albeit it is not approved for use in humans in several countries, including Germany.

Table 1 Treatment efficacies of flukicides approved for veterinary use in Germany
Adapted from Alvarez et al. (2021) [60]

Flukicide	Age of fluke (weeks post infection) and efficacy													
	1	2	3	4	5	6	7	8	9	10	11	12	13	14
Albendazole										50-70-%		80-99%		
Oxyclozanide														
Clorsulon										90-99%				
Closantel			23-73%			91-95%					97-100%			
Triclabendazole		90-99%					99-99.9%							

There is currently no commercial vaccine that can be used for the prevention of liver fluke infections [65]. However, management measures can help to reduce the risk of infection. These include pasture rotation systems, fencing off snail habitats (e.g. spring water, slow moving streams) or drainage of wet pastures [13].

1.1.6.2 Triclabendazole: mode of action

The exact mechanism by which TCBZ acts against *F. hepatica* is still not fully understood. TCBZ treatment disrupts the tegument [66],[67] and causes apoptosis in the testes, ovaries and vitelline tissue [38]. It has been shown that treatment of liver flukes with TCBZ stops mitotic and meiotic cellular division [68],[69], the movement of secretory vesicles in the tegument [67] and causes the loss of tubulin immunostaining [70]. These effects are commonly explained by the fact that TCBZ, like other benzimidazole (BZ) compounds [71], binds to β-tubulin and thereby inhibits microtubule polymerization. It is, however, assumed that the binding site or mechanism of TCBZ at the tubulin protein is different from that of other BZs, since

a) TCBZ has an unusual narrow spectrum of target species (*Fasciola spp., Fascioloides magna* & *Paragonimus spp.*), whereas classical BZs are also effective against nematodes, selected cestodes and other trematodes [72]. This has been explained by a different shape of the TCBZ molecule, which is U-shaped instead of L-shaped [72],[73].
b) *F. hepatica* is comparatively insensitive to colchicine and classical BZs [63]. This might be due to the fact that three of the six known liver fluke ß-tubulins have a tyrosine at position 200, instead of phenylalanine [74]. This confirmation is associated with BZ resistance in nematodes [75]. Even if ABZ, a classical carbamate BZ, is used against mature liver flukes, it is only effective at elevated doses, compared to other helminth species [63],[76].
c) TCBZ-resistant *F. hepatica* isolates remain sensitive to ABZ and vice versa [77],[78].

Two recent studies proposed alternative TCBZ binding mechanisms to β-tubulin. Ranjan et al. [79] used a *Haemonchus contortus* β-tubulin model and predicted that TCBZ and ABZ are binding to distinct zones within the colchicine binding domain. In contrast, Olivares-Ferretti et al. [80] created models of all six known *F. hepatica* β-tubulins and found that the nucleotide binding site had a higher affinity for TCBZ-binding, than the albendazole and colchicine binding sites. Both models still require experimental validation, leaving the exact mechanism of TCBZ action unresolved.

1.1.6.3 Drug resistance

The widespread use of TCBZ has led to the emergence of resistance in various regions worldwide. Since the first report of resistance in Australia [81], cases have been reported from South America, New Zeeland and Europe (Great Britain, Ireland, Spain, the Netherlands) [82]. Recently, the first known case of TCBZ resistance in Germany caused death of more than 300 sheep due to treatment failure [46]. Resistance has also been observed against other drugs, such as ABZ [77], clorsulon [83] and closantel [84], and there are already reports of fluke populations exhibiting multi-drug resistance [85].

The mechanisms underlying TCBZ resistance are poorly understood. Three main scenarios have been proposed: (1) mutations in the drug target, (2) increased drug efflux, and (3) increased drug metabolism [82]. In nematodes, mutations in β-tubulin are commonly associated with BZ resistance [75],[86]. However, β-tubulin sequences of TCBZ-sensitive and TCBZ-resistant liver flukes showed no differences [70],[87]. Furthermore, there were no differences in expression levels between isolates before and after exposure to TCBZ [70],[87],[88]. Since resistant parasites have been shown to contain significantly lower TCBZ concentrations [89],[90], resistance more likely involves mechanisms to eliminate the drug by either increased drug efflux or metabolism. Enhanced drug efflux involving efflux pumps such as ABC transporters is a common mechanism of multi-drug resistance in cancer cells [91] and has also been implicated as a cause of drug resistance in nematodes [92]. TBCZ is presumed to be a substrate for such transporters [93],[94] and TCBZ action could be restored in resistant liver flukes by co-incubation with P-glycoprotein inhibitors [90],[95],[96]. Regarding drug metabolism, it has been shown that the conversion of active forms of TCBZ to comparatively inert metabolites (e.g. TCBZ sulphoxide to TCBZ sulphone) was increased in TCBZ-resistant flukes [89],[97]. Furthermore, TCBZ-resistant parasites had increased expression levels and activity of glutathione S-transferases (GST) [98],[99]. As for ABC-transporters, co-incubation with inhibitors of drug-metabolizing enzymes (flavin monooxygenase, cytochrome P450) led to a potentiation of drug action in TCBZ-resistant flukes, which was not seen in TCBZ-susceptible worms [100],[101]. Ongoing research continues to explore the genetic factors contributing to resistance in *Fasciola* spp. A recent genetic crossing experiment between resistant and susceptible strains identified a single heritable locus containing 30 genes, including an ABC-B transporter, which might confer TCBZ-resistance [102]. This finding could provide new insights into resistance mechanisms in the future.

1.1.6.4 Drug development

The limited number of drugs with cross-stage activity, the lack of an effective vaccine, and the spreading resistance to TCBZ drives global research endeavors to find alternative control strategies for fasciolosis [103]. In the search for new treatments against parasites, two primary approaches are distinguished: phenotypic screening and target-based strategies [104]–[106]. Phenotypic screening was the first approach to the search for new antiparasitic drugs. It involves the (random) testing of chemical or natural substances against parasites either *in vitro* or *in vivo,* searching for lethal effects [104]–[106]. In line with this strategy, a collection of 400 anti-infective compounds ("pathogen box") [107] and various natural substances (e.g. plant extracts) were tested against *F. hepatica* [108].

A more recent and more rational approach to drug discovery is the target-based approach. This strategy is based on the assumption that targeting an essential protein could lead to the parasite's death [105],[106]. The first step is to identify a potential target protein and demonstrate its essential role for parasite survival [104]. High-throughput screenings are then conducted to find lead compounds that can effectively interact with the selected protein. After chemical optimization, lead structures are validated by testing them against whole parasites. Growing data resources (genomes, proteomes, protein models) can serve as a source of inspiration for new targets [104],[105],[109]. Not every protein, however, is suitable as a drug target. Protein classes with high druggability (the ability to be modulated by small-molecule compounds) include kinases, G protein-coupled receptors (GPCRs) and ion channels [110]. The development of novel compounds against already known target molecules has the advantage that their druggability and essentiality for the parasite has already been proven. For example, by modifying the chemical structure, derivatives of BZs [111] and TCBZ [112] were generated, which also showed fasciolicidal effects. The recently identified target of praziquantel, a drug widely used against flatworms but without activity against *Fasciola* [113], has also shown to be a promising new target in the common liver fluke. By performing structure-activity studies, the Marchant and Haeberlein labs discovered new agonists of the *F. hepatica* transient receptor membrane ion channel with potent flukicide activity [114].

Instead of taking the lengthy route of drug development, there are also attempts to repurpose approved drugs for antiparasitic treatment. For example, the Haeberlein lab has tested approved kinase inhibitors against schistosomes and liver flukes [115],[116]. Drug repurposing would be the fastest access to new treatment options. However, due to the already known effect on mammalian cells and the associated low selectivity of the drugs, an increased potential for side effects must be expected [117].

1.1.6.5 Vaccine development

A preventive control strategy for fasciolosis, such as vaccination, would be highly desirable both in terms of animal welfare and in terms of reduced drug usage and resistance development. Numerous vaccine trials have been performed over the past decades [51],[118]. Most of these studies have concentrated on proteins found in the parasite's secretome (proteins that the parasite excretes or secretes into its environment). Frequently used candidates include cathepsins, leucine aminopeptidase, glutathione S-transferases (GST) and fatty acid binding proteins (FABP) [51],[118]. These antigens were tested as single vaccines and in combination. In most cases, however, vaccination did not provide a sufficient efficiency (at least 60-70% reduced fluke counts) [51],[118]. In some trials, promising reduction in worm populations of up to 89% were achieved [119], but could not be reliably reproduced in repetition experiments [120]. As a result, no vaccine candidate has made it to market until today. One of the challenges in developing vaccines against fasciolosis is the lack of natural immunity, especially in sheep [109]. Mechanisms of immune modulation and evasion allow the parasites to escape the host's immune system, which impairs the immune response and thus the efficacy of the vaccines [51],[109]. Ideas for new vaccine candidates range from the use of tegumental proteins to stimulate antibody-dependent cytotoxicity to vaccination with extracellular vesicles and glycan-based vaccines [51]. However, it remains open whether these approaches will be more efficient.

1.1.7 'Omics' technologies in liver fluke research

Deciphering the functional role of parasite molecules is essential for the future development of new target-based control strategies [106],[109] (1.1.6.4). Important biological questions of cell biology, growth, development and host-parasite interaction cannot be answered by focusing on a single gene or protein but must be studied from a broader perspective. Advances in sequencing technologies and mass spectrometry and their application to *F. hepatica* have provided the basis for the systematic identification and characterization of biological molecules such as DNA, RNA or proteins. These approaches are summarized under the term "omics" technologies [121]. Liver fluke research has benefited greatly from omics methods and various datasets have been generated over the last decade. The genomes, transcriptomes and proteomes now provide a comprehensive picture ranging from DNA to the expression, production and post-translational modification of parasite proteins [109],[122].

1.1.7.1 Genomics

The first *F. hepatica* genome was published by Cwiklinski et al. in 2015 using an isolate from the UK [123]. Today, two genome assemblies are available via WormBase ParaSite (v19): an updated version of the UK genome (PRJEB58756) and one from the Americas (PRJNA179522, [124]). The liver fluke genome is one of the largest trematode genomes

sequenced to date with a size of about 1.3 Gb [123],[125]. Comparisons of different fluke isolates revealed high numbers of single nucleotide polymorphisms and a high level of genetic diversity, demonstrating a capacity for rapid adaptation and evolution [125],[126]. Another important finding from genome sequencing was the expansion of several gene families, highlighting importance of these molecules for successful parasitism [125]. The multi-member gene families include papain-like cysteine peptidases, cysteine peptidase inhibitors, GPCRs and kinases [109],[125].

1.1.7.2 Transcriptomics

Transcriptome analyses were performed for seven developmental stages of *F. hepatica*: eggs, metacercariae, NEJs, juveniles, immature flukes and adult parasites [123],[124]. These stage-specific transcriptomes provided information on when genes are switched on and off during development and illustrated the complex and dynamic changes that parasites undergo as they transition through their developmental stages [123],[127]. The differences in expression were particularly evident for the extended gene families (e.g. cathepsins, cysteine protease inhibitors) and tubulins [123]. In addition to the protein-coding mRNAs, stage differences in the expression of gene regulatory microRNAs were also observed [128]–[130]. In recent years, transcriptome analyses have been further used to elucidate the molecular mechanisms during the development of juvenile liver flukes *in vitro* and *in vivo,* identifying genes associated with neoblast-like stem cell proliferation [103],[131].

1.1.7.3 Proteomics

Proteomics data sets were generated from the *F. hepatica* somatic proteome [132]–[134], the intestine [135], the tegument [135],[136] and excretory/secretory (ES) proteins (secretome) [132],[134] including extracellular vesicles [137]–[139] (For a more complete list of studies see [109]). The secretome as well as the proteins of the gut and tegument were of particular interest, as they are in direct interaction with the host's immune system and thus form an interesting starting point for vaccine development [109] (1.1.6.5). ES proteins include a variety of proteases, protease inhibitors, antioxidants, immunomodulators and metabolic enzymes, which are thought to be involved not only in immunomodulation but also in the digestion of host tissue [109]. In recent years, post-translational modifications, e.g. glycosylation, of these parasite proteins has further come into focus, adding another level of complexity to the host-parasite interactions [140].

1.2 Spatial Transcriptomics

Multicellular organisms, including helminths, are composed of specialized tissues and organs that fulfill distinct biological functions and consist of a large variety of cells. Although these cells share the same genome, their gene expression patterns can be quite different [141]. The development of transcriptomic technologies and high-throughput RNA sequencing has substantially changed molecular biology in the past decade. However, a major limitation of classical bulk RNAseq approaches, as previously used to study liver fluke biology, is that the organism's transcriptome is analyzed as a whole. This results in a loss of biological details of the sample [142], as transcriptional differences between individual cells are averaged, potentially masking transcripts that only occur in rare cell types.

Therefore, new methods have emerged over the past decade aiming to overcome these limitations: single-cell transcriptomics (scRNAseq) and spatial transcriptomics. Single-cell sequencing technologies enable the analysis of the transcriptome of individual cells, providing insights into the cellular diversity of tissues and entire organisms [143]. This information is very desirable for parasite research, as it allows deeper insights into parasite biology and host-parasite interaction as well as a more strategic drug- and vaccine-target discovery [144]. Therefore, single-cell transcriptome atlases of various schistosome life stages [145],[146] and of the nematode *Brugia malayi* [147] have been created in recent years. In parallel with this work, the Haeberlein lab has generated the first single-cell transcriptomes of adult *F. hepatica* [148],[149].

Despite the high value of scRNAseq, a significant practical challenge remains: the need to release viable cells from tissue without inducing stress, cell death or cell aggregation [149],[150]. Very large, irregularly shaped cells (e.g., neurons) or syncytia, such as the tegument of the liver fluke, are particularly challenging [148],[149]. Furthermore, tissue digestion destroys the typical tissue architecture and therefore lacks spatial information that might be crucial to understand gene function [141]. As a result, ambitions grew to perform transcriptomics directly on the tissue [150]. Traditionally, spatial expression analyses were limited to a few proteins (immunohistochemistry, immunofluorescence) or expressed genes (*in situ* hybridization) [151],[152]. Recent advances in microscopy, imaging, computational methods, sequencing and barcoding technologies have led to rapid development in the field of spatial transcriptomics (ST) [141],[153]. Today, the term "spatial(ly) (resolved) transcriptomics" encompasses a wide range of strategies and technologies that all aim at visualizing and quantifying the mRNA expression of a large number of genes in the spatial context of tissues [150],[151],[154]. This capability has demonstrated high value for improving the understanding of metazoan biology including humans, insects and plants [155]–[157].

ST technologies can be broadly divided into two categories: imaging and sequencing-based technologies [152],[158]. The functional principles of these technologies are briefly summarized below. For more detailed information on the various developments within the different approaches, please refer to respective reviews [154],[159],[160]. In the following, I will compare eight commercially available platforms: GeoMx DSP (NanoString) [161], Visium (10x Genomics) [151], Curio Seeker (Curio Bioscience) [162],[163], Visium HD (10x Genomics) [164], Stereo-seq (STOmics, MGI Tech) [165], MERSCOPE (Vizgen) [166], Xenium (10x Genomics) [167] and CosMx SMI (NanoString) [168].

1.2.1 Imaging-based technologies

In imaging-based ST technologies, RNA molecules are visualized and quantified directly in their native tissue environment using fluorescent signatures [153],[159]. Imaging-based technologies can be further divided into *in situ* hybridization (ISH)-based technologies and *in situ* sequencing (ISS)-based technologies.

ISH technologies use fluorescently labeled probes, complementary to the target RNAs within the tissue [152],[159]. The visualization of hundreds or thousands of genes simultaneously, despite a limited number of fluorophores with distinguishable spectra, is made possible by sequential rounds of hybridization and imaging. This results in a unique sequence of colors or events encoding distinct target transcripts [169]. The different technologies are mainly distinguished by their probe design and coding strategies [153],[158]. Most of them, however, use at least two different probe sets, one target-specific set and a set of readout probes. This two-step labeling approach significantly diminishes the total hybridization time for an experiment, as the hybridization of the readout probes to the primary probe is much faster than direct hybridization to cellular RNA [166].

ISS technologies on the other hand, involve the amplification and sequencing of short barcode sequences or the cDNA sequence itself directly within the tissue [154],[159]. They utilize so-called padlock probes that bind a previously generated cDNA or directly to the target RNA. Upon successful hybridization, the probes undergo ligation to form circular DNA constructs, which are then amplified through rolling circle amplification (RCA). This amplification process produces multiple copies of the circular DNA, enhancing signal intensities [158]. Short sequences of this amplificate are then sequenced with help of fluorescently labelled (oligo-) nucleotides [159].

Among commercial platforms, MERSCOPE and CosMx are true ISH technologies. Xenium, on the other hand, is a hybrid technology using padlock probes in the first step, but *in situ* hybridization in the second step (Fig. 6) [153],[158].

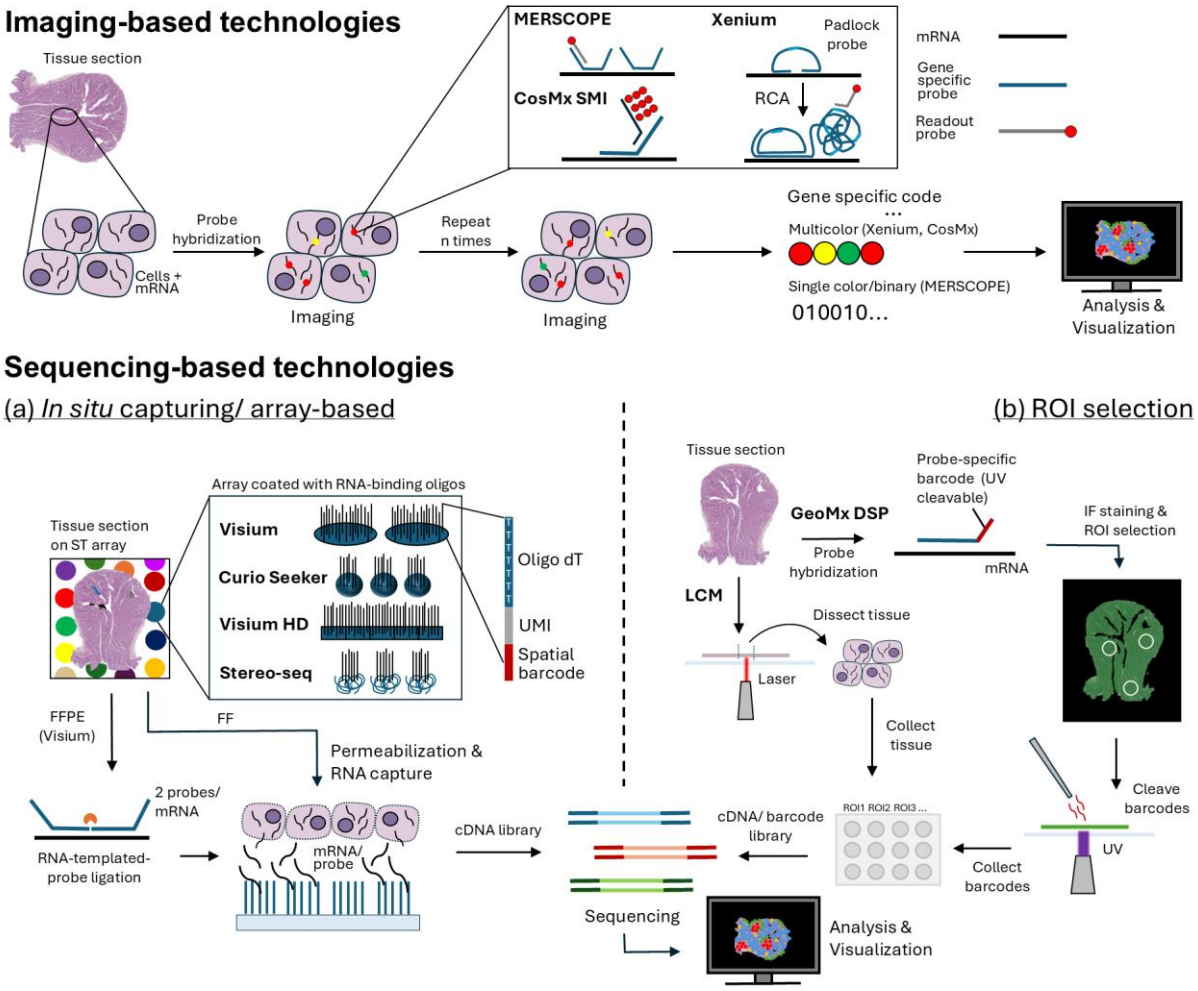

Figure 6 Spatial transcriptomics technologies.
Imaging-based technologies: MERSCOPE, CosMx and Xenium use fluorescently labeled probes to visualize RNAs (black) within the tissue. Two different probes are used: target-specific probes (blue) and readout probes (grey). In the case of Xenium, the primary probe is a padlock probe that undergoes rolling circle amplification (RCA), before readout probe hybridization. Sequential rounds of readout probe hybridization and imaging result in a unique sequence of colors or events encoding distinct target transcripts. **Sequencing-based technologies:** (**a**) *In situ* capturing technologies use oligonucleotide-coated arrays, to capture transcripts released from permeabilized tissue sections. Array technologies differ between approaches: Visium (spots or squares on glass), Curio Seeker (beads), Stereo-seq (DNA nanoballs). Oligonucleotides contain an oligo-dT region, a spatial barcode and a unique molecular identifier (UMI). Visium for FFPE uses RNA-templated probe ligation to create an imprint of the RNA in the tissue. Probes, instead of the mRNA molecules, are bound by the oligonucleotides on the slide. Following a reverse transcription, the cDNA is released from the array and used to generate a NGS library. After sequencing, the position of mRNAs is mapped-back using the spatial barcodes. (**b**) In ROI selection methods, spatial gene expression information is obtained from preselected regions of interest (ROI). Laser capture microdissection (LCM) dissects out tissue regions or cells from a tissue section, which can then be used for RNA sequencing. GeoMx DSP uses gene-specific probes equipped with UV-cleavable barcode sequences. A region of interest is selected microscopically, then exposed to UV light and the liberated barcode sequences are transferred to a well plate for subsequent sequencing. Figure including pictograms created in PowerPoint.

1.2.2 Sequencing-based technologies

In sequencing-based methods, transcripts are identified and quantified outside the tissue using next generation sequencing. Approaches based on the selection of a region of interest are distinguished from *in-situ* capturing or array-based technologies (Fig. 6) [150],[159].

In ROI selection methods (microdissection methods), spatial gene expression information is obtained by simply isolating regions of interest from a sample. This includes laser capture microdissection, which is used to dissect out tissue regions or cells from a tissue section, which can then be used for RNA extraction and bulk RNA sequencing or even scRNAseq [159]. The GeoMx DSP technology represents a further development of the ROI selection strategy [150]. It uses gene-specific probes or antibodies equipped with UV-cleavable linkers to a short gene-specific oligo. A region of interest is selected microscopically, then exposed to UV light, followed by transfer of the liberated identification sequences to a well plate for subsequent sequencing [161]. The ROI can be selected geometrically, zonally or based on immunofluorescence stainings.

In situ capturing technologies rely on oligonucleotide-coated arrays to capture transcripts released from permeabilized tissue sections [153]. The oligonucleotides contain an oligo-dT region, which is able to bind any polyadenylated mRNA. In addition, the oligonucleotides contain a spatial barcode that encodes the position on the slide and an unique molecular identifier (UMI) to identify individual RNA molecules [158]. The transcript sequence is linked to the spatial barcode sequence by reverse transcription. The cDNA can then be separated from the array and is used to generate a NGS library. After sequencing, the position of the mRNAs on the slide is mapped back using the spatial barcodes [153]. Working with formalin-fixed paraffin-embedded (FFPE) tissue, instead of fresh frozen (FF) tissue, is complicated by a higher proportion of degraded RNA [158]. The poly-A-capturing technology, however, is not suited for fragmented RNA [158]. Visium for FFPE (v2) and Visium HD therefore use RNA-templated probe ligation [170]. Upon permeabilization, ligated probes, instead of the RNA molecules themselves, are bound by the oligonucleotides on the slide in a poly-A-mediated manner. Stereo-seq, in contrast, uses random oligos, instead of oligo-dTs, for RNA capturing from FFPE tissue [171]. While different array technologies share several common features, such as the use of spatial DNA barcodes, the methods diverge in aspects like spatial resolution and array technologies [172]. While Visium works with oligonucleotides attached to a glass surface, Curio Seeker uses oligonucleotide-coated beads and Stereo-seq works with DNA nanoballs [158],[163].

1.2.3 Comparison of technologies

The field of spatial transcriptomics is still comparatively young and therefore under constant development. The information presented here is based on the information available in February 2025. An overview of the eight technologies compared is provided in Table 2.

1.2.3.1 Suitable species

A key distinction between different commercial ST technologies is their suitability for different target species. *In situ*-capturing technologies for fresh frozen tissue, working via poly-A-

capture, can be used for more or less any species (Visium v1, Curio Seeker, Stereo-seq). Stereo-seqs “random primer” approach, enables transcriptome analysis from FFPE tissues of all species as well. GeoMx DSP, Visium for FFPE (v2) and Visium HD, in contrast, are probe-based approaches and are therefore only available for human and mouse samples. The three imaging-based platforms provide pre-designed probe panels for human and mouse tissue but also support custom add-on to predesigned panels or even fully custom gene panels. The associated higher costs for custom panels might however be prohibitive (e.g. Xenium ~ 23,500 € for 16 runs with 300 genes in 2023). MERSCOPE may be more cost-effective, compared to other platforms. [158]

1.2.3.2 Resolution

A major strength of imaging-based methods is their capability to visualize RNA molecules on a subcellular level [150],[158]. Sequencing-based array technologies are, however, limited by the diameter of the RNA-capturing features (spots, squares, beads, nanoballs). While the Visium slide provides spot diameters of 55 µm and thus does not allow single-cell resolution, diameters have been significantly reduced for Curio Seeker (slide-seq) (10 µm), Visium HD (2 µm) and Stereo-seq (~0.22 µm) [150],[158]. For Visium HD and Stereo-seq, however, binning to a single cell resolution of 8-10 µm is recommended for data analysis and visualization in order to have enough transcripts per bin available for reliable statistics [158],[173],[174]. In addition, it should be noted that spot size is not the only parameter affecting the actual resolution. Lateral diffusion of transcripts during permeabilization of the tissue also has a marked impact on the spatial accuracy of transcript detection [158]. Recommended ROI size for GeoMx DSP RNA profiling is 200 µm or at least 100 cells [175].

1.2.3.3 Number of genes profiled

Sequencing-based methods deliver whole transcriptome (WT) data and are therefore suitable for unbiased gene expression profiling and hypothesis generation [150],[153]. In contrast, ISH- and most ISS-based technologies are limited to a number of preselected targets and therefore require a clear study hypothesis and prior-knowledge of gene expression in the target species [150],[159]. Clever coding strategies, partially combined with expansion microscopy, have largely overcome limitations of spectral overlap and crowding, allowing the visualization of several thousand genes [176]. Still, an increasing number of targets also increases imaging times (several days - 1 week) [158]. Currently, commercially available imaging techniques can profile ~300-5,000 genes in the case of Xenium and up to 1,000 genes in the case of MERSCOPE [158]. NanoString was the first company to launch a full transcriptome panel for CoxMx SMI in 2024, covering >18,000 human transcripts [177]. However, it has to be noted that higher multiplexing can be accompanied by lower sensitivity, amongst others due to the use of fewer probes per gene [178].

1.2.3.4 Sensitivity/ Capturing efficiency

The different ST platforms have very different RNA capturing efficiencies. In general, imaging-based technologies have a significantly higher capturing efficiency than sequencing-based methods [153],[159]. ISH-based methods are particularly sensitive and have a detection efficiency of 80-100% compared to the gold standard of single-molecule fluorescence ISH (smFISH) [150],[159]. There is lively competition among commercial technologies about who offers higher sensitivity [179],[180], and several studies aiming to compare different technologies have been released as preprints during the last year [181]–[183]. In any case, sensitivity also depends on the tissue type and tissue quality [181],[184]. Among array technologies, probe-based methods are more sensitive than poly-A based approaches, and thus superior for the detection of lowly expressed genes [158].

1.2.3.5 Feasibility/ Instrumentation

All spatial transcriptomics technologies require specialized equipment. Therefore, many were originally restricted to the laboratories in which they were developed in until increasing commercialization made them more accessible [150]. Commercial imaging-based technologies now come with appropriate instrumentation for an automated workflow, imaging and image processing. These platforms are generally acquired and operated by core facilities or service providers due to their high costs. The same applies to GeoMx DSP [150]. Commercial array technologies in contrast, do not necessarily require specialized instrumentation beyond access to next-generation sequencing (NGS) [150].

Table 2 Overview of eight commercial ST technologies

	Sequencing-based technologies					**Imaging-based technologies**		
	GeoMx	**Visium**	**Curio**	**Visium HD**	**Stereo-seq**	**MERSCOPE**	**Xenium**	**CosMx**
Species								
Human & mouse	✓	✓ (v2)		✓		✓	✓	✓
all		✓ (v1)	✓		✓	✓*	✓*	✓*
Tissue type								
FF	✓	✓ (v1)	✓	✓	✓	✓	✓	✓
FFPE	✓	✓ (v2)		✓	✓	✓	✓	✓
Cell culture						✓		
Area [mm]	35 x 14	6.5 x 6.5	3 x 3 10 x 10	6.5 x 6.5	5 x 5 - 20 x 30	up to 3 cm^2	10 x 22	15 x 20
Resolution [µm]	200 (100 cells)	55	10	2	0.22	subcellular	subcellular	subcellular
RNA binding								
Probe-based	✓	✓(v2)		✓		✓	✓	✓
Poly-A/ random		✓ (v1)	✓		✓			
No. of genes	WT	WT	WT	WT	WT	~1,000	~300/ 5k	~100 - WT

*Custom panels for 300-1000 genes available. Well annotated reference transcriptome needed. Elevated costs compared to predesigned panels.

1.3 Hepatocyte nuclear factor 4 (HNF4)

It is generally assumed that proteins expressed in the body surfaces of trematodes, tegument and intestine, are particularly suitable as drug and vaccine targets [185],[186]. These tissues are not only essential for nutrient acquisition and homeostasis but also form primary contact points with the host environment [32], making their molecular components particularly accessible for molecular compounds. An improved understanding of the molecular processes that regulate tissue development and function is therefore a promising starting point for drug target discovery.

1.3.1 Nuclear receptors

Nuclear receptors (NR) are evolutionarily related transcription factors (TF) that play diverse roles in growth, development and homeostasis [187]. The NR superfamily encompasses 21 genes in *Drosophila melanogaster,* 48 in humans, and an unexpected high number of more than 270 genes in the free-living nematode *Caenorhabditis elegans* [188],[189]. In *F. hepatica,* 22 members have been identified [190]. Based on sequence similarity, NRs have been categorized into seven subfamilies and different groups [191],[192]. Nevertheless, they all share a characteristic domain structure consisting of a highly variable N-terminal domain with ligand-independent transactivation regions (A/B domain), a highly conserved DNA-binding domain (C domain), a hinge region (D domain), a ligand-binding domain (LBD, E domain) and another variable region with transactivation functions at the C-terminus (F domain) [187],[193]. The DNA-binding domain (DBD) consists of two zinc fingers: one contains the P-box region, which is responsible for DNA-binding specificity. The other harbors the D-box, which mediates dimerization of the receptor [193]. Although the amino acid sequence of the ligand-binding domain (LBD) or E/F domain varies considerably between different NRs, they all have a common structure of 11-13 alpha helices arranged around a hydrophobic binding pocket [187],[191]. Ligands are endogenous and exogenous lipophilic molecules (e.g. steroids, fatty acids, xenobiotics). Many known receptors, however, have no identifiable physiologically relevant ligand and are termed orphan receptors [187],[191].

NRs act by transcriptional activation or repression of specific target genes, which can be controlled either by a direct DNA-binding dependent mechanism or by cross-talk with other transcriptional regulators [187]. NRs most commonly act as dimers, either as homodimers (steroid hormone receptors (SR), retinoid X receptors (RXR), hepatocyte nuclear factor 4 (HNF4)) or as heterodimers with RXRs (retinoid acid receptor, vitamin, thyroid hormone receptor) [187],[191]. NR binding sites on the DNA, called responsive elements (REs), are hexameric half-site motifs (e.g. AGGTCAxAGGTCA). These hexamers can be arranged as palindromes, direct (DR), everted (ER) or inverted repeats (IR) and separated by a spacer (x) of varying length and sequence, which together with the sequence itself determines the

uniqueness of the RE [187],[191]. REs can be located in the vicinity of the target gene promoter, but also in more distant enhancer regions that approach the transcriptional start site through the formation of chromatin loops [187]. However, the simple presence of an RE sequence in the genome does not determine whether a NR actually binds there and which downstream effects will result from binding [187],[194]. There are various mechanisms that control the interaction of NRs with DNA and the outcome of DNA binding, including structural features such as chromosomal conformation and cooperation with other transcription factors and transcriptional cofactors [194].

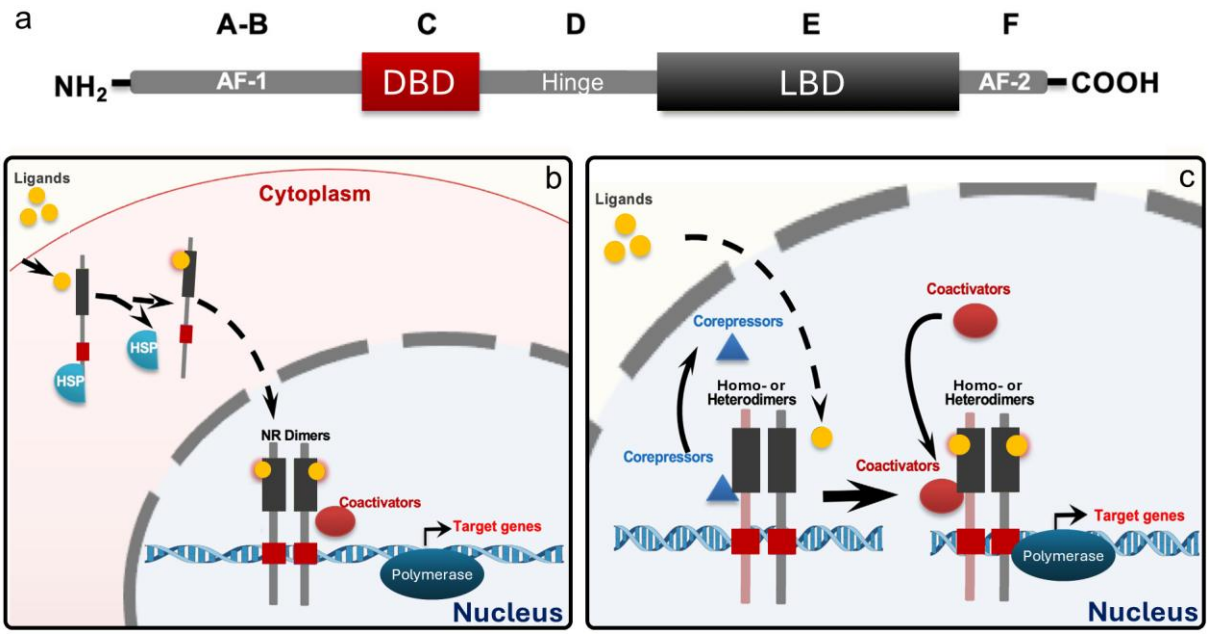

Figure 7 NR structure and mode of action.

(**a**) Domain structure of a typical NR: variable N-terminal domain with transactivation regions (AF-1) (A/B domain), DNA-binding domain (DBD, C domain), a hinge region (D domain), a ligand-binding domain (LBD, E domain) and another variable region with transactivation functions (AF-2) at the C-terminus (F domain). (**b**) Steroid hormone receptors reside in the cytoplasm in complex with heat shock proteins (HSPs). Upon ligand binding, the receptor is released from this complex and is translocated to the nucleus where it binds to response elements as a homodimer to regulate transcription. (**c**) Other NRs (e.g. TR, RAR, (HNF4)) are permanently located in the nucleus. In their unligated state, they interact with co-repressors. Upon ligand binding, co-repressors are exchanged for co-activators and transcription is initiated. Modified figure based on Xu et al. (2023) [195].

Although greatly simplified, two basic mechanisms of NR action can be distinguished: That of classical steroid hormone receptors and that of other NRs (Fig. 7).

(1) In the absence of a ligand, inactive SRs are sequestered by heat shock proteins (HSPs) in the cytoplasm. After ligand binding, a conformational change of the receptor leads to dissociation from the HSP. The SRs then form homodimers and are translocated into the cell nucleus. In the nucleus, the SR complex binds to DNA and transcriptional coactivators and is thus a substrate for the general transcription apparatus and initiates transcription of the target genes. [191],[196],[197]

(2) Other NRs, such as thyroid hormone receptors (TR) and retinoid acid receptors (RAR), do not interact with HSPs and are predominantly localized in the nucleus. In the absence of ligands, these NRs can act as transcriptional repressors together with co-repressor proteins. After ligand binding, the co-repressors are released and replaced by co-activator complexes. Many co-activators are histone-interacting proteins, which lead to chromatin remodeling and promote transcription of the target genes [191],[196],[197]. HNF4 is more similar to the latter TFs but might not involve ligand-dependent activation (1.3.2) [198].

1.3.2 HNF4 and its role for organ differentiation and function

Hepatocyte nuclear factor 4 (HNF4) is one of the most ancient and most highly conserved members of the nuclear receptor superfamily. HNF4 orthologues have been identified in a broad range of animal species ranging from sponge to human [199],[200]. A phylogenetic analysis of NRs across all classes of Platyhelminthes identified HNF4 orthologues in all of the 33 species examined [190].

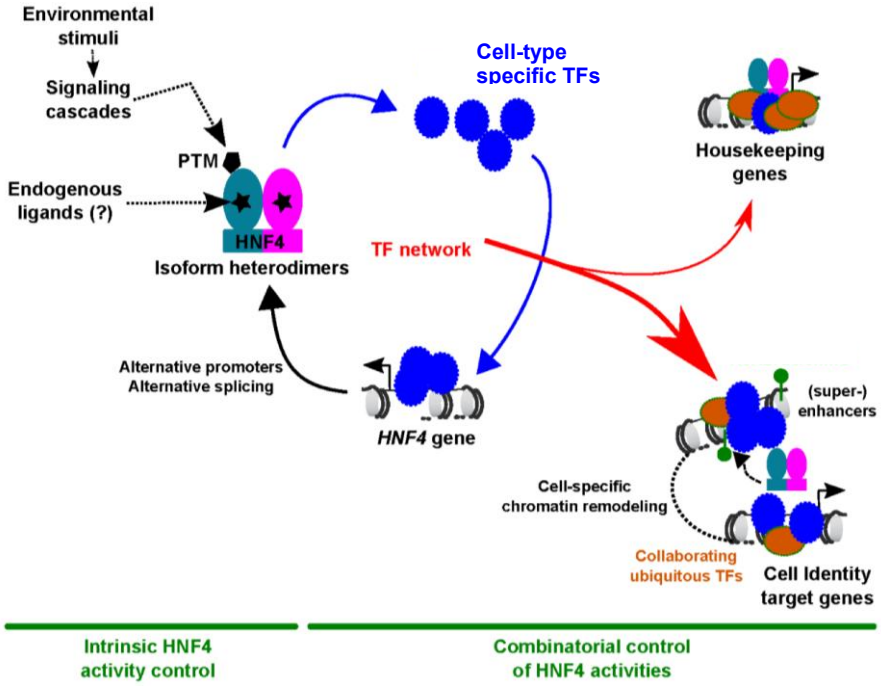

Figure 8 Mechanisms involved in the control of HNF4 activity.
Intrinsic control of HNF4 activities occurs through the expression of distinct isoforms, post-translational modifications, and potential ligands. In addition, HNF4 activity is modulated through cell-specific transcription factor (TF) networks. In these networks, TFs modulate each other's expression and coordinately regulate common (non-TF) target genes. Figure adopted from Dubois et al. (2020) [198].

HNF4 has been grouped in nuclear receptor subfamily 2 [191]. Members of this subfamily were initially characterized as orphan receptors, but later on natural ligands (fatty acids) have been identified [187],[191]. In case of mammalian HNF4α this endogenous ligand seems to be a single, essential fatty acid, linoleic acid [201]. However, it is questionable whether these fatty acids work as classical exchangeable ligands controlling HNF4 activities, as is the case with other NR classes [191],[198]. Instead, alternative cellular mechanisms of controlling TF

activities may play a more important role (Fig. 8). This includes the expression of different isoforms via alternative splicing and alternative promoter usage, which in turn have different affinities for distinct transcriptional cofactors. Post-translational modifications further allow regulation of HNF4 function by external stimuli and the cellular metabolic status [198],[202]. In addition, HNF4 fulfils its role in tight collaboration with other TFs (e.g. Forkhead Box A1 (FOXA1), GATA Binding Protein 4 (GATA4), SMAD Family Member 4, Caudal Type Homeobox 2 (CDX2)), which cross regulate each other's gene expression and collectively bind to and regulate target genes [198].

Mammalians possess two HNF4 paralogues: HNF4α and HNF4γ [202],[203]. HNF4α is expressed in multiple organs (liver, intestine, pancreas and kidneys) whereas HNF4γ is primarily expressed in the intestine [202]. In these organs, HNF4 acts as “a master regulator of cellular differentiation during development and a safekeeper of acquired cell identity in adult organs” [198]. HNF4 does not primarily determine the differentiation lineage that a stem cell undergoes. Instead, during later specification stages, it promotes the expression of genes that are required to form a fully differentiated cell [198],[202]. For example, it controls the expression of brush border genes [204] and genes involved in lipid, glucose and xenobiotic metabolism [205]. At the same time, it suppresses cell proliferation [198]. Mutations or dysregulation of HNF4 have been associated with several human diseases such as maturity onset diabetes of the young (MODY), inflammatory bowel disease (IBD), hepatocellular carcinoma and colorectal cancer [202].

In invertebrate model organisms, HNF4 was also found to be an important regulator of intestinal development, as well as lipid and glucose metabolism. In *D. melanogaster*, HNF4 knockout caused defects in midgut development, while a forkhead box protein was required for the development of the foregut and hindgut [206]. In addition, HNF4 has been shown to regulate intestinal lipid storage, lipid mobilization and β-oxidation in the fruit fly [207],[208]. In the planarian *Schmidtea mediterranea*, a free-living flatworm, *hnf4* is expressed in the gut and intestinal progenitor cells and was found to be essential for intestinal regeneration [209],[210]. A similar expression pattern was observed by Wendt et al., when creating a scRNAseq atlas of adult *Schistosoma manso*ni [146]. In the blood fluke, *hnf4* expression was highest in intestinal progenitor cells (*eled+* neoblasts) but also detected in the mature intestine. Knockdown of *hnf4* transcripts resulted in impaired food uptake and structural abnormalities of the gut, including a dilated lumen and severely reduced microvilli. Furthermore, there was a downregulation of various gut-associated genes, most notably proteases such as cathepsin B. An accumulation of proliferating cells near the intestine suggested that the absence of HNF4 impaired cellular differentiation, and caused an excessive, but unproductive proliferation of intestinal progenitor cells [146]. For liver flukes, however, there was no prior knowledge on the tissue expression or function of HNF4.

1.4 Objectives of this study

The continuing importance of liver fluke infections for human and animal health, their economic impact on the global livestock industry, and increasing anthelmintic resistance emphasize the need for new control strategies. Technological advances, such as bulk RNA sequencing, have provided valuable insights into the unique biology of *F. hepatica.* However, these technologies lack organ-specific information, limiting the depth of understanding gained from these data. A spatial transcriptome would fill this gap by providing comprehensive data on gene expression across different tissues. This approach has the potential to improve our understanding of tissue-specific gene functions in the liver fluke and to facilitate the identification and prioritization of potential drug and vaccine targets. The first part of this thesis therefore focuses on constructing a spatial transcriptome of the adult liver fluke, with the following milestones:

1) Verifying the suitability of liver fluke tissue for spatial transcriptomics by assessing RNA quality and optimizing tissue permeabilization times.
2) Conducting a spatial transcriptomics experiment using the 10x Visium platform and performing subsequent data analysis.
3) Identifying tissue-specific gene expression patterns and validating them by localizing selected marker genes through *in situ* hybridization.
4) Applying the dataset to explore tissue-specific expression patterns of large gene families and investigating its potential as a starting point for target-based drug repurposing.

The second part focusses on the intestine of the liver fluke – an organ vital for its survival. The transcription factor HNF4 is a highly conserved master regulator of gene expression in the intestine of mammals and closely related flatworms such as planarians and schistosomes. The hypothesized role of the transcription factor HNF4 for the intestinal function of the liver fluke will be investigated from a fundamental perspective but also regarding a possible control of the pathogen. The specific aims of this investigation included:

1) Confirming the presence of an HNF4 orthologue in the liver fluke genome.
2) Investigating its tissue-expression using the spatial transcriptomics dataset and *in situ* hybridization.
3) Establishing an experimental platform for post-genomic studies in immature liver flukes
4) Analyzing the relevance of HNF4 for parasite vitality, intestinal function and gut structure by performing RNA interference, transcriptome analysis and microscopic examinations.
5) Evaluating HNF4 as a potential therapeutic target.

2. MATERIALS AND METHODS

2.1 Laboratory maintenance of *F. hepatica*

2.1.1 Ethical statement

Animal experiments using rats (*Rattus norvegicus*) as model hosts were performed in accordance with Directive 2010/63/EU on the protection of animals used for scientific purposes and the German Animal Welfare Act. The experiments were approved by the Regional Council (Regierungspraesidium) Giessen (V54-19c20 15 h 02 GI 18/10 Nr. A16/2018 and V54-19c20 15 h 01 GI 18/10 Nr. V6/2023). [211],[212]

2.1.2 Infection of rats

To obtain immature and adult *F. hepatica*, I orally infected male Wistar rats at an age of 4-6 weeks with 20 (for adult worms) or 25 (for immature worms) metacercariae. Metacercariae were collected from the sheets they were provided on as follows: The sheet was unrolled in a 10 cm petri dish filled with dH_2O using two plastic tweezers. The inner side of the sheet, to which the metacercariae were attached, was kept facing upwards. Originally, the sheet was then placed in a second dish coated with chicken serum (CS) and covered with only 1-2 mm of autoclaved dH_2O. The chicken serum lining fixed the sheet to the bottom of the dish and thus facilitated further steps. However, to prevent the sheets from molding during storage, this step was omitted at later timepoints, and the sheets were simply kept floating in autoclaved dH_2O. Metacercariae were then scraped from the sheet using the tip of a scalpel or a 100 µl pipette under microscopic control, until the required amount of metacercariae was reached. It has proven to be advantageous to directly use the pipette so that detached metacercariae can be immediately pipetted up and transferred to an Eppendorf tube. This prevents counting errors and unnecessary losses of metacercariae.

One week before infection, rats were fed once with sugar water through a 1,000 µl or 200 µl pipette to familiarize them with the procedure. Working with the smaller 200 µl pipette was found superior, especially for young animals. For infection, most of the supernatant water was carefully removed from the Eppendorf tube containing metacercariae. The pipette tip was once flushed with chicken serum before adding 100-150 µl sugar water to the tube containing metacercariae. Metacercariae were resuspended by pipetting up and down and then loaded into the pipette. When the animal was attracted by the pipette, the suspension was fed drop by drop directly into the mouth of the animal. The Eppendorf tube was flushed once again with 100-150 µl of sugar water and the procedure was repeated. A fresh pipette tip was used for each animal to avoid accidental over-infection.

2.1.3 Collection of immature parasites

To isolate immature *F. hepatica,* rats were sacrificed 4 weeks p.i. by CO_2 exposure and cervical dislocation. The liver was harvested, transported in 50 ml Falcon tubes and then incubated in large Petri dishes with NaCl solution, containing 1% ABAM, at 37 °C and 5% CO_2. Dishes were checked for immature worms every 30-60 minutes. After each collection round, the liver was carefully torn into smaller pieces by hand. Then, the NaCl solution was discarded by pouring the solution slowly over the edge of the dish into a sieve (Please note: Immature worms are normally sinking to the bottom of the dish, if the solution is poured, so that the fluid just runs over the edge of the dish, the risk of losing parasites is largely minimized). When it was empty, the dish was again checked for worms. Then, fresh, prewarmed NaCl solution was added for another round of incubation. Collection was completed when the livers could not be broken up any further (approximately after four to five hours). Emigrated flukes were carefully picked up with pointed spring steel tweezers and transferred to a small petri dish containing RPMI 1640 medium supplemented with 1% ABAM solution. Worms were incubated at 37 °C and 5% CO_2 until further use.

2.1.4 Collection of adult parasites

In order to harvest adult flukes from infected rats, animals were sacrificed 12-14 weeks p.i. by CO_2 exposure and cervical dislocation. Adult flukes were then collected from the common bile duct. Worms were transported in falcon tubes and kept in petri dishes containing RPMI 1640 supplemented with 5-10% chicken serum and 1% ABAM solution at 37 °C and 5% CO_2 for at least one hour to allow them to clear their gut contents. The parasites were then used for *in vitro* experiments (2.1.6) or fixed for RNA isolation, Visium and *in situ* hybridizations, as described below (2.4.1/ 2.6.1.1).

2.1.5 *In vitro* culture of immature liver flukes

Immature *F. hepatica* were cultured in 48-well plates containing 650 µl RPMI 1640 medium, supplemented with varying percentages of chicken serum and 1% ABAM-solution, at 37 °C in a 5% CO_2 atmosphere. One to three worms were placed in each well of the plate. Medium was prepared freshly before starting a new experiment. Freshly prepared medium was then stored at 4 °C and used for up to one week. Medium aliquots were prepared in a laminar flow hood and handled only under sterile conditions throughout the *in vitro* culture. Medium was exchanged every two to three days unless the experimental procedure required other intervals. Medium exchanges were carried out as follows: First, fresh medium was added to a new plate (in a laminar flow hood) and allowed to warm up in the incubator. The culture plate was placed on a light plate for better visibility of the worms. Worms were then transferred to the new plate using spring steel tweezers. As it was necessary to observe the work from above during this step, the transfer was usually carried out non-sterile under laboratory conditions. This means

that there was a certain risk of contamination. As a minimum precaution, the light plate and tweezers were always disinfected with 70% ethanol. In addition, for some experiments, an ethanol-cleaned Plexiglas hood with access holes was used to allow semi-sterile handling of the culture plates.

2.1.6 *In vitro* culture of adult liver flukes

Adult *F. hepatica* were cultured in 12-well plates containing 3 ml medium, supplemented with 5% chicken serum and 1% ABAM-solution, at 37 °C in a 5% CO_2 atmosphere. One worm was placed in each well of the plate. Medium was exchanged daily and handled as described for immature liver flukes (2.1.5).

2.1.7 Scoring

Worm motility and phenotype were assessed with each medium exchange and documented by taking images and videos using a Leica TL3000 Ergo stereo microscope. The scoring scheme for adult *F. hepatica* was adapted from Morawietz et al. [115] using the following scores: 3 (normal motility), 2 (reduced motility), 1 (minimal and sporadic movements), and 0 (no movement even upon mechanical stimulation with tweezers was considered dead). The scoring scheme for immature *F. hepatica* was similar, but modified by adding 0.5 steps and phenotypic correlations (Tab. 3).

Table 3 Scoring scheme for immature *F. hepatica*

Score (no.)	Score (words)	Description	Phenotype
3	normal motility	regular and active movements involving the whole body	Thin edges/ body stretched out; translucent; gut structure clearly visible
2.5	slightly reduced motility	regular and active movements involving the whole body, but slower than usual/controls	Thin edges/ body stretched out; translucent; gut structure clearly visible
2	reduced motility	markedly slower movements, sometimes irregular, but still involving the whole body	Slightly contracted and darkened; gut structure washy
1.5	strongly reduced motility	irregular and slow movements, only rarely involving the whole body but mainly the head	Body contracted, opaque/ darkened; no gut structure visible
1	severely reduced motility	irregular and slow movements, not involving the whole body but only the head	Body contracted, opaque /darkened, no gut structure visible
0.5	minimal movements	Only small movements of the oral sucker	Body contracted, opaque /darkened, no gut structure visible
0	No motility/ dead	no movement even when mechanically stimulated with tweezers	Body contracted, opaque /darkened, no gut structure visible

2.2 RNA interference

RNA interference (RNAi) is a natural response to double-stranded RNA (dsRNA) that causes sequence-specific gene silencing (knockdown) by degradation of homologous mRNA [213]. The ability to trigger the RNAi apparatus with artificially generated dsRNA makes RNAi a valuable tool for functional genomics in *F. hepatica* [214],[215].

2.2.1 dsRNA and primer design

To design dsRNAs for RNAi in *F. hepatica*, I first retrieved the coding sequence (CDS) for all genes of interest from WormBase ParaSite [216]. Next, the RNAfold Web Server [217] was used to predict and assess the secondary structure of each transcript. dsRNA sequences of 400-500 bp length (shorter in exceptional cases, see Suppl. Tab. 21) were preferably selected from a region where the mRNA was predicted to form large loop structures. Whenever the mRNA was long enough, multiple (2-3) potential dsRNA sequences were selected for further processing. dsRNA specificity was verified by using siFi2 [218] for off-target prediction (Suppl. Tab. 22). Primers for the amplification of selected dsRNA template sequences from total cDNA, were designed to be 18 to 25 nucleotides long, with a GC content of 35-60% and a melting temperature (T_m) of 60 ± 1.5 °C (salt adjusted value, OligoCalc [219]). The risk of primer dimerization and hairpin formation was checked by using IDT's online tool OligoAnalyzer (limits: T_m hairpins < 40 °C, ΔG of self- and heterodimers > -9 kcal/mol). Primer specificity was verified by WormBase ParaSite BLAST against the whole *F. hepatica* transcriptome. Finally, primers were ordered from IDT. Primer sequences for all genes can be found in Supplementary Table 10.

2.2.2 dsRNA template generation via TA Cloning

Templates for dsRNA synthesis containing T7 polymerase promotors were generated by TA-mediated cloning, of selected cDNA sequences into the vector plasmid pJC53.2 [220].

2.2.2.1 Preamplification and A-tailing

The Q5 High-Fidelity DNA Polymerase was used for precise amplification of dsRNA template sequences from total *F. hepatica* cDNA (Tab. 4, Tab. 5). Successful and specific amplification was verified by agarose gel electrophoresis (1% agarose in TAE buffer + GelRed 1:40,000, 140 V, 60 min). Resulting DNA bands were visualized in an UV chamber and excised for gel extraction. Gel extraction was performed using the Monarch DNA Gel Extraction Kit according to manufacturer's instructions. Samples were eluted in 30 µl Monarch DNA Elution Buffer.

Table 4 Reaction mix for amplification of dsRNA templates from cDNA

COMPONENT	VOLUME
5x Q5 reaction buffer	4 µl
dNTPs [10 mM]	1 µl
Ethylene glycol	1.2 µl
F. hepatica cDNA*	1 µl
PCR-H_2O	10.3 µl
Q5 High-Fidelity DNA polymerase	0.5 µl
Σ Master Mix	18 µl
+ Primer forward [10 mM]	1 µl
+ Primer reverse [10 mM]	1 µl
Σ	20 µl

*derived from 1 µg total RNA of an adult parasite (2.4.1).

Table 5 Thermocycling conditions for amplification of dsRNA templates from cDNA

STEP		TEMP	TIME
Initial Denaturation		98 °C	3 min
35x	Denaturation	95 °C	20 s
	Annealing	60 °C	20 s
	Elongation	72 °C	30 s
Final Extension		72 °C	2 min

In order to allow TA-mediated cloning, the cleaned PCR product was then added to a second PCR using AccuPrime Taq DNA Polymerase (Tab. 6, Tab. 7). This polymerase preferentially adds an adenine to the 3'-end of PCR products.

Table 6 Reaction mix for A-tailing PCR

COMPONENT	VOLUME
AccuPrime PCR buffer I [10x]	5 µl
PCR H_2O	22 µl
DNA from gel extraction	20 µl
Primer forward [10 mM]	1 µl
Primer reverse [10 mM]	1 µl
AccuPrime Taq DNA polymerase	1 µl
Σ	50 µl

Table 7 Thermocycling conditions for A-tailing PCR

STEP		TEMP	TIME
Initial Denaturation		94 °C	3 min
5x	Denaturation	94 °C	20 sec
	Annealing	57.2 °C	20 sec
	Elongation	68 °C	5 min
Final Extension		68 °C	2 min

The PCR product was purified with the Monarch PCR and DNA Cleanup Kit and eluted in 15 µl Monarch DNA Elution Buffer. DNA concentration was determined by photometry.

2.2.2.2 Ligation

The purified PCR product was ligated with AhdI-digested pJC53.2 [220]. First, the vector plasmid was digested by incubating the following reaction mix (Tab. 8) at 37 °C for one hour.

Table 8 Reaction mix for vector digestion

COMPONENT	VOLUME/AMOUNT
pJC53.2	1 µg
CutSmart buffer [10x]	5 µl
AhdI	1 µl
PCR H_2O	Ad 50 µl

The two fragments, resulting from AhdI digestion, were separated by agarose gel electrophoresis (1% agarose in TAE buffer + GelRed 1:40,000, 140 V, 60 min). The larger fragment (3,240 bp) was excised and purified by gel extraction using the Monarch DNA Gel Extraction Kit according to manufacturer's instructions.

For ligation, the insert and vector were combined in a molar ratio of 5:1. The required amount of insert was calculated as follows:

$$m_i = \frac{m_v \cdot s_i \cdot r}{s_v} = \frac{50\ ng \cdot s_i \cdot 5}{3240\ bp}$$

$$v_i = \frac{m_i}{c_i}$$

m_i = insert mass [ng]; m_v = vector mass [ng]; s_i = size insert [bp]; r = ratio insert: vector; s_v = size vector [bp]; c_i = insert concentration [ng/µl], v_i = insert volume [µl]

Table 9 Ligation mix

COMPONENT	VOLUME/AMOUNT
AhdI digested pJC53.2	50 ng
cDNA fragment (insert)	v_i [µl] (depending on insert size and concentration, see calculation above)
T4 DNA ligase buffer [10x]	2 µl
T4 DNA ligase	1 µl
PCR H_2O	Ad 20 µl

The ligation mix (Tab. 9) was incubated at 4 °C overnight. Within the plasmid, the dsRNA template sequence was flanked by T3, SP6 and T7 promotor sequences, which are necessary for dsRNA and riboprobe synthesis by *in vitro* transcription (Fig. 9).

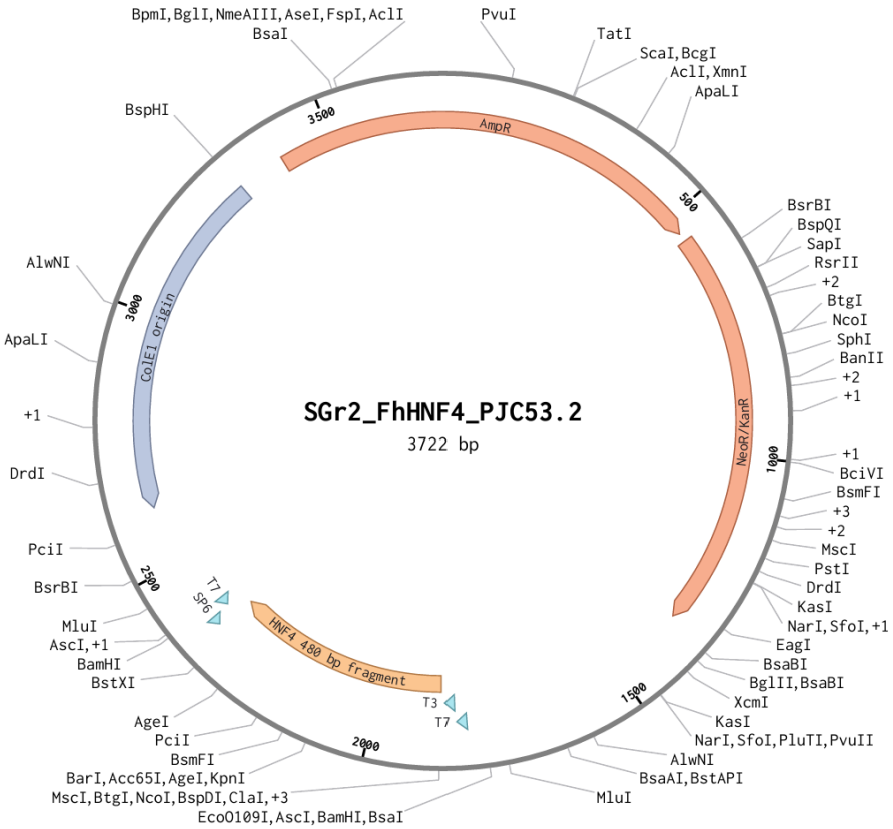

Figure 9 Recombinant pJC53.2 plasmid for dsRNA and riboprobe synthesis.
Plasmid map of pJC53.2 after AhdI digestion and ligation with a 480 bp fragment of Fh*hnf4*, showing insert location, T3, SP6 and T7 promotor positions, restriction sites, ColE1 origin of replication as well as neomycin/kanamycin (NeoR/KanR) and ampicillin (ampR) resistance genes. Created in Benchling [221].

2.2.2.3 Transformation and clone selection

The ligation product (2.2.2.2) was used to transform 5-alpha or 10-beta competent *E. coli* (Suppl. Tab. 2). Competent *E. coli* were taken from their -80 °C storage and thawed on ice. 10 µl ligation product were added to 100 µl competent cells and mixed by gently pipetting up and down. After 20 minutes on ice, a short heat shock was performed at 42 °C for one minute, followed by another three minutes on ice. Finally, 600 µl LB medium were added and the mixture was incubated at 600 rpm and 37 °C for one hour.

After transformation, the *E. coli* suspension was centrifuged at 2,000 g for five minutes and most of the supernatant was discarded, leaving only about 100 µl. *E. coli* were resuspended in the remaining medium and plated on LB selection plates (containing 50 µg/ml kanamycin). Plates were incubated at 37 °C overnight. The next day, five colonies per plate were picked using 10 µl pipette tips and transferred to individual reaction tubes containing 50 µl of LB medium. This colony suspension was then used as template for colony PCR (Tab. 10, Tab. 11) in order to verify the presence and correct assembly of the cloned DNA constructs.

Table 10 Reaction mix for colony PCR

COMPONENT	VOLUME
10x buffer B	1.25 µl
$MgCl_2$ [25 mM]	1.25 µl
T7 ext. primer	1 µl
dNTPs [10 mM]	0.25 µl
FIREPol polymerase (5 U/µl)	0.25 µl
PCR H_2O	6.5 µl
Σ Master Mix	10 µl
+ Plasmid DNA	2.5 µl
Σ	12.5 µl

Table 11 Thermocycling conditions for colony PCR

STEP		TEMP	TIME
Initial Denaturation		95 °C	5 min
35x	Denaturation	95 °C	30 s
	Annealing	58.4 °C	30 s
	Elongation	72 °C	1 min
Final Extension		72 °C	2 min

Successful and specific amplification was verified by agarose gel electrophoresis (1% agarose in TAE buffer + GelRed 1:40,000, 140 V, 60 min). Resulting DNA bands were visualized in an UV chamber. If the colony PCR proved the presence of an insert in the correct size, liquid cultures (4 ml of LB medium containing 50 µg/ml of kanamycin) were inoculated with 20 µl of the colony suspension and incubated at 150 rpm and 37 °C overnight. Generally, I proceeded with two PCR-positive clones per dsRNA template sequence.

2.2.2.4 Plasmid isolation and sequence confirmation

3 ml liquid culture per clone were used for plasmid isolation using the Monarch Plasmid Miniprep Kit. The kit was used according to the manufacturer's instructions. Plasmid DNA was finally eluted with 30 µl of Monarch DNA Elution Buffer.

To confirm the target-specificity of the cloned sequences, plasmids were sent for Sanger sequencing (Microsynth Seqlab, Germany) and subsequently verified by WormBase ParaSite BLAST (Genome: PRJNA179522). Samples for sequencing were prepared as shown in Table 12.

Table 12 Sample preparation for Sanger sequencing

COMPONENT	VOLUME/AMOUNT
Plasmid DNA	400 -1,200 ng
Sequencing primer: pJC53.2_seq_s	3 µl
PCR H_2O	Ad 15 µl

To obtain a fresh *E. coli* culture, 4 ml of fresh LB medium containing 100 µg/ml of kanamycin were inoculated with 30 µl of the previous culture. After incubation at 150 rpm and 37 °C overnight, 800 µl of the culture and 200 µl glycerol were added to a cryogenic tube and frozen at -80 °C.

2.2.2.5 Template generation

Templates for *in vitro* transcription were generated by PCR amplification (Tab. 13, Tab. 14) from plasmids using Q5 High-Fidelity DNA polymerase and an extended T7 primer. [211],[212]

Table 13 Reaction mix for dsRNA template amplification

COMPONENT	VOLUME
5x Q5 Reaction buffer	10 µl
dNTPs [10 mM]	2 µl
Ethylene glycol	3 µl
T7 extended primer	5 µl
PCR H_2O	28.5 µl
Q5 High-Fidelity DNA polymerase	0.5 µl
Σ Master Mix	49 µl
+ Plasmid DNA	1 µl
Σ	20 µl

Table 14 Thermocycling conditions for dsRNA template amplification

STEP		TEMP	TIME
Initial Denaturation		98 °C	3 min
35x	Denaturation	95 °C	10 s
	Annealing	58.4 °C	20 s
	Elongation	72 °C	45 s
Final Extension		72 °C	2 min

DNA templates for synthesis of neomycin dsRNA were generated from pJC53.2 by PCR amplification using FIREPol DNA polymerase and primers with a T7 promotor extension (Tab. 15, Tab. 16).

Table 15 Reaction mix for neomycin dsRNA template amplification

COMPONENT	VOLUME
10x buffer B	5 µl
$MgCl_2$ [25 mM]	5 µl
Ethylene glycol	3 µl
dNTPs [10 mM]	1 µl
Primer forward & reverse	2 µl
Plasmid DNA	1 µl
FIREPol polymerase (5 U/µl)	1 µl
PCR H_2O	30 µl
Σ	50 µl

Table 16 Thermocycling conditions for neomycin dsRNA template amplification

STEP		TEMP	TIME
Initial Denaturation		95 °C	3 min
5x	Denaturation	95 °C	30 s
	Annealing	65 °C	30 s
	Elongation	72 °C	30 s
30x	Denaturation	95 °C	30 s
	Annealing	60 °C	30 s
	Elongation	72 °C	30 s
Final Extension		72 °C	1 min

PCR products were size checked and purified by agarose gel electrophoresis (1% agarose in TAE buffer + GelRed 1:40,000, 140 V, 60 min) and the Monarch DNA Gel Extraction Kit. The kit was used according to the manufacturer's instructions. Samples were eluted in 30 µl Monarch DNA Elution Buffer.

2.2.3 dsRNA synthesis

In vitro transcription of 300-500ng DNA template was performed for four hours or overnight at 37 °C using a T7 RNA polymerase (Tab. 17).

Table 17 Reaction mix for dsRNA synthesis

COMPONENT	VOLUME/AMOUNT
cDNA template	300-500 ng
Reaction buffer [10x]	10 µl
rNTPs [25 mM]	20 µl
IPP	1 µl
T7 RNA polymerase	5 µl
DEPC H_2O	Ad 100 µl

When the incubation time was over, 5 µl of DNase I were added to the reaction and incubated at 37 °C for 30 minutes to remove the DNA template. Then, the dsRNA was precipitated by adding an equal volume of 7.5 M LiCl solution and incubation at -80 °C for at least 30 minutes. Next, the RNA was pelleted by centrifuging at full speed (≥16,000 rpm) and 4 °C for 30 minutes. The supernatant was removed, and the pellet was washed by centrifugation with 500 µl ice cold 70% ethanol at 4 °C for five minutes. The supernatant was removed again and the pellet was dried for two minutes in a thermomixer set to 55 °C (lid open). Finally, the dsRNA was dissolved in 200 µl of DEPC H_2O at 55 °C for 30 minutes. Concentration and purity were checked by photometry. Finally, 8.5 µl of a 1:10 dilution were denatured at 85 °C for 3 minutes, immediately placed back on ice and size checked by agarose gel electrophoresis (1% agarose in TAE buffer + GelRed 1:40,000, 140 V, 60 min). dsRNA was stored at -20 °C until use.

2.2.4 Assessing dsRNA stability under *in vitro* culture conditions

dsRNA stability under *in vitro* culture conditions was assessed by incubating 50 ng/µl dsRNA in different culture media for two hours at 37 °C. RPMI 1640 without chicken serum, RPMI 1640 with 10% heat-inactivated chicken serum (65 °C, 30 min) and RPMI with 10% native chicken serum were compared. When the incubation time was over, the dsRNA was heat-denatured at 85 °C for three minutes and immediately placed on ice. 50 ng/µl of the same dsRNA in RPMI, without any further incubation, were included as a control. dsRNA integrity was then checked by agarose gel electrophoresis (1% agarose in TAE buffer + GelRed 1:40,000, 140 V, 60 min).

2.2.5 dsRNA soaking

RNA interference in immature *F. hepatica* was performed by adding 50 ng/µl dsRNA to the *in vitro* culture. Worms were cultured in 48-well plates with 650 µl medium as described above (2.1.5). Instead of native chicken serum, 10% heat-inactivated chicken serum was used to prevent fast dsRNA degradation. dsRNA against the bacterial neomycin resistance gene was used as dsRNA control. DEPC H_2O served as negative control. Experiments were performed for varying time spans ranging from 7-15 days. During the first three days, medium and dsRNA were exchanged daily, thereafter the medium was changed every second or third day (Tab. 18). Before each medium exchange, fluke phenotype, motility and viability were assessed by scoring (2.1.7).

Table 18 Medium exchange (ME) schedule for a 14-day RNAi experiment

0	1	2	3	4	5	6	7	8	9	10	11	12	13	14
Tu	We	Th	Fr	Sa	Su	Mo	Tu	We	Do	Fr	Sa	So	Mo	Tu
Start	ME	ME	ME			ME		ME		ME			ME	Stop

2.3 Compound treatments

To assess the activity of small-molecule compounds against immature and adult liver flukes, compounds were added to the *in vitro* culture (2.1.5 & 2.1.6). For better comparability with RNAi experiments, heat-inactivated chicken serum was used for compound tests on immature *F. hepatica* as well.

The HNF4 inhibitor BI6015 [222] was dissolved in DMSO at a stock concentration of 25 mM and stored at -80 °C. Following initial experiments with 12.5, 25 and 50 µM performed by Lisa Bauer [223], the inhibitor was used at 25 µM for follow-up experiments. An equal volume of DMSO was used as negative control. Experiments were carried out for 24 and 72 hours. Medium and inhibitor were exchanged daily. Before each medium exchange, fluke phenotype, motility and viability were assessed by scoring (2.1.7).

The PKCβ inhibitor ruboxistaurin [224] was dissolved in DMSO at a stock concentration of 10 mM. The experiments were performed by Simone Häberlein. The inhibitor was used at 100, 50 and 20 µM. An equal volume of DMSO was used as negative control. Equal concentrations of TCBZ served as positive control. Experiments were carried out for 72 hours. Medium and inhibitor were exchanged daily. Before each medium exchange, fluke phenotype, motility and viability were assessed by scoring (2.1.7).

2.4 Expression analyses via qRT-PCR

2.4.1 RNA extraction

Total RNA was isolated from parasites using the Monarch Total RNA Miniprep Kit. One sample (biological replicate) consisted out of 1-2 immature flukes and ½ adult fluke (cut in half from anterior to posterior). Worms were fixed in 150 µl of 1x Monarch DNA/RNA Protection Reagent, snap frozen in liquid nitrogen and stored at -80 °C until RNA isolation. For RNA isolation, worms were thawed and refrozen three to five times in liquid nitrogen and manually homogenized using pestles. Following homogenization, another 150 µl 1x Monarch DNA/RNA Protection Reagent were added to each sample. RNA was then isolated according to the manufacturer's instructions for homogenized tissue and lymphocytes. RNA was finally eluted in 30-50 µl nuclease-free water and stored at -80 °C.

2.4.2 RNA quantification & quality check (QC)

Concentration and integrity of isolated RNA were assessed by electropherogram analysis using the Bioanalyzer 2100 system and the Agilent RNA 6000 Nano or Pico Kit according to manufacturer’s instructions. The only deviation from the protocol was to omit RNA denaturation prior to analysis. Intact liver fluke RNA was characterized by a prominent 18S ribosomal RNA (rRNA) peak and a mostly smaller 28S rRNA peak with a flat baseline between the two peaks and below the 18S rRNA peak (i.e. absence of short fragments). In addition to electropherogram analyses, RNA purity (absence of protein or solvent contaminations) was checked photometrically by determining A230/260 and A280/260 ratios.

2.4.3 Reverse transcription

cDNA used for expression analyses via qRT-PCR was generated by reverse transcription of 30-1,000 ng total RNA using the QuantiTect Reverse Transcription Kit. The concentration of all samples in an experiment was adjusted with DEPC H_2O so that the same amount of RNA was contained in 12 µl of each sample. Potential remnants of genomic DNA (gDNA) were digested with 2 µL of gDNA wipeout buffer at 42 °C for two minutes. The following reaction mix (Tab. 19) was then incubated at 42 °C for 30 minutes.

Table 19 Reaction mix for reverse transcription

COMPONENT	VOLUME
RNA	14 µl
5x RT buffer [10x]	10 µl
RT primer mix	20 µl
Reverse transcriptase	1 µl
Σ	20 µl

Finally, the RT enzyme was heat-inactivated at 95 °C for 3 min. cDNA was stored at -20 °C until use. For qRT-PCR cDNA was diluted 1:5-1:40, depending on the amount of RNA used for reverse transcription.

2.4.4 qRT-PCR primer design

Primers for qRT-PCR were designed based on coding sequences (CDS) provided in WormBase ParaSite [216] (Genome: PRJEB25283). Primers were designed to amplify a sequence of 160 ± 20 bp. When possible, sequences were spanning different exons to distinguish cDNA from potential gDNA contaminations. Primers were 18 to 25 nucleotides long, with a GC content of 35-60% and a melting temperature of 60 ± 0.5 °C (salt adjusted value, OligoCalc [219]). The risk of primer dimerization and hairpin formation was minimized by using IDT's online tool OligoAnalyzer (limits: Tm hairpins < 40 °C, ∆G of self- and heterodimers > -9 kcal/mol). Primer specificity was verified by WormBase ParaSite BLAST against the whole *F. hepatica* transcriptome. Finally, primers were ordered from IDT. Sequences for all qRT-PCR primers used in this study can be found in Supplementary Table 12.

2.4.5 qRT-PCR primer validation and testing of primer efficiency

Each newly designed qRT-PCR primer pair was checked for its function and specificity by performing a standard PCR with *F. hepatica* cDNA as a template (Tab. 20, Tab. 21).

Table 20 Reaction mix for qRT-PCR primer test PCR

COMPONENT	VOLUME
10x buffer B	5 µl
$MgCl_2$ [25 mM]	5 µl
dNTPs [10 mM]	1 µl
F. hepatica cDNA* (1:40)	2 µl
FIREPol polymerase (5 U/µl)	1 µl
PCR H_2O	29 µl
Σ Master Mix	46 µl
+ Primer forward	2 µl
+ Primer reverse	2 µl
Σ	50 µl

*derived from 1 µg total RNA of an adult parasite (2.4.1).

Table 21 Thermocycling conditions for qRT-PCR primer test PCR

STEP		TEMP	TIME
Initial Denaturation		95 °C	5 min
35x	Denaturation	95 °C	30 s
	Annealing	60 °C	30 s
	Elongation	72 °C	1 min
Final Extension		72 °C	2 min

PCR product size and purity were checked by agarose gel electrophoresis (1.5% agarose in TAE buffer + GelRed 1:40,000, 140 V, 60 min). DNA bands were visualized in an UV chamber. If the primers were found to be specific, gel extraction was performed using the Monarch DNA Gel Extraction Kit according to manufacturer's instructions. Samples were eluted in 30 µl Monarch DNA Elution Buffer. The resulting PCR product was then used to create a 10-fold dilution series with five dilutions ranging from 100,000 to 10 amplicons/µl. This dilution series was then used as a template for qRT-PCR (2.4.6). Resulting Ct values were plotted against the amount of DNA concentration and linear regression was performed to obtain the slope of the regression line. Primer efficiency was then calculated using the following formula [225],[226]:

$$E = 10^{-1/m} - 1$$

E = primer efficiency; m = slope

The efficiency should range between 90-110% [225]. Amplification efficiencies of all qRT-PCR primer pairs designed in the course of this work are displayed in Supplementary Table 12.

2.4.6 qRT-PCR

qRT-PCR was performed to determine the relative expression of selected genes in *F. hepatica*. The quantification of PCR products was based on the SYBR Green chemistry. The qRT-PCR master mix (Tab. 22) was prepared in a PCR chamber, which was UV-irradiated for 15 minutes before use. Each reaction was performed as technical triplicate. No template controls (NTC) were included for each pair of primers used in the experiment. qRT-PCRs were run in the Rotor Gene Q qRT-PCR cycler under the following conditions (Tab. 23).

Table 22 Reaction mix for qRT-PCR

COMPONENT	VOLUME
qPCR MasterMix*	10 µl
Primer forward	0.8 µl
Primer reverse	0.8 µl
PCR H_2O	3.4 µl
Σ Master Mix	15 µl
+ sample cDNA	5 µl
Σ	20 µl

* PerfeCTa SYBR Green SuperMix or KAPA SYBR FAST qPCR Kit Master Mix (2x) Universal

Table 23 Thermocycling conditions for qRT-PCR

STEP		TEMP	TIME
Initial Denaturation		95 °C	3 min
45x	Denaturation	95 °C	10 s
	Annealing	60 °C	15 s
	Elongation	72 °C	20 s

Following each qRT-PCR run, the temperature was gradually increased from 60 °C to 95 °C to enable a melting curve analysis. After each qRT-PCR run, the resulting curves were checked for homogeneity of technical replicates and for the absence of DNA contamination in no template controls. If a curve deviated by more than one Ct from the other two curves of a technical triplicate, this curve was considered an outlier and excluded from further analysis. The absence of unwanted PCR products was assessed using the melt peak curve of all samples. If the melting temperature was the same in all samples, the amplification was considered specific.

2.4.7 Data analysis

In this work, I performed relative quantification of gene expression using the delta-delta-Ct-method [227]. To account for technical variations in different samples (e.g. varying RNA/ cDNA input), the expression of each gene of interest (GOI) was normalized to a reference gene. The reference gene glutamyl-prolyl-tRNA synthetase (*eprs*) has been shown to be stably expressed in all relevant life stages and is therefore suited as a reference gene in *F. hepatica* [228]. Normalized GOI expression was calculated as follows:

$$\Delta\mathrm{Ct} = \mathrm{Ct}_{\mathrm{GOI}} - \mathrm{Ct}_{\mathrm{ref}}$$

Relative gene expression levels in dsRNA or inhibitor treated samples compared to untreated controls, were then determined with the following formula:

$$\Delta\Delta\mathrm{Ct} = \Delta\mathrm{Ct}_{\mathrm{treated}} - \Delta\mathrm{Ct}_{\mathrm{control}}$$

The fold change (FC) was finally calculated by exponentiating two with the negative $\Delta\Delta$Ct.

$$\mathrm{FC} = 2^{-\Delta\Delta\mathrm{Ct}}$$

If several control samples were used, the fold-change values of all samples were finally divided by the mean fold change of the controls. This sets mean GOI expression in controls to 100%. Knockdown (KD) efficiency was defined as the difference of GOI expression in dsRNA treated parasites and untreated controls.

$$\text{KD efficiency}\,[\%] = \mathrm{FC}_{\,\mathrm{Ctrl}}\,(100\%) - \mathrm{FC}_{\,\mathrm{RNAi}}[\%]$$

2.5 Expression analyses via RNAseq

For RNAseq, I treated immature *F. hepatica* with *hnf4* dsRNA or HNF4 inhibitor, as described in 2.2.5 and 2.3. RNA was isolated and quality checked as described in 2.4.1 and 2.4.2. Each sample consisted of two worms of the same treatment group that were pooled for RNA isolation (2.4.1). I calculated the knockdown efficiency, after performing reverse transcription and qRT-PCR as described in 2.4. RNA was stored at -80 °C until it was transferred to the sequencing facility at the Center for Infection and Genomics of the Lung (CIGL, JLU Giessen). There, RNA QC, library preparation and sequencing were performed as described in Patrice Tegni Sontia's master's thesis [229]. Sequencing QC, read preprocessing, mapping and differential gene expression analysis were performed by Patrice Tegni Sontia [229] using the Curare pipeline [230]. During this work, the sequencing data was reanalyzed in RStudio [231] using R [232] and the DESeq2 package [233].

2.5.1 Data preparation

For differential gene expression analysis, the DESeq2 package requires untransformed count data [234]. Raw counts were extracted from the "exon.txt"-file provided by Patrice Tegni Sontia and stored in a separate csv-file using Excel. This file was then loaded into RStudio. Expression data (counts) were combined with sample metadata (treatment group) to create a DESeqDataSet data object. For downstream analyses other than differential gene expression analysis – e.g. for visualization or clustering - it is recommended to use homoscedastic data. In RNAseq data, however, variance grows with the mean expression strength of a gene. As a solution, DESeq2 offers the regularized-logarithm (rlog) transformation, such that the rlog-transformed data are approximately homoscedastic [234].

2.5.2 Data QC

To assess the overall similarity between samples, Euclidean distances were calculated using the sampleDists function. The results were visualized as heatmap, using the function heatmap.2 from the gplots package [235]. In addition, principal component analysis (PCA) was performed to visualize sample-to-sample variation.

2.5.3 Differential expression analysis and visualizations

Differential expression analysis was performed by running the DESeq function. Results were inspected, ordered, and filtered for genes with a minimum two-fold up- or downregulation ($-1 > log2FC > 1$) and an adjusted p-value below 0.05.

To obtain an overview of the significance and magnitude of changes in gene expression, a volcano plot was created using the EnhancedVolcano package [236]. It plots the significance ($-\log_{10}$ of adjusted p-values) against the binary logarithm ($\log_2$) of the fold-change (log2FC). Colors were set to highlight genes with significant changes in gene expression (p-value < 0.05)

and genes whose gene expression changed at least two-fold compared to controls (-1 > log2FC > 1). Upregulated genes were colored red. Downregulated genes were colored blue. For labeling, a combined score was calculated by multiplying the $-\log_{10}$ of the adjusted p-value and the log2FC for each gene. The ten genes with highest and lowest score values were then selected for labelling. Volcano plots with group specific coloring (gut/not gut, transcription factors), were created by setting “keyvals” for all genes in that group to “red”, while the rest was colored in grey. For transcription factors (Fig. 42b), a zoomed version of the original volcano plot was created by setting visualization thresholds for log2FC and p-value. Genes exceeding this threshold were indicated as arrow heads at the respective outer border of the plot.

A heatmap was created to visualize the expression of the top 50 significantly up- and down regulated genes (ordered by log2FC) across all RNAi samples individually. The visualization was based on Z-scores, which were calculated by relating the expression level of each gene in a given sample to the mean expression level of that gene across all samples. rlog transformed count values were used for Z-score calculation. The Z-score heatmap was combined with additional columns showing the log2FC of each gene and its average expression (baseMean).

2.5.4 GO term enrichment analysis

The Gene Ontology (GO) is a system for the hierarchical classification of genes or gene products by terms organized in a graph structure (or ontology) [237]. The terms are grouped into three categories: molecular function, biological process and cellular component. Each gene can be described (annotated) with several terms. GO can be used to functionally profile groups of genes (e.g. differentially expressed genes in an RNAseq experiment) and to determine which GO terms occur more frequently than would be expected by chance. GO term enrichment analysis thus tests whether a GO term is statistically enriched for the given group of genes [238].

GO annotation for *F. hepatica* (PRJNA179522) was retrieved from WormBase ParaSite (WBPS18) and complemented by Oliver Puckelwaldt by performing InterProScan [239]. GO term enrichment analysis was conducted using the topGO package [240] in R. The analysis followed the code published by Diaz Soria et al [145], which was adapted to *F. hepatica* by Oliver Puckelwaldt. The weight01 method was used for two categories (BP and MF) with a node size ≥7. The significance of a term’s overrepresentation was assessed using a two-sided Fisher's exact test, using all expressed genes as reference gene set. [211],[212]

2.5.5 Comparison of RNAi and inhibitor experiments

To visualize the proportions of shared and unique DEGs in different experimental groups, a Venn diagram was generated using the VennDiagram package [241]. In addition, a heatmap showing log2FC of all genes that were differentially expressed both in RNAi and inhibitor treated parasites, was created using the ComplexHeatmap package [242]. To add information, an annotation column containing group assignment (gene regulated in all three groups or in only two of them) was included in the figure.

2.6 Spatial Transcriptomics

I performed spatial transcriptomics using the Visium Spatial Gene Expression Solution (10x Genomics) for Fresh Frozen tissue. The methodology described here largely corresponds to that in Gramberg et al. (2024) [211]. The involvement of the co-authors in individual work steps is indicated at the relevant points.

2.6.1 Preparation of the Visium experiment

2.6.1.1 Parasite freezing & embedding

To embed adult parasites for cryosectioning, they were placed in a 20 x 15 x 5 mm cryomold and gently dried with the edge of a paper towel. To immobilize the worm, the mold was placed on ice or within a fridge for one minute. Subsequently, the worm was covered with O.C.T. compound and frozen on a prechilled metal block on dry ice. Tissue blocks were stored in sealed plastic bags at −80 °C. [211]

2.6.1.2 Cryosectioning

Using a Microm HM525 cryostat, 10 µm thick transverse cryosections were obtained from adult *F. hepatica* embedded in O.C.T. compound. The chamber temperature was set to -23 to -25 °C. Tissue blocks and glass slides were prechilled in the cryostat chamber for temperature adjustment for 30 minutes and the blocks were trimmed with a scalpel to match the capture area size (6.5 x 6.5 mm) of a Visium slide. To maintain orientation and identify regions of interest during sectioning, sections were stained every 50–100 µm using a Diff Quick staining and examined with brightfield microscopy. Slides with tissue sections were transported on dry ice and stored at -80 °C until use. [211]

1.1.1.1 H&E staining

H&E staining was performed following the 10x Genomics protocol “Methanol Fixation, H&E Staining & Imaging for Visium Spatial Protocols” [243] with minor changes (for alternative reagents see Suppl. Tab. 3 & 4). Slides with tissue sections were taken from the -80 °C storage, transported on dry ice and placed on a heat plate at 37 °C for one minute. Then, they were transferred to a falcon tube containing prechilled methanol and fixed at -20 °C for 30 minutes. After fixation, the sections were covered with isopropanol and incubated for one

minute. Hematoxylin staining was carried out for seven minutes, followed by three minutes bluing using 0.1% (w/v) sodium hydrogen carbonate solution. Eosin Y (0.5%) was diluted 1:10 in TRIS-acetic acid buffer, before adding it to the sections. Staining was performed for one minute. All washing steps were carried out in clean glass beakers, filled with DEPC H_2O. Stained sections were then dried on a heat plate at 37 °C for five minutes. [211]

1.1.1.2 RNA quality assessment of cryosections

To verify the RNA integrity of cryosections intended for the spatial transcriptomics experiment, sections derived from the same tissue blocks were checked beforehand. First, three sets of 10 cryosections were collected in prechilled Eppendorf tubes. Subsequently, 300 µl 1x Monarch DNA/RNA Protection Reagent were added, and the sample was stored at -80 °C until RNA isolation. For RNA isolation, the samples were subjected to three freeze-thaw cycles using liquid nitrogen. RNA was then extracted using the Monarch Total RNA Miniprep Kit, following the manufacturer's protocol for homogenized tissue and lymphocytes. RNA was finally eluted in 50 µl nuclease-free water. RNA quality was assessed as described in 2.4.2. [211]

1.1.1.3 Tissue optimization

Prior to the spatial transcriptomics experiment, the Visium tissue optimization workflow was performed using the Visium Spatial Tissue Optimization Slide and Reagent Kit (10x Genomics) to evaluate the compatibility of liver fluke tissue with the Visium platform and determine the optimal permeabilization parameters.

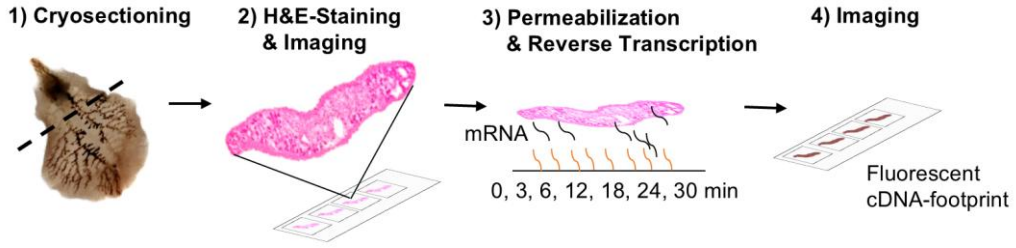

Figure 10 The Visium tissue optimization workflow.
Scheme describing the tissue optimization workflow. Seven transversal cryosections of an adult liver fluke were placed on a 10x Visium Spatial Tissue Optimization slide, H&E-stained and imaged. Tissue sections were enzymatically permeabilized in a time series (0, 3, 6, 9, 12, 18, 30 min). Released mRNA was captured by oligonucleotides on the slide and subsequently reverse transcribed into fluorescently labelled cDNA. Fluorescence microscopy was then used to assess the cDNA footprint on the slide. Scheme created in PowerPoint.

Seven consecutive *F. hepatica* cryosections were prepared as described in 2.6.1.2 and placed on a Visium Tissue Optimization slide. H&E staining was performed, as described in 1.1.1.1. A coverslip was mounted with 180 µl 80% glycerol and the slide was imaged using multiple image alignment (MIA) on the Olympus IX81 microscope. The coverslip was removed by immersing the slide in in 3x SSC. Then, each tissue section was permeabilized for a different

duration (0, 3, 6, 12, 18, 24 and 30 min). A 3 µl drop of *F. hepatica* RNA (700 ng/µl) was used as positive control (prepared as described in 2.4.1). Released mRNA captured on the Visium tissue optimization slide was then reverse transcribed into fluorescently labeled cDNA and visualized using the Olympus IX81 microscope and XM10 camera (see also: 2.10.4). The optimal permeabilization time for the following Visium Spatial Gene Expression workflow was determined by selecting the condition that produced the brightest fluorescence with minimal signal diffusion (blurring). An overview of the workflow is shown in Figure 10. [211]

2.7 Visium Spatial Gene Expression workflow

The following steps were performed using the Visium Spatial Gene Expression Slide and Reagent Kit following the manufacturer's instructions with minor changes (for alternative reagents see Suppl. Tab. 3 & 4) [211],[212]. An overview of the workflow is shown in Figure 11.To prevent RNAse contamination, all laboratory items and surfaces were wiped with RNase AWAY before starting the experiment. Self-made buffers and solutions were prepared with DEPC H_2O and autoclaved prior to the experiment.

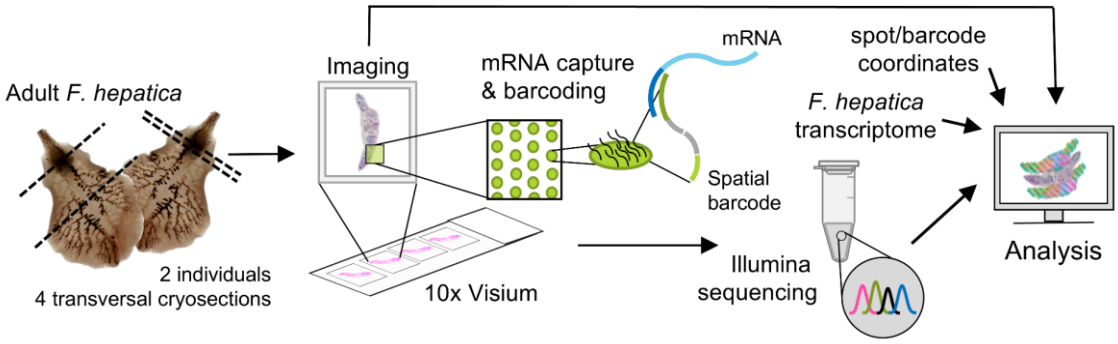

Figure 11 Visium spatial gene expression workflow.
Scheme describing the experimental workflow: Four transversal cryosections of two adult liver flukes were placed on a Visium Spatial Gene Expression slide, stained and imaged. mRNA release, barcoding and sequencing were performed according to the Visium protocol. During the analysis, all transcripts were mapped back to their corresponding spots on the slide and annotated using the reference transcriptome. Scheme created in PowerPoint. [211],[212]

2.7.1.1 Cryosectioning, H&E-staining & imaging

Tissue sections were prepared, as described in 2.6.1.2. Once a region of interest was reached, the consecutive section was transferred onto the Visium slide. In total, I processed four transversal cryosections derived from two different individuals (Adult 1: capture area A & B, Adult 2: capture area C & D). The final sections included ovary, testis and uterus in at least one of the two sections per individual. All four sections contained tegument, vitellarium, parenchyma and intestinal tissue. Mehlis gland was only present in section D. Visium slides with cryosections were transported on dry ice and stored in a sealed bag with desiccant at −80 °C until the following day. H&E-staining was performed as described in 1.1.1.1. Prior to imaging the Visium Spatial Gene Expression slide, a coverslip was mounted with 180 µl 80% glycerol and 7.5 µl RNAse Inhibitor. Tile scanning was conducted using a Leica DMi8

microscope with a DMC2900 color camera. To ensure even sharpness, manual focus points were set all over the tissue section. Software adjustments and scanning of the four sections took two hours in total. After imaging, the slide was transported and stored on a metal plate on ice until permeabilization. [211],[212]

2.7.1.2 Permeabilization, reverse transcription & cDNA release

After imaging, the coverslip was removed by immersing the slide in in 3x SSC. Next, the tissue was enzymatically permeabilized for 12 minutes to release mRNA. This was followed by reverse transcription, second-strand synthesis, and denaturation, according to the manufacturer's instructions. The cDNA from each capture area was then transferred to corresponding PCR tubes for amplification and library construction. [211],[212]

2.7.1.3 cDNA quantification, amplification & QC

I performed qRT-PCR to determine the optimal number of PCR cycles for cDNA amplification in order to generate enough cDNA for library construction. As the two-step protocol given by the manufacturer did not perform well on our qRT-PCR cycler in a test PCR, a modified three step thermocycling protocol (similar to the PCR protocol used for amplification afterwards) was used instead (Tab. 24). [211],[212]

Table 24 Thermocycling conditions used for cDNA amplification

STEP		TEMP	TIME
Initial Denaturation		98 °C	3 min
40x	Denaturation	98 °C	15 s
	Annealing	63 °C	20 s
	Elongation	72 °C	60 s

The four samples reached the threshold of 25% of maximum fluorescence after 12-14 cycles. Accordingly, the cDNA of all samples was amplified using 13 PCR cycles (Veriti 96-Well Thermal Cycler) following manufacturer's instructions. After a cleanup using magnetic beads (SPRIselect) the cDNA was quality checked and quantified using the Agilent 2100 Bioanalyzer system and a high sensitivity DNA chip (Suppl. Fig. 1). [211],[212]

2.7.1.4 Library preparation & sequencing

Library construction and sequencing were performed at the Cologne Center for Genomics (University of Cologne, Germany). Libraries were sequenced on an Illumina Novaseq 6000 with a sequencing depth of about 100,000 reads/ spot covered by tissue. To calculate the required sequencing depth per sample, the number of tissue-covered spots was determined using the Visium Manual Alignment Wizard in Loupe Browser. All raw sequence data were deposited in the Sequence Reade Archive (SRA) under accession number PRJNA1047549. [211],[212]

2.7.2 Spatial transcriptomics data analysis

Code used for data analysis has been deposited at Zenodo (https://doi.org/10.5281/zenodo.10245261) [244]. The resulting dataset can be accessed online using the following link: https://www.uni-giessen.de/haeberlein-lab/en/info (code for online presentation provided by Zhigang Lu, realization: Oliver Puckelwaldt).

2.7.2.1 Mapping

Tissue and fiducial frames in each H&E image were manually aligned with the spot grid of the corresponding capture area using the Visium Manual Alignment Wizard in Loupe Browser. The spaceranger count pipeline was then run by Oliver Puckelwaldt. This pipeline required brightfield images, alignment files, slide information, sequencing data and a reference transcriptome as input data. During the analysis, sequencing reads were mapped to the *F. hepatica* transcriptome and the spatial localization of transcripts was identified based on their spatial barcode. In WBPS17, which served as genomic resource for the analysis, two *F. hepatica* genomes were available: PRJEB2528372 [123] and PRJNA179522 [124]. PRJEB2528372 offered a higher genome assembly quality (BUSCO ASSEMBLY 70.1% vs. 65.6%) and was less fragmented (N50: 1.9 Mb vs. 161.1 kb). However, PRJNA179522 showed slightly better gene annotation (BUSCO ANNOTATION 69.9% vs. 71%), which notably influenced the mapping rate of the sequencing data to the transcriptomes (56% vs. 63% of the mean 118,604 reads per spot confidently mapped to the transcriptome). Furthermore, PRJNA179522 provided more gene descriptions and thus much more biological information, whereas many genes in PRJEB25283 were not annotated (NA). Consequently, PRJNA179522 was selected as the reference genome for analyzing the ST data. The genome was slightly modified by Oliver Puckelwaldt by adding the mitochondrial genome (NC_002546.1). [211]

2.7.2.2 QC

After the spaceranger run, QC was performed by looking at the html output file, giving information on the number of genes and UMIs that were detected per spot, as well as the mapping rate. Data from spaceranger was then imported into R studio for further analysis using the Seurat package [245]. There, the percentage of mitochondrial genes per spot was examined. No filters for gene counts or mitochondrial percentages per spot were applied. However, only tissue-covered spots (selected manually, 2.7.2.1) were included in the further analysis. Data derived from empty spots was excluded. [211],[212]

2.7.2.3 Clustering

Raw count data from each of the four samples was first normalized to account for technical variance (e.g. sequencing depth) across data points using SCTransform with default parameters. The four datasets were then merged in a combined SeuratObject, to enable joint dimensional reduction, clustering and visualization. Linear dimensionality reduction was

performed using principal component analysis (RunPCA). This technique simultaneously removes noise and lowers computation intensity, while keeping the most important information [270],[271]. The principal components (PC) represent sets of genes that are the greatest source of variation in the dataset. Therefore, instead of comparing the expression of >9,000 genes across all spots, I used eight principal components (PC) to find similarities between the spots in the dataset. The optimal number of principal components for dimensionality reduction was determined by examining the ElbowPlot, which plots the standard deviation of each PC. Technical variance between the four different samples (batch effect) was corrected by running RunHarmony [246] (dims.use = 1:8, theta = 0, lambda = 4.7). Subsequently, clustering was performed using Seurat's FindNeighbors (reduction = "harmony", dims = 1:8), FindClusters (resolution = 3) and RunUMAP (reduction = "harmony", dims = 1:8). This initial clustering was then reviewed and annotated based on the underlying tissue types in the H&E images (vitellarium, tegument, parenchyma, gut, uterus, testis, ovary, and Mehlis' gland). For a few spots, the cluster ID did not align with the tissue seen in the histological image. Therefore, spot-barcodes with corresponding cluster IDs and UMAP coordinates were exported from Seurat to Loupe Browser to manually correct mismatching cluster IDs of those spots. New cluster IDs were then re-imported into Seurat to proceed with marker gene analysis. [211],[212]

2.7.2.4 Marker gene identification

Seurat's FindAllMarkers function was used to identify marker genes for each cluster (test.use = "roc", only.pos = TRUE). Gene descriptions for all gene IDs were retrieved from WBPS BioMart and attached to the marker gene list. Following the release of WBPS18, gene descriptions were adopted according to this new version. To identify marker genes for the two cell types of the Mehlis' gland, spots covered by S1 and S2 cells were manually selected in Loupe Browser. Spots associated with other organs and tissues were termed "other." Barcodes and corresponding cluster IDs were then imported into Seurat to perform differential gene expression analysis. Finally, the FindMarkers function was used to identify marker genes for each cell type (test.use = "wilcox" (two-sided Wilcoxon rank sum test), assay = "SCT", only.pos = TRUE). Annotations were added as described above. [211],[212]

2.7.2.5 Visualizations

Spatial expression patterns of marker genes and other genes of interest were displayed using the SpatialFeaturePlot function in Seurat (crop = FALSE, pt.size.factor = 1, alpha = c(0.1,1), image.alpha = 0, stroke = 0.5,). This plot displays log1p transformed count values encoded by color. In addition, to summarize the expression of multiple genes, the DotPlot function was utilized. For selected gene families the average expression of each gene per cluster was calculated an visualized as heatmaps using the ComplexHeatmap package [242]. The heatmaps, similar to the DotPlot, display scaled expression values, which were determined by

calculating the Z-score (= the number of standard deviations of individual cluster expression values from the mean expression value) for each gene individually. [211],[212]

2.7.2.6 Spatial co-expression analysis

To uncover spatial gene expression patterns independent of Seurat-derived clusters, a spatial co-expression analysis was conducted using Giotto [247]. First, a new Giotto object was created that contained the gene expression matrix and barcode locations from section C. Raw counts were normalized via the normalizeGiotto function. To define the spatial relationships between different spots, a spatial network based on Delaunay triangulation was created. The BinSpect-kmeans algorithm was then applied to identify the 2,500 most spatially coherent genes (= genes whose expression correlates with the location in the tissue, i.e. genes with similar expression levels in neighboring spots). The degree of similarity between the spatial expression patterns of different genes (spatial correlation) was then calculated using the detectSpatialCorFeats function. The results were visualized as a heatmap using the function heatmSpatialCorFeats. Clustering resulted in 15 co-expression modules whose spatial expression patterns were summarized as metagenes and visualized using the spatCellPlot function. To compare these metagenes with Seurat clusters, a correlation matrix was calculated after normalizing metagene expression values to a 0–1 range. The correlation results were then displayed as a heatmap using the ComplexHeatmap package [242]. [211]

2.7.2.7 GO term enrichment analysis

GO term enrichment analysis of Seurat cluster markers was performed as described in 2.5.4 with a node size restricted to ≥10. Only marker genes with power values exceeding the 25% percentile of each cluster were considered for this analysis (“top 75%”). For GO term enrichment analysis of genes included in Giotto metagene 1 & 5, the node size was restricted to ≥7. [211],[212]

2.7.3 Drug target prediction

Genes expressed in the tegument and gut were selected for the drug repurposing analysis using the following criteria: First, all genes with very low expression levels were filtered out by only selecting genes whose log1p transformed average expression in all clusters was >1 (sum of all cluster values) and > 0.25 in the respective cluster. This filtering step yielded 3,329 genes for the tegument and 2,962 genes for the gut. The expression data was then scaled by Z-score calculation to identify genes enriched in either the tegument or the gut cluster. Only genes with a scaled expression value >1 were kept for the following drug target prediction, resulting in 474 tegument- and 246 gut-enriched genes. A list of eukaryote single protein targets of approved drugs or compounds in phase 3 clinical trials was retrieved from the ChEMBL database [248]. To identify *F. hepatica* protein orthologs, Oliver Puckelwaldt performed BLAST+ [249] searches against the sequences of all 426 ChEMBL targets, applying an E-value cut-off of 10^{-}

^{5} and only considering the best matches. In cases where two proteins had identical E-values (only E-values of 0.0), both *F. hepatica* proteins were included. A total of 218 *F. hepatica* proteins met these criteria and were therefore classified as potential drug targets. 11 and 10 of these targets were also present in the list of tegument- and gut-enriched genes, respectively. [211]

2.8 *In silico* characterization of *F. hepatica* genes and proteins

2.8.1 Identification of genes and proteins by database search and BLAST

Starting points for the search for selected *F. hepatica* genes or proteins in the PRJNA179522 genome were:

- Protein sequences from other organisms (Ly6, HNF4)
- Keyword searches in WormBase ParaSite (glutathione S-transferase, ABC transporter)
- Lists of gene IDs from the other *F. hepatica* genome assembly PRJEB25283 (stem cell and cell cycle-associated genes)

When sequences from other organisms (*F. gigantica*, schistosome, human) were used, reciprocal BLASTp searches were performed in WormBase ParaSite and NCBI with default parameters to identify *F. hepatica* orthologs (Suppl. Tab. 24 & 27). The glutathione S-transferase and ABC transporter sequences found via the keyword search were verified using BLASTp against *F. hepatica* protein sequences provided in NCBI, model organism proteomes and domain analyses (2.8.2). In the case of stem cell and cell cycle associated genes, the homology information was extracted directly from WormBase ParaSite BioMart without being verified by BLAST.

2.8.2 Protein domain analyses

The domain structure of *F. hepatica* genes of interest and their orthologs was obtained by performing SMART [250] analysis. For HNF4, I additionally used NCBIs Conserved Domain Database (CDD) [251].

2.8.3 Protein secondary structure analysis

The Phyre2 [252] web portal was used to predict the secondary structure of FhHNF4 based on homology to sequences in the Protein Data Bank (PDB). The analysis was run in normal modelling mode.

2.8.4 Alignment and phylogenetic tree construction

Alignments of tegumental Ly6 proteins, PKCβ catalytic domain sequences and HNF4 DNA- and ligand-binding domains were produced using the Muscle (Multiple Sequence Comparison by Log-Expectation) tool of the European Molecular Biology Laboratory (EMBL) [253]. To construct phylogenetic trees, amino acid sequences of GSTs, ABC transporters, and HNF4

were first aligned using the Muscle algorithm implemented in the Molecular Evolutionary Genetics Analysis (MEGA) software version X [254]. Phylogenetic trees were subsequently generated using the maximum likelihood method and JTT matrix-based model with 1,000 bootstrap replicates in MEGA X. [211],[212]

2.8.5 Protein-Protein interaction analyses

Protein-protein interaction analyses were carried out using the STRING online tool [255] after uploading the *F. hepatica* proteome (PRJNA179522, WBPS17), which is now accessible via the organism identifier STRG0085JJO. For HNF4, I used the single protein search, to predict potential interaction partners of this protein, based on the full proteome. To predict protein-protein interactions between cluster markers in the spatial transcriptomics dataset, I entered the top 75% of marker genes per cluster into the multiple protein search. The analysis was performed using default settings with a minimum interaction (confidence) score of 0.4 (medium level of confidence). [211],[212]

2.8.6 Search for HNF4 binding motifs in the *F. hepatica* genome

To search for potential HNF4 binding motifs, I first downloaded the 3,000 bp region upstream the transcriptional start site (TSS) of all genes in the *F. hepatica* genome (PRJNA179522 [124], WPBS18) from WBPS BioMart. Potential HNF4 binding motifs were retrieved from the literature and different databases and inserted into the python-based FRAME tool written by the master student Benedikt Wiebach. Motifs that were used are listed in Table 25.

Table 25 HNF4-binding motifs (IUPAC nucleotide code)

MOTIF NAME	SEQUENCE	REFERENCE
DR1	AGGTCANAGGTCA	[256]
JASPAR3	RGKTCAAAGTYCA	MA0114.3 [257] (modified)
HOCOMOCO	VRGKBCAAAGTYCVN	HNF4A.H12CORE.0.PSM.A [258]
H4-SBM	CAAAGTCCA	[256], MA0114.5 [257]

Lists of genes containing one of these motifs in upstream their TSS were then imported into RStudio. The number of overlaps between those genes found for different motifs and all genes regulated after *hnf4* RNAi was visualized as a Venn diagram using the VennDiagram [241] package.

2.9 *In situ* hybridization

The RNA *in situ* hybridization technique is based on the complementary binding of RNA probes to a specific target sequence (here: mRNA) [259]. These riboprobes are labelled with haptens (e.g. digoxigenin), which can be visualized by immunolocalization. The methodology described here partially corresponds to that in Gramberg et al.(2024) [211]. Supplementary Table 10 indicates which probes were designed and synthesized by Oliver Puckelwaldt. Tobias Schmitt provided technical support for primer design, cloning and *in situ* hybridization.

2.9.1 Probe and primer design

In order to design riboprobes for *in situ* hybridization in *F. hepatica*, I first retrieved the coding sequence (CDS) for all genes of interest from WBPS (Genome: PRJEB25283 & PRJNA179522). The RNAfold Web Server [217] was then used to predict and assess the secondary structure of each transcript. Probe sequences of 400-500 bp length (shorter in exceptional cases, see Suppl. Tab. 21) were preferably selected from a region where the mRNA was predicted to form large loop structures. The riboprobe sequence itself was then again checked for secondary structures (RNAfold [217]) and melting temperature (OligoCalc [219]). Probes with least base-base interactions characterized by large loops in their predicted secondary structure and lowest melting temperature were preferred. Whenever the mRNA was long enough, multiple (2-3) potential probe sequences were selected for further processing. Probe specificity was verified by WormBase ParaSite BLAST against the whole *F. hepatica* transcriptome (<25 bp match with other transcripts, exception: cathepsin L, vitellin protein B1 & cytoplasmic actin: isoforms with high similarity, but no other off-targets). Primers for the amplification of riboprobe template sequences from total cDNA were designed as described for dsRNA in 2.2.1. Primer sequences for all riboprobes used in this work can be found in Supplementary Table 10.

2.9.2 Riboprobe template generation via TA Cloning

Templates for dsRNA synthesis containing T3 and SP6 polymerase promotors were generated by TA-mediated cloning, as described for dsRNA in 2.2.2. BLAST results confirming specificity of cloned riboprobe template sequences can be found in Supplementary Table 21.

2.9.3 Probe synthesis

In vitro transcription of 300-500 ng cDNA template was performed overnight at 28 °C using T3 or SP6 RNA polymerases with the addition of Digoxigenin-11-UTP (Tab. 26). [211],[212]

Table 26 Reaction mix for riboprobe synthesis

COMPONENT	VOLUME/AMOUNT
cDNA template	300-500 ng
Reaction buffer [10x]	2 µl
DIG-NTPs	2 µl
Murine RNase inhibitor	0.6 µl
T3 or SP6 RNA polymerase	1 µl
DEPC H_2O	Ad 20 µl

The next day, 1 µl of DNase I was added to the reaction and incubated at 37 °C for 15 minutes to remove the DNA template. Probes were precipitated by adding an equal volume of 7.5 M LiCl solution and incubation at -80 °C for at least 30 minutes. Next, the RNA was pelleted by centrifuging at full speed (≥16,000 rpm) at 4 °C for 30 minutes. The supernatant was removed, and the pellet was washed with 500 µl ice cold 70% ethanol and centrifugation at 4 °C for five minutes. The supernatant was removed again, and the pellet was air-dried for 10 minutes in a laminar flow hood. Finally, the RNA was dissolved in 20 µl of DEPC H_2O. Concentration and purity were checked by photometry. Finally, 8.5 µl of a 1:10 dilution were denatured at 85 °C for three minutes, immediately placed back on ice and size checked by agarose gel electrophoresis (1% agarose, 140 V, 60 min). Probes were stored at -20 °C or -80 °C.

2.9.4 Cryosections

Parasites were fixed as described in 2.6.1.1. cryosections of 10 µm thickness from adult *F. hepatica* were prepared as described in 2.6.1.2 but placed on Epredia SuperFrost Plus Adhesion slides. From December 2022, sections were prepared using the Epredia CryoStar NX50 cryostat with the specimen temperature set to -7 to -8 °C. For ISH validation of tissue markers from the spatial transcriptomics atlas, I usually placed four to five tissue sections from the “middle part” of the worm (starting behind the ventral sucker) on each slide. These sections contained various combinations of the following reproductive tissues: uterus, ovary, Mehlis’ gland and testis, next to tegument, intestine, vitellarium and parenchyma, which were present in all of the tissue sections. Organs were identified by Diff Quick staining and brightfield microscopy, as described before (2.6.1.1). It was found convenient to prepare about 24 of these slides from one adult parasite.

2.9.5 *In situ* hybridization

In situ hybridizations (ISH) (chromogenic (CISH) or fluorescent (FISH)) were performed following the protocol of Castillo and Koziol [260], with minor modifications. Cryosections were thawed for 30 minutes at room temperature before being post-fixed in 4% formaldehyde in 1x PBS for 15 minutes. Sections were then transferred to a glass cuvette and permeabilized with PBSTx for 10 minutes. For FISH experiments, endogenous peroxidase activity was quenched by incubating the slides in 0.03% H_2O_2 prepared in 4x saline sodium citrate (SSC) buffer for 30 minutes. After washing twice with 4x SSC for five minutes, the slides were transferred to a humid chamber and covered with pre-warmed hybridization buffer. After 10 minutes incubation at 55 °C, the buffer was exchanged and prehybridization was continued for 90 minutes. During the last 15 minutes of prehybridization, probes were diluted to 1 µg/ml in hybridization buffer. Buffer containing probes was heated to 80 °C for three minutes and then pipetted onto the slides. Slides were covered with a piece of parafilm and incubated at 55 °C overnight. The next day, the parafilm was carefully removed by immersing the slide in pre-warmed 2x SSC. This was followed by several washing steps with pre-warmed hybridization washing buffer (2x 20 min) and decreasing concentrations of SSC (2x SSC, 0.2x SSC, 0.1x SSC, 2x 10 minutes each). After washing, the sections were placed in a humid chamber, covered with antibody blocking solution and blocked for one hour at room temperature. Next, blocking buffer containing antibodies in appropriate dilutions (anti-DIG-POD (1:200, FISH) or anti-DIG-AP (1:2000, CISH) was added and the slides were incubated for two hours at room temperature. After washing three times with MAB-T for 10 minutes, the development reaction was carried out. For FISH, I used the TSA Plus Cyanine 3 Kit. The substrate was diluted 1:100 in amplification diluent and 150-200 µl of this solution were pipetted on the slide. Development was carried out for 10-15 minutes in the dark. The reaction was stopped by washing three times in 1x PBS for 10 minutes each. Tissue sections were counterstained with Hoechst 33342 (1 µg/ml) in PBS for 10 minutes and mounted with ROTImount FluorCare. For CISH, the sections were first incubated with 5 mM levamisole in AP buffer for 15 minutes to inactivate endogenous AP activity. Then, the development was started by adding CISH development solution (BCIP/NBT in AP buffer) and carried out under microscopic control until a satisfactory signal was reached. The reaction was stopped by washing in 1x PBS and sections were mounted with 80% glycerol. Imaging of *in situ* hybridizations was performed using the Leica DM IL or the Olympus IX81 microscope (2.10). Numbers of ISH experiments performed for each gene are listed in Supplementary Table 21. When performing ISH, I always used both probes (T3 and SP6) in parallel, one being complementary to the mRNA in the tissue and yielding a specific signal and the other serving as sense control (Suppl. Fig. 4). [211],[212]

2.10 Stainings and Imaging

2.10.1 Carmine staining

Carmine (C.I. 75470) (calcium-aluminum lacquer of carminic acid) stains cell components like nuclei and glycogen [261] and enables high-contrast imaging of parasite organ morphology by confocal laser scanning microscopy [262]. Therefore, this staining was used to assess alterations in gut morphology upon *hnf4* RNAi. To perform carmine staining in immature *F. hepatica,* worms were flat fixed between two glass slides, placed in a small petri dish filled with acidic formaldehyde (AFA) solution and incubated for four hours at room temperature or overnight at 4 °C. After fixation, worms were stored in fresh AFA at 4 °C until use. On the day of staining, worms were placed in netwell inserts in a 12-well plate and incubated in alcoholic hydrochloric acid carmine solution [263] for 30 minutes with gentle agitation. Then, the worms were destained in acidic ethanol until they reached a light pink color (5-15 min). The acidic ethanol was replaced several times during this step. Finally, the flukes were dehydrated in 90% and 100% ethanol for five minutes each and mounted on glass slides using Euparal and a high precision coverslip. When the mounting medium was hardened, samples were evaluated by confocal laser scanning microscopy (2.10.4).

2.10.2 EdU staining

To detect proliferating cells in *F. hepatica,* 500 µM of 5-ethynyl-2′-deoxyuridine (EdU) were added during the last 24 hours of *in vitro* culture [264]. EdU is a nucleoside analogue of thymidine that is incorporated into the DNA during DNA replication (S-phase of the cell cycle) [265]. The molecules' ethynyl groups can be labelled with azide-modified fluorescent dyes through a click chemistry. At the end of the culture, the worms were placed between two glass slides and immobilized with 0.6 M $MgCl_2$ solution (2 M stock diluted with culture medium). Using spring steel tweezers, worms were transferred to small cryomolds, covered with O.C.T. compound and frozen on a metal plate placed on dry ice. Cryosections of immature parasites were prepared similar to what was described for adult parasites (2.6.1.2). Worms were sectioned horizontally, but otherwise under the same settings. The day of staining, sections were thawed at room temperature for 30 minutes and fixed with 4% formaldehyde in 1x PBS for 15 minutes. Fixation was followed by two washing steps in 1x PBS for 5 minutes. Sections were then permeabilized with PBSTx for 10 minutes. After permeabilization, the tissue was washed twice with 1x PBS for three minutes. Click-iT reaction was performed using the Click-iT Plus EdU Cell Proliferation Kit for Imaging according to manufacturer's instructions. 250 µl reaction cocktail were used for each slide. EdU detection was followed by two more washing steps for three minutes in 1x PBS. To the second wash, 1 µg/ml Hoechst 33342 were added and the sections were incubated for another 10 minutes. Finally, a high precision coverslip was mounted using ROTIMount FluorCare and evaluated by fluorescence microscopy (2.10.4).

2.10.3 Tegumental staining using fluorescent dextran

Dextran-labelling of the parasite tegument was performed as described for schistosomes [266]. Immature worms were placed in a 5 mg/ml solution of tetramethylrhodamin(TAMRA)-conjugated dextran in ultrapure water and constantly agitated by gentle vortexing for 5 minutes. The fixing procedure was based on the NA/FA fixation protocol by Guerrero-Hernández et al. [267]. Worms were placed between two glass slides and immobilized with NA solution (Please note: Worms curl on contact with the NA solution if they are not weighted down). When they stopped moving (after 1-2 min), NA solution was replaced by FA solution and the worms were flat-fixed for two hours at room temperature. Next, the samples were washed two times in PBSTx for 10 minutes and then dehydrated in 50% MeOH/ PBSTx and 100% MeOH at RT for 10 minutes each. Worms were stored in fresh 100% MeOH at -20 °C until further use. To stain nuclei, the samples were rehydrated in 50% MeOH/PBSTx and PBSTx for 10 minutes each and then incubated with 1 µg/ml Hoechst 33342 in 1x PBS overnight at 4 °C. For imaging, worms were mounted on glass slides using ROTIMount FluorCare and high precision coverslips and then evaluated by confocal laser scanning microscopy (2.10.4).

2.10.4 Fluorescence and confocal laser scanning microscopy (CLSM)

Three different fluorescence microscopes were used to evaluate and image the fluorescent stainings created in this work: Leica DMIL LED Fluo, Olympus IX81 and a confocal laser scanning microscope (CLSM, Leica TCS SP5). For each fluorophore, appropriate filter cubes or lasers were selected according to Table 27. Illumination settings were chosen considering pixel saturation heatmaps and adjusted so that only few saturated pixels were present. When negative controls were available (e.g. for FISH), the exposure time was selected so that no background signal was visible in the control. In contrast to the DMIL, the IX81 had a motorized stage and a Multiple Image Alignment (MIA) function, which was used to create overview images of entire tissue sections. Brightness and contrast of the acquired images were linearly adjusted using Fiji. The adjustments were applied separately to each fluorescence channel before the channels were merged.

Table 27 Fluorescent dyes, wavelengths and filters/ lasers used on different microscopes

Dye	Purpose	Exc λ	Em λ	DM-IL	IX81	CLSM
Hoechst 33342	Staining of DNA/Nuclei	346 nm	460 nm	A/DAPI	DAPI	405 nm Diode
Carmine	Carmine staining	Spectrum broad [268]	585 nm	-	-	Argon 488 nm
Alexa 488	EdU staining	495 nm	520 nm	GFP	GFP/FITC	Argon 488 nm
Cy3	ISH	550 nm	570 nm	N2.1	DsRed/ RFP	Yellow Diode 561 nm
TRITC/ TAMRA	Visium TO, dextran staining	555 nm	580 nm	N2.1	DsRed/ RFP	Yellow Diode 561 nm

Confocal laser scanning microscopy was used to examine carmine-stained flukes, dextran stainings and detailed imaging of EdU stainings and *in situ* hybridizations. Optical section thickness and background signals were defined by setting the pinhole size to 1 Airy unit. The line average was 4-16 and the resolution was set to 1,024 x 1,024 pixels. For carmine staining, gain and offset were optimized for each sample individually. If different groups were to be compared, gain and offset were adjusted for a control sample and kept constant for all other samples of the same experiment. Pictures of multicolor stainings were taken using sequential scanning (frame by frame).

2.10.5 Transmission electron microscopy (TEM)

For TEM, immature worms were flat-fixed in 0.1 M sodium cacodylate buffer containing 4% (v/v) formaldehyde and 2.5% (v/v) glutaraldehyde for three hours at room temperature. The fixative was refreshed, and fixation was continued overnight at 4 °C in 2 ml Eppendorf tubes placed on a rotating device. Fixed flukes were stored in 0.1 M cacodylate buffer containing 0.4% (v/v) formaldehyde at 4 °C before being cut into three pieces: Using a scalpel, two sagittal sections were performed on the left and right of the apical conus. One of the lateral parts as well as the median part were then placed in a specimen jar containing 0.4% (v/v) formaldehyde in 0.1 M cacodylate buffer for further processing. The following steps were performed by Sabine Agel at the BFS Imaging Unit (JLU Giessen): Samples were postfixed using 0.1 M cacodylate buffer containing 1% (v/v) formaldehyde for one hour at room temperature. After rinsing three times with cacodylate buffer and ultra-pure water each, samples were contrasted using 2% uranyl acetate over night at 4 °C. The next day, samples were rinsed three times with ultra-pure water, dehydrated through a graded ethanol series, before being infiltrated and embedded to Araldite (2 worms) or LR-White (1 worm) embedding resin. Ultrathin sections (70 nm) were prepared using a Reichert Ultracut S ultramicrotome and placed on copper slot grits (coated with Formvar). Sections were contrasted using UranyLess and lead citrate for one minute each. Images were captured with a LEO 912 AB transmission electron microscope, operating at an accelerating voltage of 120 kV.

2.11 Statistics and reproducibility

The spatial transcriptomics workflow was conducted once using a single Visium Spatial Gene Expression slide. The spatial transcriptome was analyzed from $n = 4$ tissue sections derived from two individual parasites, which had been collected at different time points from different host animals. Each tissue section was considered as biological replicate. Statistical analysis of spatial transcriptomics data was performed in R using Seurat, Giotto and topGO as described in previous methods sections (2.7.2). [211]

The bulk RNAseq experiment was performed once using n=3 samples per group (two worms/sample). The samples were derived from a single *vitro* culture experiment in the case of RNAi and 24-hour inhibitor treatment. In the case of the 72-hour timepoint, I pooled worms from two independent experiments. Each sample was considered as biological replicate. Statistical analysis of RNAseq data was performed in R using DESeq2 and topGO as described in previous methods sections (2.5).

Numbers of replicates and statistical details for *in vitro* culture experiments and qRT-PCRs are indicated in the respective figure legends. For *in vitro* cultures, individual parasites were considered as biological replicates. For qRT-PCR one sample consisted of one to two immature worms. Statistical analysis and visualizations were performed using GraphPad Prism. Data was tested for normality using four tests embedded in GraphPad Prism (D'Agostino-Pearson omnibus (K2), Anderson-Darling (A2*), Shapiro-Wilk (W), Kolmogorov-Smirnov (distance)) and by examining the QQ plot. When data was normally distributed, a parametric test (ANOVA) were performed. For non-normally distributed data a non-parametric test (Mann-Whitney test) was used. Post-hoc analyses (Tukey's multiple comparisons test or Holm-Šídák method) were performed when comparing multiple groups or analyzing multiple timepoints.

In situ hybridizations in adult parasites were conducted using $n = 2–5$ tissue sections per independent experiment to ensure consistency of expression patterns. Replicates were carried out on sections obtained from different individual parasites [211]. The number of independent ISH experiments performed for each gene is detailed in Supplementary Table 21. Replicate numbers for FISH of RNAi parasites, carmine stainings, TEM and EdU stainings are indicated in the figure legends. Individual parasites were considered biological replicates. [211]

3. RESULTS

This work is divided into two parts. The first part (3.1), focusses on the generation of a spatial transcriptome for adult *F. hepatica*, including its validation and examples for its application. In the second part (3.2), I will describe the identification and characterization of the transcription factor HNF4 and its putative role in the intestine of *F. hepatica.*

3.1 Spatial Transcriptomics

In this part of the thesis, I will describe how the Visium technology (10x Genomics) was used to generate a spatial transcriptome for the adult life stage of *F. hepatica*. The data presented in this chapter has been published in Gramberg et al. (2024) [211]. Please note that the term “expression” in this work always refers to transcript levels and not protein levels.

3.1.1 RNA integrity determination and tissue optimization

The Visium technology requires RNA with an RNA integrity number (RIN) >7. Therefore, in advance of the spatial transcriptomics experiment, total RNA was extracted from cryosections and analyzed using capillary electrophoresis. The electropherograms of both samples showed a prominent 18S rRNA peak and a flat baseline, proving the absence of short fragments resulting from degradation (Fig. 12). However, RIN calculation was not possible, as the 18S rRNA peaks were considerably larger than the 28S peak.

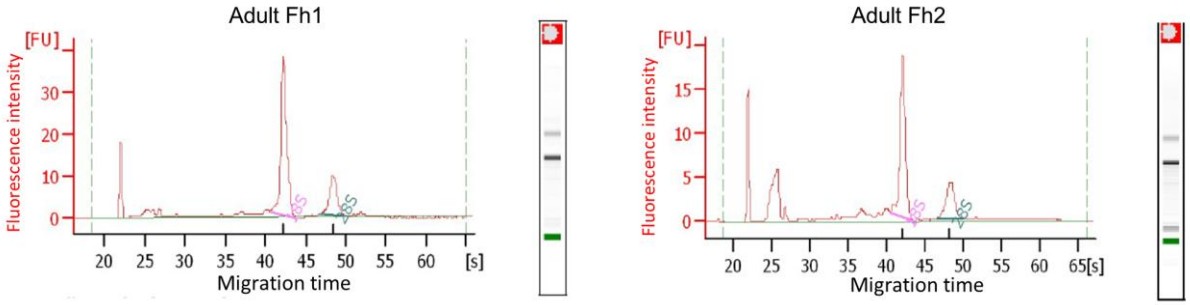

Figure 12 *F. hepatica* cryosections provided good RNA quality.
Agilent Bioanalyzer electropherograms of RNA derived from *F. hepatica* tissue sections. 18S and 28S rRNA peaks are labeled. Both samples used in the spatial transcriptomics experiment are shown. [211],[212]

To test whether the Visium digestion protocol was generally suited for liver fluke tissue and to determine the optimal tissue permeabilization time, the 10x Visium tissue optimization (TO) workflow was performed on liver fluke cryosections. The tissue sections used, corresponding permeabilization times and resulting cDNA footprints are shown in Figure 10. The positive control produced a strong fluorescent signal, while the non-permeabilized section (negative control) showed no fluorescence. Permeabilized tissue sections yielded fluorescent cDNA footprints that matched the shape of the tissue sections on the slide, but with varying fluorescence intensity depending on the tissue permeabilization time. The permeabilization

time, which produced the strongest fluorescence signal with minimal signal diffusion, was 12 minutes (Fig. 13). [211]

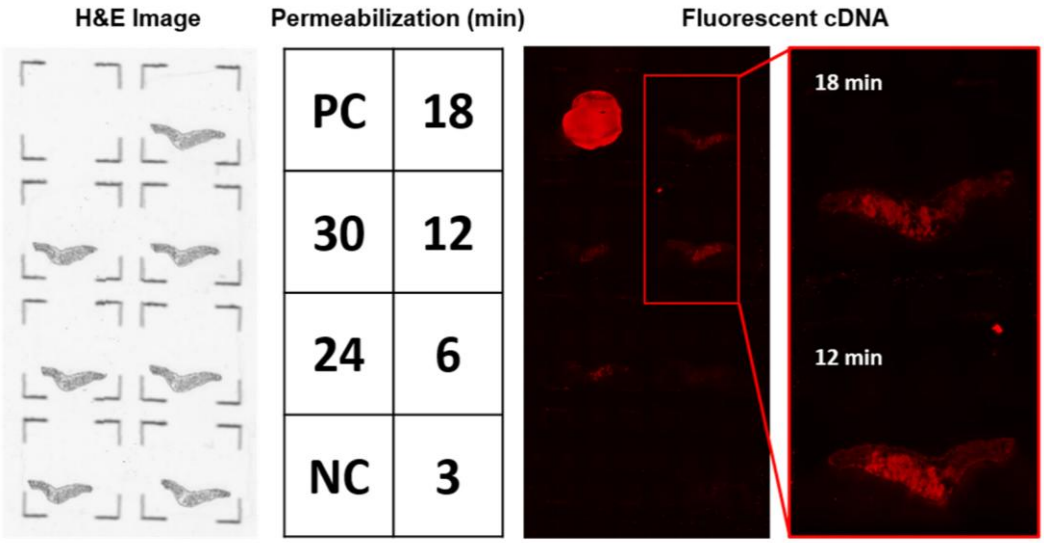

Figure 13 The optimal permeabilization time for liver fluke tissue sections.
H&E-stained tissue sections (left), corresponding permeabilization times (middle) and fluorescent (TRITC-labeled) cDNA (right, incl. magnified view of the 12 & 18 min timepoint). Six sections were treated with permeabilization enzyme, the seventh was kept untreated and served as negative control (NC, 0 min permeabilization). The frame on the upper left did not contain a tissue section, but a drop of *F. hepatica* RNA, which served as positive control (PC). [211],[212]

3.1.2 Generating a spatial transcriptome of adult liver flukes

3.1.2.1 9,847 liver fluke genes captured by spatial transcriptomics

After completion of the TO experiment, the Visium Spatial Gene Expression workflow was performed (Fig. 11). The four cryosections used together covered a total of 2,020 mRNA-binding spots. Each of the spots captured a median of 2,192 genes and 6,138 UMIs (unique molecular identifiers) (Tab. 28). In total, over all spots, the experiment detected transcripts of 9,847 different genes, constituting 79.3% of all gene transcripts in the *F. hepatica* transcriptome [124]. These values were comparable between the different samples. Only section B provided somewhat lower gene and UMI counts per spot.

Table 28 Sample metrics

Sample	Capture area	No. of spots under tissue	Mean reads/ spot	Median genes/ spot	Total no. of genes	Median UMIs/spot
Adult Fh1, 12w p.i.	A	777	111,038	2,355	9,068	6,603
	B	481	119,253	1,635	9,029	4,635
Adult Fh2, 14w p.i.	C	412	119,585	2,426	9,234	6,925
	D	350	133,354	2,152	8,758	6,069
Whole dataset		**2,020**	**118,604**	**2,192**	**9,847**	**6,138**

When assessing the gene and UMI counts in a 2D projection of all spots, it became apparent that the two parameters showed significant regional variability. A comparison with the H&E image showed that the spots in the area of the gonads, ovary and testis, exhibited a high level of transcriptional activity and diversity of expressed genes (Fig. 14a). [211],[212]

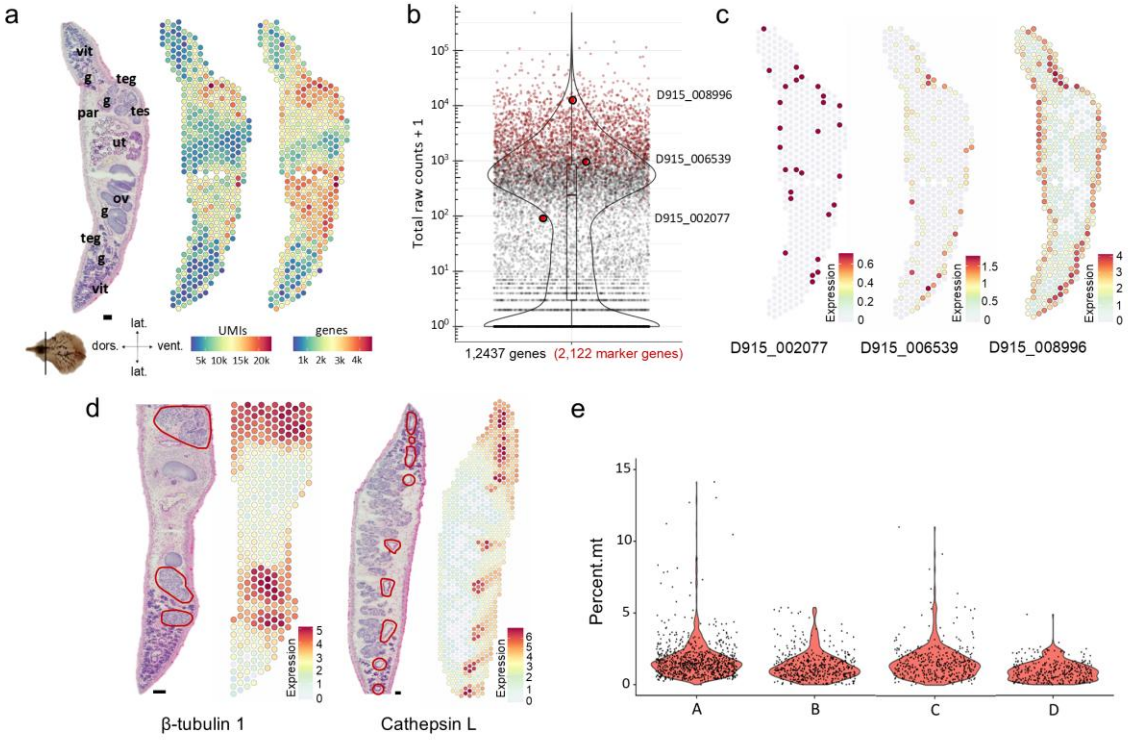

Figure 14 QC metrics.
(**a**) Left to right: H&E-stained tissue section (section C) and corresponding spatial projection of 412 mRNA-binding spots covered by this tissue section. Sectioning plane and orientation are indicated underneath. Scale = 100 µm. g: gut, ov: ovary, par: parenchyma, teg: tegument, tes: testis, ut: uterus, vit: vitellarium. The two spatial projections display the distribution of UMIs (Unique Molecular Identifier, middle) and genes (right), respectively. The number of UMIs and genes is encoded by color (blue – red = low – high). (**b**) Violin, scatter and box and whisker plot showing total raw counts per gene (sum of all counts detected on each of the 2020 spots). The liver fluke genome (incl. mitochondrial genes) encompasses 12,437 genes. Genes that were classified as marker genes for one of the eight tissues in the dataset (see 3.1.2.2) are highlighted in red (2,122 genes). Three genes were selected for spatial visualization (e) and are highlighted as large red dot with black outline. (**c**) Spatial projections showing expression profiles of tegument-associated genes with different total expression levels (from low to high): ß-tubulin 3b (D915_002077, 91 counts), ABC-B transporter (D915_006539, 973 counts), Ly6-B (D915_008996, 12,612 counts). Clearness of the spatial pattern decreases with the expression level. (**d**) H&E-stained tissue sections and spatial projections showing expression of two highly expressed tissue markers and their detection outside the actual target tissue: β-tubulin 1 (D915_007398, 143,256 total raw counts, testis marker) and the digestive enzyme cathepsin L (D915_010675, 113,491 total raw counts, gut marker). Testis (left) and (gut) right are highlighted in the H&E-stained tissue section (red). Scale = 100 µm (**c,d**) Expression level encoded by color (grey = low, red = high). (**e**) Violin Plot showing the percentage of mitochondrial genes per spot split by tissue section. [211],[212]

The median total expression per gene was 240 raw counts, i.e. slightly more than one transcript per 10 spots (Fig. 14b). The gene with the highest transcript numbers was HDM1/MF6 (D915_007621, 482,041 raw counts). When assessing the spatial expression patterns of genes with different total expression levels, it became apparent that the lower the total expression of a gene, the more difficult it was to recognize a clear expression pattern (Fig. 14c). Spatial visualization was best for genes with > 1,000 total raw counts (~ top 25%). Genes with very high expression levels, on the other hand, demonstrated a certain unsharpness in

their expression profiles. For example, β-tubulin 1 (D915_007398, 143,256 total raw counts) and the digestive enzyme cathepsin L (D915_010675, 113,491 total raw counts), were clearly associated with the flukes testis and gut, respectively, but their transcripts were also detected in spots that were not directly overlying the respective tissue type (Fig. 14d). In the case of cathepsin L, the transcripts were even showing a directional spread, starting from spots with highest expression levels where the gut was seen in the tissue section.

The last QC parameter examined was the percentage of mitochondrial genes. Dying cells often exhibit an elevated proportion of mitochondrial genes. Therefore, this value is commonly used to determine cell viability in scRNAseq experiments [[269]]. In the samples analyzed, the percentage of mitochondrial genes per spot mostly was below 5% (Fig. 14e)

3.1.2.2 Clustering identified eight transcriptionally distinct tissues

To further explore the spatial expression differences, a clustering analysis was performed, which identified groups of spots with similar gene expression profiles. In total, the analysis revealed eight distinct clusters, which were visualized using uniform manifold approximation and projection (UMAP) and spatial projections (Fig. 15). When examining their spatial arrangement, a strong correspondence was observed between the cluster distribution and the spatial organization of tissues in the H&E- stained tissue sections. Therefore, each cluster was annotated according to the underlying tissue type: tegument (561 spots), gut (154 spots), parenchyma (410 spots), vitellarium (279 spots), uterus (134 spots), ovary (92 spots), testis (354 spots) and Mehlis' gland (36 spots) (Fig. 15). [211],[212]

Next, a marker analysis was conducted to identify differentially expressed genes that best characterized the different tissues in the dataset (further called "marker genes"). Figure 16a illustrates that each tissue cluster was associated with a set of cluster-defining markers whose average expression in that cluster was significantly higher than in the other clusters. In total, 131 maker genes were identified for the tegument, 100 for the gut, 48 for the parenchyma, 98 for the vitellarium, 108 for the uterus, 719 for the ovary, 813 for the testis and 105 for Mehlis' gland (top 15 marker genes per cluster are shown in Suppl. Tab. 23). Most of these marker genes were found to have moderately high total gene expression levels, exceeding 1,000 raw counts (Fig. 14b). Gene Ontology (GO) enrichment analysis of the marker gene sets revealed characteristic biological processes and molecular functions characteristic for each cluster (Fig. 16b,c). Finally, to validate these findings experimentally, I performed *in situ* hybridizations for 22 selected genes, confirming the spatial expression patterns across different liver fluke tissues. Detailed descriptions of individual tissues, including representative marker genes, *in situ* hybridization results and enriched GO terms, are presented in the following results section (3.1.3). [211],[212]

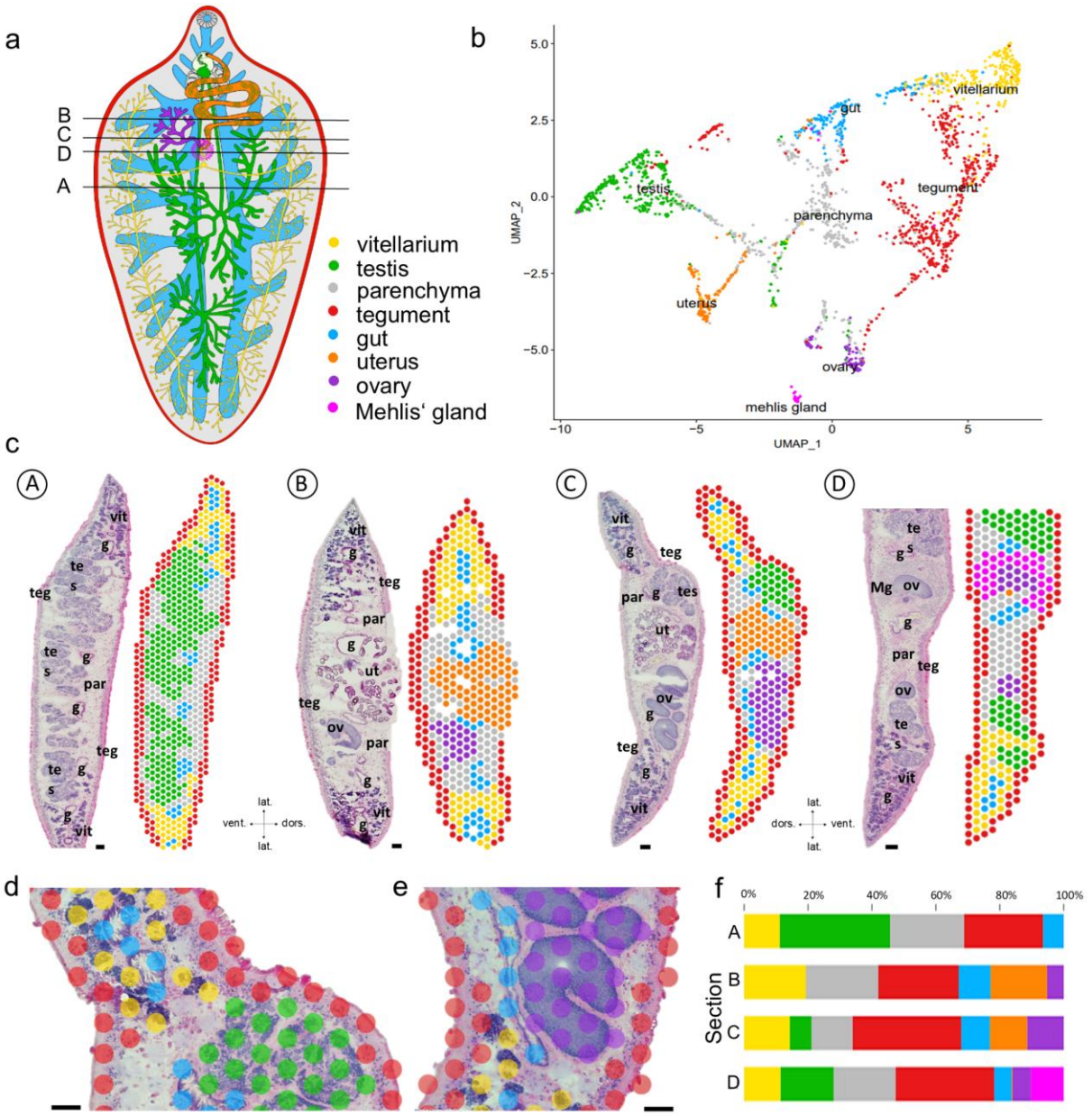

Figure 15 Transcriptome-based clusters match anatomical features of the liver fluke.
(**a**) Schematic showing anatomical features of adult *F. hepatica*: Vitellarium (yellow), testis (green), parenchyma (grey), tegument (red), gut (blue), uterus (orange), ovary (violet), Mehlis' gland (pink). Lines indicating sectioning planes of the four tissue sections (A-D) used to generate the spatial transcriptome. Created in Inkscape based on [Kazakova Maryia]/Adobe Stock [42]. (**b**) Uniform Manifold Approximation and Projection (UMAP) of 2,020 spots derived from all four *F. hepatica* sections in the dataset. Clusters are colored and labeled according to anatomical features shown in (a). (**c**) H&E-stained tissue sections and corresponding spatial projections of 777, 481, 412 and 350 mRNA-binding spots covered by these tissue sections, respectively. Clusters are colored according to anatomical features in (a). Section orientation applies to A and B as well as C and D together. g: gut, Mg = Mehlis' gland, ov: ovary, par: parenchyma, teg: tegument, tes: testis, ut: uterus, vit: vitellarium. Scale = 100 µm. (**d, e**) Magnified view of an overlay of the H&E-stained tissue section (section C) and the spatial cluster projection. Spots are colored according to anatomical features in (a). Scale = 100 µm (**f**) Stacked bar graph showing the tissue proportions per sample (A-D). Colors according to (a). [211],[212]

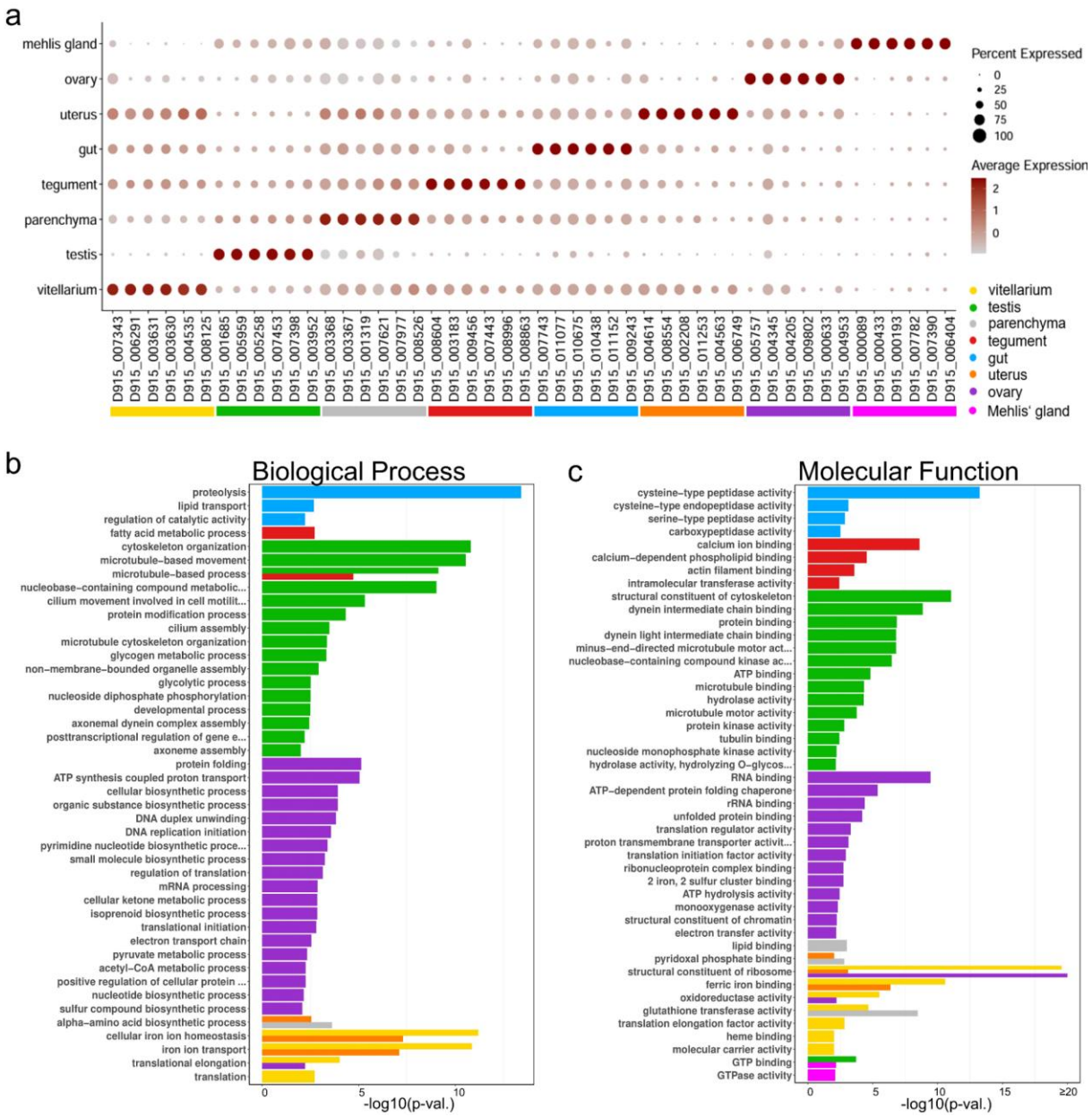

Figure 16 Eight transcriptionally distinct tissues in adult liver fluke cross sections.
(**a**) DotPlot showing expression profiles of the top 6 marker genes (sorted by "predictive power") for the eight tissue clusters in the ST dataset. Dot color encodes the average expression level (Z-score scaled counts) across all spots within a cluster. Dot size encodes the percentage of spots within a cluster that have captured this transcript. (**b, c**) Gene ontology analysis of marker genes (top 75% per cluster) revealed characteristic biological processes (b) and molecular functions (c) for each cluster. Overrepresented functional terms for each cluster were identified using a two-sided Fisher's exact test (p-value < 0.05). Bars for individual clusters are colored according to the legend in (a). [211],[212]

3.1.2.3 Spatial co-expression analysis revealed shared gene expression patterns

In addition to the clustering analysis, I performed a spatial co-expression analysis to identify shared spatial expression patterns among locally enriched transcripts. The 2,500 most spatially coherent genes were selected and a co-expression matrix was created showing how similar the expression pattern of one gene is to that of the other 2,500 genes (Fig. 17b). Finally, 15 groups of genes (metagenes) with similar spatial expression patterns were formed by clustering (Fig. 17b). When comparing these expression patterns with the corresponding H&E staining of the section, it became clear that most patterns corresponded to a particular tissue or organ in the section and therefore correlated with the tissue clusters from the Seurat analysis (Fig. 17c,d, Suppl. Fig. 2). For example, metagene 11 was expressed in the outer edge of the section and metagene 6 mainly in the area of the ovary. However, there were also groups of genes such as metagenes 1 and 5, which were co-expressed in more than one tissue, in this case in the testis and ovary (Fig. 17c, d). [211]

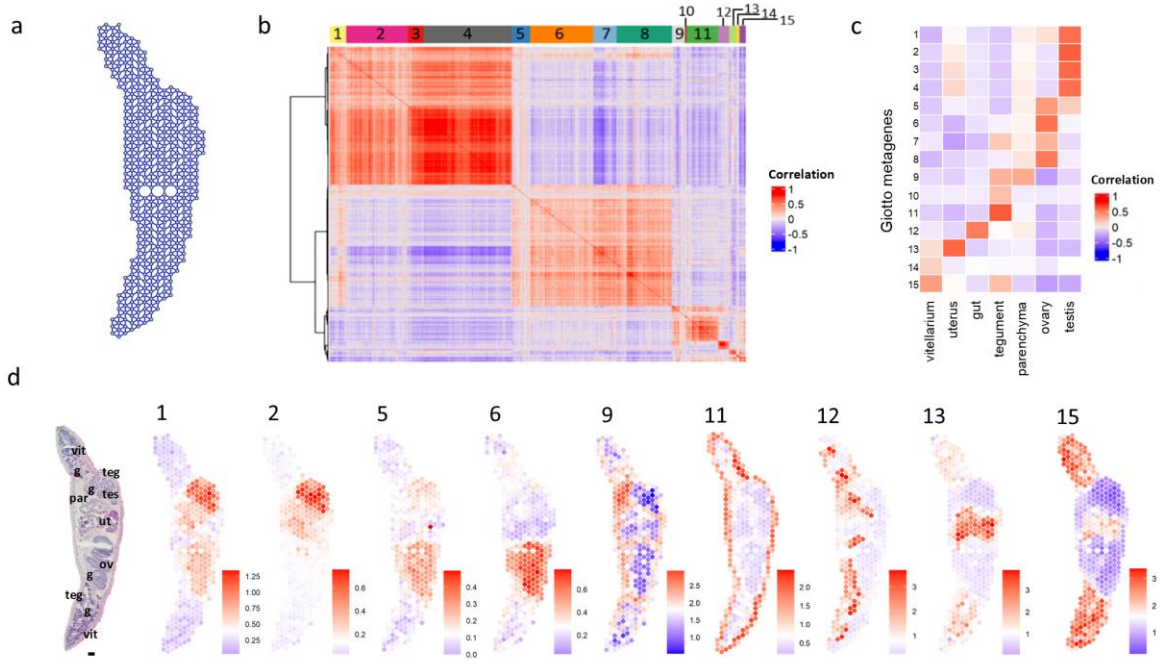

Figure 17 Spatial co-expression analysis revealed recurrent gene expression patterns.
(**a**) Giotto represents spatial relationships between different spots as a spatial network, which is required to identify individual genes with spatial coherent expression patterns. (**b**) Heatmap showing the correlation of spatial expression patterns among the 2,500 most spatially coherent expressed genes in the dataset. Groups of genes with similar expression profiles were clustered into 15 spatial co-expression modules, which are indicated with different colors on top. (**c**) Heatmap showing correlation of Seurat cluster assignment and Giotto co-expression modules. (**d**) H&E staining and metagene visualizations for selected spatial co-expression modules. See Suppl. Fig. 2. for visualizations of metagenes 3,4,7,8,10 & 14. Scale = 100 µm. g: gut, ov: ovary, par: parenchyma, teg: tegument, tes: testis, ut: uterus, vit: vitellarium. [211]

3.1.3 Transcriptional characterization of tissues in the liver fluke using ST

3.1.3.1 Male and female gonads: A highly dynamic germ cell production machinery

The ovary and testis of the liver fluke are branched, tubular organs and structured in a way that germ line stem cells reside in the periphery of the tubules while more differentiated stages are found in the center (Fig. 21b, c) [38]. In the ST data, the gonads exhibited the highest transcriptional levels and the greatest diversity of expressed genes compared to all other tissues (Fig. 18). Furthermore, the GO term enrichment analysis of Giotto metagenes 1 and 5 (0) revealed several genes involved in mitosis, cell cycle and DNA repair (Fig. 19a) among the genes expressed in both gonads. [211],[212]

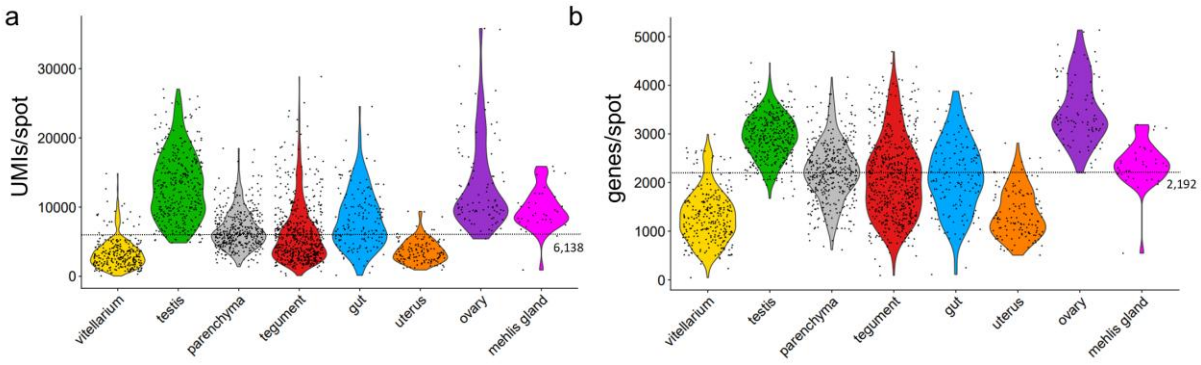

Figure 18 Transcript and gene counts per cluster.
Violin plot displaying UMI counts (**a**) and gene counts (**b**), per spot, split by cluster. The median UMI and gene count across all spots is indicated by the dashed line. [211],[212]

Based on these results, the dataset was further analyzed for the expression of other genes associated with stem cell function and cell cycle regulation. A list of cell cycle-associated genes in *F. hepatica* was adopted from Robb et al. [103], which included components of the conserved minichromosome maintenance (MCM2-7) complex (D915_009918, D915_01033, D915_006290, D915_005936), cell division cycle genes (cdc-20cdc-20/ D915_006257, cdc-45cdc-45/ D915_007655), histones (D915_002864, D915_002825) and DNA polymerases (D915_004675, D915_001192, D915_003363). Many of these genes were largely overrepresented in the gonads of the fluke (Fig. 19d). Of the 79 genes analyzed, 55 showed above-average expression levels in the testis, and 74 were enriched in the ovary. [211]

Manual inspection of genes included in metagene 1 & 5, further identified several genes with known roles in meiosis (Fig. 19b, c), including HORMA domain containing protein 2 (HORMAD2, D915_003478) and two synaptonemal complex proteins (SYCP1/D915_004084, SYCP2/D915_003691), which are involved in meiotic chromosome segregation [270]. In addition, the list contained meiosis-specific with OB-fold (MEIOB, D915_001989), which is essential for meiotic recombination in mammals [271]. [211]

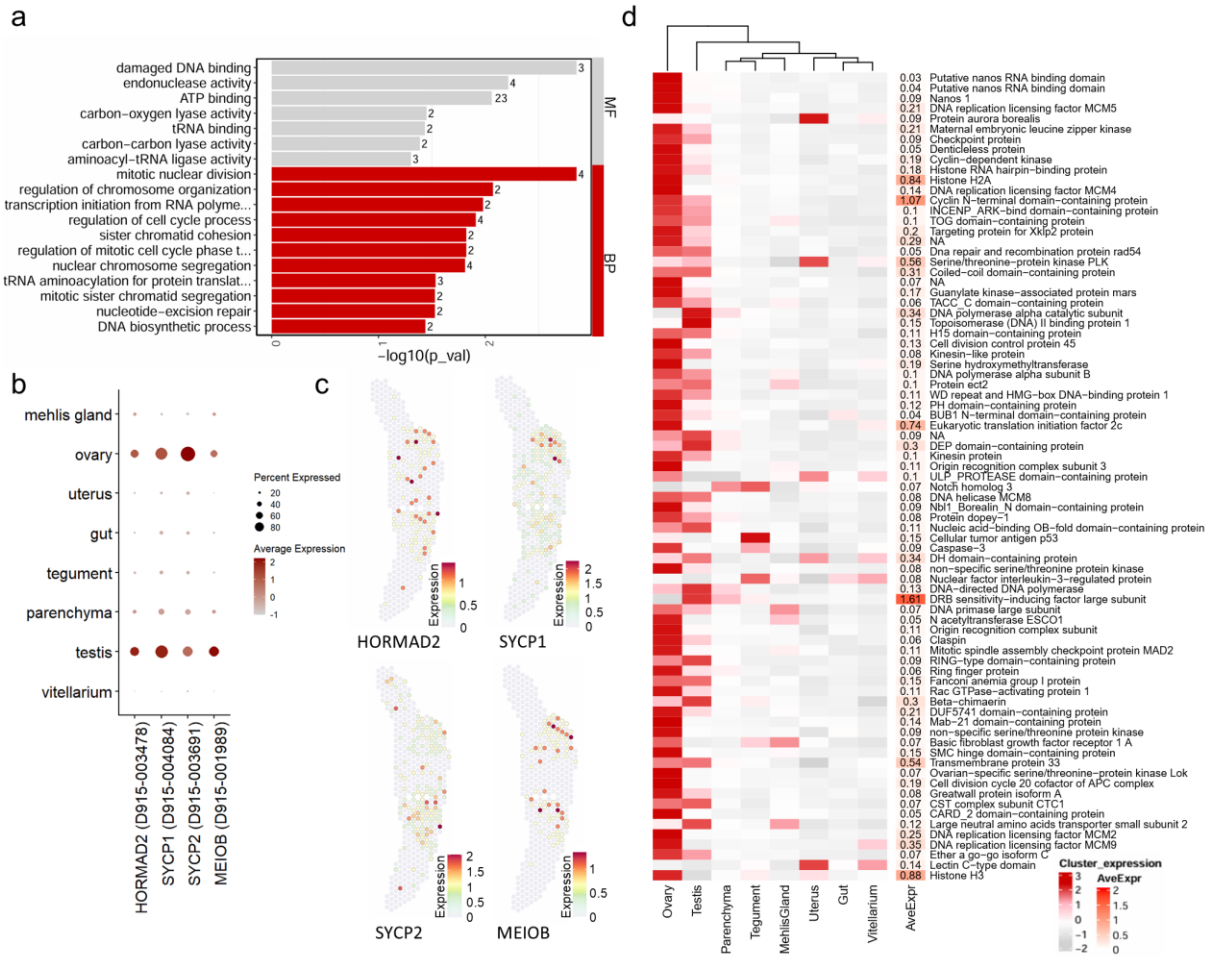

Figure 19 Stem cell- and cell cycle-associated genes in liver fluke gonads.
(**a**) Gene ontology enrichment analysis of genes co-expressed in both gonads (Giotto metagenes 1 & 5, Fig. 8c, d) revealed characteristic biological processes (BP) and molecular functions (MF). Overrepresented functional terms were identified using a two-sided Fisher's exact test (p-value < 0.05). (**b**) DotPlot showing expression profiles of four meiotic genes: HORMAD2 (D915_003478), two synaptonemal complex proteins (SYCP1/D915_004084, SYCP2/D915_003691) and MEIOB (D915_001989). Dot color encodes the average expression level (Z-score scaled counts) across all spots within a cluster. Dot size encodes the percentage of spots within a cluster that have captured this transcript. Please note: While spatial plots (c) are shown for only one representative section, the DotPlot includes expression data from all four tissue sections in the data set. (**c**) Spatial projections showing expression profiles of meiotic genes shown in (b). (**d**) Left: Heatmap of 79 stem cell- and cell cycle-associated genes showing their average expression per cluster (Z-score scaled counts). Right: Heatmap showing the average expression of those genes in the whole dataset (log1p transformed counts). [211]

Furthermore, the marker analysis revealed an increased expression of seven and eight different zinc finger proteins in the ovary and testis, respectively. Among them were two CCCH domain-containing proteins (D915_005258, D915_003685), which, unlike most zinc fingers that bind DNA, act as regulators of RNA metabolism [272]. Indeed, when performing protein-protein interaction analysis, the ovary-enriched CCCH zinc finger D915_003685 was identified within a STRING subnetwork of ovarian marker genes that showed significant functional enrichment for "mRNA processing" and "RNA splicing" (Fig. 20b). In addition, the expression of zinc finger CCCH domain-containing protein 31 (D915_005258) in the testis was validated by ISH (Fig. 21j). [211],[212]

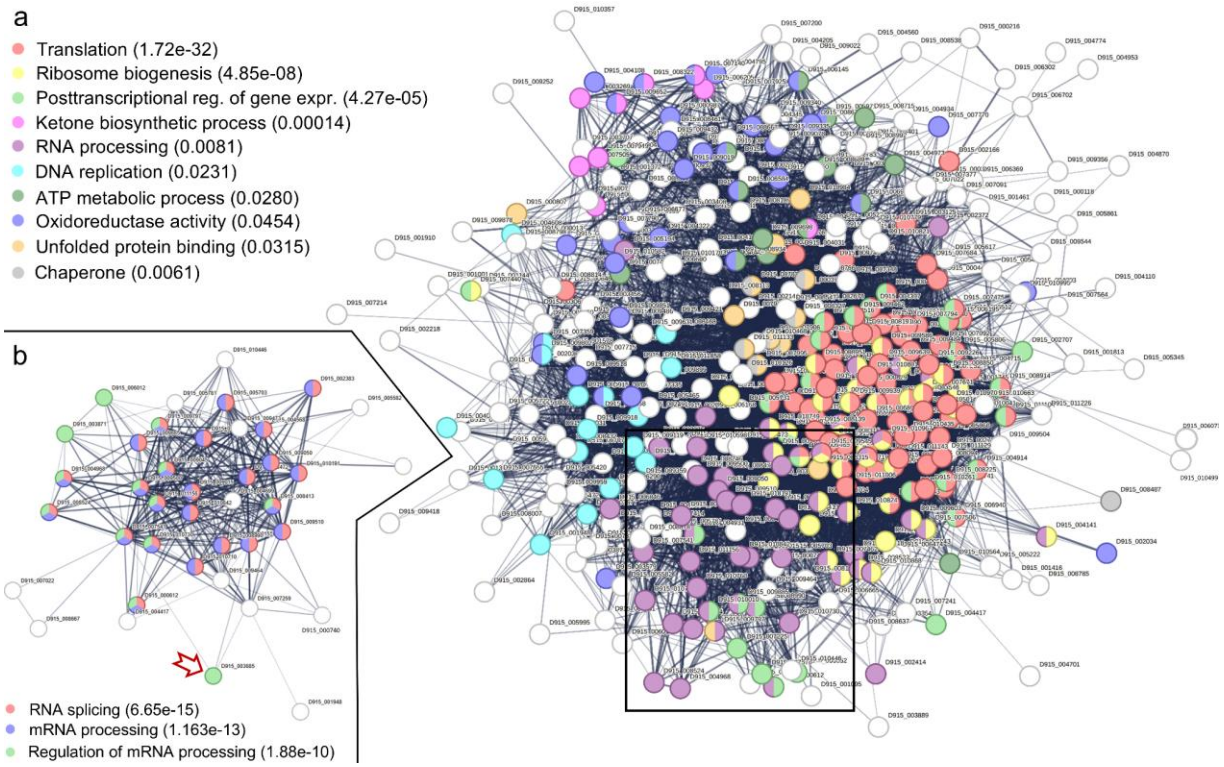

Figure 20 Protein-protein interactions among markers of the ovary.
(**a**) STRING analysis of marker genes (top 75%) of the ovary. Default settings were used to predict interactions with a minimum interaction (confidence) score of 0.4 (medium level of confidence). Lines (edges) are indicating interactions that were predicted based on the function of homologues. Disconnected nodes are not shown. Functional enrichments in the network were predicted by STRING. Selected terms are highlighted in color and labelled (false discovery rate in brackets). The subnetwork in (**b**) resulted from k-means clustering in STRING (number of clusters = 10). The rectangle in (a) marks where the corresponding genes are located in the full network. Arrow indicates Zinc finger CCCH domain-containing protein 3 (D915_003685). [211],[212]

In addition to these commonalities, the Seurat analysis provided marker gene profiles that were unique for the liver fluke ovary and testis. The markers of the ovary cluster, which were used for cluster validation, were two C-type lectins of unknown function (D915_005862, D915_005757). ISH revealed that the two genes exhibit distinct spatiotemporal expression patterns during oocyte differentiation (Fig. 21e, h, k). One of these genes, the bone marrow proteoglycan (BMPG, D915_005862), was mainly expressed in early primary oocytes, and only weakly detected in late primary oocytes (Fig. 21h). Transcripts of D915_005757 in contrast, were detected in both early and late primary oocytes (Fig. 21k). GO term enrichment and STRING analysis of the ovary cluster suggested that the identified transcripts encode proteins primarily associated with biosynthetic pathways, including (ribo-)nucleotide and small-molecule synthesis, DNA replication, and translation (Fig. 16b & Fig. 20). [211],[212]

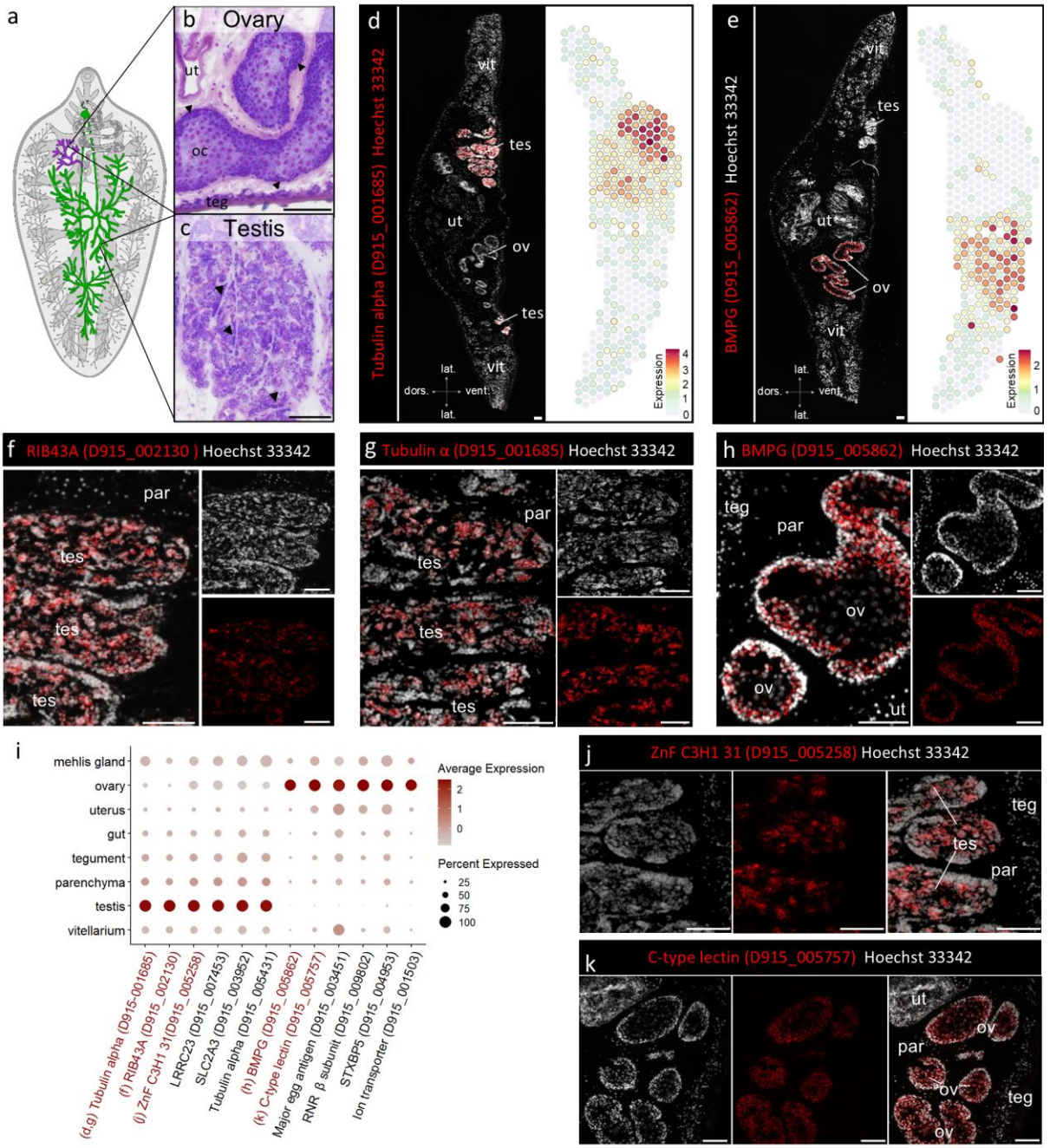

Figure 21 Spatial expression of marker genes for liver fluke ovary and testis.
(**a**) Schematic showing anatomical features of adult *F. hepatica*. Ovary (violet) and testis (green) are highlighted Created in Inkscape based on [Kazakova Maryia]/Adobe Stock [42]. (**b, c**) Histology of the liver fluke ovary and testis (Diff Quick staining). Arrows mark germ line stem cells (oogonia/spermatogonia) located in the periphery of the tubules. (**d, e**) Fluorescent *in situ* hybridization (FISH) overview (left) and spatial projection (right) of (d) a testis-specific tubulin alpha (D915_001685) and (e) the ovary marker bone marrow proteoglycan (BMPG, D915_005862). Section orientation is indicated at the bottom (dors: dorsal, vent: ventral, lat: lateral). Expression level encoded by color (gray = low, red = high). (**f**) FISH of the ribbon protein RIB43A (D915_002130). (**g, h**) Magnified view of FISH stainings for genes shown in (d) and (e), respectively (different tissue section, same experiment). (**i**) DotPlot showing expression profiles of selected marker genes for testis and ovary. Dot color encodes the average expression level (Z-score scaled counts) across all spots within a cluster. Dot size encodes the percentage of spots within a cluster that have captured this transcript. Please note: While spatial plots (b, c) are shown for only one representative section, the DotPlot includes expression data from all four tissue sections in the dataset. Genes labeled in red were validated by FISH. Figure panels showing the respective FISH experiment are indicated. (**j**) FISH of Zinc finger C3H1 domain-containing protein 31 (D915_005258). (**k**) FISH of C-type lectin domain-containing protein (D915_005757). (**b–h, j, k**) Scale = 100 µm. ov: ovary, oc: oocyte, par: parenchyma, teg: tegument, tes: testis, ut: uterus, vit: vitellarium. (**d-h, j, k**) Nuclei counterstained with Hoechst 33342. For numbers of ISH replications, see Suppl. Tab. 21. Sense controls were found to be negative (Suppl. Fig. 4a-e). [211],[212]

STRING analysis of testis markers revealed a densely interconnected protein-protein interaction network (Fig. 22), with significant functional enrichment for terms related to “cytoskeleton”, “microtubule”, “cilium” and “axoneme”. Among the most prominent markers were several α- and β-tubulins and the flagellar ribbon protein RIB43A (D915_002130) (Fig. 21i). ISH confirmed expression of α-tubulin D915_001685 and RIB43A during most stages of spermatogenesis, with the exception of spermatogonia, which are situated in the periphery of the testicular tubules (Fig. 21f, g). [211],[212]

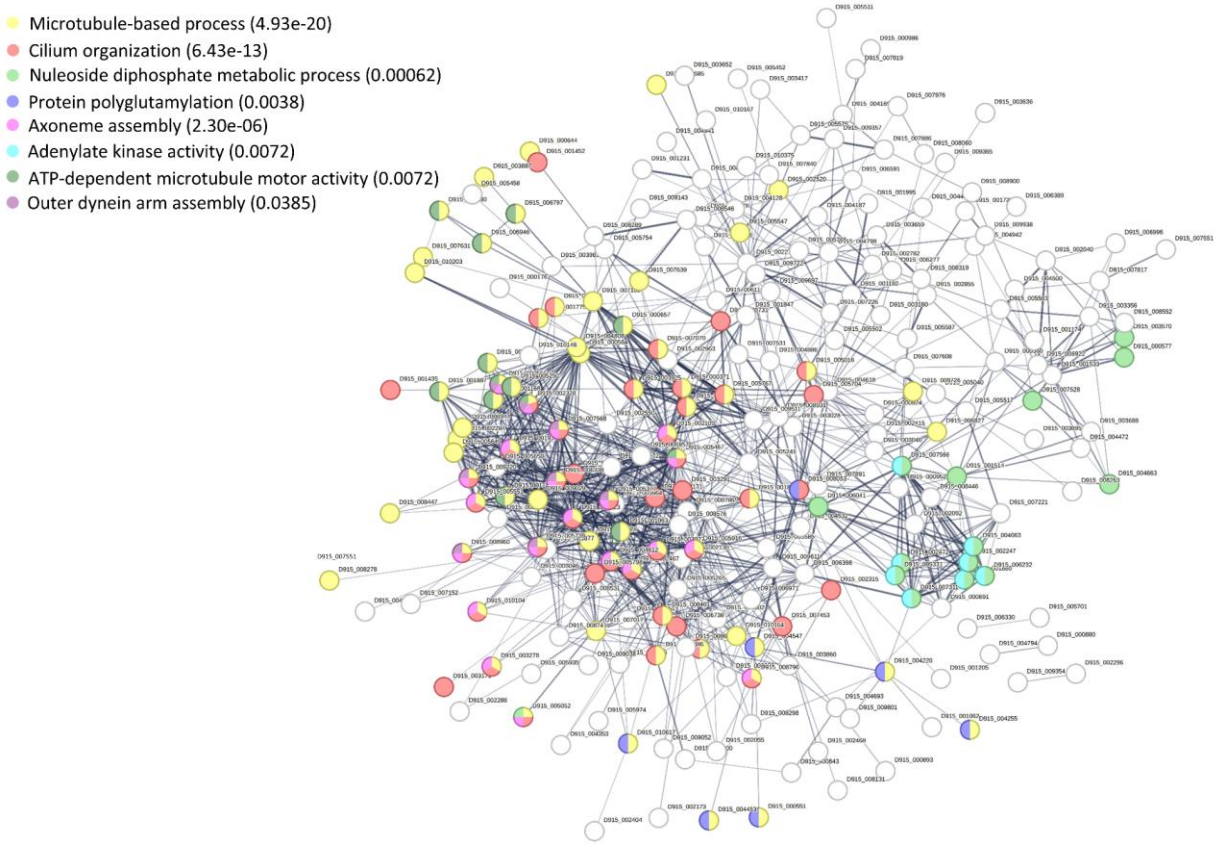

Figure 22 Protein-protein interactions among testis markers.
STRING analysis of marker genes (top 75%) of the testis. Default settings were used to predict interactions with a minimum interaction (confidence) score of 0.4 (medium level of confidence). Lines (edges) are indicating interactions that were predicted based on the function of homologues. Disconnected nodes are not shown. Functional enrichments in the network were predicted by STRING. Selected terms are highlighted in color and labelled (false discovery rate in brackets). [211],[212]

3.1.3.2 The liver fluke egg production apparatus: from vitellarium to uterus

Trematode eggs consist of an oocyte and about 30 vitelline cells, which are enclosed in an eggshell (Fig. 23c). Vitelline cells are produced in vitelline follicles along the lateral margins of adult liver flukes (Fig. 23a,d) and provide nutrients for the developing embryo as well as proteins and enzymes required for eggshell formation [41]. These include several eggshell proteins (e.g. D915_004535, D915_010963) and two tyrosinases (D915_002197, D915_002718), phenol oxidases catalyzing shell polymerization [41]. Both groups of genes were found among the leading markers of the vitellarium in the ST data (Fig. 23e) [211],[212]. The GO term analysis revealed an enrichment of translation-associated genes, reflecting an active protein synthesis in the vitellarium. Additional marker genes of the vitellarium were two polysaccharide-forming glycogenins (D915_003707, D915_007816), several iron-binding proteins such as ferritins and myoglobin (Fig. 16c) as well as antioxidant enzymes, e.g. two oxidoreductases (aldehyde dehydrogenase (D915_004795), carbonyl reductase (D915_010573)) and three glutathione-dependent enzymes (glutathione S-transferases (D915_001201, D915_001421), glyoxalase (D915_009832).

Besides these functional insights, spatial transcriptomics also provided information regarding the specific stage of vitelline cells that expresses particular genes. For example, tyrosinase 1 and 2 were exclusively expressed in early vitellocytes within the vitellarium, while other markers, such as vitelline protein B1 (D915_010963), were also found in mature vitelline cells present in eggs within the uterus (Fig. 23e, f, h). These expression patterns were confirmed for tyrosinase 2 and vitelline protein B1 by performing *in situ* hybridization (Fig. 23g, i-k). Furthermore, several genes were identified, that were predominantly expressed within the uterus cluster. These included glutamine synthetase D915_002208, phenylalanine 4-monooxygenase (PAH) D915_006412 and the mRNA-binding protein TIS11 (D915_008728 (Fig. 23e, l). [211],[212]

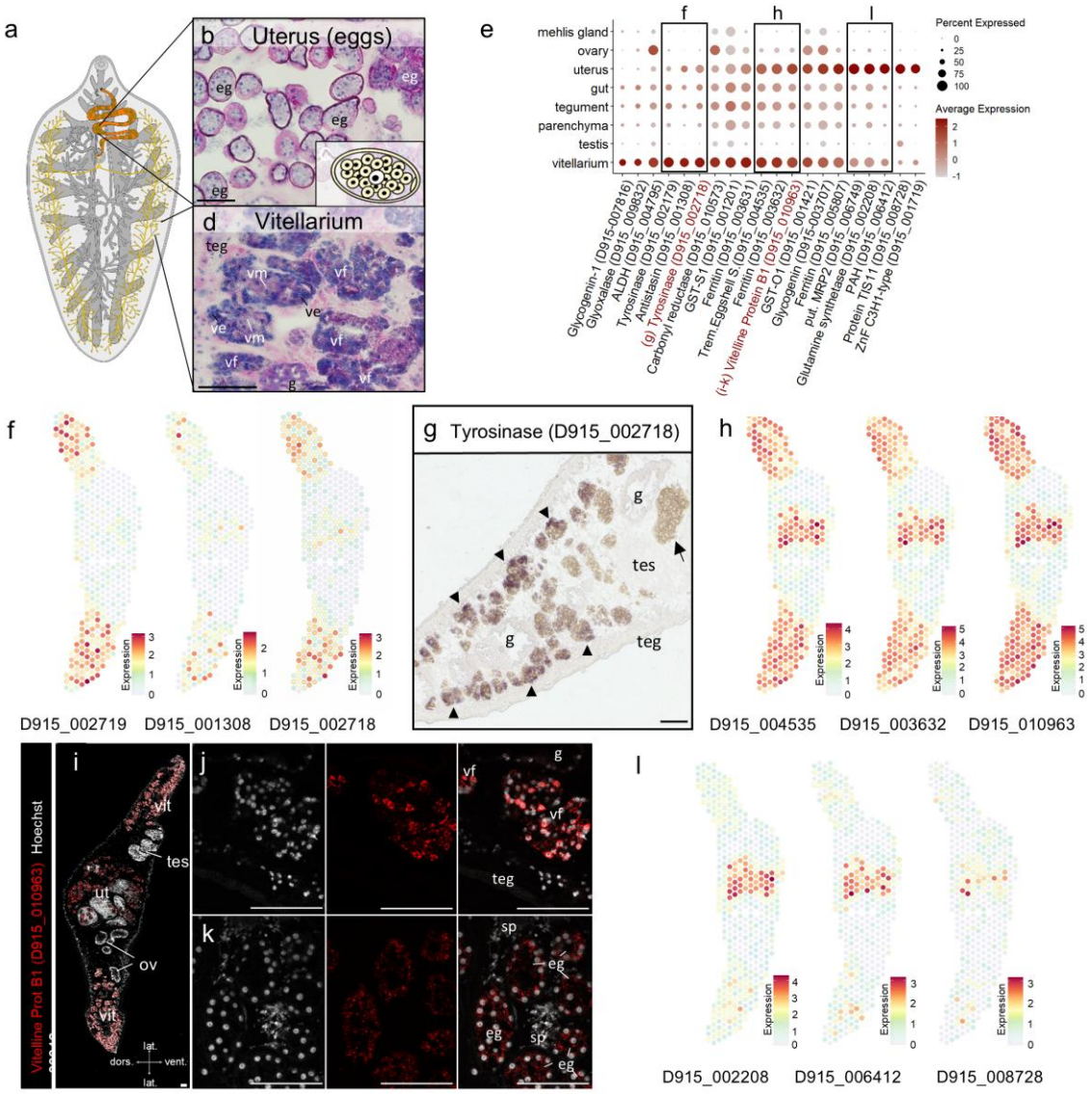

Figure 23 The liver fluke egg production apparatus: from vitellarium to uterus.
(**a**) Schematic showing anatomical features of adult *F. hepatica*. Vitellarium (yellow) and uterus (orange) are highlighted. Created in Inkscape based on [Kazakova Maryia]/Adobe Stock [42]. (**b, d**) Histology (H&E staining) of the liver fluke uterus (b) and vitellarium (d). (**c**) Scheme of an *F. hepatica* egg containing one oocyte (white) and multiple vitellocytes (yellow). (**e**) DotPlot showing expression profiles of selected tissue markers of the vitellarium and uterus cluster. Dot color encodes the average expression level (Z-score scaled counts) across all spots within a cluster. Dot size encodes the percentage of spots within a cluster that have captured this transcript. Please note: While spatial plots (f, h l) are shown for only one representative section, the DotPlot includes expression data from all four tissue sections in the data set. Genes labelled in red were validated by (F)ISH. Boxes indicate the panel showing spatial projections of the respective genes. For spatial projections of GSTs see Fig. 30. (**f**) Spatial projections showing expression patterns of three genes with predominant expression in the vitellarium: tyrosinase 1 (D915_002197), antistasin (D915_001308) and tyrosinase 2 (D915_002718). (**g**) Chromogenic ISH of the vitellarium-specific tyrosinase 2 (D915_002718). Black arrowheads indicate indigo dye deposition within vitelline follicles. No staining was observed within mature vitelline cells in the vitelline duct (black arrow). (**h**) Spatial projections showing expression patterns of three genes with expression in both vitellarium and uterus: eggshell protein (D915_004535), ferritin (D915_003632), vitelline protein B1 (D915_010963) (**i-k**) FISH of vitelline protein B1 (D915_010963) expression. Nuclei counterstained with Hoechst 33342. (**i**) Overview. Section orientation is indicated at the bottom (dors: dorsal, vent: ventral, lat: lateral). (**j, k**) Magnified view of vitelline follicles (j) and eggs (k). (**l**) Spatial projections showing expression patterns of three genes with predominant expression in the uterus: glutamine synthetase (D915_002208), phenylalanine 4-monooxygenase (D915_006412) and TIS11 (D915_008728). **(f, h, l)** Expression level encoded by color (grey = low, red = high). (**b, d, g, i**) Scale = 100 µm. vit: vitellarium, vf: vitelline follicle, ve: early vitellocyte, vm: mature vitellocyte, ut: uterus, eg: egg, sp: spermatozoa, tes: testis, ov: ovary, teg: tegument, g: gut. (**g, i, j, k**) For number of ISH experiments, see Suppl. Tab. 21. Sense controls were found to be negative (Suppl. Fig. 4f,v). [211],[212]

3.1.3.3 Mehlis' gland is composed of two transcriptionally distinct cell types

The Mehlis' gland, also known as shell gland, is another component of the female reproductive system involved in egg formation (Fig. 24a). GO term enrichment analysis from the ST data was not very conclusive (Fig. 16b, c). Still, there was an enrichment of GTPases, represented by three Rab proteins (D915_002606, D915_002781, D915_003764) and Rho1 (D915_004867) (Fig. 16c Fig. 24c).

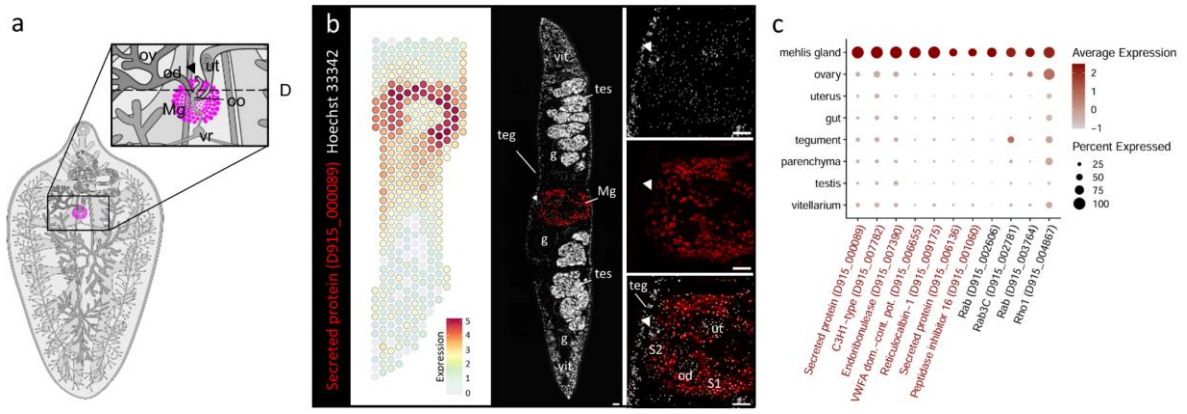

Figure 24 Ras superfamily GTPases are enriched in Mehlis' gland.
(**a**) Scheme showing anatomical features of the liver fluke. Mehlis' gland (pink) is highlighted. Insert showing a magnified view of the egg production apparatus. Created in Inkscape based on [Kazakova Maryia]/Adobe Stock [42]. (**b**) Spatial projection and fluorescent *in situ* hybridization (FISH) showing the expression of the Mehlis' gland marker D915_000089. Expression level encoded by color (grey = low, red = high). Arrowhead marks Laurer's canal (dorsal). Nuclei counterstained with Hoechst 33342. For numbers of ISH experiments see Suppl. Tab. 21. Sense control was found to be negative (Suppl. Fig. 4g). Scale = 100 µm, g: gut, Mg: Mehlis' gland, od: oviduct, oo: ootype, ov: ovary, S1: S1 cells, S2: S2 cells, teg: tegument, tes: testis, vr: vitelline reservoir (**c**) DotPlot showing expression profiles of selected tissue markers of the Mehlis' gland cluster. Dot color encodes the average expression level (Z-score scaled counts) across all spots within a cluster. Dot size encodes the percentage of spots within a cluster that have captured this transcript. Please note: While the spatial plot in (b) shows only one representative section, the DotPlot includes expression data from all four tissue sections in the data set. Genes labelled in red were validated by FISH. [211]

When comparing the marker genes of the Mehlis' gland cluster, three different spatial expression patterns became obvious. While the top marker, the secreted protein D915_000089, was tissue-wide expressed within the Mehlis' gland (Fig. 24b), other markers, such as the secreted protein D915_006136 and a VWFA domain-containing protein (D915_006655), displayed more localized expression in the dorsal and lateral, or ventral region of the gland (Fig. 25d). These regions agree with the known arrangement of S1 and S2 cells in the Mehlis' gland of *F. hepatica*, which has only been described morphologically so far [38]. When examining the histology of the tissue section, histological characteristics of these cell types were recognized: S1 cells are smaller and have a denser and more basophilic cytoplasm, while S2 cells are larger and have a paler and more eosinophilic cytoplasm [38] (Fig. 25e). Consequently, it was possible to manually select spots representing either S1 or S2 cells using Loupe Browser, and subsequently perform differential gene expression analysis in Seurat to compare the gene expression of the two cell types. FISH confirmed that S1 cells were characterized by the expression of poly(U)-endoribonuclease (D915_007390), a von

Willebrand factor A (VWFA) domain-containing protein (D915_006655), and a C3H1-type domain-containing protein (D915_007782). Reticulocalbin (D915_009175), peptidase inhibitor 16 (D915_001060) and the secreted protein D915_006136, in contrast, were exclusively expressed in S2 cells (Fig. 25c-i). GO term enrichment analysis for the two subtypes was inconclusive, as only few markers possessed GO annotation (data not shown). [211],[212]

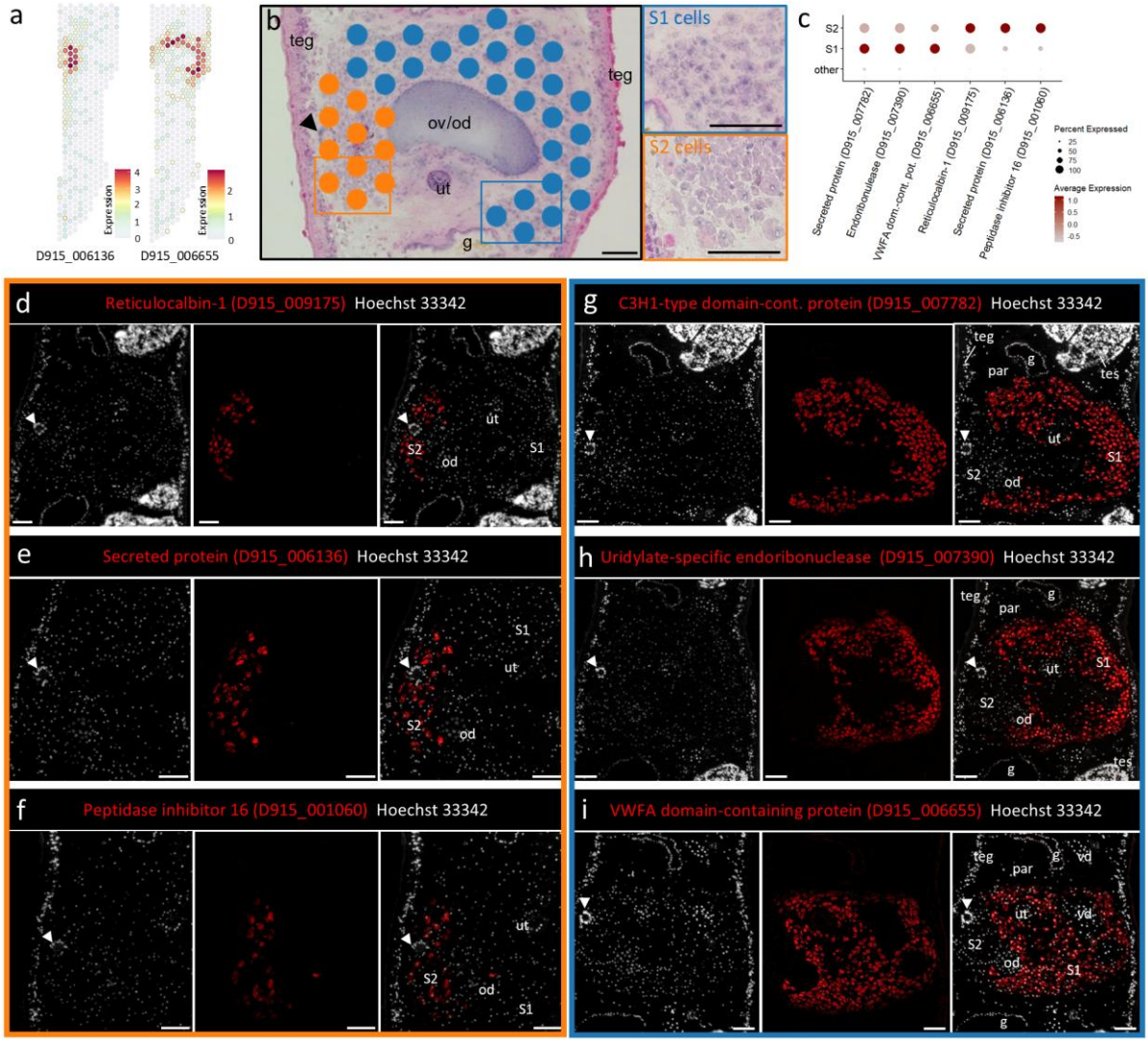

Figure 25 Mehlis' gland is composed of two transcriptionally distinct cell types.
(**a**) Spatial projection showing the spatial expression of secreted protein D915_006136 and a VWFA domain containing protein (D915_006655). Expression level encoded by color (grey = low, red = high). (**b**) Locations and histology of S1 (blue) and S2 cells (orange) in the tissue section used for ST. (**c**) DotPlot showing expression profiles of selected markers of S1 & S2 cells. "Other" includes all remaining spots in the spatial dataset. Dot color encodes the average expression level (Z-score scaled counts) across all spots within a cluster. Dot size encodes the percentage of spots within a cluster that have captured this transcript. (**d-i**) FISH of Poly(U)-endoribonuclease (D915_007390), von Willebrand factor A (VWFA) domain-containing protein (D915_006655), a C3H1-type domain-containing protein (D915_007782), reticulocalbin (D915_009175), peptidase inhibitor 16 (D915_001060) and another secreted protein (D915_006136). Nuclei counterstained with Hoechst 33342. Scale = 100 µm, g: gut, od: oviduct, S1: S1 cells, S2: S2 cells, teg: tegument, tes: testis, ut: uterus, vd: vitelline duct, arrowhead marks Laurer's canal (dorsal). For numbers of ISH experiments performed for each gene, see Suppl. Tab. 21. Sense controls were found to be negative (Suppl. Fig. 4h-m). [211],[212]

3.1.3.4 Digestive functions of the liver fluke gut: A dual role in nutrition and defense?

The gastrodermis of liver flukes consists of a single major cell type, columnar cells with long lamellae that cycles between secretory and absorptive functions [273]. During secretion, the cell releases a variety of degrading enzymes to digest ingested host blood, while in the absorptive phase, it takes up the resulting cleaved products.

In the ST dataset, the digestive function was well represented by 18 digestive enzymes, mainly proteases, among the top 50 marker genes of the gut cluster. Specific expression of the two cysteine proteases legumain (D915_002224) and cathepsin L (D915_011077) in the intestinal epithelium was confirmed by FISH (Fig. 26c, d, f, g) [211],[212]. In addition, the marker list included three saposin B-like proteins (D915_011126, D915_010001, D915_008831) (Fig. 26h). Those proteins have been shown to induce lysis of human erythrocytes *in vitro* [274], releasing cellular contents that can then be further cleaved by the degrading enzymes. In contrast to mammalians, where cathepsins are lysosomal enzymes, cathepsins in *F. hepatica* are secreted to the intestinal lumen for extracellular digestion of hemoglobin [275]. Still, I found transcripts of potential lysosome-associated proteins among the intestinal marker genes. These included the lysosome associated membrane glycoprotein 2 (D915_004818), NCUG1-B (D915_001420) and lipopolysaccharide induced TNF factor (LITAF, D915_009880) (Fig. 26h, i). Whether these proteins are associated with cathepsin zymogen-containing secretory vesicles or endocytotic cytoplasmic bodies remained unclear. Protease activity must be regulated to prevent self-damage. Consistent with this, three known cysteine protease inhibitors, stefin 1-3 (D915_009335, D915_009861, D915_001085) [276] were found among the markers of the gut cluster (Fig. 26h, i).

Finally, I noted that transcripts of two potential pattern recognition receptors, a DM9 domain containing protein (D915_003994) and a PGRP domain-containing protein (D915_006630) were enriched in the intestine (Fig. 26h, i). Pattern recognition is an evolutionarily conserved process in multicellular organisms to detect pathogen-associated molecular patterns (PAMPs) [277]. The transcriptomics data suggests that the liver fluke gut, besides its central role in nutrition, may also play a role in defending against microbial pathogens.

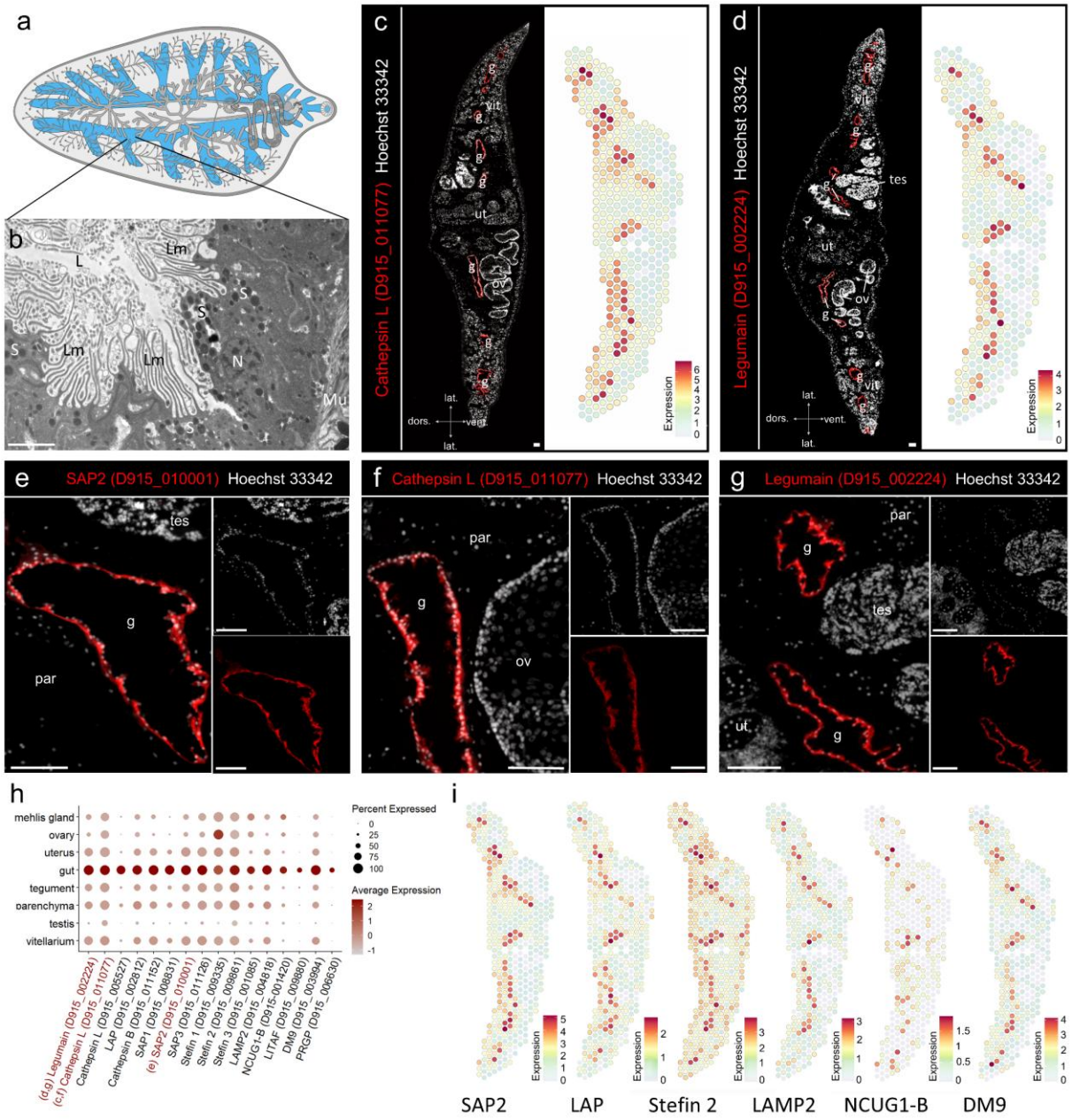

Figure 26 Digestive enzymes, lysosomal proteins and pattern recognition receptors of the liver fluke gut. Scheme showing anatomical features of the liver fluke. The gut (blue) is highlighted. Created in Inkscape based on [Kazakova Maryia]/Adobe Stock [42]. (**b**) Transmission electron microscopic image of the liver fluke gastrodermis. Scale = 2 µm, L: lumen, Lm: lamellae, Mu: muscle, N: nucleus, S: secretory bodies. (**c**, **d**) Fluorescent *in situ* hybridization (FISH) overview (left) and spatial projection (right) of the gut markers cathepsin L (D915_011077) and legumain (D915_002224). Section orientation is indicated at the bottom (dors: dorsal, vent: ventral, lat: lateral). (**e**) FISH of saposin 2 (SAP2, D915_010001) (**f, g**) Magnification of (c) and (d), respectively. (**h**) DotPlot showing expression profiles of selected tissue markers of the gut cluster. Dot color encodes the average expression level (Z-score scaled counts) across all spots within a cluster. Dot size encodes the percentage of spots within a cluster that have captured this transcript. Please note: While spatial plots (c, d, i) are shown for only one representative section, the DotPlot includes expression data from all four tissue sections in the dataset. Genes labeled in red were validated by FISH. Figure panels showing the respective FISH experiment are indicated. (**i**) Spatial projections showing expression patterns of selected gut marker genes: saposin-like family protein 2 (SAP2, D915_010001), leucine aminopeptidase (LAP, D915_002812), stefin 2 (D915_009335), LAMP2 (D915_004818), NCUG1-B (D915_001420), DM9 (D915_003994). Expression level encoded by color (gray = low, red = high). (**c-g**) Nuclei counterstained with Hoechst 33342. Scale = 100 µm. g: gut, ov: ovary, par: parenchyma, teg: tegument, tes: testis, ut: uterus, vit: vitellarium. For numbers of ISH experiments performed for each gene, see Suppl. Tab. 21. Sense controls were found to be negative (Suppl. Fig. 4n-p). [211],[212]

3.1.3.5 Cytoskeletal proteins are shaping the transcriptome of the tegument

The tegument is a unique feature of parasitic flatworms. It consists of mesenchymal cells that form a syncytial layer at the body surface, with the cell bodies located below the body wall musculature and connected to the syncytium via cytoplasmic protrusions (Fig. 28b) [32]. With spot diameters of 55 µm and a spot-to-spot distance of 100 µm [278], the Visium approach was not able to resolve these different layers of the flukes body wall (Fig. 15d, e & Fig. 27a). Therefore, the spots of the tegument cluster captured both orthologues of schistosome tegument markers as well as orthologues of muscle marker genes (Fig. 27b & c). [211]

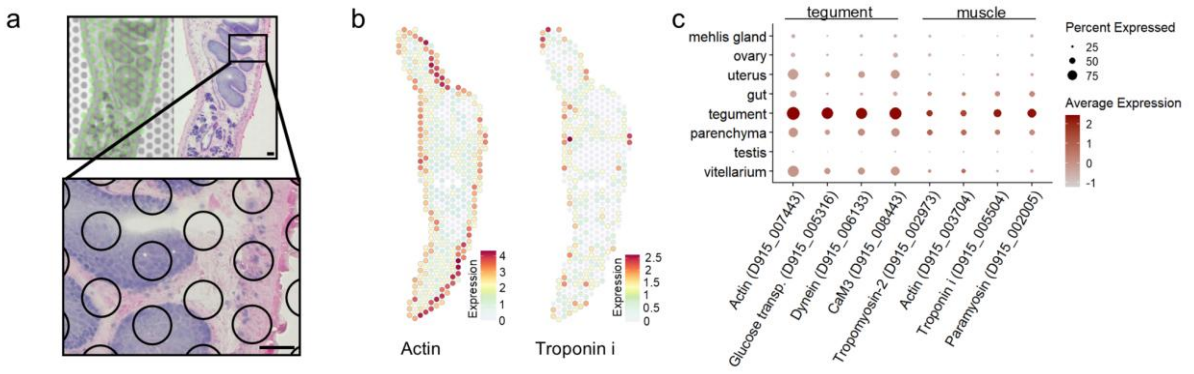

Figure 27 Body musculature is included in the tegument cluster.
(**a**) Overlay of mRNA-binding spots on the Visium slide and an H&E-stained tissue section. Spots have a diameter of 55 µm and therefore span multiple cells and sometimes different tissues. For example (**b, c**), tegumental and subtegumental muscle cells are combined in the tegument cluster. Markers for tegument and muscle cells in *S. mansoni* were retrieved from published scRNAseq data [146]. The corresponding *F. hepatica* orthologues were retrieved from WBPS. (**b**) Spatial projections showing expression profiles of the tegument marker actin (Smp_203130/ D915_007443) and the muscle marker troponin (Smp_018250/ D915_005504). (**c**) DotPlot showing expression profiles of selected *F. hepatica* orthologs of schistosome tegument and muscle markers. Tegument markers: actin (Smp_203130/D915_007443), glucose transporter (Smp_105410/ D915_005316), dynein (Smp_095520/D915_006133), calcium-binding protein (Smp_267080/D915_008443). Muscle markers: Tropomyosin 2 (Smp_031770/ D915_002973), actin (Smp_307020, D915_003704), troponin (Smp_018250/ D915_005504), paramyosin (Smp_085540/ D915_002005). Dot color encodes the average expression level (Z-score scaled counts) across all spots within a cluster. Dot size encodes the percentage of spots within a cluster that have captured this transcript. Please note: While spatial plots (b) are shown for only one representative section, the DotPlot includes expression data from all four tissue sections in the data set.

The tegument forms a protective layer at the host-parasite interface, but also fulfills metabolic functions such as nutrient uptake and osmoregulation [32]. These functions were well reflected by the marker genes of the tegument in the ST data. Regarding nutrient import, a glucose transporter (D915_005316) and an amino acid transporter (D915_001928) showed increased expression in the tegument cluster. GO term analysis for the tegument cluster further revealed several cytoskeletal proteins involved in microtubule-based processes and actin filament binding (Fig. 16b, c). The high number of dynein motor proteins among these genes (D915_006133, D915_006131, D915_008269, D915_001373, D915_000254, D915_000253) is consistent with active transport processes in the fluke's surface layer (Fig. 28h, i). [211],[212]

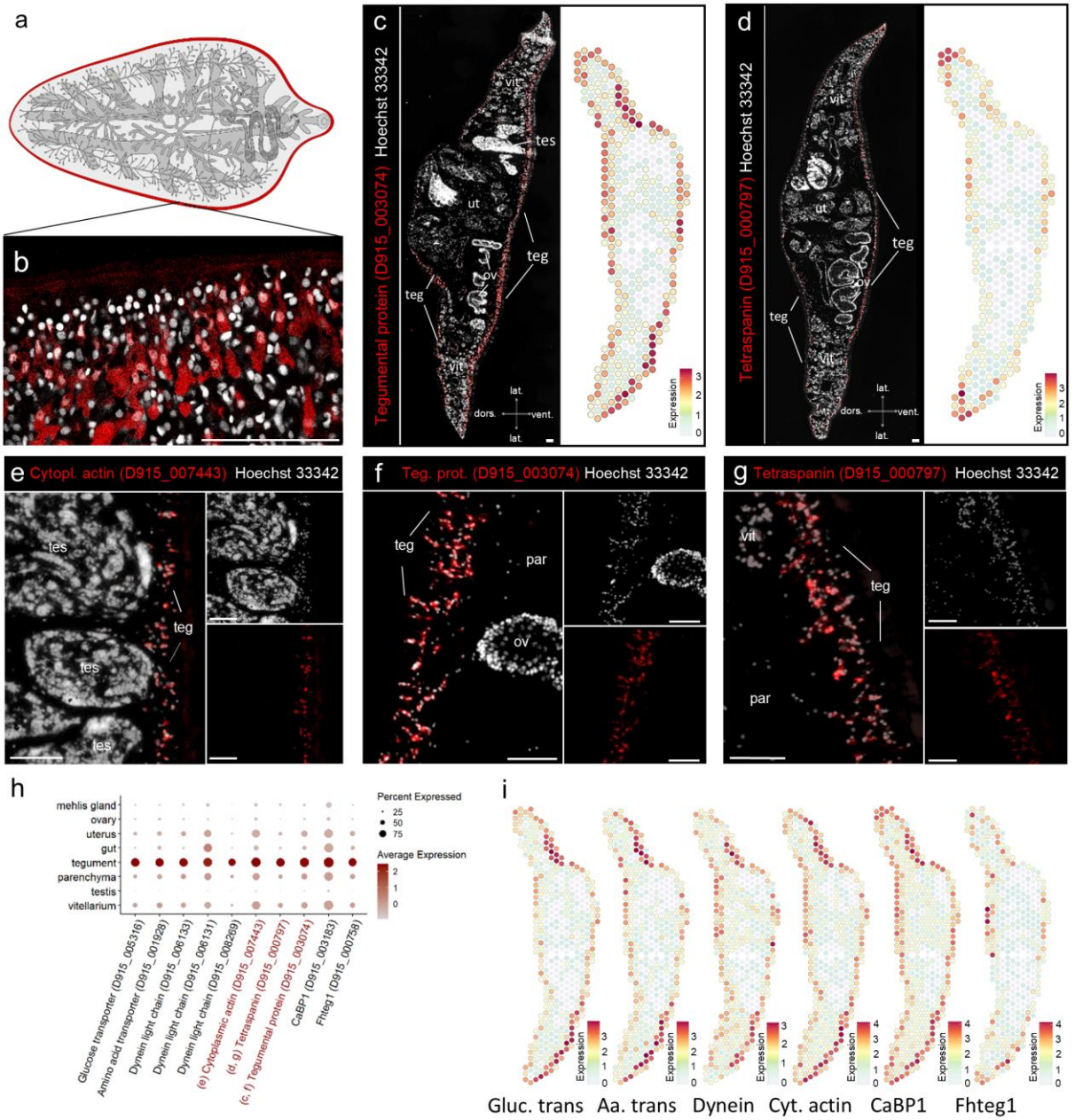

Figure 28 Nutrient transporters and cytoskeletal proteins of the liver fluke tegument.
Scheme showing anatomical features of the liver fluke. The tegument (red) is highlighted. Created in Inkscape based on [Kazakova Maryia]/Adobe Stock [42]. (**b**) Confocal image of the liver fluke tegument. Tegumental cell bodies (red) were stained with fluorescent dextran. (**c**, **d**) Fluorescent *in situ* hybridization (FISH) overview (left) and spatial projection (right) of the tegumental protein D915_003074 and tetraspanin (D915_000797). Section orientation is indicated at the bottom (dors: dorsal, vent: ventral, lat: lateral). (**e**) FISH of cytoplasmic type actin (D915_007443). (**f, g**) Magnification of (c) and (d), respectively. (**h**) DotPlot showing expression profiles of selected tissue markers of the tegument cluster. Dot color encodes the average expression level (Z-score scaled counts) across all spots within a cluster. Dot size encodes the percentage of spots within a cluster that have captured this transcript. Please note: While spatial plots (c, d, i) are shown for only one representative section, the DotPlot includes expression data from all four tissue sections in the dataset. Genes labeled in red were validated by FISH. Figure panels showing the respective FISH experiment are indicated. (**i**) Spatial projections showing expression patterns of selected tegument marker genes: glucose transporter (D915_005316), amino acid transporter (D915_001928), dynein (D915_006131), cytoplasmic type actin (D915_007443), calcium binding protein CaBP1 (D915_003183), tegumental protein Fhteg1 (D915_000758). Expression level encoded by color (gray = low, red = high). (**b-g)** Nuclei counterstained with Hoechst 33342. Scale = 100 µm. g: gut, ov: ovary, par: parenchyma, teg: tegument, tes: testis, ut: uterus, vit: vitellarium. For numbers of ISH experiments performed for each gene, see Suppl. Tab. 21. Sense controls were found to be negative (Suppl. Fig. 4q-s). [211],[212]

Other cytoskeletal and membrane-associated proteins such as cytoplasmic-type actin (D915_007443) and tetraspanin (D915_000797) probably contribute to the protective function of the tegument by maintaining its stability and structural organization. ISH confirmed their expression in groups of cells sitting below the outer syncytial layer (Fig. 28d, e, g). GO term enrichment analysis also showed an enrichment of calcium ion binding and calcium-dependent phospholipid binding proteins (Fig. 16c), which included three annexins, one calmodulin 3, one alpha-actinin and seven EF hand domain-containing proteins (e.g. D915_003074, D915_003183). Tegumental EF-hand domain-containing calcium-binding proteins are an atypical protein family only found in parasitic flatworms [279]. Their exact role is still unclear, but it has been suggested that they play an important role in the regulation of cytoskeletal processes within the tegument [279]. ISH for the EF-hand domain-containing protein D915_003074 confirmed its expression in tegumental cell bodies (Fig. 28c, f). [211],[212]

3.1.3.6 Diverse markers of a functionally divers tissue: The parenchyma

The parenchyma is an interstitial tissue embedding all other organs (Fig. 29a, b). For this reason, and because of the aforementioned resolution problem (3.1.3.5), its markers appeared not as unique as for the other clusters (Fig. 29c). Nevertheless, I performed GO term enrichment analysis to get an idea of its biological role. The analysis indicated that lipid and amino acid metabolism are two of its main metabolic functions (Fig. 16b, c). These functions were represented by multiple fatty acid binding proteins (FABP, D915_003368, D915_003367, D915_008422) and three de- or transaminases (D915_004674, D915_004407, D915_008390) (Fig. 29c). In addition, two cysteine proteases were found in the parenchyma marker list, a cathepsin L (D915_005615) and a cathepsin B (D915_007096). which, unlike related enzymes, were not restricted to the intestine, but predominantly expressed in the parasite's parenchyma (Fig. 29c, d, f). This unusual cathepsin expression pattern was previously described for schistosomes [145], but not for liver flukes and I was able to confirm cathepsin B expression in parenchymal cells by ISH (Fig. 29d). [211],[212]

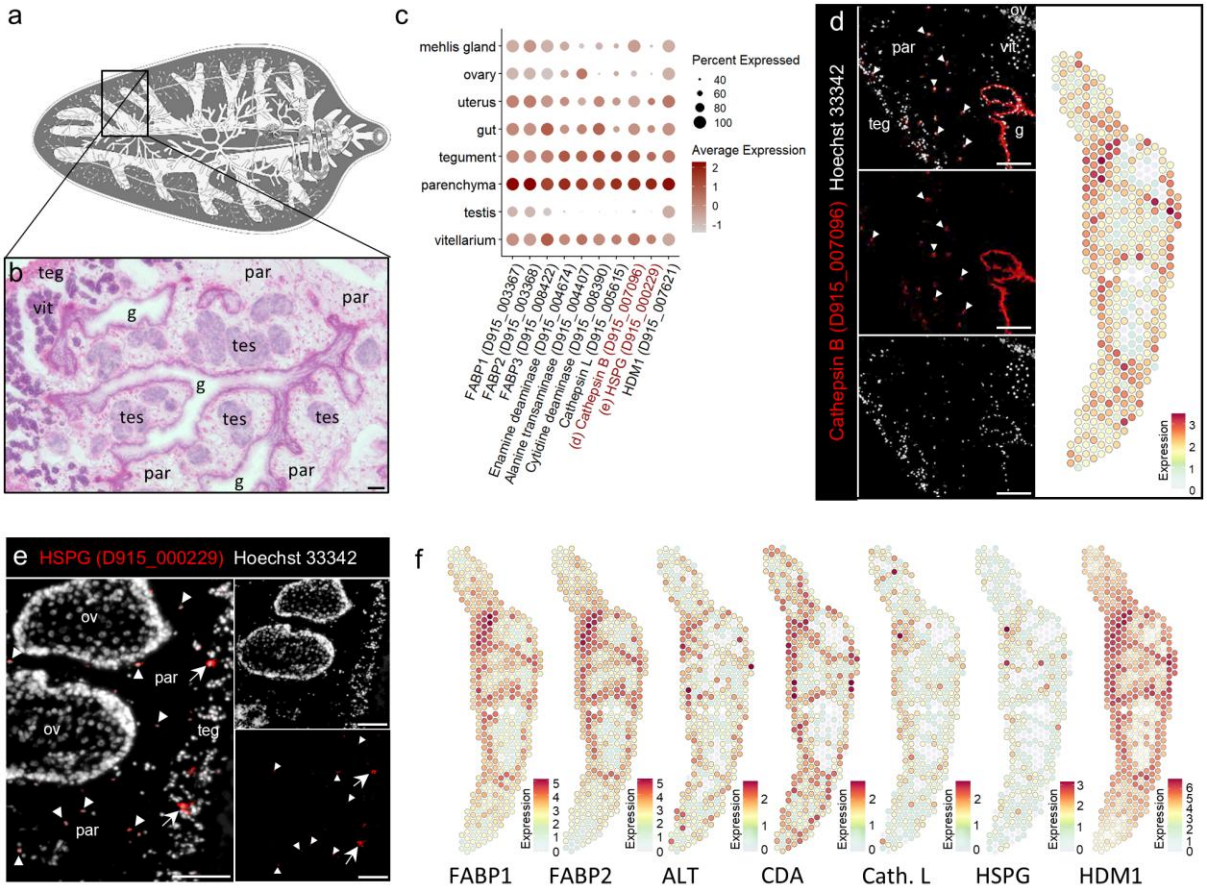

Figure 29 Marker gene expression in the liver fluke parenchyma.
(**a**) Scheme showing anatomical features of the liver fluke. The parenchyma (grey) is embedding all other organs. Created in Inkscape based on [Kazakova Maryia]/Adobe Stock [42]. **(b**) Horizontal tissue section of an adult *F. hepatica* (H&E staining). (**c**) DotPlot showing expression profiles of selected tissue markers of the parenchyma. Dot color encodes the average expression level (Z-score scaled counts) across all spots within a cluster. Dot size encodes the percentage of spots within a cluster that have captured this transcript. Please note: While spatial plots (d, f) are shown for only one representative section, the DotPlot includes expression data from all four tissue sections in the dataset. Genes labeled in red were validated by FISH. Figure panels showing the respective FISH experiment are indicated. (**d**) FISH (left) and spatial projection (right) of cathepsin B (D915_007096). This cathepsin B is expressed in the worm parenchyma as well as in the gut, white arrowheads indicate positive parenchymal cells. (**e**) FISH of basement membrane-specific heparan sulfate proteoglycan core protein (HSPG) (D915_000229). HSPG is expressed in small cells within the worm's parenchyma (white arrowheads) as well as in larger cells below the tegument (white arrows). (**f**) Spatial projections showing expression patterns of selected markers of the parenchyma: fatty acid binding protein 1(FABP1, D915_003367), FABP2 (D915_003368), alanine transaminase (ALT, D915_004407), cytidine deaminase (CDA, D915_008390), cathepsin L (D915_005615), HSPG (D915_000229), helminth-defense molecule 1 (HDM1, D915_007621). Expression level encoded by color (gray = low, red = high). (**b, d, e**) Scale = 100 µm. g: gut, ov: ovary, par: parenchyma, teg: tegument, tes: testis, ut: uterus, vit: vitellarium. (**d, e**) Nuclei counterstained with Hoechst 33342. For numbers of ISH experiments performed for each gene, see Suppl. Tab. 21. Sense controls were found to be negative (Suppl. Fig. 4t,u). [211],[212]

A second marker of the liver fluke parenchyma, whose parenchymal expression was confirmed by FISH (Fig. 29e), was a heparan sulfate proteoglycan (HSPG, D915_000229). This extracellular matrix protein showed sequence similarities to human HSPG2, which is a functionally diverse protein that can bind various extracellular matrix components, cells, low-density lipoproteins and growth factors (Suppl. Fig. 5) [280]. Finally, the parenchyma cluster was also enriched with genes linked to glutathione transferase activity (Fig. 16c). Glutathione S-transferases (GST) are thought to protect the parasite from immune-induced damage and may also contribute to the cellular detoxification of drugs [281]. Due to their potential role in TCBZ resistance [99], this gene family will be addressed in a separate results section (3.1.4.1). The expression of helminth defense molecule 1 (HDM1/MF6, D915_007621) (Fig. 29c, f), which is thought to be involved in immunomodulation [282], further reinforces a defense function of the parenchyma. The ST data thus supports the previous assumption that the parenchyma functions as a flexible skeleton as well as a site of metabolism, storage and transport of nutrients [32],[283], but also revealed a prominent expression of defense-related proteins. [211],[212]

3.1.4 Studying the spatial expression of liver fluke gene families

3.1.4.1 Spatial distribution of GSTs supports a detoxifying role of the parenchyma

GSTs are a family of metabolic enzymes that detoxify both endogenous compounds and foreign chemicals such as antiparasitics [281],[284]. Previous work has identified and characterized four classes of GSTs (Mu, Sigma, Omega, and Zeta) in *F. hepatica* [285]–[287]. To identify these genes in the *F. hepatica* genome used here, a phylogenetic analysis was performed together with known liver fluke sequences and human GSTs (Suppl. Fig. 6). GST expression patterns were then analyzed using the ST data, providing information on the spatial expression of 11 cytosolic (6x Mu, 2x Sigma, 2x Omega, 1x Zeta) and two microsomal GSTs (Fig. 30a, c). [211],[212]

Most Mu-class GSTs were enriched in the parenchyma (Fig. 30a, c). The exception was GST-Mu5 (D915_002901), which was only weakly expressed in the parenchyma and showed a predominant expression in the tegument (Fig. 30a, c). The expression of Mu27/47 in the ovary and uterus was almost as high as in the parenchyma, while the expression of Mu 29/1 and Mu 28/7 in gonads was significantly lower. The two Sigma-class GSTs differed in their spatial expression patterns. The expression of GST-S1 (D915_001201) in the vitellarium was significantly higher than in all other organs while GST-S2 (D915_006844) expression was highest in the parenchyma, and thus displayed a similar pattern as the Mu-class GSTs. Distinct spatial expression patterns were also noted for the two omega-class GSTs. GST-O1 transcripts (D915_001421) were detected in the vitellarium and uterus and slightly less in the

ovary, whereas GST-O2 (D915-001777) was predominantly expressed in the parasite's tegument. Finally, I examined the two microsomal GSTs, which appeared to complement each other in their expression patterns. While GST-m1 (D915_002950) was expressed in almost all tissues except testis, GST-m2 (D915_007840) was strongly enriched in spots of the testis cluster. [211],[212]

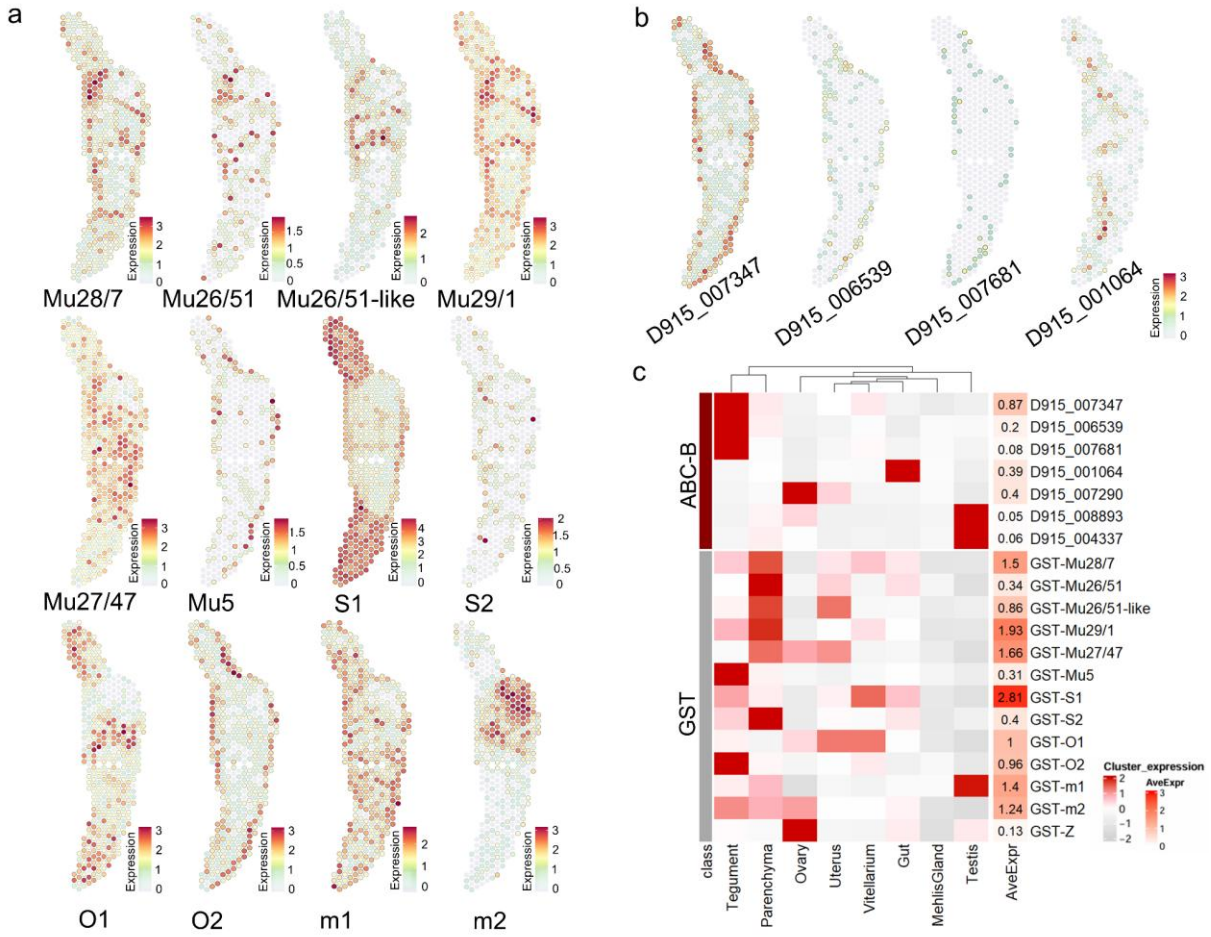

Figure 30 Tissue-specific expression of glutathione S-transferases and ABC transporters.
(**a**) Spatial projections showing expression patterns of *F. hepatica* glutathione S-transferases (GSTs). Mu-class GSTs: Mu28/7 (D915_008526), Mu26/51 (D915_008966), Mu26/51-like (D915_008366), Mu29/1 (D915_007977), Mu27/47 (D915_010266), Mu5 (D915_002901); Sigma-class GSTs: S1 (D915_001201), S2 (D915_006844); Omega-class GSTs: O1 (D915_001421), O2 (D915_001777); and microsomal GSTs: m1 (D915_007840), m2 (D915_002950). Zeta class GST (D915_006391) is shown in Suppl. Fig. 3a. For GST phylogeny, see Suppl. Fig. 6. (**b**) Spatial projection showing expression patterns of selected *F. hepatica* ABC-B transporters. See Suppl. Fig. 3b for spatial projections of ABC-B genes not shown in (b). For ABC-transporter phylogeny, see Suppl. Fig. 7. (**a, b**) Expression level encoded by color (gray = low, red = high). (**c**) Left: Heatmap of GSTs and ABC-B transporters showing the average expression per cluster (Z-score scaled counts). Please note: While spatial plots (a, b) are shown for only one representative section, the heatmap includes expression data from all four tissue sections in the dataset. Right: Heatmap showing the average expression of those genes in the whole dataset (log1p transformed counts). The two testis-associated ABC-B transporters (D915_008893 and D915_004337) and D915_007290, which is preferentially expressed in the ovary, are not shown in (b). See Suppl. Fig. 3b for their spatial expression patterns. [211],[212]

3.1.4.2 The liver fluke gut and tegument express distinct ABC-B transporters

ABC transporters are a second interesting protein family that may be involved in the defense against toxic products, including drugs such as TCBZ, by mediating drug efflux from the parasite [82]. However, to date, very little information has been available on the spatial expression of ABC transporters in *F. hepatica*. Furthermore, a comprehensive list of ABC transporter subtypes in *F. hepatica* was lacking. Therefore, all ABC transporter sequences available in WBPS were submitted to phylogenetic modelling together with human and *C. elegans* ABC transporters from all subfamilies (A,B,C,D,E,F,G). This analysis identified four ABC-A, twelve ABC-B, three ABC-C, two ABC-D, one ABC-E, two ABC-F and three ABC-G members in the *F. hepatica* genome (Suppl. Fig. 7). Since subfamily B is particularly interesting with regard to drug resistance due to its similarity to the multidrug resistance protein MDR1 [82], further investigations focused on this subfamily. Of the twelve ABC-B subfamily members, five were only weakly expressed and appeared rather scattered (Suppl. Fig. 3b). For the seven others, however, I was able to detect an association with specific organs (Fig. 30b, c). Among the most significant findings was the expression of four genes (D915_007347 D915_006539, D915_007681 and D915_001064) at the host-parasite interface, with D915_007347 showing particularly high expression of in the tegument. In contrast, D915_001064 was the only ABC-B transporter that was predominantly expressed in the intestine. [211],[212]

3.1.4.3 Differential tissue and life stage expression of liver fluke tubulins

Tubulins are of research interest as they are molecular targets of TCBZ, the drug of choice to treat fasciolosis [82]. Five α-tubulins (α1-5) and six β-tubulins (β1-6) of *F. hepatica* have been described in literature [74]. All of these tubulins were detected in the spatial transcriptome and it was possible to identify two major groups of tubulins based on their spatial expression. α-tubulins 1, 4 and 5, as well as β-tubulins 1, 5, and 6 were predominantly expressed in the testis (Fig. 31a, d, e), while α2, α3, β2, β3 and β4 were expressed in different other tissues (Fig. 31b, d, f). α-tubulin 2 as well as β-tubulin 3a and 4, showed highest expression in the flukes' ovary. α-tubulin 3 and β-tubulin 2, on the other hand, were primarily expressed in non-reproductive tissues, with the peak expression observed in the tegument. β-tubulin 3b showed relatively low expression levels compared to other tubulin genes. As already mentioned (3.1.2.1), this made it more difficult to localize, but it also seemed to be associated with the tegument (Fig. 31c). The comparison of the tissue expression profiles with published life stage expression data revealed that the tubulin genes enriched in the testis of the worm were only weakly expressed in NEJs and upregulated during parasite maturation, whereas the other tubulin genes were more or less uniformly expressed at all life stages (Fig. 31d). [211],[212]

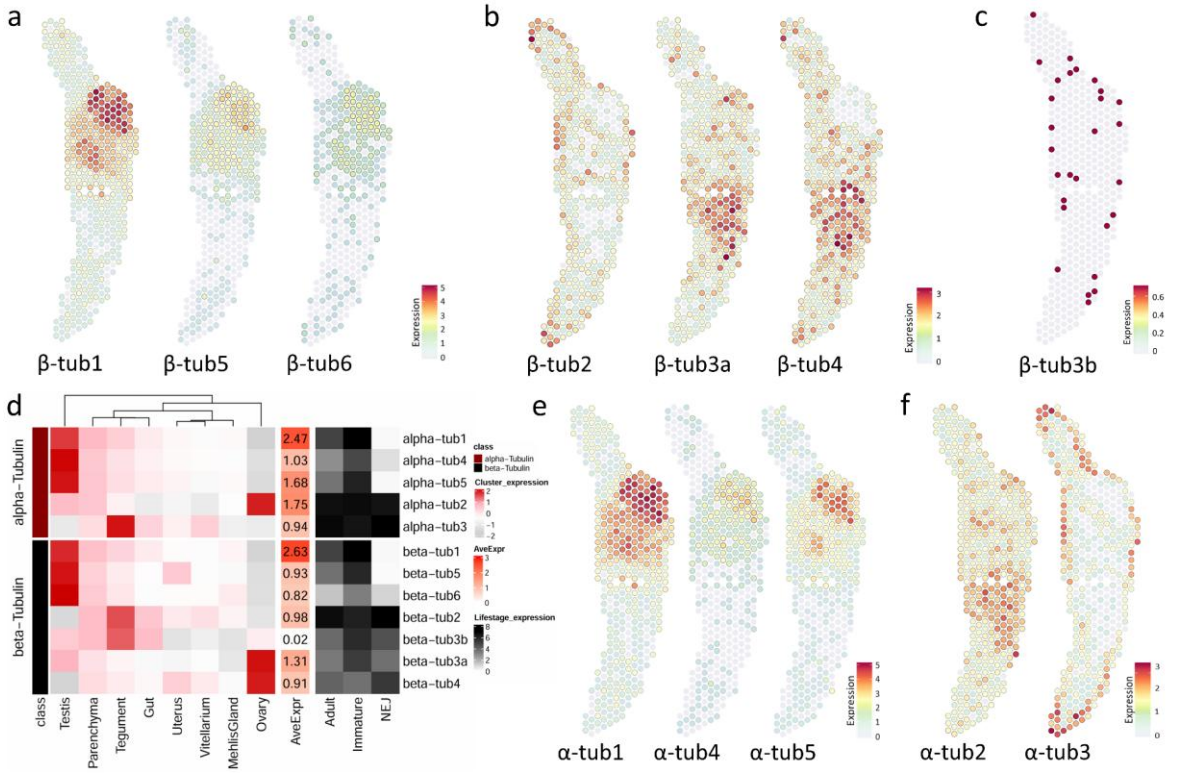

Figure 31 Tubulins upregulated during maturation are expressed the liver fluke testis.
(**a-c**) Spatial projections showing expression patterns of *F. hepatica* β-tubulins. β-tub1 ("beta-tub1"/D915_007398), β-tub2 ("beta-tub2"/D915_002311), β-tub3a ("beta-tub3.1"/D915_004911), β-tub3b ("beta-tub3"/ D915_002077), β-tub4 ("beta-tub4"/D915_001342), β-tub6 ("beta-tub6"/D915_008457). β-tubulin 5 was found fragmented with D915_005076 and D915_003963 representing two halves of the complete β-tubulin 5. Figures show D915_003963. (**d**) Left: Heatmap showing the average expression (Z-score scaled counts). of all α- and β-tubulins per cluster. Please note: While spatial plots (a-c & e, f) are shown for only one representative section, the heatmap includes expression data from all four tissue sections in the data set. Source data are provided as Source data file. Middle: Heatmap showing the average spot expression of all α- and β-tubulins in the whole dataset (log1p transformed counts). Right: Heatmap showing tubulin life stage expression data from Cwiklinski et al. [S7] (log1p transformed TPM values) for adult, immature and newly excysted juvenile (NEJ) *F. hepatica*. Mean values of 2-3 biological replicates. (**e**) Spatial projections showing α-tubulins with predominant expression in the testis: α-tub1 ("alpha-tub1"/ D915_009242), α-tub4 ("alpha-tub4"/ D915_009559), α-tub5 ("alpha-tub5"/ "D915_005959). (**f**) Spatial projections of α-tub2 ("alpha-tub2"/ D915_005370) and α-tub3 ("alpha-tub3"/ D915_8616). (**a-c & e, f**) Expression level encoded by color (grey = low, red = high). [211],[212]

3.1.4.4 Ly6 proteins are expressed at the host-parasite interface

CD59-like proteins of the Ly6 (lymphocyte antigen 6) family are thought to be involved in parasite-host interactions and has been proposed as vaccine candidate for *Fasciola* spp. [118],[288]. To learn more about their spatial expression, I first performed a WormBase ParaSite BLASTp based on *F. gigantica* Ly6 protein sequences to identify all Ly6 proteins in the *F. hepatica* genome used in this study. In total, 19 FhLy6 proteins were identified (Suppl. Tab. 24). Among those, four genes were predominantly expressed in the tegument (Ly6-B (D915_008996), Ly6-F (D915_008863), Ly6-N (D915_007373), Ly6-Q (D915_008394)), three in the parenchyma (Ly6-A (D915_001097), Ly6-D (D915_006706), Ly6-U (D915_000333)) and two were weakly expressed but potentially intestinal Ly6 proteins (Ly6-K (D915_009743), Ly6-L (D915_008235)) (Fig. 32). Three others (Ly6-M, Ly6-O, Ly6-R) were predominantly

expressed in the testis, while the remaining genes did not show a clear tissue preference (Suppl. Fig. 3). [211],[212]

Human CD59 acts as an inhibitor of the complement system by binding complement proteins via four conserved residues [289]. To assess whether tegumental FhLy6 proteins might fulfill similar functions, I performed amino acid sequence alignment together with human CD59 (Suppl. Fig. 8). However, apart from R78 in FhLy6-Q, no other residues were conserved in tegumental FhLy6 proteins.

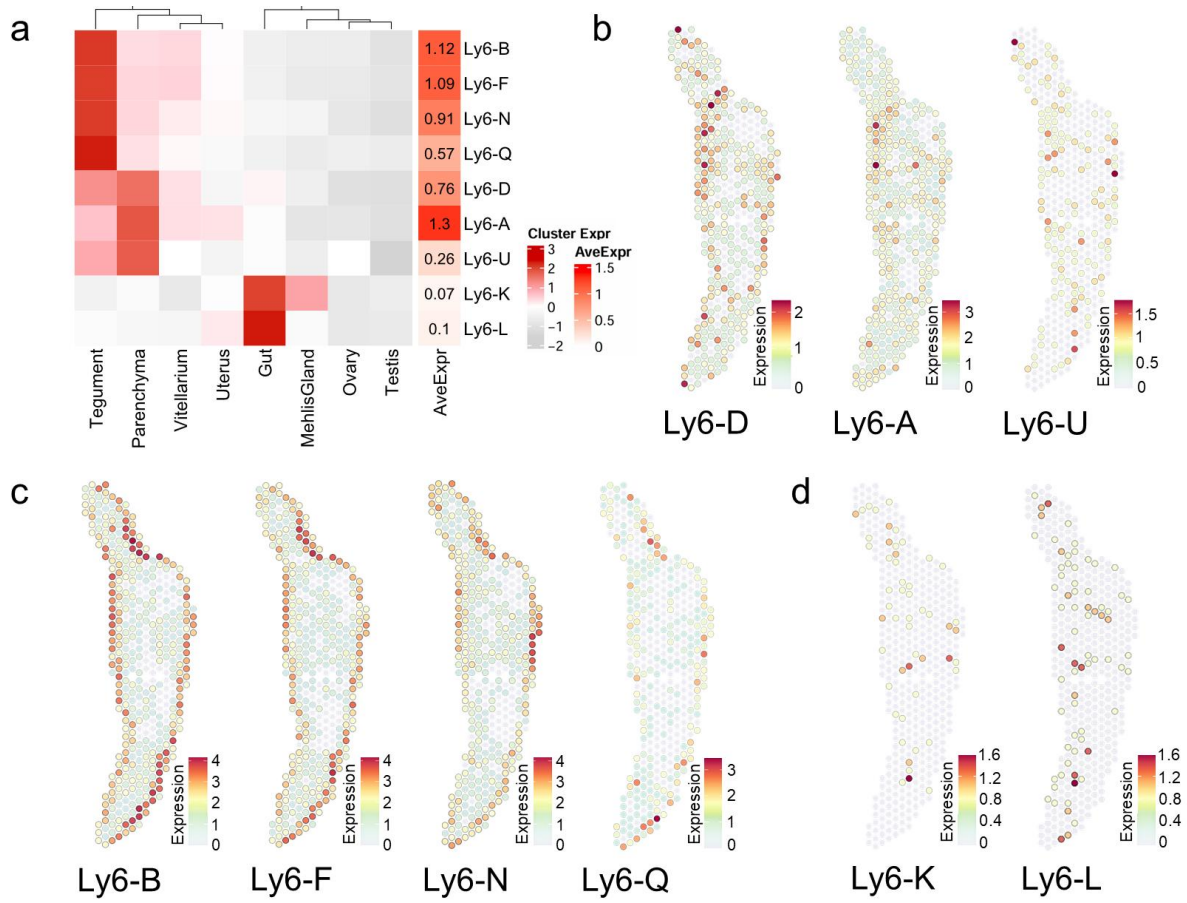

Figure 32 Spatial expression of *F. hepatica* Ly6 proteins.
(**a**) Left: Heatmap of selected Ly6 proteins showing the average expression per cluster (Z-score scaled counts). Please note: While spatial plots (**b, c**) are shown for only one representative section, the heatmap includes expression data from all four tissue sections in the dataset. Right: Heatmap showing the average expression of those genes in the whole dataset (log1p transformed counts). (**b-d**) Spatial projections showing expression patterns of tegumental, parenchymal and potentially intestinal *F. hepatica* Ly6 proteins. Expression level encoded by color (gray = low, red = high). (**b**) Ly6 proteins with prominent expression in the parenchyma: Ly6-D (D915_006706), Ly6-A (D915_001097), Ly6-U (D915_000333). (**c**) Tegumental Ly6 proteins: Ly6-B (D915_008996), Ly6-F (D915_008863), Ly6-N (D915_007373), Ly6-Q (D915_008394). (**d**) Ly6 proteins expressed in the gut cluster: Ly6-K (D915_009743), Ly6-L (D915_008235). See Suppl. Fig. 3c for Ly6 proteins not shown in (**b**–**d**). [211],[212]

3.1.5 Prioritizing tegument- and gut-expressed genes for drug repurposing

Assuming that good drug targets are mainly found among the proteins of the tegument or the intestine (organs vital for the parasite), these clusters were examined for possible candidates. First, all genes were selected from the data set whose expression in the tegument or gut cluster was higher than the mean expression of these genes in all clusters. This approach included the cluster markers as well as other transcripts that were enriched in these organs but not necessarily exclusive to them. This resulted in the identification of 474 genes for the tegument cluster and 246 genes for the gut cluster (Fig. 33a). In the second step, these gene lists were searched for orthologs of eukaryotic target proteins listed in the ChEMBL compound database [248], specifically those targeted by small-molecule drugs that have reached at least phase 3 clinical development and are thus considered suitable candidates for drug repurposing. This resulted in 11 potential targets of 20 drugs in the tegument and 10 targets of 37 drugs in the intestine (Fig. 33, Suppl. Tab. 25 & 26). Among them were three ABC-B transporters (tegument: D915_007347 & D915_006539, gut: D915_001064), two solute carriers (gut: D915_004198 & D915_004176), two proteases (gut: D915_008045, D915_001479) and a chloride ion channel (tegument: D915_008739). [211]

Building on previous work of the Haeberlein lab on protein kinases in *F. hepatica* [115], I focused on this particular class of druggable proteins. The list of tegument-expressed target genes contained two kinases: Serine/threonine kinase D915_002343 and protein kinase C beta (PKCβ, D915_006901). One kinase was found for the intestine: mitogen-activated protein kinase kinase 15 (D915_004118) (Suppl. Tab. 25 & 26). The protein kinase C beta (D915_006901) was one of four *pkc* genes found in the *F. hepatica* genome (Sagar Ajmera, personal communication) and the only one that was enriched in the tegument cluster (Fig. 33b, c). Because of a 73.36% amino acid identity between the catalytic domains of *F. hepatica* and human PKCβ (Fig. 33d), Simone Häberlein tested the highly isoform-specific human PKCβ inhibitor ruboxistaurin (LY333531) [224] against adult *F. hepatica* to determine whether targeting of PKCβ causes anthelminthic effects. 50 µM ruboxistaurin killed adult *F. hepatica* within 72 hours *in vitro*, showing a similar efficiency as the gold standard TCBZ (Fig. 33 e-f). This example thus demonstrates how the spatial transcriptome can aid in drug discovery and target prioritization. [211],[212]

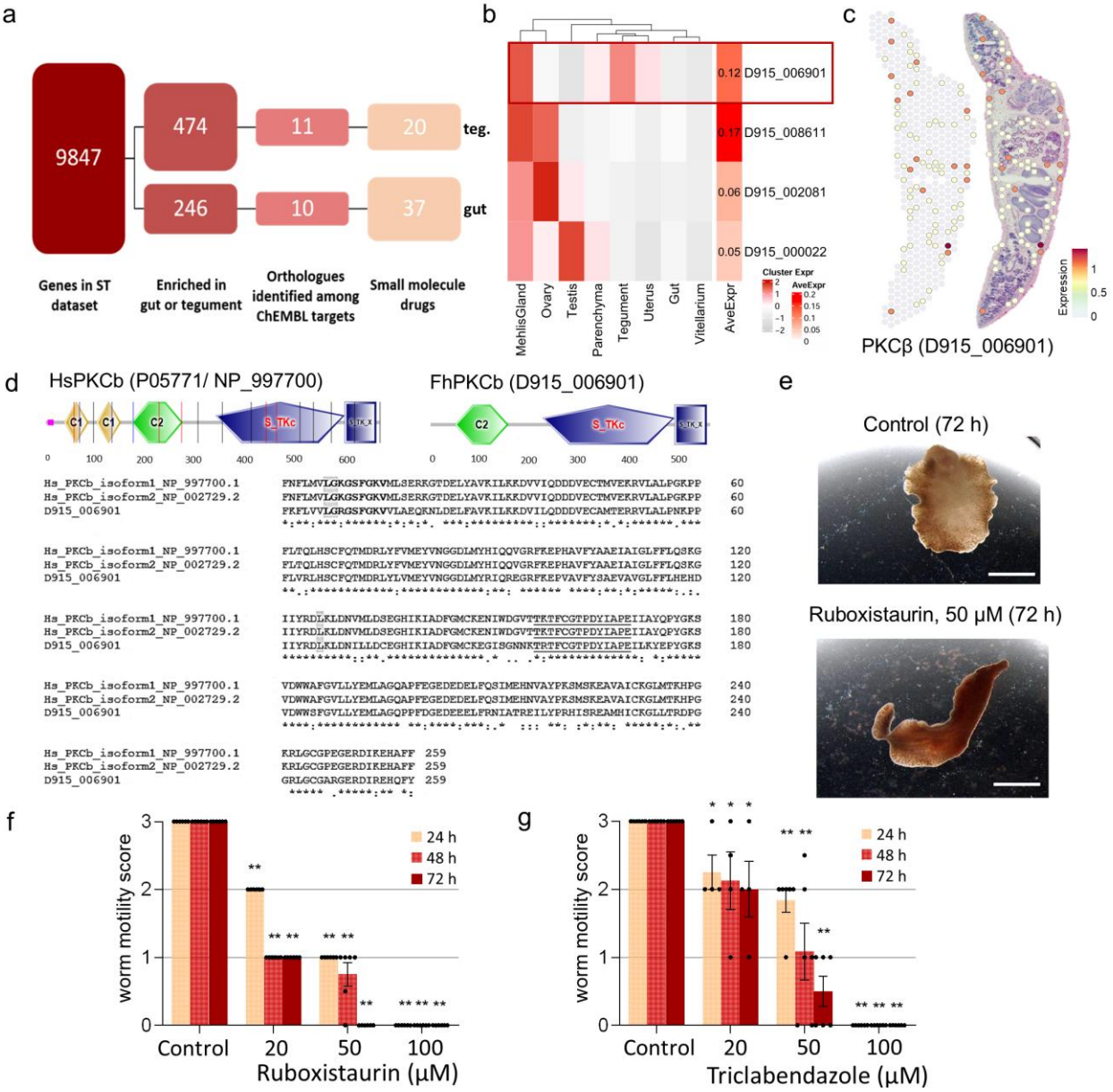

Figure 33 Prioritizing tegument- and gut-expressed genes for drug repurposing.
(**a**) Number of genes and identified compounds in the drug repurposing analysis. 11 and 10 potential targets of 20 and 37 drugs were predicted in the tegument and gut, respectively. (**b**) Left heatmap: average expression of different PKC genes per cluster (Z-score scaled counts). Right heatmap: average expression in the whole dataset (log1p transformed counts). Rectangle marks PKCβ with tegumental expression. Please note: While the spatial plot is shown for one representative section, the heatmap includes expression data from all four tissue sections in the dataset. (**c**) Spatial projection (left) and overlay with H&E-stained tissue section (right) showing expression of *pkcb* (D915_006901). Expression level encoded by color (gray = low, red = high). Several positive spots can be seen along the tegument of the parasite. There is no Mehlis' gland in this section. For spatial projections of other *pkc* genes see Suppl. Fig. 3d. (**d**) SMART analysis and alignment of catalytic domains of human and liver fluke PKCβ. The domain composition (C2 regulatory domain in front of the kinase domain) classifies both as conventional PKCs [224]. The catalytic domain of human PKCβ, which is bound by ruboxistaurin, shows 73.36% identity to the Fh ortholog. The conserved ATP binding site (bold) and the activation loop residues (underlined) are marked. Main residues involved in ruboxistaurin binding to human PKCβ are Lys349, Gly350 and Lys467 (gray) [224]. (**e–g**) Adult flukes were treated for 72 h with the PCKβ isoform-specific inhibitor ruboxistaurin (20–100 µM) or TCBZ as positive control. Motility was assessed every 24 h. Control worms were treated with DMSO. Representative images are shown in (e) and motility scores for all time points and concentrations in (f) and (g) (score 3 = normal, 2 = reduced, 1 = severely reduced, 0 = no motility). Data represents the mean ± SEM of n = 4 (TCBZ at 20 µM) or n = 6 flukes (others) from 2 (TCBZ at 20 µM) or 3 independent experiments (others) with 2 worms per condition and experiment. significant differences to controls are indicated with *p = 0.0333 and **p = 0.0022 (two-sided Mann-Whitney U test). Scale bars correspond to 5 mm. Data and images were provided by Simone Häberlein. [211],[212]

3.2 Molecular and functional characterization of HNF4 in the liver fluke *F. hepatica*

In this part of the thesis, I will describe how functional genomics, transcriptomics and bioinformatics were used to molecularly and functionally characterize the transcription factor HNF4 in *F. hepatica*. This project was carried out by myself and two master students, Lisa Bauer and Patrice Tegni Sontia, from the fields of biology and bioinformatics who performed their experiments and analyses under my supervision. The master students' results were reproduced and validated as part of this work. Overlaps are indicated at the appropriate points.

3.2.1 The transcription factor HNF4 is conserved in *F. hepatica*

To address the role of HNF4 in *F. hepatica*, the first step was the identification of an HNF4 orthologue in the liver fluke genome. This was done by performing reciprocal BLASTp searches of *S. mansoni* HNF4 (SmHNF4, Smp_174700) and two human HNF4 (HsHNF4α & HsHNF4γ) amino acid sequences. D915_003315 was the top hit for *F. hepatica* in all searches (Suppl. Tab. 27). A multiple sequence alignment using Muscle [253] showed 29.04% identity to SmHNF4 and 38.99% identity to HsHNF4α.

SMART protein domain analysis of D915_003315 identified a zinc finger domain of the nuclear hormone receptor-type (PF00105) and a nuclear hormone receptor-ligand binding domain (PF00104), which is a shared structural feature of nuclear receptors (NR) (Fig. 34a). In the Conserved Domain Database (CDD) [290], D915_003315 was also classified as a nuclear hormone receptor family protein (domain architecture ID 10161303) and the DNA-binding domain (DBD) was even annotated as DBD of hepatocyte nuclear factor 4 (cd06960, specific hit, e-value = 3.60e-42). In the Muscle alignment, the DBD had 86.96% and 82.61% and the LBD 49.35% and 45.26% identity with the DBD of schistosome and human HNF4α, respectively (Fig. 34a, b, c). The DBD possessed the typical NR-DBD architecture consisting of two zinc fingers with four cystein residues each (Fig. 34b). FhHNF4 had an insertion of 25 amino acids in the first zinc finger, when compared to human and schistosome HNF4. The P-box was fully conserved among the species examined, while the D-box was more variable. Phyre2 modelling revealed the characteristic α-helical sandwich structure of the ligand-binding domain (LBD), which forms the ligand binding pocket (Fig. 34c, d). However, the LBD of liver fluke and schistosome HNF4 was considerably larger than in human HNF4s, caused by 162 and 114 additional amino acids between alpha helix 5 and 6.

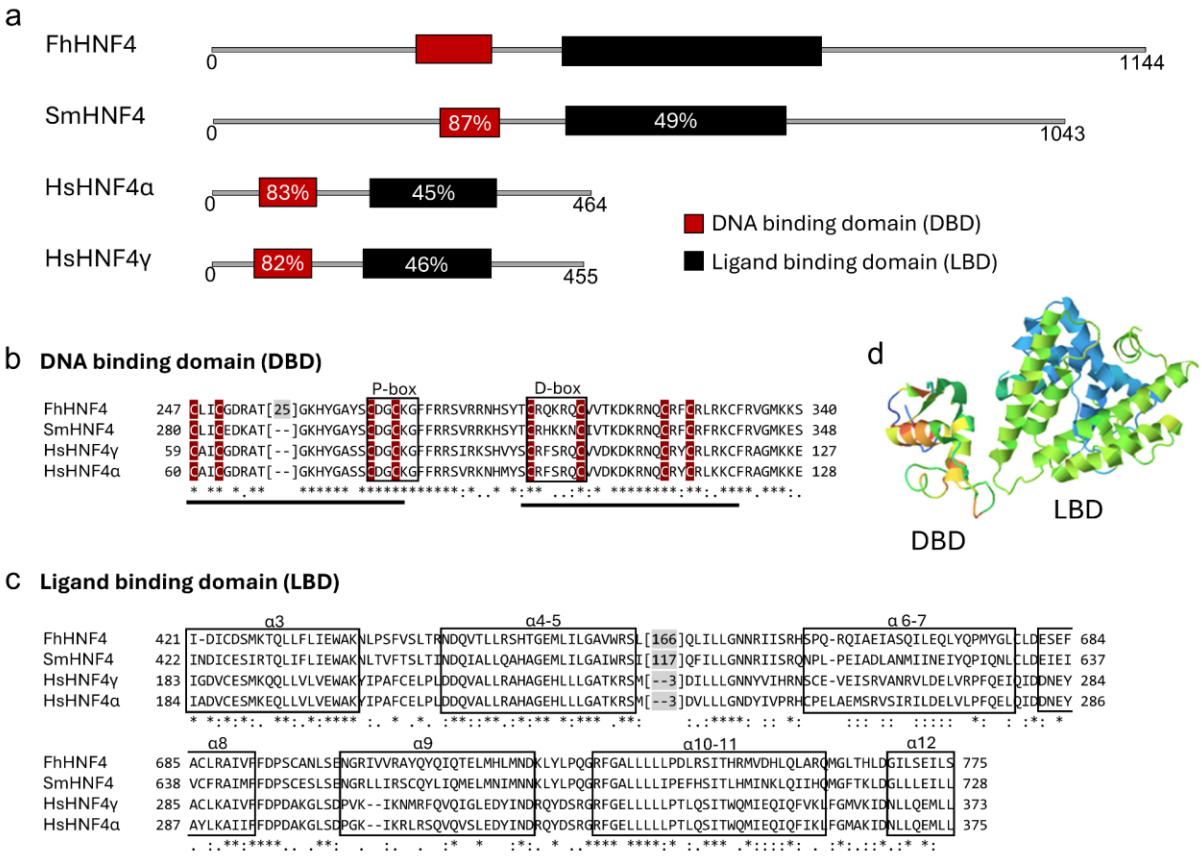

Figure 34 Domain structure and homology of liver fluke HNF4.
(**a**) Schematic of domain structure of *F. hepatica* (Fh) HNF4 (D915_003315), *S. mansoni* (Sm) HNF4 (Smp_174700) and human (Hs) HNF4α (NP_849180) and HNF4γ (NP_004124). DBD (red) = DNA-binding domain, LBD (black) = Ligand-binding domain. Percent identity resulting from Muscle alignment of DBD and LBD amino acid sequences, as shown in (b) and (c). (**b**) Alignment of liver fluke, schistosome and human HNF4 DBD amino acid sequences. The DBD consisted of two zinc fingers (black bar) with four cystein residues (dark red) each. P- and D- box are highlighted (black rectangles). (**c**) Alignment of HNF4 LBD amino acid sequences. Locations of α-helices as predicted by Phyre2 modelling are marked by black rectangles. (**d**) Potential 3D model of FhHNF4 produced by Phyre2. The first ranking model with highest confidence is shown. The structure of Protein Data Bank (PDB) entry 4IQR (Multi-domain organization of the HNF4alpha nuclear receptor complex on DNA) served as template. The model only displays the conserved regions of the DBD & LBD. Interspacing regions are not shown. The coloring encodes the level of relative conservation: blue = low, high = red.

To confirm that D915_003315 is indeed related to HNF4 of other species, I performed a phylogenetic analysis based on amino acid sequences of vertebrate and invertebrate HNF4 as well as human, schistosome and liver fluke sequences of a closely related NR, the retinoic x-receptor (RXR). D915_003315 clustered in the immediate vicinity of *F. gigantica* HNF4 and was located on a common branch together with the HNF4 proteins of other evolutionary related trematodes, including *S. mansoni* (Fig. 35).

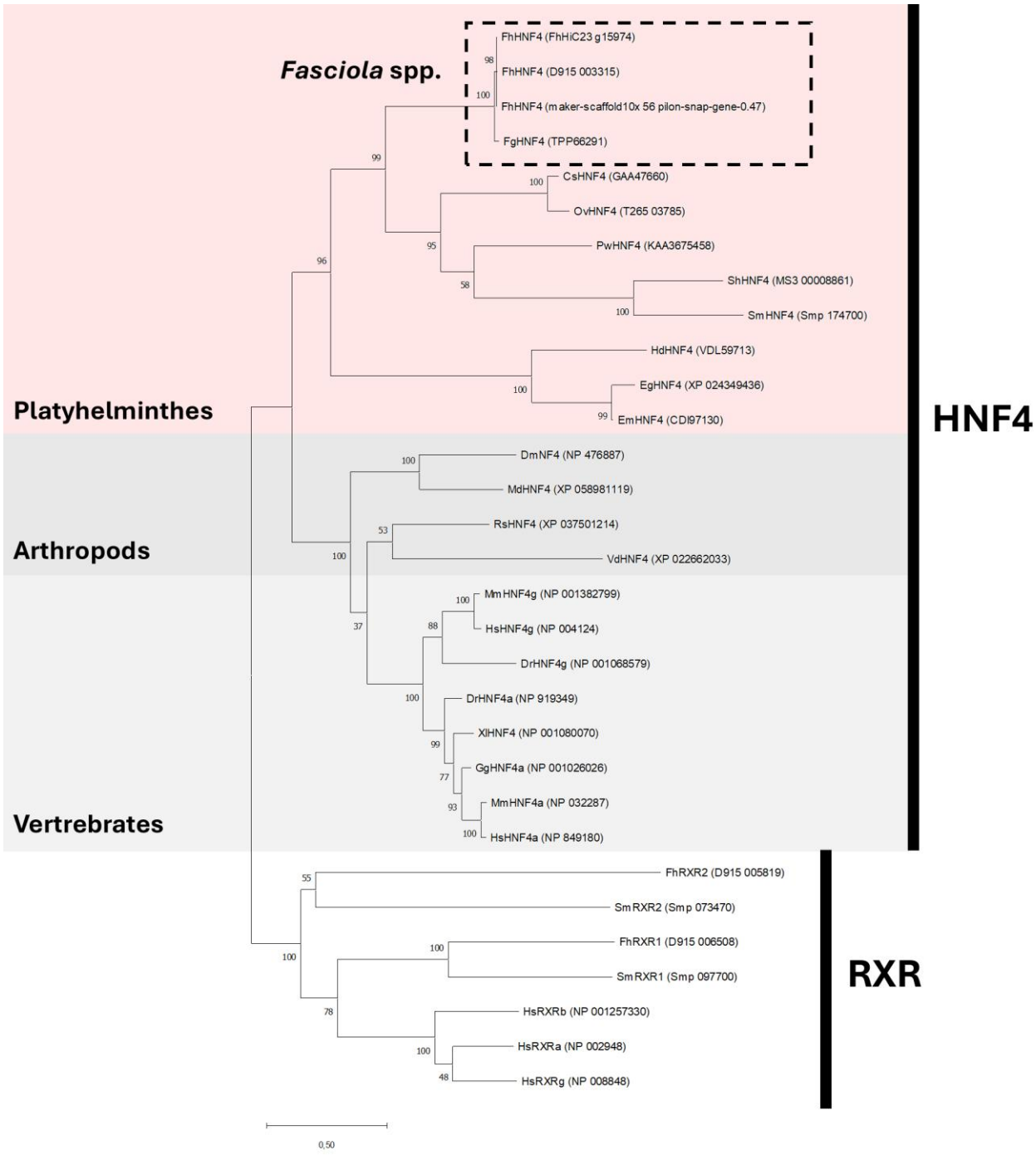

Figure 35 Phylogenetic analysis of *F. hepatica* HNF4.
Phylogenetic tree of HNF4 orthologs of *F. hepatica* and other species. Fh: *F. hepatica*, Fg: *F. gigantica*, Cs: *Clonorchis sinensis*, Ov: *Opisthorchis viverrini*, Pw: *Paragonimus westermani*, Sh: *Schistosoma haematobium*, Sm: *S. mansoni*, Hd: *Hymenolepis diminuta*, Eg: *Echinococcus granulosus*, Em: *Echinococcus multilocularis*, Dm: *Drosophila melanogaster*, Md: *Musca domestica*, Rs: *Ripicephalus sanguineus*, Vd: *Varroa destructor*, Dr: *Danio rerio*, Xl: *Xenopus laevis*, Gg: *Gallus gallus*, Mm: *Mus musculus*, Hs: *Homo sapiens*. Sequences were retrieved from WormBase ParaSite and NCBI's protein database. Accession numbers in parentheses. Maximum likelihood analysis was performed in MegaX to 1,000 bootstraps with JTT substitution. Human, schistosome and liver fluke retinoid acid receptor (RXR) sequences served as outgroup.

3.2.2 Life stage and tissue expression of *hnf4* in the liver fluke

To explore expression data across the liver fluke lifecycle, I used published life stage expression data [123] and found that *hnf4* expression was highest in adult worms, followed by immature parasites and juveniles (Fig. 36a). In the spatial transcriptome, the capturing rate of *hnf4* transcripts was quite low (123 total raw counts) and therefore not clearly assignable (see 3.1.2.1), but statistically enriched in spots of the gut cluster (Fig. 36b, c). FISH of Fh*hnf4* revealed gene expression in the entire gastrodermis of adult parasites (Fig. 36d). Localization of *hnf4* transcripts in immature liver flukes was not successful (data not shown).

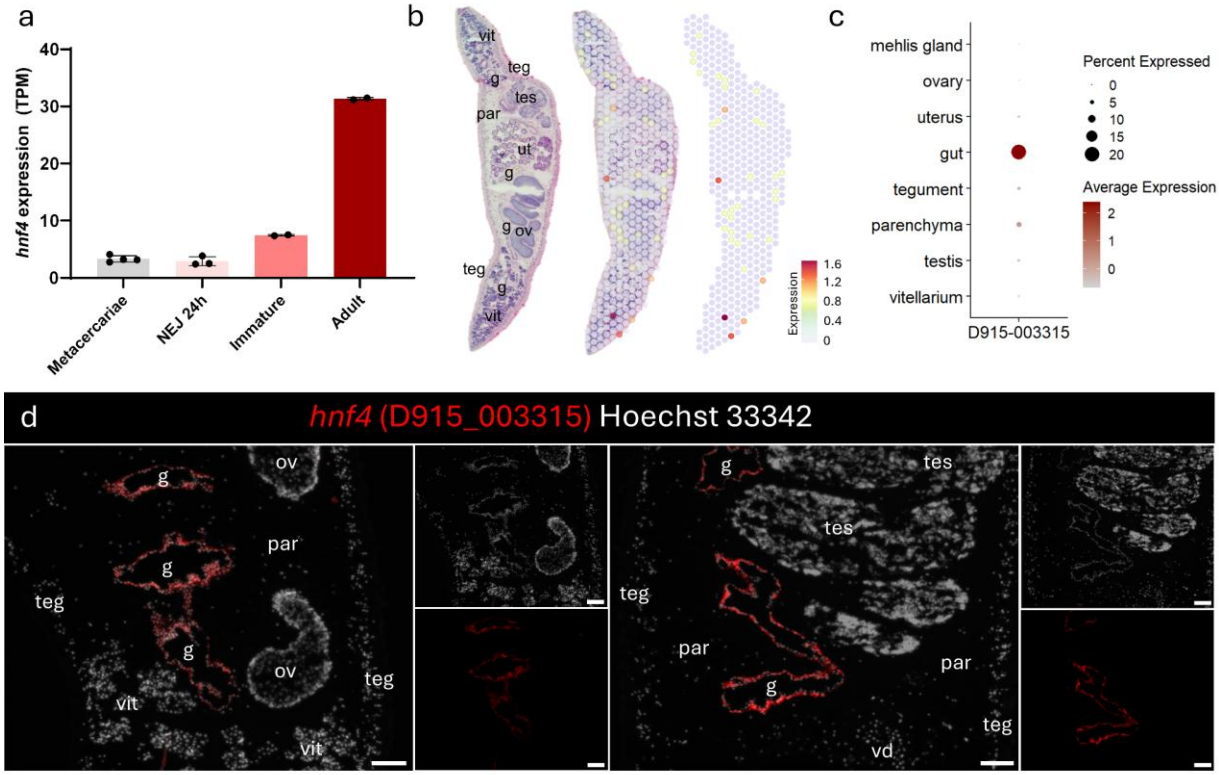

Figure 36 Life stage and tissue expression of *hnf4* in *F. hepatica*.
(**a**) *hnf4* (D915_003315) expression in different liver fluke life stages. Mean values ± standard deviation of 2-4 biological replicates. TPM = transcripts per million reads. Raw reads were produced by Cwiklinski et al. [123]. Re-mapping to the genome version used in the work was performed by Oliver Puckelwaldt. (**b**) H&E-stained tissue section, overlay and spatial projection showing the expression of *hnf4* in the liver fluke spatial transcriptome. Gene expression encoded by color (grey = low, high = red). g: gut, ov: ovary, par: parenchyma, teg: tegument, tes: testis, ut: uterus, vit: vitellarium. (**c**) DotPlot showing the expression profile of *hnf4* among spatial transcriptomics clusters. Dot color encodes the average expression level (Z-score scaled counts) across all spots within a cluster. Dot size encodes the percentage of spots within a cluster that have captured this transcript. Please note: While the spatial plot in (b) is shown for only one representative section, the DotPlot includes expression data from all four tissue sections in the dataset. (**d**) Fluorescent *in situ* hybridization (FISH) of *hnf4* in adult *F. hepatica*. Nuclei counterstained with Hoechst 33342. Scale = 100 µm. g: gut, ov: ovary, par: parenchyma, teg: tegument, tes: testis, vd: vitelline duct, vit: vitellarium. For the number of replications see Suppl. Tab. 21. Sense controls were found to be negative (Suppl. Fig. 4w).

3.2.3 Establishing RNA interference for immature *F. hepatica*

To functionally characterize HNF4 in the liver fluke, I conducted RNAi experiments in immature (4w *in vivo* grown) liver flukes. Since there was no information on RNAi in immature liver flukes in the literature, an RNAi system was first established for this life stage.

To ensure that the worms could survive a longer *in vitro* culture, as needed for RNAi experiments, two immature *F. hepatica* were cultured in either RPMI without chicken serum, RPMI with 10% native chicken serum or 10% heat-inactivated chicken serum. No differences in worm vitality were seen between the different groups over a period of 14 days (Fig. 37a). In a second step, it was determined whether there are differences in terms of the stability of dsRNA in the different culture media. Plain RPMI, RPMI with 10 % heat-inactivated chicken serum and RPMI with 10 % native chicken serum were compared. The dsRNA in plain RPMI was still intact after two hours at 37 °C, while the medium containing native chicken serum caused a marked dsRNA degradation. This effect was largely reduced when using heat-inactivated chicken serum (Fig. 37b).

Finally, it was tested whether gene expression is downregulated when treating immature *F. hepatica* with specific double stranded RNA. RNAi against the cysteine protease cathepsin L was performed by adding 50 ng/µl cathepsin L dsRNA to the culture media. Plain RPMI and RPMI with 10% heat-inactivated chicken serum were used in comparison. Worms treated with nuclease free water or with dsRNA against the bacterial neomycin resistance gene, served as controls. After seven days of treatment, the worms still showed normal vitality. On the RNA level, however, cathepsin L expression was decreased 14 and 25-fold, respectively, in the cathepsin L dsRNA-treated groups compared to the controls (knockdown efficiency: 93% and 96%) (Fig. 37c). A two-way ANOVA was performed to analyze the effect of treatment and medium on relative cathepsin L expression. The analysis showed that the treatment did have a statistically significant effect on cathepsin L expression ($p < 0.0001$), while the choice of medium did not have a significant effect ($p = 0.4552$) and did not interact with the treatment effect ($p = 0.6295$) (Suppl. Tab. 28). Relative cathepsin L expression was not significantly different between both control groups ($p\_adj = 0.9319$ and 0.8753) (Fig. 37c).

Based on these results, RPMI 1640 containing 10% heat-inactivated chicken serum and 50 ng/µl dsRNA were used in all RNAi experiments performed to functionally characterize HNF4 in *F. hepatica*. Since the availability of parasites was always limited, only the dsRNA control was included in future experiments, while the water control was omitted.

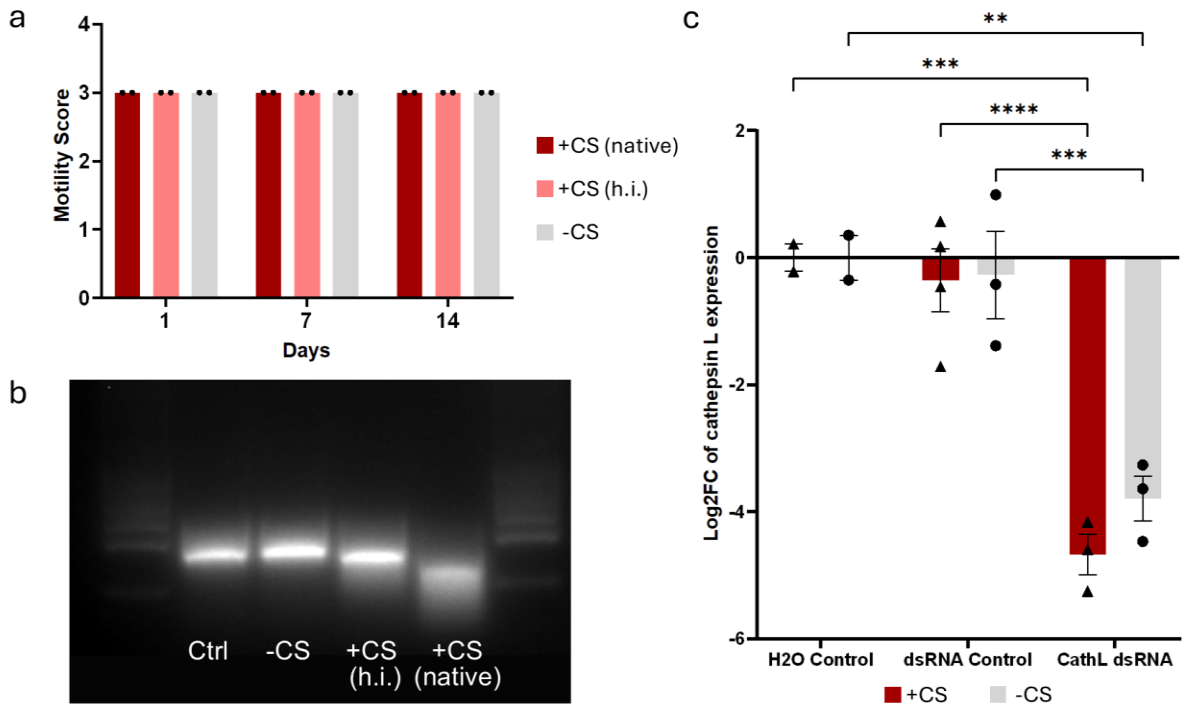

Figure 37 Testing conditions for RNAi in immature *F. hepatica.*
(**a**) Immature liver flukes were cultured in either RPMI without chicken serum (CS), RPMI with 10% native CS or 10% heat-inactivated CS for 14 days. Motility was assessed every 2-3 days. Motility scores for day 1, 7 and 14 are shown (Score: 3 = normal, 2.5 = slightly reduced 2 = reduced, 1.5 = strongly reduced, 1 = severely reduced, 0.5 = minimal, 0 = no motility/dead (Tab. 3)). Data represents the mean of n = 2 worms. (**b**) Agarose gel electrophoresis image showing 50 ng/µl dsRNA in RPMI without incubation (Ctrl), as well as 50 ng/µl dsRNA in RPMI (-CS), RPMI + 10% heat-inactivated CS (+CS h.i.) and RPMI + 10% native CS after incubation at 37 °C for 2 h. dsRNA was markedly degraded after incubation in RPMI containing native CS, which was largely reduced by heat inactivation. (**c**) Log2FC of cathepsin L (CathL, D915_010438) expression in immature *F. hepatica,* determined by qRT-PCR, after 7 days of treatment with 50 ng/µl cathepsin L specific dsRNA, neomycin dsRNA (dsRNA Control) or an equal amount of DEPC water (H_2O Control). Worms were cultured in plain RPMI (-CS) or RPMI + 10% heat-inactivated CS (+CS). Cathepsin L expression was normalized against the reference gene *eprs*. Data represents the mean ± standard deviation of n = 2-4 worms per group. Statistical analysis was done by performing two-way ANOVA (see Suppl. Tab. 28) and Tukey's test for multiple comparisons. Significant differences are indicated: **p<0.01, ***p<0.001, ****p<0.0001.

3.2.4 Functional characterization of FhHNF4 by RNAi-mediated knockdown

3.2.4.1 *hnf4* RNAi affected viability of immature *F. hepatica in vitro*

To characterize the role of HNF4 in *F. hepatica*, RNAi-mediated knockdown was performed in immature parasites. The first RNAi experiments for *hnf4* were performed by the master student Lisa Bauer [223], where the conditions from above mentioned test experiments (3.2.3) proofed to be successful. Therefore, when I repeated the experiments, immature worms were exposed to 50 ng/µl *hnf4*-specific dsRNA for 10-15 days *in vitro* (Fig. 38a). Worms treated with dsRNA against the bacterial neomycin resistance gene served as controls. At the end of each experiment, the knockdown efficiency was determined by qRT-PCR and ranged from 68-86% (Fig. 38b). Worm viability started to decrease from day 10 and significantly dropped after 13 days of dsRNA treatment (Fig. 38c). dsRNA-treated flukes showed reduced and only sporadic movements, while the control flukes showed regular and active movements. Treated worms appeared contracted, darkened and the intestinal structure was less or barely visible (Fig. 38d, e).

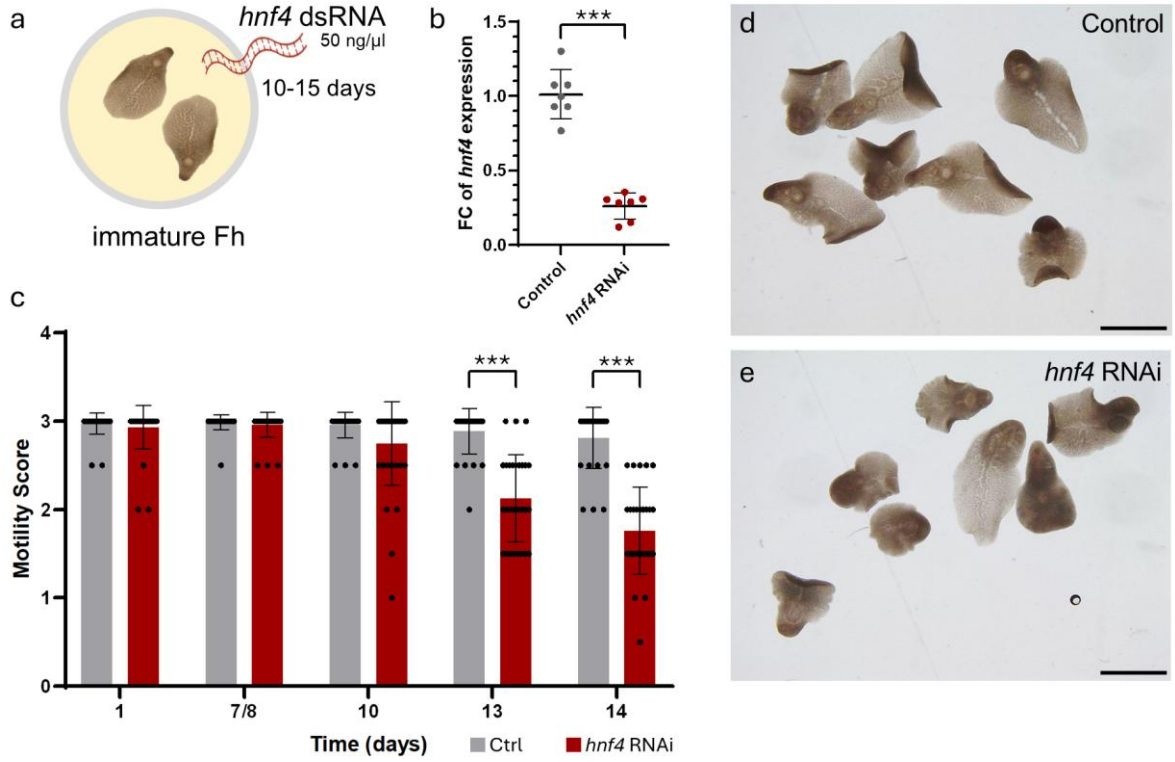

Figure 38 *hnf4* RNAi affected viability of immature *F. hepatica in vitro*.
(**a**) Scheme depicting experimental conditions for *hnf4* RNAi in immature *F. hepatica*. Parasites were exposed to 50 ng/µl *hnf4* dsRNA or neomycin dsRNA (control RNAi) for 10-15 days *in vitro*. (**b**) Relative *hnf4* expression (fold change (FC)) after 10-15 days of dsRNA treatment, determined by qRT-PCR. *Hnf4* expression was normalized against the reference gene *eprs*. Data represents the mean ± standard deviation (SD) of three independent experiments (n = 7 samples per group, 1-2 worms per sample). ***p = 0.0006 (two-sided Mann-Whitney test). (**c-e**) Motility and phenotype were assessed every 1-3 days. (**c**) Motility scores for selected time points. Motility was unaffected during the first week of culture, but decreased in knockdown worms by the end of the second week. Score: 3 = normal, 2.5 = slightly reduced 2 = reduced, 1.5 = strongly reduced, 1 = severely reduced, 0.5 = minimal, 0 = no motility/dead (Tab. 3). Data represents the mean ± SD of three independent experiments (n = 26-35 worms per condition & timepoint). Significant differences are indicated. ***p <0.001 (multiple Mann-Whitney test, corrected for multiple comparisons using the Holm-Šídák method). (**d, e**) Representative images of neomycin dsRNA-treated controls (d) and *hnf4* dsRNA-treated parasites (e) taken after 15 days of dsRNA treatment. Scale = 2 mm.

3.2.4.2 *hnf4* RNAi caused downregulation of gut-associated genes

To further explore the biology of HNF4 in *F. hepatica*, RNAseq analyses were conducted on immature *F. hepatica* treated with *hnf4* specific dsRNA for 10 days (Fig. 39a). I chose this early timepoint, when worm motility was almost not affected, to be able to address effects of *hnf4* knockdown, without being influenced by an overall decreased viability of the worms. RNA was isolated and handed to the CIGL genomics core facility (JLU Giessen) for sequencing. Sequencing QC and mapping were performed by the master student Patrice Tegni Sontia [229]. The same applies to the first analysis of the sequencing data. Starting from the mapped reads (raw counts), I performed differential gene expression analysis and the gene ontology term enrichment analysis using the DEseq2 [233] and topGO [240] packages in R.

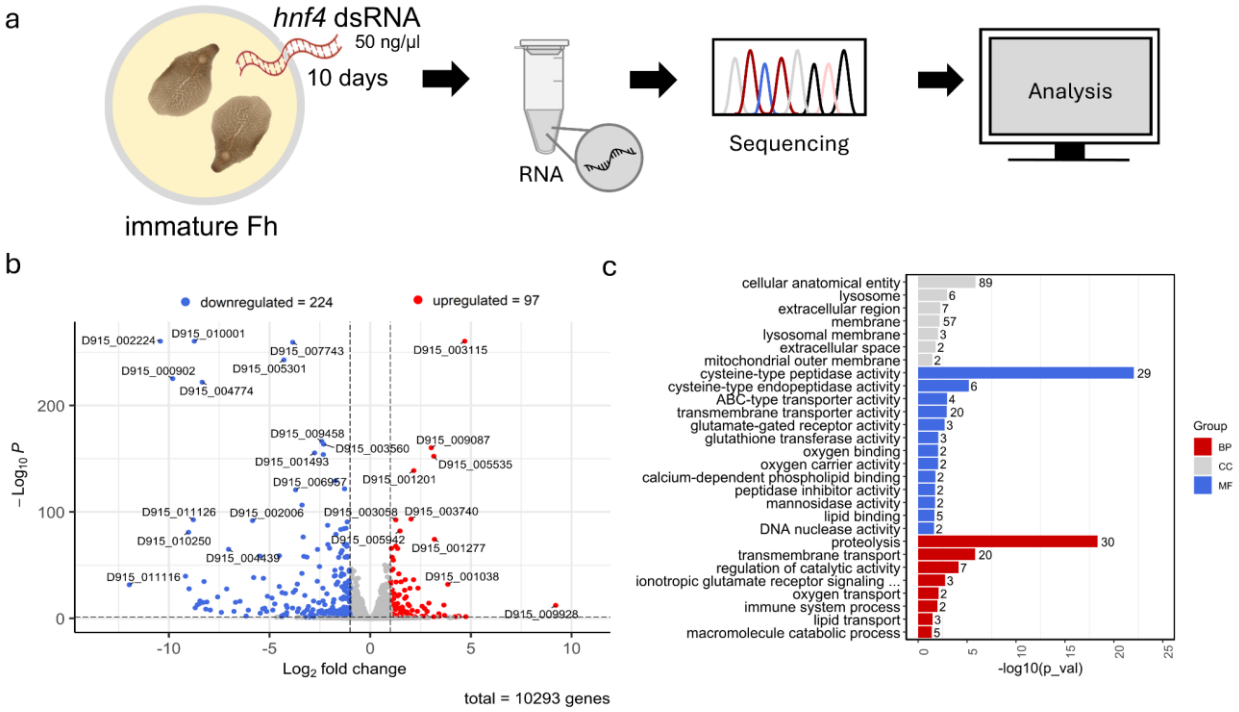

Figure 39 *hnf4* RNAi altered gene expression in immature *F. hepatica*.
(**a**) Scheme depicting the RNAseq workflow. Immature *F. hepatica* were treated with 50 ng/µl *hnf4* dsRNA for 10 days. Neomycin dsRNA-treated worms served as controls. Two worms each were pooled for RNA isolation to generate three samples (biological replicates) per group. Library preparation and Illumina sequencing were performed by the CIGL genomics core facility. Mapping and QC were performed by Patrice Tegni Sontia. Subsequent analysis was performed in R. (**b**) Volcano plot showing the significance and magnitude of changes in gene expression upon *hnf4* RNAi compared to controls. Each dot represents one gene. Genes with significant changes in gene expression (p-value < 0.05) and genes whose gene expression changed at least two-fold (-1 > log2FC > 1) are highlighted (red = upregulated, blue = downregulated). Benjamini and Hochberg-corrected Wald test. (**c**) Gene ontology analysis of downregulated genes revealed characteristic biological processes (BP), molecular functions (MF) and cellular components (CC) associated with these genes. Overrepresented functional terms were identified using a two-sided Fisher's exact test (p-value < 0.05).

224 genes were found downregulated following *hnf4* RNAi, when compared to neomycin dsRNA-treated controls (p_adj < 0.05) (Fig. 39b). GO term enrichment analysis showed that downregulated genes were most frequently associated with proteolysis (30 genes) and transmembrane transport (20 genes) (Fig. 39c). 21 of the top 50 genes with strongest downregulation were proteases, including nine cathepsins and seven legumain-like proteins (Fig. 40). A 9.2-fold downregulation of cathepsin L (D915_010438) expression in RNAi parasites was also found by qRT-PCR (Fig. 41c). In addition, six of the hemolytic saposin B-type proteins were among the most downregulated genes after *hnf4* RNAi (Fig. 40). Downregulated transporters included four ABC transporters, three ionotropic glutamate receptors and various solute carriers, e.g. for glucose, nucleosides and amino acids. Proteases and transporters were also present in lower numbers among the 97 genes upregulated upon *hnf4* RNAi (Suppl. Fig. 10), indicating a dysregulation of these biological functions. In addition, there was a notable upregulation of signaling proteins, such as several tyrosine and serine/threonine kinases (Fig. 40).

To see if differentially expressed genes were preferably associated with certain organs, I examined their tissue expression in the spatial transcriptomics atlas. Of the top 100 downregulated genes (sorted by log2FC), 26 genes were not or only weakly expressed in the spatial dataset. Of the remaining 74 genes, 50 were expressed above average in the gut cluster (Fig. 41a, b). To confirm these findings, I performed FISH for three of the downregulated digestive proteins: cathepsin L (D915_011077), saposin B (D915_010001) and legumain (D915_002224). Their transcripts were all detected in the gastrodermis of control-parasites, while in dsRNA-treated parasites no fluorescent signal could be observed, indicating a lack of the respective mRNA target (Fig. 41d, Suppl. Fig. 9).

In an attempt to explain the effects of RNAi on the expression of gut-associated genes, I searched the *F. hepatica* genome for potential HNF4 binding sites. In general, HNF4 is thought to bind DR1 repeat motifs [256]. I found slight variations of this motif in the literature and different databases (Tab. 25). In addition, there was a shorter, HNF4-specific binding motif [256]. Finally, four different motifs were searched in the 3,000 bp flanking region upstream the CDS of all *F. hepatica* genes, using a python-based tool written by Benedikt Wiebach. There were large differences in the number of hits and few similarities between some of the motifs and the list of differentially expressed genes after RNAi (Suppl. Fig. 11). Therefore, this approach was not further pursued.

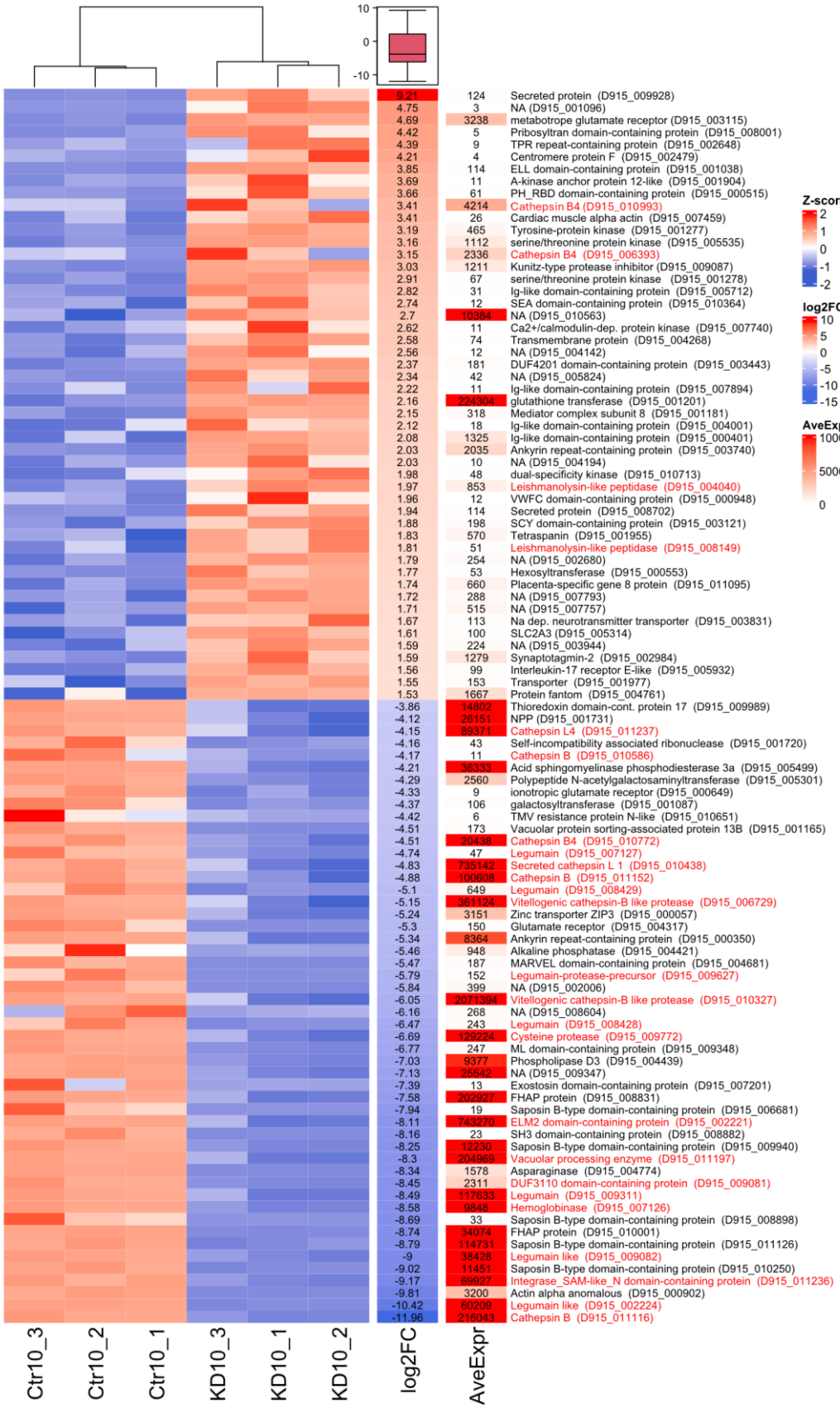

Figure 40 Proteolytic enzymes were downregulated upon *hnf4* RNAi.
Heatmap showing the expression (Z-score) of the top 50 significantly up- and downregulated genes (ordered by log2FC) per sample. Ctrl = Control. KD = Knockdown/ *hnf4* RNAi. Expression values were scaled for each row (each gene) individually (blue = expression lower than the average of all samples, red = expression higher than average). Additional columns on the right show the log2FC and the genes average expression across all samples (baseMean). Proteases are labelled in red.

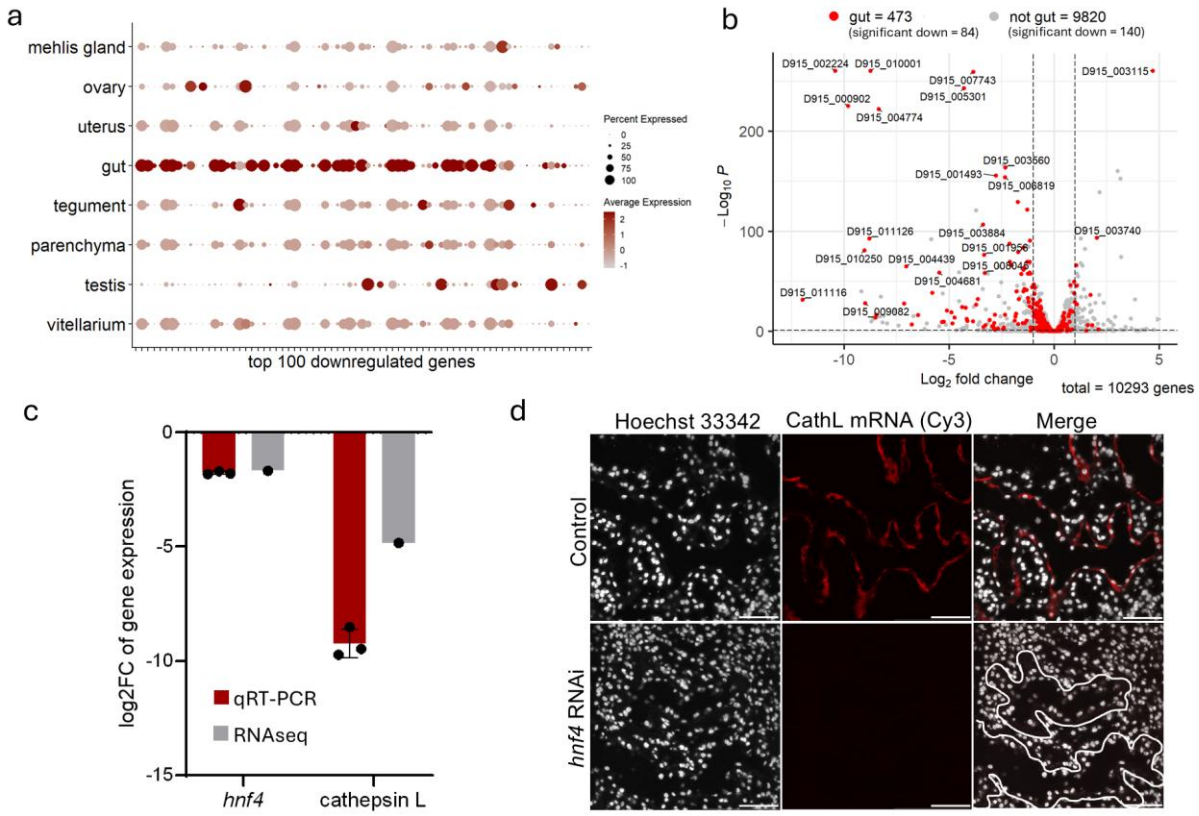

Figure 41 Downregulated genes after *hnf4* RNAi were associated with the parasite gut.
(**a**) DotPlot based on a spatial transcriptome of adult parasites, showing tissue expression profiles of the top 100 downregulated genes (sorted by log2FC) after *hnf4* RNAi. Dot color encodes the average expression level (Z-score scaled counts) within a tissue-cluster. Dot size encodes the percentage of spots within a cluster that have captured this transcript. (**b**) Volcano plot showing differential expression of gut-associated genes upon *hnf4* RNAi. Genes whose expression in the spatial transcriptomics gut cluster was one standard deviation above its average expression in all clusters are highlighted in red. Zoom of plot in Fig. 39**.** Genes exceeding axis limits are indicated as arrow heads. Selected genes are labelled. (**c**) Log2FC of *hnf4* and cathepsin L (D915_010438) expression in immature *F. hepatica* relative to neomycin dsRNA-treated controls after 10 days of dsRNA treatment, determined by RNAseq and qRT-PCR in comparison. For qRT-PCR, target gene expression was normalized against the reference gene *eprs.* qRT-PCR data represents the mean ± standard deviation of the same n = 3 biological replicates that were used for RNAseq. (**d**) FISH of cathepsin L (D915_011077) performed after 15 days of dsRNA treatment. Controls showed cathepsin L expression in the gastrodermis. No signal was observed after *hnf4* RNAi. White lining marks the contour of the gastrodermis. Images are representative for four out of five (Control) and 6/6 (RNAi) biological replicates derived from two independent experiments. Nuclei counterstained with Hoechst 33342. Scale = 50 µm.

3.2.4.3 *hnf4* RNAi in *F. hepatica* caused downregulation of *foxA* expression

In vertebrates, HNF4 is part of large transcription factor networks that can also regulate each other's transcription [198]. Therefore, I performed STRING protein-protein interaction analysis, which revealed potential interaction partners of FhHNF4, based on homology data (Fig. 42a). These included seven transcription factors and three transcriptional co-repressors (Tab. 29). The transcription of most of these genes was not affected by *hnf4* RNAi. Three of them, however, were significantly downregulated in dsRNA-treated worms: the MAD protein D915_004797, Mothers against decapentaplegic 4 (D915_002365) and the forkhead protein D915_003573, with the latter showing the strongest downregulation (Tab. 29). A reciprocal BLAST search revealed that D915_003573 is an orthologue of FOXA, a known interaction partner of HNF4 [198] and also a marker gene for intestinal progenitor cells in

schistosomes [146]. Based on these findings, I was interested in the differential regulation of further transcriptions factors after *hnf4* RNAi. A list of 422 transcription factors in *F. hepatica*, based on homology to planarian and human transcription factors, was provided by Oliver Puckelwaldt [149]. Of this list, 12 transcription factors were found significantly downregulated post RNAi, including *hnf4* and *foxA*, but also two other forkhead proteins (*foxD3* (D915_002176), *foxL1* (D915_003286)) and the myoblast determination protein (D915_006419) (Fig. 42b, Suppl. Tab. 29). On the other hand, there were only four TFs that were found significantly upregulated, among them the tonicity-responsive enhancer-binding protein NFAT5 (D915_005933) and DNA-binding protein inhibitor ID-2A (D915_001142) (Fig. 42b, Suppl. Tab. 29).

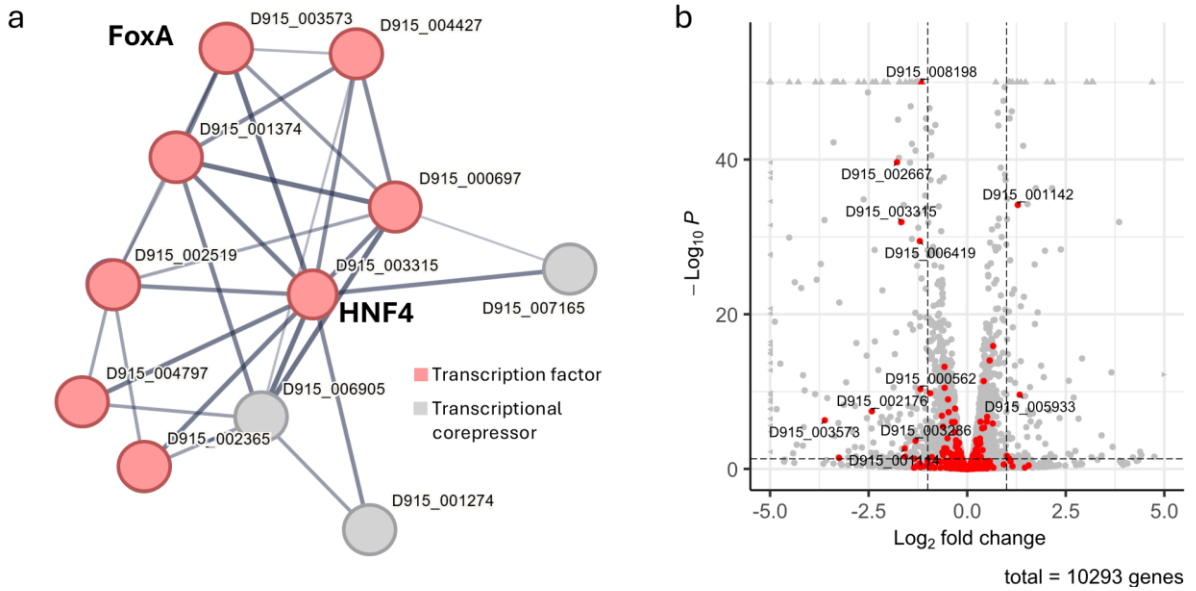

Figure 42 Differential expression of transcription factors after *hnf4* RNAi.
(**a**) STRING analysis of FhHNF4. Default settings were used to predict proteome-wide protein-protein interactions with a minimum interaction (confidence) score of 0.4 (medium level of confidence). Interactions are indicated as lines (edges). See Tab. 29 for gene descriptions and differential expression upon *hnf4* RNAi. (**b**) Volcano plot showing differential expression of transcription factors (TFs) upon *hnf4* RNAi. TFs are highlighted in red. Zoom of plot in Fig. 39. Genes exceeding axis limits are indicated as arrow heads. The list of transcription factors was provided by Oliver Puckelwaldt.

Table 29 Predicted interaction partners of FhHNF4 (sorted by log2FC)

Gene-ID	Gene description	Classification	P-value	Log2FC
D915_003573	Forkhead protein	**Transcription factor**	5.16E-07	-3.6135
D915_002519	Sloppy paired	**Transcription factor**	NA	-3.8290
D915_004797	MAD protein	**Transcription factor**	1.13E-15	-0.6064
D915_002365	Mothers against decapentaplegic 4	**Transcription factor**	1.02E-09	-0.4857
D915_001374	NURR1	**Transcription factor**	0.0606	-0.2314
D915_001274	Interferon regulatory factor 2-binding protein 2-B	**Transcriptional corepressor**	0.6816	-0.0888
D915_000697	Nuclear receptor subfamily 2 group C member 2	**Transcription factor**	0.9486	-0.0077
D915_006905	Nuclear receptor co repressor ncor	**Transcriptional corepressor**	0.1213	0.1020
D915_004427	Nuclear receptor subfamily 1 group I	**Transcription factor**	0.5567	0.1092
D915_007165	Proliferation-associated protein 2G4	**Transcriptional corepressor**	0.5188	0.0480

3.2.4.4 *hnf4* RNAi caused structural abnormalities of the gut

To assess the structure of the gastrodermis upon RNAi, I performed carmine stainings and confocal laser scanning microscopy. When I evaluated my results, I also took the results from Lisa Bauer into account [223]. For her work, we had concluded that there were no differences between knockdown worms and controls. In my repetition experiments, however, I observed treatment effects that were already visible in Lisa Bauer's work, but were not recognized at that time due to a lack of experience and a low number of replicates.

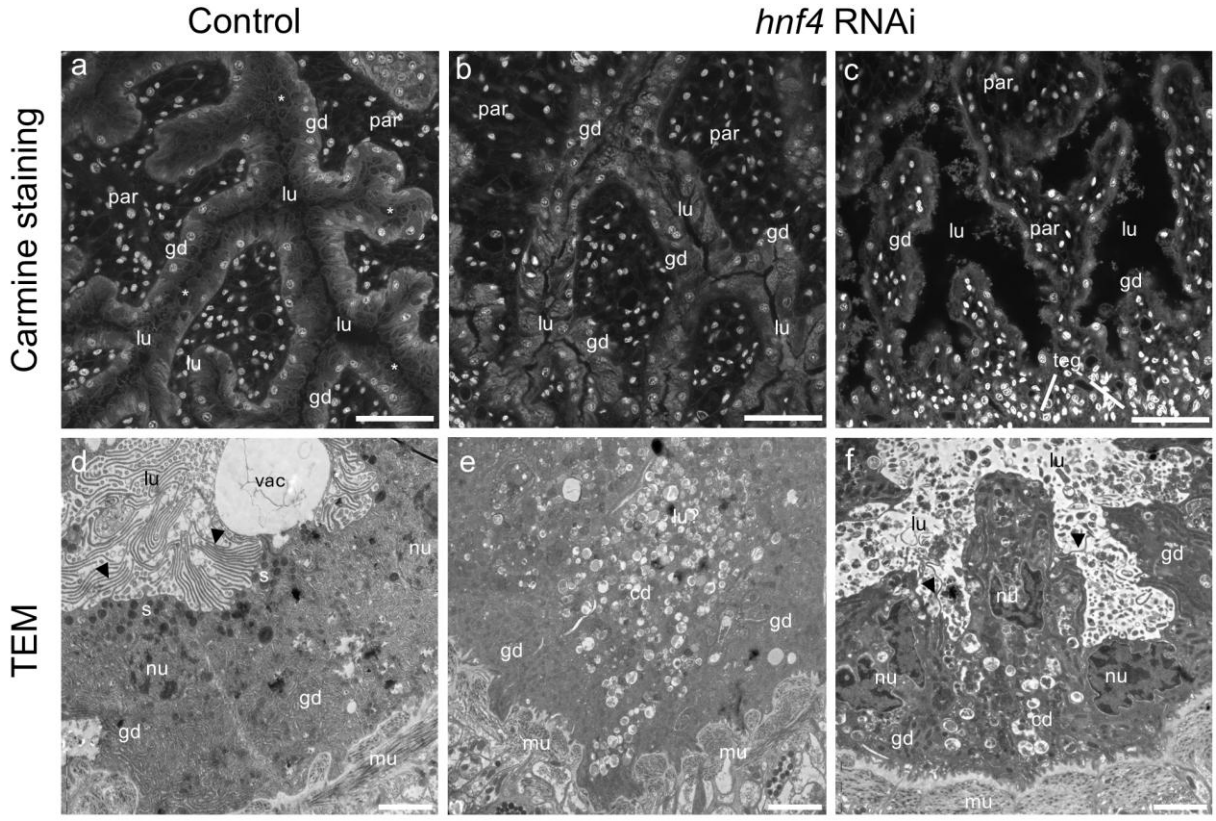

Figure 43 *hnf4* RNAi caused structural abnormalities of the gut.
(**a-c**) Confocal laser scanning microscopic images of carmine-stained immature liver flukes after 14-15 days of dsRNA treatment. Images are representative for (a) 7 out of 9 (Control) (b) 5/9 (RNAi) and (c) 3/9 (RNAi) biological replicates derived from three independent experiments (one experiment performed by Lisa Bauer, two experiments in this study). Asterisks in (a) mark presumptive vacuoles. Scale = 50 µm. (**d-f**) Transmission electron microscopic images of immature liver flukes after 15 days of dsRNA treatment. Images are representative for (d) 6/6 (Control) (b) 4/6 (RNAi) and (c) 3/6 (RNAi) samples derived from three parasites per group in one experiment (2 samples per parasite). Black arrowheads mark lamellae. Scale = 2 µm. (**a-f**) cd: cellular debris, gd: gastrodermis, lu: lumen, mu: muscle, nu: nucleus, par: parenchyma, s: secretory vesicles, teg: tegument, vac: vacuole.

The gastrodermis of control worms was characterized by large columnar cells with an irregular luminal border (Fig. 43a). This is probably due to epithelial lamellae extending into the lumen. However, individual lamellae could not be resolved. In several places, roundish, unstained structures were visible at the luminal interface, which are probably large vacuoles surrounded by lamellar bundles as known from electron microscopic studies (Fig. 43d) [273]. Parasites treated with *hnf4* dsRNA lacked these irregular surface structures and vacuoles (Fig. 43b, c). As a result, the demarcation between epithelium and lumen appeared sharper than in controls.

The gastrodermis appeared patchy and partially condensed. Denser areas often had a granular structure. In other places, the gut was distended with a flattened epithelium and flocculent contents.

For a more detailed view, TEM was performed with help from the BFS imaging unit. This confirmed the findings of the previous carmine staining: While intestinal cells in control worms showed their typical columnar structure with long lamellae [273], the number and density of lamellae in knockdown worms was either largely reduced or completely replaced by numerous small vacuoles and indefinable cellular debris (Fig. 43e, f). In many cases, the lumen could not be demarked. In addition, I observed almost no secretory vesicles in the intestinal cells of *hnf4* dsRNA treated parasites.

3.2.4.5 The effect of *hnf4* RNAi on cell proliferation remained inconclusive

In mammalians, HNF4 is known to promote cell differentiation and inhibit cell proliferation [198]. Therefore, EdU stainings were performed to visualize proliferating cells in tissue sections of *hnf4* dsRNA-treated worms and controls. In both groups however, I was not able to visualize proliferating cells with prominent EdU signal (Fig. 44).

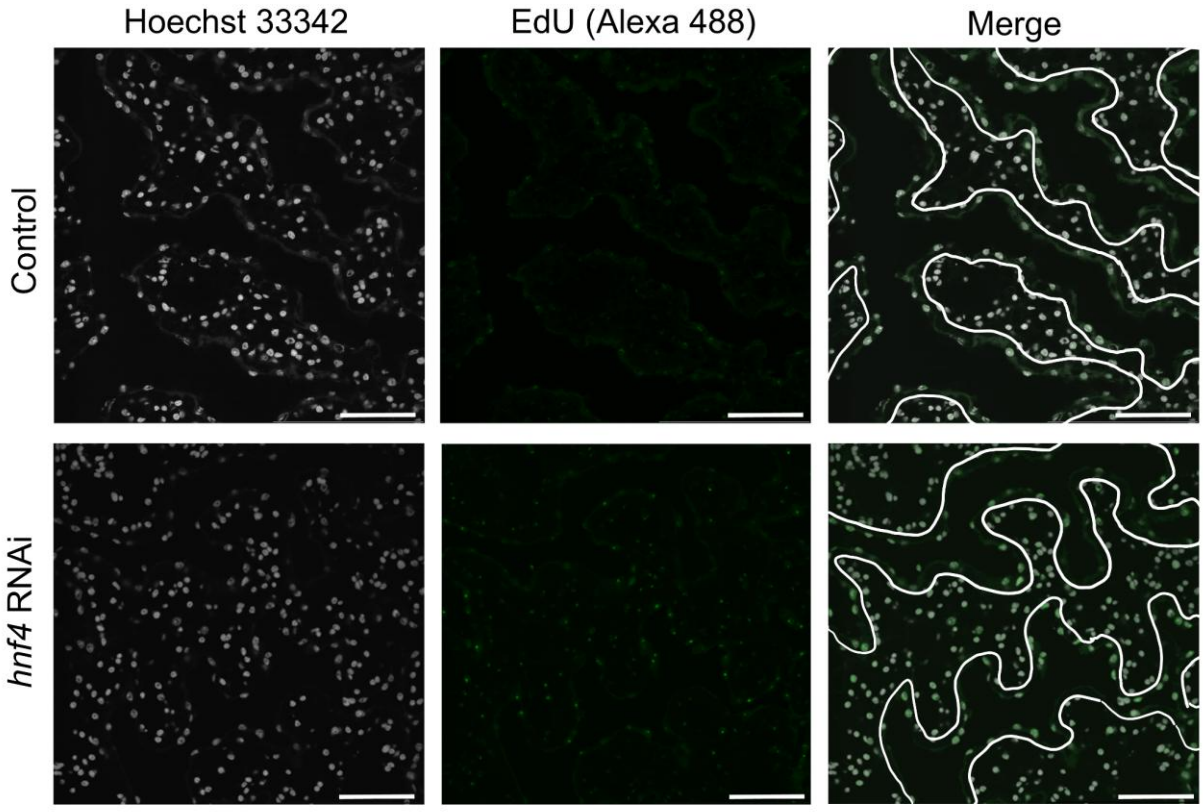

Figure 44 The effect of *hnf4* RNAi on cell proliferation remained inconclusive.
Confocal laser scanning microscopic images of EdU-stained tissue sections of immature liver flukes after 14-15 days of dsRNA treatment. Images are representative for 5 out of 5 (Control) and 6/6 (RNAi) biological replicates derived from two independent experiments. White lining marks the contour of the gastrodermis. Nuclei counterstained with Hoechst 33342. Scale = 50 µm.

3.2.4.6 The HNF4 inhibitor BI6015 affected gene expression in the flukes' testis

To shed light on the druggability of HNF4, immature liver flukes were treated with the small-molecule HNF4 inhibitor BI6015 [222]. Lisa Bauer tested this inhibitor at concentrations of 50, 25 and 12.5 µM. At 25 µM, worm viability was significantly reduced after 72 hours of inhibitor treatment [223]. To further explore the effects of HNF4 inhibition in *F. hepatica*, we subjected immature *F. hepatica* treated with 25 µM BI6015 to RNAseq. I chose two timepoints (24 hours & 72 hours), to be able to distinguish early and late effects of the treatment. The initial RNAseq analysis was again part of Patrice Tegni Sontia's master thesis [229]. As for RNAi, I reanalyzed the data starting from mapped counts and created own data visualizations.

The effect of the inhibitor on gene expression increased with the duration of the treatment. After 24 hours, 240 genes were significantly regulated, while this number rose to 1132 genes after 72 hours (Fig. 46b). For genes that showed a trend after 24 hours, the effect often increased towards the 72-hour time point (Fig. 45). 148 genes that were significantly regulated after inhibitor treatment were also found among the genes regulated following *hnf4* RNAi (Fig. 45 & Fig. 46b). A comparison of the direction of regulation revealed both similarities and differences between the two treatments (Fig. 45). For example, the gut-associated proteases cathepsin and legumain, as well as various saposin B genes, were also downregulated after treatment with the inhibitor, some already after 24 hours. In contrast to RNAi, however, *foxA* was upregulated after 72 hours of treatment with the inhibitor. The largest discrepancies were found among the upregulated genes. Only two of them, the early growth response protein (D915_005261) and the unknown protein D915_010563, were significantly upregulated in all three groups.

As for RNAi, the tissue expression of downregulated genes after 72 hours BI6015 treatment was assessed using the spatial transcriptome. Of the 879 significantly downregulated genes, 72 were detected predominantly in the gut cluster (Fig. 46d). The most downregulated genes (sorted by log2FC), however, were associated with the testis of the fluke (Fig. 46c) and not with the gut.

Figure 45 Comparison of gene regulation after *hnf4* RNAi and BI6015 treatment.
Heatmap showing log2 fold changes of significantly regulated genes (n = 148) that were common between RNAi and inhibitor treatments (24 & 72 h). dark gray = transcript not detected. The annotation column on the right shows whether the gene was similarly or oppositely regulated across the different treatments. Proteases are labelled in red.

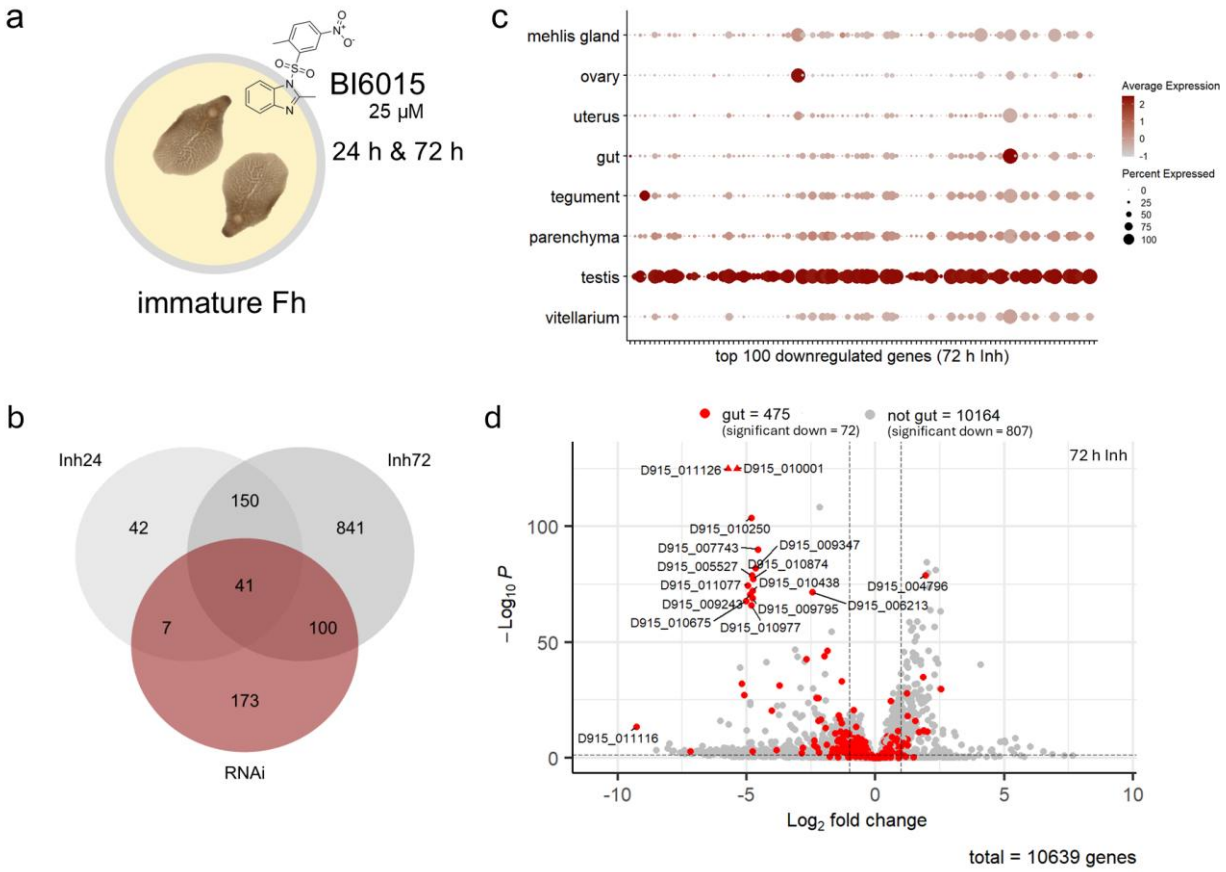

Figure 46 The HNF4 inhibitor BI6015 affected gene expression in the flukes' testis.
(**a**) Scheme depicting experimental conditions for treatment of immature *F. hepatica* with the HNF4 inhibitor BI6015. Parasites were exposed to 25 µM BI6015 or an equal volume of DMSO (control) for 24 or 72 h *in vitro*. (**b**) Venn diagram illustrating overlaps in significantly regulated genes after *hnf4* RNAi and BI6015 treatments (**c**) DotPlot based on a spatial transcriptome of adult parasites, showing tissue expression profiles of the top 100 downregulated genes (sorted by log2FC) after *72* h of inhibitor treatment. Dot color encodes the average expression level (Z-score scaled counts) within a tissue-cluster. Dot size encodes the percentage of spots within a cluster that have captured this transcript. (**d**) Volcano plot showing differential expression of gut-associated genes after 72 h of BI6015 treatment. Genes whose expression in the spatial transcriptomics gut cluster was two-fold higher than its average expression in all clusters are highlighted in red. Selected genes are labelled.

4. DISCUSSION

4.1 Spatial Transcriptomics

“Omics” technologies have accelerated the study of key molecules involved in the biology, pathogenicity, and virulence of liver flukes [109]. However, knowledge of tissue-specific gene expression within the parasite remains limited and many other aspects of liver fluke biology are still poorly understood: Which genes are involved in the reproduction of the worm and thus ensure the persistence of the parasite cycle? Which molecular mechanisms sustain the parasite's outer barriers and help to defend against toxic products? Which genes are involved in parasite-host interaction and might be suitable as vaccine targets? This lack of knowledge also hinders the development of new drugs and vaccines against fasciolosis [109]. [211]

The idea to analyze the proteome or transcriptome of individual parasite tissues to answer such questions exists for quite some time. Methodologically, however, one was limited to methods in which individual body regions, organs or tissues were laboriously isolated from the rest of the worm. For example, different physical and enzymatic preparation techniques were used to detach the tegumental syncytium from the worm surface and study its proteome using mass spectrometry [136],[291]. Hahnel et al. used another digestion protocol to isolate the reproductive organs of male and female schistosomes, which were subsequently investigated using RNAseq [292]. Additionally, an RNA tomography approach, combined with laser capture microdissection (LCM), provided valuable insights into the spatial and tissue-specific transcriptome of the *Brugia malayi* head region [293]. LCM has also been used to study the liver fluke gut and tegument proteome [135] as well as the transcriptome of *S. japonicum* intestine, vitellarium and ovary [294]. [211],[212]

A major breakthrough for helminth research was the introduction of single-cell transcriptomics, which has been applied to *S. mansoni* [145],[146], *B. malayi* [147] and recently also *F. hepatica* [148] so far and allowed to identify and characterize the cellular composition of these parasites. However, a limitation of scRNAseq is its inability to reveal the spatial organization of gene expression in the parasite. For this purpose, traditional techniques like *in situ* hybridizations or immunohistochemistry are still required, both of which involve the time-consuming production and testing of transcript- or protein-specific riboprobes or antisera. Modern spatial transcriptomics technologies therefore represent a valuable alternative or supplement to single-cell data. They allow to analyze the expression of hundreds and thousands of gene simultaneously [295]. Sounart et al. were the first to apply the Visium platform to a multicellular parasite, the filarial nematode *B. malayi*, identifying four transcriptionally distinct tissue regions in the posterior part of the worm [296]. In the present study, I successfully generated a more comprehensive spatial gene expression atlas of a metazoan parasite, encompassing 9,847

transcribed genes across eight distinct tissue types in *F. hepatica*. In contrast to the previous study, I performed ISH to confirm that the ST data accurately reflects transcript localization within the parasite and can predict tissue-specific markers. So overall, I was able to show that the 10x Visium technology is suitable to provide spatial gene expression data of the liver fluke. Reasons for choosing this particular technology and the associated strengths and weaknesses are discussed in more detail below. [211],[212]

4.1.1 Choice of technology

When choosing a spatial transcriptomics technology to perform spatial expression analysis in *F. hepatica*, several technical factors needed to be considered (1.2.3). Imaging-based technologies, for example, require a preselection of targets for probe design, which requires prior knowledge of the organism and a well-defined study hypothesis [150]. As previous knowledge of tissue-specific gene expression in *F. hepatica* was very limited and the aim of the study was to generate a dataset that would serve as a resource for the formation of new hypotheses, a sequencing-based approach was of greater value. Visium and GeoMx DSP were the only sequencing-based technologies available on the market when I performed my experiments. However, only Visium was suitable for many different species, including parasites [158],[296]. Another advantage of Visium was the availability of an H&E staining of the same tissue section from which the spatial transcriptome was generated. This greatly helped with tissue annotation during the analysis. [211]

The ST dataset currently includes most of the large tissues of liver flukes. Further interesting features, such as the musculature of the suckers or neuronal structures in the head region, are missing due to the chosen sectioning plane. Now that it is proven that the technology is applicable to parasitic flatworms, it would be very interesting to investigate further sectional planes or even create a whole 3D transcriptomics atlas of the parasite, as has been demonstrated for planarians or the *Drosophila* larva [156],[297]. Spatial transcriptomics is a rapidly developing field and several more *in situ*-capturing technologies are commercially available today. Examples are Visium HD [164], Slide-seq [162]/ Curio Seeker or Stereo-seq [165], which now provide (near to) single-cell resolution. While Visium HD is restricted to mouse and human tissue samples, I would clearly encourage the future use of Curio Seeker or Stereo-seq in parasite research. The improved cellular resolution of these technologies is especially beneficial for the analysis of smaller life stages, e.g. immature liver flukes. Smaller structures in adult liver fluke, such as the ganglia of the head or individual cell types within the gonads, could also be captured in more detail. [211]

4.1.2 Technical challenges and limitations

As Visium was developed using mammalian tissue and nobody had used the technology on parasites or related model organisms such as planarians when I started my work, it was first necessary to determine whether it was possible to isolate RNA of sufficient quality from *F. hepatica* cryosections. High-quality RNA is characterized by the presence of two distinct RNA peaks corresponding to 18S and 28S rRNAs [298]. The height of the 28S peak is one of the features used to calculate the RNA integrity number (RIN), which is a commonly used RNA integrity value [298]. In *F. hepatica,* the 28S RNA, however, tends to split into two smaller 28S rRNA subunits (28Sα and 28Sβ), probably due to the presence of a 28S rRNA gap region [299]. This is particularly relevant when RNA is heat-denatured prior to electropherogram analysis. During denaturation, the 28S rRNA is almost completely cleaved into two fragments of similar size that co-migrate with the 18S rRNA of the parasite [299]. When assessing the RNA quality of the cryosections, this heating step was omitted. Nevertheless, the 18S rRNA peak was considerably larger than the 28S peak, possibly due to partial cleavage, so that RIN calculation was not possible. Therefore, RNA quality was only determined by visual assessment of the electropherogram.

When analyzing the Visium dataset, three main limitations became apparent: resolution, sensitivity and a certain amount of lateral diffusion. Although adult liver flukes are comparatively large parasites, the entire organism and its organs are very small compared to mammals, for which the Visium technology was developed. With the given spot size of 55 µm, eight major parasite tissues could be distinguished, but specific cell types or stages could only be characterized in the case of the Mehlis' gland and vitellarium. Furthermore, due to the limited resolution, transcripts from neighboring tissues may overlap in one spot, and some tissues were even completely included in other clusters. This was demonstrated for the subtegumental musculature, which became part of the tegument cluster, but also applies to the protonephridial excretory system, which is most likely included in the parenchyma cluster. This fact must be taken into account when assigning genes to specific tissues based on the ST data. For a more precise or even (sub)cellular localization of individual transcripts, techniques with higher resolution such as ISH are still required. In the future, it is planned to integrate the spatial transcriptome dataset with the newly generated single cell dataset of the adult liver fluke [149] to benefit from both spatial context and single cell resolution. A first attempt in this regard, using the initial, incomplete scRNAseq data set, already showed promising results for the localization of germline stem cells in the gonads [149]. [211],[212]

In situ capturing technologies such as Visium are generally known to have lower capturing efficiencies or sensitivities than imaging-based technologies such as *in situ* hybridization [153],[159]. The capturing efficiency of Spatial Transcriptomics, the precursor of Visium, was determined to be around 6.9% when compared to single-molecule FISH. Visium's efficiency is

expected to be slightly higher [154],[159], but there will still be are large percentage of transcripts in the tissue that is not captured on the array. As a result, genes with low expression levels, such as many transcription factors, may not be reliably detected [153]. Indeed, I demonstrated that the displayability of a gene's spatial expression is reduced as its overall expression decreases. For example, the transcription factor *hnf4* showed a significant enrichment in spots of the intestinal cluster, which could however not be recognized in the spatial projection. [211]

On the other hand, especially for genes with very high expression levels, I noticed a certain amount of lateral diffusion of transcripts. Minimizing this factor is one of the goals when performing the tissue optimization workflow prior to the Visium gene expression experiment [300]. This workflow is used to determine the permeabilization time at which enough RNA is released to generate a strong fluorescent cDNA footprint that matches the tissue section without blurring, indicating minimal diffusion [300]. Despite a successful optimization experiment, diffusion was still noted in my data. There are two possible explanations for this: First, the specimen used in the tissue optimization workflow was different from the specimens used in the final experiment. Even though the sectioning plain and most of the organs contained were similar, there might be slight differences between different specimens. Secondly, it has been shown that the tissue type in general has a large influence on the amount of diffusion [172]. Therefore, I suspect that diffusion can never be completely avoided in multicellular parasites, as the tissue sections will always contain multiple different tissues that can be assumed to react differently to enzymatic digestion.

The last limitation to mention, which is inherent in the nature of spatial transcriptomics technologies, is the fact that the localization of an mRNA can only determine the site of protein synthesis, but does not necessarily correspond to the final destination of this protein in the parasite (e.g. for secreted proteins [301]). To close this gap, several manufacturers now offer the option of combining spatial transcriptomics with protein detection [150],[295]. However, due to the limited availability of species-specific antibodies, these technologies are often restricted to humans and mice.

4.1.3 New insights into fundamental questions of liver fluke biology

By comparing the transcriptomes of the eight tissue clusters in the ST data set, I identified genes that were characteristic for distinct liver fluke tissues. These analyses suggested that the clusters are molecularly distinct, and that the dataset represents the different biological functions of liver fluke tissues. The marker genes included numerous known but also new markers for previously poorly characterized organs, such as parenchymal cells or the Mehlis' gland. GO term enrichment analyses allowed first insights into biological processes and molecular functions associated with the marker genes of these tissues.

To confirm that the expression patterns identified by ST accurately reflect the distribution of transcripts within the tissue, the markers were compared with existing knowledge from previous publications on the liver fluke and related organisms. This comparison revealed that established tissue markers for the liver fluke, such as cathepsin L [302], leucine aminopeptidase [303], legumain [304], and saposin B [305] for the intestine, calcium-binding proteins for the tegument [136],[306], fatty acid-binding proteins for the parenchyma [281], and vitelline protein B1 for the vitellarium and eggs [307], were also present among the markers of these tissues in the dataset. For *S. mansoni*, a well-studied trematode related to *F. hepatica*, spatial transcriptomics data are not available. However, comparisons were made with existing scRNAseq data [145],[146]. Several marker genes highlighted in this study, including parenchymal cathepsin B, ovarian bmpg, and vitelline tyrosinase 1 and 2, were also identified among the marker genes for the same tissues in *S. mansoni* (data not shown). In addition, as an experimental validation, I performed *in situ* hybridizations for 22 genes, confirming the spatial expression patterns of selected markers in different liver fluke tissues. [211],[212]

In a further step, I focused on gene families associated with drug action, drug resistance and parasite-host interaction, which are of great interest for parasitology. I was able to visualize the spatial expression of 13 glutathione S-transferases, 12 ABC-B transporters, 12 tubulins and 19 Ly6 proteins. Several of these genes exhibited unique expression patterns indicating tissue-specific biological functions. In the following, I will focus on how the dataset offered new insights into the open questions of liver fluke biology by highlighting selected examples. [211],[212]

4.1.3.1 Which genes are involved in the reproduction of the worm and thus ensure the persistence of the parasite cycle?

Reproductive tissues made up five out of the eight tissue clusters in the spatial transcriptomics dataset, which reflects their high proportion in the fluke’s body. Ovary and testis were characterized by a particularly high level of transcriptional activity and diversity with a particularly high proportion of cell cycle-associated genes. In addition, the ovary and vitellarium were enriched for genes involved in protein biosynthesis and other biosynthetic processes. All of this ensures the worm's outstanding output of 4,000 - 50,000 eggs per day [29]. Interrupting the reproductive cycle of the liver fluke has been suggested as a possible strategy to prevent further spread of the disease [82]. The search for such measures could be supported by the data presented here, as it serves as a starting point for a better understanding of germ cell and egg formation in the liver fluke.

Gene expression in the gonads was studied by using two different analytical approaches. In the classical approach, the transcriptomes of the different spots were compared with each other and grouped by similarity of their gene expression profiles. This identifies cluster specific

marker genes. The alternative approach using Giotto focused on the spatial expression patterns of genes within a section. This enabled the identification of genes with characteristic spatial expression patterns that go beyond the boundaries of individual clusters and was used to characterize genes that were expressed in both the testis and ovary. Among these genes, I identified conserved meiosis genes, including two synaptonemal complex proteins, HORMA domain containing protein 2, and the meiosis-specific with OB-fold (MEIOB). Against my expectations, however, the GO analysis did not reveal a significant overrepresentation of meiosis-related genes in the gonads, likely reflecting limitations in the current GO annotation data. Mammalian MEIOB orthologs are a ssDNA-binding proteins that play essential roles in meiotic recombination during oogenesis and spermatogenesis [271],[308]. In this context, a connection between MEIOB loss-of-function and primary ovarian insufficiency and azoospermia has been demonstrated [309]. Similar to the liver fluke in the ST data, the *meiob* orthologue of *S. mansoni* (Smp_333540) is transcribed in the male testis and female ovary, with an particular enrichment in early germ cell differentiation stages (germline stem cell progeny) [146]. Moescheid et al. recently characterized MEIOB in the schistosome ovary [310]. They found that SmMEIOB was essential for oocyte differentiation and maturation. RNAi affected the number of mature oocytes in the ovary, total egg numbers as well as the number zygote-containing eggs. All together suggests that MEIOB is a highly conserved regulator of germ cell formation and most likely fulfills a similar role in *F. hepatica.*

Another outstanding group of marker genes with presumptive regulatory functions in liver fluke reproduction were RNA-binding zinc finger proteins. Zinc finger proteins are a large superfamily with many of them having important functions as DNA-binding transcription factors [311]. In contrast, the CCCH zinc finger protein subfamily functions as RNA-binding proteins, regulating RNA metabolism, including mRNA splicing, polyadenylation, export, translation and decay [272]. In the ST data, several CCCH zinc finger proteins were identified as markers for reproductive tissues, including testis, ovary, Mehlis' gland and uterus. Most interestingly, the zinc finger protein TIS11, whose expression was significantly enriched in the uterus, is an ortholog of vertebrate ZFP36-like proteins. Members of the ZFP36 family (formerly known as the TIS11 or tristetraprolin (TTP) family) are amongst the best-studied CCCH zinc fingers [312].They bind to AU-rich sites in the 3'UTR of transcripts and promote their deadenylation and degradation [313]. It has been shown that ZFP36 proteins are important regulators of immune responses, vascularization and hematopoiesis [314]–[316]. However, they have also been implicated as maternally derived genes that regulate oocyte maturation and early embryonic development [317]. In *Xenopus laevis*, ZFP36L4 was shown to be essential for meiotic progression by regulating mRNA turnover at critical timepoints during oocyte maturation [317],[318]. Furthermore, ZFP36L2 was found essential for the proliferation of early embryos past the two-cell stage in mice [319]. The enriched expression of FhTIS11 in the

uterus of *F. hepatica*, containing several newly formed eggs, suggests similar functions of the protein in the liver fluke.

The testis of the liver fluke was characterized by the expression of multiple tubulins and other microtubule-associated proteins in the ST data. The sperm flagellum, like in mammals, consists of a microtubule system, but with two staggered axonemes instead of just one [41]. In total, *F. hepatica* expresses at least five α-tubulins and six β-tubulins [74],[123], some of which might be involved in axoneme formation. Differential expression of tubulin isoforms in different cell types is commonly observed in eukaryotes, implying that certain isoforms are specialized for distinct cellular functions [320]. By linking information on the differential expression of different tubulins during the life cycle [87],[123] with their spatial expression in the ST data, a previous assumption [109] that there are two functional subgroups of alpha- and beta-tubulins in the liver fluke was reinforced: Tubulins exhibiting constitutive expression levels across all life stages and a presumed “housekeeping” role, were found broadly expressed in multiple tissues, including the parenchyma, tegument, and ovary in the ST data. In contrast, tubulins upregulated in immature and adult flukes were almost exclusively detected in the testis, indicating a specialized role in spermatogenesis. In studies on tubulins from *Drosophila*, unicellular organisms, and mammals, it was suggested that the amino acid sequence EGEFXXX (where X is an acidic amino acid) near the C-terminus is required for ciliary function and assembly [321]–[323]. Liver fluke β-tubulin 1 contains this signal sequence [74] and is therefore likely involved in the formation of the sperm flagellum. This fits with the fact that the protein was previously localized in liver fluke spermatozoa using immunohistochemistry [87]. In contrast, the localization of β-tubulin 5 and 6 was previously unknown, but has now been detected in the liver fluke testis as well. The fact that those tubulins do not possess the axonemal signal sequence [74] suggests that they fulfill other roles in the testis rather than spermatozoa motility. Functional genomics studies using RNA interference against distinct β-tubulins would be an interesting follow-up study to prove this theory. [212]

The Mehlis’ gland is a flatworm-specific organ that was extensively studied histologically and biochemically in the mid-20th century [324]–[326]. The most widely accepted theory of the gland’s functions are: 1. provision of an alkaline pH to allow fusion of eggshell proteins, 2. induction of the shell protein release and 2. activation of tyrosinases (tanning enzymes) [41],[327]. However, the molecular processes and proteins involved remain largely unknown. In the ST data, the glandular nature was confirmed by the expression of multiple secreted proteins, Rab family proteins, and other factors of secretory pathways. Rab GTPases are membrane-anchored proteins, regulating different steps of vesicular and membrane trafficking [328], while Rho GTPases in contrast are regulators of intracellular actin dynamics [329]. Furthermore, reticulocalbin was found to be expressed in the large eosinophilic S2 cells located on the dorsal aspect of the gland. In mammals, members of the CREC protein family,

including reticulocalbin, are multiple EF-hand-domain-containing proteins involved in calcium-dependent processes in the secretory pathway [330]. Many of the secreted liver fluke proteins, however, did not have homology to known proteins from better-studied organisms in the databases. At the same time, several markers from the Mehlis' gland cluster were also identified as Mehlis' gland markers in scRNAseq data from adult *S. mansoni* (e.g. reticulocalbin (Smp_158150), two secreted proteins (Smp_319870 & Smp_083800), and the VWFA domain-containing protein (Smp_144510)) [146],[331]. This highlights the unique, but conserved nature of Mehlis' gland among flatworms. The presence of two different cell types within the Mehlis' gland of *F. hepatica* has been described by several groups [38],[326],[332], but this study is the first to show that these cell types not only differ in staining, size, and localization, but also in the expression of several marker genes. The ST data thus provided first insights into the molecular components that contribute to the function of the Mehlis' gland, but further research is needed to characterize the different cell types in the liver fluke Mehlis' gland and their involvement in eggshell formation.

In summary, spatial transcriptomics provided valuable insights into the molecular components and gene expression profiles involved in liver fluke reproduction, particularly in the gonads and Mehlis' gland. These findings pave the way for future research, which could ultimately contribute to new strategies for controlling the spread of fasciolosis.

4.1.3.2 Which molecular mechanisms sustain the parasite's protective barriers and help to defend against toxic products?

The intestine and tegument, as internal and external body surfaces, are both in direct contact and constant interaction with the parasite's environment. Common core functions of both tissues include nutrient supply, as well as protection against harmful external influences, such as the host's immune system, microbes and toxic compounds [36],[185]. Here, I will discuss selected molecular mechanisms of antimicrobial defense and detoxification that were identified in the ST data. Mechanisms of parasite-host interaction and immunomodulation are addressed in the following chapter (4.1.3.3).

In contrast to earlier assumptions, the bile duct is not a sterile environment [333]. Therefore, the liver fluke, like gastrointestinal parasites, is in constant interaction with microorganisms and needs to prevent the invasion of pathogens into its tissues [334],[335]. In this context, the gut is an important barrier against the invasion of microorganisms and also fulfills functions of the innate immune system in various invertebrate species [336]–[338]. Evidence suggesting that the liver fluke intestine may also have an immune function came from the presence of two potential pattern recognition receptors (PRRs) among the markers of the gut cluster. PRRs can recognize pathogen-associated molecular patterns (PAMPs), such as double-stranded RNA from viruses and lipopolysaccharides and other glycans from bacteria, and induce a

cellular immune response against these microorganisms [339]. The two PRRs found in the gut cluster were a PGRP domain-containing protein and a DM9 domain-containing protein. Peptidoglycan recognition proteins (PGRPs) are a highly conserved family of PRRs that recognize peptidoglycans (PGN) of bacterial cell walls [340]. Some PGRPs from mammals and insects possess catalytic activities and are able to cleave PGNs, possibly leading to loss of cell wall integrity and thereby causing direct bactericidal effects [341],[342]. Other PGRPs lack enzymatic activity but activate IMD, Toll and prophenol oxidase (PPO) signaling pathways, three major immune effector mechanisms in insects that induce the production of antimicrobial peptides, amongst others [341],[343]. DM9 domain-containing proteins (DM9CPs) are less characterized than PGRPs. However, studies on oyster and crab-derived DM9CPs have shown that they bind a variety of PAMPs such as mannose, lipopolysaccharide and peptidoglycan and fulfil roles in the innate immunity of these species [344]–[346]. Interestingly, both the PGRP gene family, as well as the DM9 family, have undergone expansion in the rumen fluke *C. daubneyi*, a flatworm closely related to *F. hepatica* [335]. This parasite lives in the microbe-rich environment of the rumen, which probably leads to an increased need for microbe sensing and protective proteins [335]. A recombinant *C. daubneyi* PGRP has been shown to specifically bind cell wall peptidoglycan of different bacteria and caused bacteria agglutination, which could confer protection against colonization of the fluke tissues by pathogenic bacteria [335]. Similarly, DM9CPs obtained from oysters and crabs, as well as DM9CPs from *F. gigantica*, induced agglutination of bacteria and fungi [345]–[347]. It would be interesting to further explore whether similar antimicrobial activities of *F. hepatica* contribute to observed changes in the host microbiome [348] and in how far this causes a modulated host immunity [349] or favors the formation of gallstones [350].

In addition to the immune system and microorganisms, the tegument and gut are also the first organs to come into contact with anthelmintics and other toxic substances. The emergence of resistance to various anthelmintics indicates that parasites have mechanisms to protect themselves from the harmful effects of such compounds. ABC transporters are transmembrane transporters that can transport a variety of compounds by cleaving ATP [351],[352]. It has been shown that ABC transporter inhibitors (ivermectin, verapamil) are able to restore TCBZ activity in resistant worms. Therefore, ABC transporters have been proposed as candidate genes potentially involved in TCBZ resistance [82],[90],[353] and might represent interesting targets for developing drugs that enhance the efficacy of existing treatments or directly disturb the physiology of the parasite [354]. However, there has been almost no information on the tissue localization of ABC transporters in the liver fluke, which would provide insights into their biological function and hint at those involved in TCBZ resistance. Using the spatial transcriptome, I identified four ABC-B transporters with predominant expression at the host-parasite interface – three in the tegument and one in the

gut. The Haeberlein lab, among others, have demonstrated that TCBZ-uptake occurs via the parasite's tegument [355],[356]. Therefore, it can be assumed that a mutation or increased expression of tegumental ABC transporters would protect the parasite against TCBZ and thus represent a mechanism of TCBZ resistance. The ABC-B gene (marker-scaffold10x_157_pilon-snap-gene-0.179 = D915_004337), which was recently localized within a putative TCBZ resistance locus in the *F. hepatica* genome [102], however, was mainly associated with the testis in the ST data, suggesting a role in protecting the germline against xenobiotics rather than vital functions. In contrast, D915_007347, as well as two other ABC-B transporters, were found to be predominantly expressed in the tegument. A single nucleotide polymorphism in D915_007347 has been described as a possible cause of resistance in a small number of TCBZ-resistant liver flukes [357], but this finding could not be confirmed in subsequent studies. However, a very recent study suggested that resistance markers probably differ in different *F. hepatica* populations [358]. Furthermore, it is possible that mechanisms other than ABC gene mutation lead to an increased expression or transport activity of tegumental ABC-B transporters in TCBZ-resistant *F. hepatica*. [211],[212]

Besides an increased drug efflux, accelerated drug metabolism has also been discussed as a potential mechanism of TCBZ resistance [82]. In this context, increased GST activity has been observed in resistant parasites [99]. In previous studies, GSTs have been widely detected in different liver fluke tissues, especially in the parenchyma [359],[360]. However, the localization of individual isoforms, particularly those of the Mu-class, has been challenging due to their high sequence similarity and the cross-reactivity of antisera [361]. By applying Visium, I was able to distinguish the different isoforms and found that most Mu-class GSTs were enriched in the parenchyma. The high diversity of expressed GST genes together with the overexpression of other defense molecules such as HDM1 in this tissue, suggests that the parenchyma has a central role in compound metabolism and detoxification. The recently identified GST-Mu5, however, did not share the common preference of other GST-Mu genes for the parenchyma and was particularly expressed in the tegument of the worm. This fits with the fact that it was found to be phylogenetically more distant from the other GST-Mu enzymes and showed lower glutathione binding affinities in previous studies [287]. This suggests that it might fulfil a different tegument-specific role in the worm's metabolism. Further biochemical studies are, however, required to further elucidate the role of GST-Mu5 for the parasite. [211],[212]

Taken together, ST indicates that liver flukes, and in particular their gut and tegument, possess important molecular mechanisms for protecting the parasite from harmful external influences, including microorganisms and toxic substances. The identification of PRRs, ABC transporters and GSTs in these tissues underscores their putative role in antimicrobial defense, detoxification, and possibly in conferring resistance to anthelmintics.

4.1.3.3 Which genes are involved in parasite-host interaction and might be suitable as vaccine targets?

The mechanisms by which *Fasciola spp.* interact with their hosts have been studied intensively in recent decades, with a focus on excretory-secretory (ES) proteins, extracellular vesicles (EVs) and the tegument [109],[362],[363]. Many proteins found in ES products are derived from the parasite's tegument, gut and parenchyma and have been shown to exhibit immunomodulatory effects [32],[43]. For example, cathepsin L proteases can cleave immunoglobulins, while FABPs dampen the secretion of the proinflammatory cytokines, by inhibiting toll-like pattern recognition receptors [302],[364]. An effective vaccine needs to overcome the immunomodulation of the parasite, and the parasite should ideally be detected early after infection, when it is still small and more likely to be neutralized by the immune system [109]. The tegument is thought to be an important target of immunological processes during early infection, particularly for the killing of juvenile flukes through antibody-dependent cellular cytotoxicity, making it an attractive target for vaccine development [118],[136]. Against this background, the EF-hand domain-containing protein calcium-binding protein 1 (CaBP1) and Fhteg1 were investigated as vaccine candidates [365],[366]. Both were found among the markers of the tegument cluster in the ST data. [211]

Encouraged by these findings and as an example of how the spatial transcriptomics dataset could support the selection of new vaccine candidates, the Ly6 (Lymphocyte antigen-6) protein family was presented. Ly6 proteins are an interesting gene family with regard to parasite-host interactions [118], and *in silico* characterization of these proteins in liver flukes has recently revealed several new members and a high diversity of this gene family in *F. hepatica* [212],[288]. Ly6 proteins are membrane-anchored or secreted, cysteine-rich proteins that share a common structure but differ in their tissue expression patterns and functions [367]. The human Ly6 protein CD59 prevents the formation of the complement membrane attack complexes against cells of the same species [368] and overexpression of Ly6 proteins in cancer cells has been shown to modulate anti-tumor immunity, facilitating immune escape [369],[370]. It would therefore be intriguing to determine whether these proteins perform similar immunomodulatory functions in the liver fluke. CD59 homologs have been identified in a number of parasitic helminths, including *S. mansoni*, *F. hepatica* and *Opisthorchis viverrini* [371]. Attempts to characterize two surface-associated schistosome Ly6 proteins (SmLy6 A & B) were unable to demonstrate complement inhibitory functions [372]. Still, they were found to elicit antibody responses during infection in humans [373]. A preliminary vaccine trial using another tegumental Ly6 protein (SmLy6D) showed promising results with >50% reduction in adult worm burden and reduced liver pathology in the mouse model [374].

Although there is no direct homologue to SmLy6D, the high level of diversity observed in the Ly6 proteins of *Fasciola* spp. encourages the discovery of a corresponding candidate. Only FhLy6Q (a homologue of SmLy6A [288]) has been detected in the tegumental proteome of adult *F. hepatica* so far [136], but the localization of other family members was unknown. This complicated candidate selection for functional and vaccine studies. Using the spatial transcriptome, I was able to identify four tegumental, two parenchymal and two intestinal Ly6 proteins that might be involved in host-parasite interactions. However, the four tegumental FhLy6 proteins (FhLy6B, F, N Q) did not possess the key residues required for membrane attack complex inhibition in human CD59. This indicates that, similar to *S. mansoni*, they do not act as complement inhibitors, but rather fulfill other functions. Nevertheless, given the promising results for schistosomes, it may be worthwhile to investigate their potential as vaccine candidates for *F. hepatica*. Thus, spatial transcriptomics could expand the knowledge about the spatial expression of FhLy6 proteins and allow prioritization of potential candidates for future vaccine trials. [211]

4.1.4 Spatial transcriptomics-based drug target discovery

The vital functions of the tegument and intestine, along with their direct exposure to the environment, make tegumental and intestinal proteins major targets for therapeutic interventions [185],[186]. The spatial transcriptome, which maps the expression of hundreds of genes within these tissues, therefore represents a powerful tool to identify or prioritize potential drug targets in these tissues. As a proof of concept, I leveraged my dataset to identify targets of approved drugs and preclinical candidates among genes expressed in the tegument or gut cluster. During this process, I identified PKCβ, a protein kinase expressed in the tegument, as a promising target.

Protein kinases are particularly attractive for drug development against parasitic helminths due to their involvement in key biological processes like cell cycle, migration, and signal transduction [117]. In addition, the availability of numerous small-molecule inhibitors from cancer research offers new opportunities for drug repurposing, which could greatly accelerate the drug development process [117]. Recent studies from the Haeberlein lab have highlighted the potential of this approach against *F. hepatica*: Inhibitors targeting Abl1 and Plk1 kinases have shown promising results, with imatinib killing both immature and adult liver flukes, and the Plk1 inhibitor BI2536 affecting the viability of immature worms and egg production in adults [115].

Despite their significance, the role of protein kinases in parasitic flatworms, and PKCs in particular, remains poorly understood. A study on neuropeptide signaling in isolated body strips proposed a role for PKCs in body contraction and muscle function in liver flukes [375]. Furthermore, in *S. mansoni* PKC activity has been detected in the adult tegument, musculature

and esophagus and PKCs signaling has been implicated in neuromuscular functions involved in movement, attachment, pairing and egg release [376]. In this study, I identified four liver fluke PKCs, based on their homology with human kinases. Spatial transcriptomics revealed that one of the four PKC genes was expressed along the tegument, while the others were associated with the Mehlis' gland, ovary and testis. In our single-cell transcriptomics dataset (lacking tegumental cells), the same PKCβ that was part of the ST tegument cluster, was detected within the neuromuscular *elf5+* cluster [148]. As mentioned earlier, it is not possible to resolve tegumental cells and subtegumental neuromuscular cells in the ST data. The precise cellular localization of PKCβ in the fluke's body wall therefore remains to be confirmed through further experiments, such as *in situ* hybridization. Targeting the neuromuscular cells underneath the tegument, either in addition to the tegument itself or as an alternative, still is an equally promising strategy: *elf5+* cells also expressed the recently identified praziquantel target $trpm_{PZQ}$ [148], whose overstimulation with agonists has shown strong flukicidal effects [114].

Ruboxistaurin, a selective PKCβ inhibitor [224], has been evaluated in clinical trials for the treatment of diabetic neuropathy, demonstrating both safety and oral bioavailability in patients [377]. The drug is primarily excreted via bile, with its metabolites retaining activity against PKCβ, suggesting that parasites would be exposed to the active compound *in vivo* [378]. In addition, the binding site for ruboxistaurin in human PKCβ was shown to be highly conserved in the tegumental liver fluke PKCβ, making it an intriguing candidate for treating *F. hepatica* infections. In our *in vitro* testing, treatment with 50 µM ruboxistaurin killed adult *F. hepatica* within 72 hours of culture, a concentration comparable to the *in vitro* effective dose of TCBZ and within the range of maximum bile concentrations of TCBZ metabolites in sheep [379]. Currently, there is no information available on the bile concentrations of ruboxistaurin achieved in laboratory animals or humans. Nevertheless, due to its promising *in vitro* activity and its already mentioned pharmacokinetic properties, ruboxistaurin might be an interesting candidate for follow-up studies, including *in vivo* testing of this drug in infected animals. In addition or as an alternative, structure-based drug design involving *in silico* modeling of human and liver fluke PKCβ followed by molecular docking of virtual compound libraries could be considered to identify inhibitors with higher specificity for the liver fluke enzyme. Promising compounds could then be validated through enzyme activity assays and *in vitro* compound screenings. While these investigations would slow down the drug development process, they could lead to a more targeted and effective treatment with fewer side effects for the host.

In conclusion, spatial transcriptomics has proven to be a promising tool for identifying potential drug targets. As a next step, additional compounds identified by my integrative database search should be evaluated as potential antiparasitic agents. In addition, the expression data could be explored for other members of highly druggable protein families such as GPCRs and

ion channels. This might reveal further target candidates for new treatments against fasciolosis.

4.2 HNF4

As already described, the structural integrity and functionality of the digestive system is a prerequisite for nutrient acquisition and survival in the host. Interference with essential components of the parasite gut could disrupt intestinal function and thus be used to control the parasite [185]. Therefore, in the second part of this work, the transcription factor HNF4 was chosen as a starting point to gain insights into tissue-specific regulatory mechanisms in the liver fluke gut. I confirmed the presence of an HNF4 orthologue in the liver fluke genome and located *hnf4* transcripts within the parasites gastrodermis. To functionally characterize HNF4 in immature liver flukes, I successfully set up an experimental platform for RNAi in this life stage. This allowed me to study the relevance of HNF4 for parasite vitality, intestinal function and gut structure using transcriptome analyses and microscopic examinations. Finally, I evaluated the druggability of HNF4 using the HNF4 inhibitor BI6015.

4.2.1 Establishing RNA interference for immature *F. hepatica*

Immature liver flukes are a highly interesting life stage for functional studies due to their high pathogenicity [45]. However, to my knowledge, RNAi had not been performed in this life stage so far. Therefore, as part of this work, a platform was established to conduct functional genomics experiments using RNAi in immature flukes. It was shown that immature flukes can be maintained *in vitro* for several weeks and that dsRNA soaking successfully reduced target gene expression. It was further shown that native chicken serum degrades dsRNA, which could be reduced by heat inactivation. Compared to *in vitro*-excysted worms, the immature life stage has the disadvantage that it is dependent on animal models and thus only a limited and variable number of worms can be obtained per animal. Therefore, the protocol used here should be seen as a proof-of-concept rather than a comprehensive methodological validation, and there is still potential for optimization if sufficient worms are available. Possible improvements are discussed below.

4.2.1.1 Considerations for optimizing the *in vitro* culture of immature *F. hepatica*

An effective culture system is fundamental for successful *in vitro* experiments and functional genomics studies in liver flukes [264]. Several different culture methods have been reported for *F. hepatica* with varying success in keeping parasites alive and culture them for extended periods. This included *Fasciola* saline (supplemented DMEM medium) as well as NCTC 135 and RPMI 1640 media supplemented with different sera (chicken, human…), cells (red blood cells, cell monolayer) and other components (serotonin, salts (calcium, magnesium), glucose)

[214],[380]–[383]. Finally, McCusker et al. performed a systematic comparison of different culture media and supplements for the *in vitro* culture of newly excysted juvenile flukes [264]. They found that RPMI supplemented with 50% chicken serum was most successful in keeping juvenile liver flukes over culture period of several weeks and even stimulated growth and organ development associated with stem cell proliferation. Therefore, this combination was adopted in the Häberlein group for the culture of all intra-mammalian life stages of the liver fluke. The serum concentration, however, was reduced to 10%, as it is common in other cell and parasite *in vitro* culture systems [310],[384]. This was not least because of the fact that serum components are known to interfere with compounds or dsRNA used for treatments [385],[386]. McCusker et al. [243] demonstrated that 50% native chicken serum, as used in their *in vitro* culture system for juvenile liver flukes, caused complete dsRNA degradation after two hours at 37 °C. Therefore, they performed dsRNA soakings overnight in RPMI 1640 without chicken serum and then added the regular culture medium, containing native chicken serum, the next day. As an alternative, to facilitate experimental procedures, I demonstrated that using heat-inactivated chicken serum largely reduced dsRNA degradation in the culture media.

There were no phenotypic differences between immature liver flukes cultured in plain RPMI 1640 and medium containing 10% native or heat-inactivated chicken serum. Considering however that in the *hnf4* RNAi experiments hardly any cell proliferation was detectable after two weeks *in vitro*, it is possible that the medium was not sufficient to maintain cell proliferation along the culture. Therefore, test cultures should be repeated using higher serum concentrations with and without heat inactivation (e.g. 20%, 50%) and in addition to a phenotypic assessment, further parameters should be included in the evaluation of the culture. These include cell proliferation assays by EdU staining and possibly also TUNEL experiments to determine the apoptosis rate at different time points (e.g. day 0, day 7, day 14 *in vitro*). It would also be very interesting to see to what extent the *in vitro* culture alters gene expression in the parasite. Ideally, the *in vitro* culture should affect the worm's metabolism as little as possible to be comparable to the situation *in vivo*. An RNAseq study of freshly harvested immature worms compared to immatures cultured *in vitro* would be most suitable for this evaluation.

4.2.1.2 Considerations for optimizing RNAi in immature *F. hepatica*

The ability to induce sequence-specific gene silencing makes RNAi a valuable tool for functional genomics in *F. hepatica* [214],[215]. In this project, I successfully performed RNA interference in immature *F. hepatica*, by adding 50 ng/µl dsRNA to the *in vitro* culture for a duration of 7-14 days. In addition to cathepsin L and *hnf4* shown here, a significant knockdown of *pak4* [149], $trpm_{PZQ}$ [223], as well as *p53-1* and *h2b* transcripts (unpublished data), could be achieved using this protocol. Successful knockdown was, however, only demonstrated on the RNA level. In the case of the *hnf4* knockdown, the observed effects on worm vitality, gene

expression, and intestinal structure strongly suggest that the knockdown was successful at the protein level as well. However, it is important to note that a reduction in mRNA does not always correlate with a significant decrease in the corresponding protein, particularly if the protein has a long half-life [387]. Initial trials of RNAi in adult *F. hepatica*, for example, succeeded in inducing cathepsin L transcript knockdown, but protein expression remained unchanged [215]. Therefore, ideally, all RNAi experiments should be confirmed by Western blot analysis [387], which is however complicated by the lack of antibodies against liver fluke proteins.

The selected dsRNA concentration in this study was an average of different data from the literature. Systematic testing of different dsRNA concentrations had to be omitted due to the limited availability of parasites. For my experiments, I used 50 ng/µl, which is at the upper end of what was recommended by Rinaldi et al. (2.5-50 ng/µl) [388], but only half of the concentration used in recent studies of McCusker et al. (100 ng/µl) [131],[214]. In following RNAi experiments on a transient receptor membrane ion channel, I doubled the dsRNA concentration to 100 ng/µl. This concentration was well tolerated by immature worms, but did not achieve a significant difference in knockdown efficiencies when compared to 50 ng/µl (data not shown). Both the 50 ng/µl and 100 ng/µl concentration are however considerably higher than the concentrations normally used for adult *S. mansoni* (2.5-30 ng/µl) [310],[389] or the carcinogenic liver fluke *Opisthorchis viverrini* (2 ng/µl). Therefore, lower concentrations might also be efficient for immature *F. hepatica* as well. Ideally, the optimal dsRNA concentration for each target gene should be systematically tested to ensure that the amount of dsRNA used is sufficient for efficient knockdown, but as low as possible to reduce off-target effects [390]. The probability of sequence-dependent off-target effects against genes with partial homology is reduced when using lower dsRNA concentrations [387]. Excessively high concentrations can also lead to target-unspecific off-target effects, which may even be fatal for the organism [391],[392]. One possible mechanism is the overloading of the RISC complex with the artificially supplied RNA, so that it is no longer available for normal gene regulatory and homeostatic cellular processes [387],[393].

In order to exclude the misinterpretation of an RNAi phenotype based on toxic or target-unspecific effects of dsRNA treatment, the use of a dsRNA control is essential when performing RNAi [392],[394]. For this purpose, species-unspecific sequences are used, which are assumed not to occur in the target organism. In parasite research, fluorescent protein genes (eGFP, mCherry, luciferase) [390],[392],[395] and bacterial resistance genes [131],[396] are frequently used for this purpose. For this study, the bacterial neomycin/ kanamycin resistance gene was chosen as a control, following previous studies in *F. hepatica* [214],[215]. During my test knockdown, the average target gene expression (cathepsin L) remained unchanged by neomycin dsRNA treatment, but showed greater variability compared to the water control. This might be explained either by unspecific effects of the relatively high dsRNA concentration as

described above or by sequence-dependent off-target effects of the dsRNA. Such off-target effects of neomycin dsRNA have recently been described in *S. mansoni* [394]. To optimize future RNAi experiments, a similar RNAi control study, comparing the degree of off-target effects for various control gene candidates, should also be performed in *F. hepatica.*

4.2.2 HNF4 as a regulator of gut biology in *F. hepatica*

In this project, liver fluke *hnf4* was found expressed in the parasite's gastrodermis. *Hnf4* knockdown resulted in impaired fluke viability and a reduced expression of gut-associated genes. Confocal and transmission electron microscopy further revealed that *hnf4* RNAi affected the structural integrity of the gut, with RNAi parasites having fewer microvillous-like structures, unusual vacuolization of the gastrodermis and occasional dilatations. These results indicated that HNF4 is an important regulator of intestinal function in the liver fluke, similar to mammals and related flatworms [146],[202]. In the following, open questions regarding the cellular expression of *hnf4* and its role in intestinal renewal will be discussed. Furthermore, I will compare my results to a similar study in *S. mansoni* and address further steps that could clarify the target genes of HNF4 as well as its putative interaction with FOXA in regulating the gut biology in *F. hepatica*.

4.2.2.1 Open questions regarding the cellular expression of *hnf4* in *F. hepatica*

HNF4 has been shown to be expressed in intestinal cells of various animal species, e.g. mice, fruit flies and different Platyhelminthes [146],[206],[210],[397]. Concordantly, I was able to successfully localize *F. hepatica hnf4* in the intestine of adult parasites using FISH. In the spatial transcriptomics data, *hnf4* transcripts were also associated with this tissue. However, due to limited sensitivity in detecting weakly expressed genes, *hnf4* was not identified as a marker of the gut cluster. In addition, *hnf4* transcripts were not detected by FISH in immature liver flukes, likely due to lower expression levels in this life stage. This is also suggested by RNAseq data available for this life stage [123], but contrasts with the results of Lisa Bauer who found by qRT-PCR that *hnf4* expression was higher in immature parasites, compared to adults [245]. Despite the difficulties in localizing *hnf4* in immature *F. hepatica*, RNAi and subsequent RNAseq analysis revealed that HNF4 plays a crucial role for intestinal structure and protease expression in immature flukes, suggesting a similar expression pattern as found in adult worms. To confirm this, FISH sensitivity may be improved using more advanced methods like hybridization chain reaction (HCR)-FISH [398]. In addition, immunohistochemistry with antibodies produced specifically for FhHNF4 could be employed to visualize the protein and confirm whether transcript localization corresponds to the final protein localization.

Apart from these initial findings, the specific types or stages of gut-associated cells in *F. hepatica* that express *hnf4* remain unclear. Consistent with the proposed role of HNF4 in intestinal differentiation, the expression of schistosome *hnf4* was higher in gut progenitor cells

compared to mature intestinal cells [146]. These progenitor cells originate from so-called neoblasts, which are located outside the mature organs within the parenchyma and have been identified as the only somatic proliferating cells in *S. mediterranea* and *S. mansoni* [396],[399]. In the course of differentiation, tissue progenitor cells then migrate towards their target organs [396],[400]. Accordingly, in both *S. mediterranea* and schistosomes, *hnf4* expression was detected by FISH in the mature intestinal epithelium as well as in undifferentiated cells in the parenchyma [146],[210]. *Hnf4* RNAi in schistosomes impaired intestinal renewal, most likely due to a failure of progenitor cell differentiation, leading to an accumulation of undifferentiated cells around the gut [146].

The concept of neoblasts, including their migration from the parenchyma towards their final destination has also been hypothesized for *Fasciola* spp. [401]. Furthermore, given the highly conserved role of HNF4 in gut differentiation [146],[202], it is expected that *hnf4* is also expressed in intestinal progenitor cells of in liver flukes. In this study, however, *hnf4* expression was not detected outside the intestinal epithelium in adult *F. hepatica* using FISH, raising questions about the localization of intestinal precursor cells in the liver fluke. Previous studies using transmission electron microscopy have revealed undifferentiated cells in the liver fluke parenchyma, but also situated between the secretory cells in the basal gastrodermis. These gastrodermal stem cells had retained the ability to undergo mitosis [401],[402]. This finding aligns with my own observations, where I detected single EdU and histone 2B (H2B)-positive cells in the gastrodermis of both adult and immature parasites (data not shown). When looking beyond the intensively studied species *S. mediterranea* and *S mansoni* in the literature, gastrodermal stem cells have also been reported for the intestinal epithelium of other flatworms, for example *Macrostomum lignano* [403],[404]. And more recently, a study on an early branching flatworm, *Stenostomum brevipharyngeum*, completely challenged the widely accepted concept of parenchymal neoblasts in Platyhelminthes. Instead of neoblasts, dividing cells were associated with differentiated tissues in this species [405].

It therefore remains to be determined to what extent tissue-resident proliferating cells serve as a source of novel intestinal cells in adult liver flukes and in how far parenchyma-derived neoblasts are required for this renewal. Co-localization studies with proliferation markers like EdU or H2B might reveal if the putative intestinal stem cells are expressing *hnf4*. Furthermore, if EdU co-staining proves successful, conducting a pulse-chase experiment to track progenitor cell fate with and without *hnf4* silencing would be an intriguing next step to understand the role of *hnf4* in intestinal differentiation. Also, examining the new, more comprehensive scRNAseq dataset [149] might reveal alternative markers of the gut lineage in *F. hepatica*, providing valuable tools for more detailed co-localization studies that will further advance our understanding of *hnf4* expression and gut differentiation.

4.2.2.2 HNF4 function is conserved in two parasitic flatworms

Despite the potential differences between gut progenitor cells in *Fasciola* and schistosomes, I identified several functional similarities regarding the role of HNF4 in the gut biology of both species. These will be discussed in more detail below.

To functionally characterize HNF4, RNAi-mediated knockdown was performed in *F. hepatica* (this study) and *S. mansoni* [146]. After dsRNA treatment, *hnf4* expression was reduced by 68-86% in immature liver flukes, which is above the mean 50% achieved in *S. mansoni*. Immature liver flukes exhibited decreased vitality upon *hnf4* RNAi, suggesting essential roles of HNF4 in liver fluke physiology. While there is no information on the *in vitro* phenotype of *S. mansoni* after RNAi treatment, *in vivo* studies showed a reduction in worm size and egg-induced liver pathology, also indicating impaired parasite fitness. To investigate the mechanisms underlying the effects of *hnf4* knockdown, RNA-seq analyses of RNAi-treated worms were conducted in both species. The results revealed a significant impact of RNAi on gene expression, with a substantial number of downregulated genes being associated with the parasite's gut. Downregulated genes in both liver flukes and schistosomes included various proteases, such as cathepsins. A reduction in cysteine protease activity in schistosomes was also confirmed through protease assays. However, a direct 1:1 comparison of regulated genes between the two species was inconclusive due to the absence of clear orthologs for many genes (data not shown). This is particularly true for cysteine L proteases, which form an expanded protein family in the liver fluke [406]. It has been found that members of this family generally find their closest relatives within the liver fluke cathepsin L lineage, indicating that these genes arose independently after the divergence of the *Fasciola* spp. from *S. mansoni* and other species [407],[408]. In addition, the overall protease profiles expressed by liver flukes and schistosomes are distinct: While schistosomes use a diverse proteolytic network involving various cathepsins (e.g. B, D, F and L) to digest host blood, adult liver flukes rely almost exclusively on cathepsin L [409]. Each parasite thus has its own set of proteases, adapted to its specific lifestyle. Consequently, HNF4 appears to regulate different yet functionally similar genes in the two species.

Structurally, the schistosome intestine differs from the liver fluke gut in that the intestinal cells form a syncytium, whereas the liver fluke intestine consists of single cells [409]. However, similar to the liver fluke, the syncytium of the schistosome intestine carries lamellar structures for surface enlargement [410]. In both species, *hnf4* RNAi caused a reduced number of lamellae and occasional dilatations of the gut lumen, suggesting a conserved role in the formation of normal gut tissue. Loss of HNF4 in the intestinal epithelium of mice led to a downregulation of brush border genes, causing similar alterations in the brush border architecture as seen in parasites, including disorganized and shortened microvilli [204]. Further exploring the trematode RNAseq datasets for homologues of murine brush border genes might

show if similar mechanisms cause the reduction of microvillus-like structures observed in schistosomes and liver flukes.

In summary, HNF4 is essential for parasite fitness, the expression of gut-associated genes, and the maintenance of normal gut morphology in both schistosomes and liver flukes. These functions are thus conserved across species, highlighting the fundamental role of HNF4 in gut biology. Further investigation into the mechanisms underlying these similarities - and especially the differences - could provide valuable insights into how each species has specifically adapted to its individual ecological niche.

4.2.2.3 Interaction of HNF4 and FoxA in regulating gut-specific gene expression

It is well established that HNF4 acts as part of transcriptional networks, maintaining cell identity and metabolic homeostasis in adult organs [198]. Therefore, in addition to examining the impact of *hnf4* knockdown on protease gene expression, I also investigated its effects on the expression of other transcription factors. From the predicted interaction network of HNF4, a FoxA orthologue stood out, which was significantly downregulated following *hnf4* knockdown.

The FoxA family is a group of forkhead box transcription factors that play a central role in the development and function of various organs [411]. During embryonic development, FoxA is required for the formation of the foregut, from which endodermal-derived organs like the liver, lung and pancreas arise in mammals [411],[412]. Similarly, the FoxA orthologues of *Drosophila*, schistosomes and planarians play roles in foregut, esophageal gland and pharynx development, respectively, highlighting the conserved function of FoxA across species [206],[413],[414]. In fully developed organs, FoxA remains a critical component of those regulatory networks that maintain cell identity and metabolic homeostasis [415]. Within the liver, FoxA factors have shown a synergistic interaction with HNF4, with both factors regulating the expression of genes important for glucose and lipid metabolism [412]. Hereby, FoxA acts as a “pioneer factor” that opens the chromatin structure and enables HNF4 to access the target genes [412],[416]. Despite being less studied than in the liver, FoxA was also found in intestinal epithelial cells, regulating functions such as cell morphogenesis and solute transport [417]. In *S. mansoni*, a *foxA* orthologue was expressed in the same intestinal progenitor cells that also expressed *hnf4* [146], suggesting that both genes could also have a synergistic role in intestinal cell differentiation in trematodes. In contrast to *hnf4* RNAi, however, knockdown of schistosome *foxA*, did not affect intestinal progenitor proliferation or cathepsin B expression in adult parasites [146],[414]. Other effects of this knockdown on intestinal morphology or functions have not been reported.

To investigate potential interactions between FoxA and HNF4 in the intestine of *F. hepatica*, several follow-up experiments could be conducted. First, it should be determined whether *foxA*

and *hnf4* are co-expressed in the intestine, which could be tested using double FISH. Next, the effects of *foxA* knockdown on worm viability, intestinal gene expression, and intestinal structure should be assessed. A double knockdown of *foxA* and *hnf4* would further be useful to explore whether the absence of both transcription factors exacerbates the knockdown phenotype. Finally, a bioinformatic analysis could be performed to search for binding motifs in the promoters of both *foxA* and *hnf4*, as well as in gut-associated genes from the ST dataset. This could reveal whether these transcription factors regulate each other or share common targets in the intestine of the liver fluke, shedding light on potential molecular interactions.

4.2.2.4 Search for a liver fluke HNF4 binding motif to decipher HNF4 target genes

To explain the effects of *hnf4* RNAi on the expression of gut-associated genes, I searched the *F. hepatica* genome for potential HNF4 binding sites. In general, HNF4 is thought to bind DR1 repeat motifs [203]. Four different variants of the motif from the literature, including a shorter, potentially HNF4-specific motif [256], were used for this analysis. However, only a small overlap was found between the genes in which such motifs were identified and the genes that were regulated after RNAi. Although the DNA-binding domain of HNF4 appeared to be highly conserved (>80% identity) and the P-box involved in DNA binding was identical in all species studied, the most likely explanation for the failure of this approach is that the HNF4 binding motif in liver flukes differs from that in mammals or that the motifs used did not contain sufficient degrees of freedom to include relevant variants of the motif. The latter is supported by the fact that recently published studies in planarians identified HNF4 motifs in promotors of intestinal genes based on similarities to sequences available in the databases [418],[419]. The motif thus appears to be largely conserved between invertebrates and vertebrates. In addition, the 3,000 bp region upstream the CDS analyzed in this study was above the size used in previous studies (500-2,000 bp [418],[420],[421]), and also above the median HNF4 binding distance in *S. mediterranea* (~1,600 bp) [419], so I assume that I should have captured most of the relevant motifs [419].

It is however important to note that motif searches themselves have inherent limitations. Nuclear receptor responsive elements were defined *in vitro* using naked DNA templates [187],[194]. A genome-wide bioinformatic search for such consensus sequences, however, often results in a rather high number of matches at least every 500-1,000 bp [187]. This frequency stands in contrast to the number of actual NR-binding sites identified through chromatin immunoprecipitation and sequencing (ChIP-seq) experiments (thousands), as well as the number of regulated genes observed under experimental conditions (only a few hundred) [187]. Moreover, regulatory sequences can be located far from the TSS in a linear sequence, either upstream or downstream, which further complicates interpretation [187]. In

addition, it has been proposed that HNF4 does not necessarily have to bind directly to DNA, but can also interact with other transcription factors, resulting in an even more complex network that also includes indirect regulatory mechanisms [222]. Experimental alternatives to *in silico* motif searches, such as ChIP-seq, offer more direct and reliable options for identifying HNF4 binding sites. This approach relies on target specific antibodies and is more labor intensive and costly, but it allows for the identification of genome-wide TF binding sites by isolating chromatin regions bound by a TF and sequencing them [422]. In order to delve deeper into HNF4 biology in the liver fluke, I would strongly encourage the use of such technologies.

4.2.3 Assessing the druggability of HNF4

Dysregulation of HNF4 is implicated in many different human diseases [202]. As a result, HNF4 has been proposed as a drug target for the treatment of gastrointestinal cancer and metabolic disorders [423]–[425]. Generally, HNF4 is a nuclear receptor with a large, hydrophobic ligand binding pocket that could favor the uptake of small-molecule inhibitors [202]. However, to my knowledge, no compounds targeting HNF4 have progressed to clinical trials. This is probably partly due to the high risk of unwanted side effects given the pleiotropic functions of HNF4 and the large number of regulated genes [202],[426]. Still, there is a human HNF4α inhibitor, BI6015, which is available for research purposes [222]. This compound has been shown to bind to HNF4a with high affinity and altered expression of a large number of HNF4 target genes. In addition, BI6015 had a selective cytotoxic effect on neoplastic cell lines, but not on untransformed liver cells [202],[222].

For our *in vitro* studies against immature liver flukes, we used BI6015 at comparable concentrations, as in these published cell culture experiments. Lisa Bauer demonstrated during her master's thesis that 25 µM BI6015 significantly reduced worm viability within 72 hours [223]. To investigate whether this phenotype is underlying similar downstream mechanisms as the *hnf4* knockdown, we performed RNAseq on inhibitor treated parasites. I demonstrated that 46% of the genes dysregulated upon RNAi were also altered 72 hours after inhibitor treatment, including a variety of gut-associated proteases. This suggests that BI6015 might indeed inhibit HNF4 in liver flukes, supporting the idea that HNF4 is a druggable target in *F. hepatica*. However, the inhibitor also affected the expression of several testis-related genes, suggesting that the inhibitor might have additional targets besides HNF4 in the liver fluke. Due to this, together with the known effects of BI6015 on HNF4 in mammals and the associated risk of side effects, BI6015 is probably not an optimal drug candidate for the treatment of fasciolosis. However, as discussed for ruboxistaurin, structure-based drug design could be considered to identify inhibitors that are more specific for the worm protein.

Based on the promising results from our HNF4 knockdown experiments, a quite novel RNAi-based therapeutic approach could be explored as an alternative to chemical compounds. This

approach would bypass the need for a parasite-protein-specific inhibitor and instead use the interfering RNA itself as a therapeutic agent [427]. While RNAi in parasite research has primarily been used to identify potential targets for chemical compounds [427], studies in *S. japonicum* have shown that intravenously injected dsRNA or small interfering RNA (siRNA) can affect parasite gene expression *in vivo* and reduce worm viability [428],[429]. However, RNAi therapeutics come with their own challenges, including the prevention of early RNA degradation and the targeting of specific organs or tissues [427]. Recent advances in chemically modifying siRNAs have addressed these issues by improving the stability and enabling control over organ localization [430]. As a result, there are now several RNAi-based drugs approved by the FDA for human use [431]. Of particular interest is that many of these approved drugs target the liver [430], which offers a promising starting point for developing an RNAi-based therapy against fasciolosis. Although RNAi-based treatments remain very costly [431] and are therefore not suitable for widespread use in veterinary medicine, they offer an exciting prospect for the future.

4.3 Conclusion and Outlook

In conclusion, this work provides the first spatial transcriptome of a parasitic flatworm, the common liver fluke *F. hepatica*. The resulting dataset provides the most comprehensive information on tissue-specific gene expression in this parasite available to date. It was shown how the dataset can be used to explore tissue-specific gene expression patterns, profile large gene families, and even facilitate spatial transcriptomics-inspired drug repurposing. Finally, by combining functional genomics and bulk RNAseq with the spatial transcriptomics data, a highly tissue-specific role of HNF4 in the gut of the liver fluke was uncovered. Insights into the spatial expression of genes have thus proven valuable in improving our understanding of their functions, deepening our knowledge of fluke biology and allowing the identification of new drug targets against liver flukes. The public availability of this dataset now enables continued analysis and promotes further research into the molecular mechanisms underlying the tissue-specific functions in *F. hepatica*.

At the same time, this study served as a proof of concept, validating the applicability of spatial transcriptomics for parasitic research. While the data presented here focused on adult liver flukes, recent advancements in ST technologies with higher resolution could be used to investigate other life stages, particularly the pathogenic immature worms. Finally, I envision these data as a source of inspiration for the exploration of other understudied multicellular parasites, expanding our knowledge of their biology and aiding in the discovery of new treatments. [211],[212]

5. REFERENCES

5.1 Literature

1. Andrews, S. J., Cwiklinski, K. & Dalton, J. P. (2021) 1 The discovery of *Fasciola hepatica* and its life cycle. In: J. P. Dalton (ed). Fasciolosis, 2nd ed. pp. 1–22. *CABI, Wallingford, UK*. DOI: 10.1079/9781789246162.0000.
2. Mas-Coma, S. (2005) Epidemiology of fascioliasis in human endemic areas. *J Helminthol* 79(3), pp. 207–216. DOI: 10.1079/joh2005296.
3. Agatsuma, T., Arakawa, Y., Iwagami, M. *et al.* (2000) Molecular evidence of natural hybridization between *Fasciola hepatica* and *F. gigantica*. *Parasitol Int* 49(3), pp. 231–238. DOI: 10.1016/s1383-5769(00)00051-9.
4. Kuerpick, B., Conraths, F. J., Staubach, C. *et al.* (2013) Seroprevalence and GIS-supported risk factor analysis of *Fasciola hepatica* infections in dairy herds in Germany. *Parasitology* 140(8), pp. 1051–1060. DOI: 10.1017/S0031182013000395.
5. Togerson, P. & Claxton, J. (1999) 4 Epidemiology and Control. In: J. P. Dalton (ed). Fasciolosis. pp. 113–149. *CABI, Wallingford, UK.* ISBN: 9780851992600.
6. World Health Organization (2010) WHO report on neglected tropical diseases 2010. Working to overcome the global impact of neglected tropical diseases. *World Health Organization, Geneva, CH.* ISBN: 9789241564090.
7. Mas-Coma, S., Valero, M. A. & Bargues, M. D. (2024) 5 Fascioliasis. In: R. Toledo & B. Fried (eds). Digenetic trematodes, 3rd ed. Advances in experimental medicine and biology. *Springer Nature Switzerland, Cham, CH*. DOI: 10.1007/978-3-031-60121-7.
8. Rim, H.-J., Farag, H. F., Sornmani, S. *et al.* (1994) Food-borne trematodes: ignored or emerging? *Parasitol Today* 10(6), pp. 207–209. DOI: 10.1016/0169-4758(94)90111-2.
9. Hopkins, D. R. (1992) Homing in on helminths. *Am J Trop Med Hyg* 46(6), pp. 626–634. DOI: 10.4269/ajtmh.1992.46.626.
10. Keiser, J. & Utzinger, J. (2005) Emerging foodborne trematodiasis. *Emerg Infect Dis* 11(10), pp. 1507–1514. DOI: 10.3201/eid1110.050614.
11. Beesley, N. J., Caminade, C., Charlier, J. *et al.* (2018) *Fasciola* and fasciolosis in ruminants in Europe: identifying research needs. *Transbound Emerg Dis* 65(Suppl 1), pp. 199–216. DOI: 10.1111/tbed.12682.
12. Deplazes, P. *et al.* (eds.) (2021) Parasitologie für die Tiermedizin. *Georg Thieme Verlag, Stuttgart, DE*. DOI: 10.1055/b-006-163221.
13. Knubben-Schweizer, G., Rössler, A.-S., Schade-Weskott, E. *et al.* (2021) 6 Epidemiology and control. In: J. P. Dalton (ed). Fasciolosis, 2nd ed. *CABI, Wallingford, UK*. DOI: 10.1079/9781789246162.0000.
14. Nansen, P., Andersen, S., Harmer, E. *et al.* (1972) Experimental fascioliasis in the pig. *Exp Parasitol* 31(2), pp. 247–254. DOI: 10.1016/0014-4894(72)90115-4.
15. Nansen, P., Andersen, S. & Hesselholt, M. (1975) Experimental infection of the horse with *Fasciola hepatica*. *Exp Parasitol* 37(1), pp. 15–19. DOI: 10.1016/0014-4894(75)90049-1.
16. Aldona: Common liver or sheep liver fluke (*Fasciola hepatica*) life cycle. #360219522, Adobe Stock. Standard License (25.06.2021).
17. nicolasprimola: Digital 3d render of human body organs. #226838422, Adobe Stock. Standard License (25.06.2021).

18. FineSilhouettes: Holstein Cow. #91500809, Adobe Stock. Standard License (25.06.2021).

19. pic0bird: Nutria rat Coypu sitting on a stone in the water and gnawing foodpy] Holstein Cow. #334696703, Adobe Stock. Standard License (21.09.2025).

20. Pvect02: Deer illustration in color outline and silhouette with white background. #1576439578, Adobe Stock. Standard License (21.09.2025).

21. MohammadMonirul: Vector illustration of a rabbit. #852338458, Adobe Stock. Standard License (21.09.2025).

22. Rowcliffe, S. A. & Ollerenshaw, C. B. (1960) Observations on the bionomics of the egg of *Fasciola hepatica*. *Ann Trop Med Parasitol* 54(2), pp. 172–181. DOI: 10.1080/00034983.1960.11685973.

23. Thomas, A. P. (1883) The life history of the liver fluke (*Fasciola hepatica*). *J Cell Sci* S2-23(89), pp. 99–133. DOI: 10.1242/jcs.s2-23.89.99.

24. Hodgkinson, J. E., Cwiklinski, K., Beesley, N. *et al.* (2018) Clonal amplification of *Fasciola hepatica* in *Galba truncatula*: within and between isolate variation of triclabendazole-susceptible and -resistant clones. *Parasit Vectors* 11(1):363. DOI: 10.1186/s13071-018-2952-z.

25. Howell, A. K. & Williams, D. J. L. (2020) The epidemiology and control of liver flukes in cattle and sheep. *Vet Clin North Am Food Anim Pract.* 36(1), pp. 109–123. DOI: 10.1016/j.cvfa.2019.12.002.

26. Dixon, K. E. (1966) The physiology of excystment of the metacercaria of *Fasciola hepatica* L. *Parasitology* 56(3), pp. 431–456. DOI: 10.1017/s0031182000068931.

27. Schumacher, W. (1956) Untersuchungen über das Eindringen der Jugendformen von *Fasciola hepatica* L. in die Leber des Endwirts. *Z Parasitenkd* 17(4), pp. 276–281. DOI: 10.1007/BF00261426.

28. Boray, J. C. (1969) Experimental fascioliasis in Australia. *Adv Parasitol* 7, pp. 95–210. DOI: 10.1016/s0065-308x(08)60435-2.

29. Happich, F. A. & Boray, J. C. (1969) Quantitative diagnosis of chronic fasciolosis. 2. The estimation of daily total egg production of *Fasciola hepatica* and the number of adult flukes in sheep by faecal egg counts. *Aust Vet J* 45(7), pp. 329–331. DOI: 10.1111/j.1751-0813.1969.tb05012.x.

30. Leiper, J. W. G. (1938) The longevity of *Fasciola hepatica*. *J Helminthol* 16(3), pp. 173–176. DOI: 10.1017/S0022149X00018551.

31. Sumruayphol, S., Siribat, P., Dujardin, J.-P. *et al.* (2020) *Fasciola gigantica, F. hepatica* and *Fasciola* intermediate forms: geometric morphometrics and an artificial neural network to help morphological identification. *PeerJ* 8:e8597. DOI: 10.7717/peerj.8597.

32. Robinson, M. W., Hanna, R. E. B. & Fairweather, I. (2021) 3 Development of *Fasciola hepatica* in the mammalian host. In: J. P. Dalton (ed). Fasciolosis, 2nd ed. pp. 65–111. *CABI, Wallingford, UK*. DOI: 10.1079/9781789246162.0000.

33. Littlewood, D. T. J. (2006) The evolution of parasitism in flatworms. In: A. G. Maule & N. J. Marks (eds). Parasitic flatworms. Molecular biology, biochemistry, immunology and physiology. *CABI, Wallingford, UK*. DOI: 10.1079/9780851990279.0001.

34. Bennett, C. E. (1975) Scanning electron microscopy of *Fasciola hepatica* L. during growth and maturation in the mouse. *J Parasitol* 61(5), pp. 892–898.

35. Adell, T., Martín-Durán, J. M., Saló, E. *et al.* (2015) 3 Plathelminthes. In: A. Wanninger (ed). Evolutionary developmental biology of invertebrates. Lophotrochozoa (Spiralia). *Springer Vienna, Vienna*. DOI: 10.1007/978-3-7091-1871-9.

36. Dalton, J. P., Skelly, P. & Halton, D. W. (2004) Role of the tegument and gut in nutrient uptake by parasitic platyhelminths. *Can J Zool* 82(2), pp. 211–232. DOI: 10.1139/z03-213.

37. Sukhdeo, S. C., Sukhdeo, M. V. & Mettrick, D. F. (1988) Neurocytology of the cerebral ganglion of *Fasciola hepatica* (Platyhelminthes). *J Comp Neurol* 278(3), pp. 337–343. DOI: 10.1002/cne.902780304.

38. Hanna, R. (2015) *Fasciola hepatica*: histology of the reproductive organs and differential effects of triclabendazole on drug-sensitive and drug-resistant fluke isolates and on flukes from selected field cases. *Pathogens* 4(3), pp. 431–456. DOI: 10.3390/pathogens4030431.

39. Terasaki, K., Itagaki, T., Shibahara, T. *et al.* (2001) Comparative study of the reproductive organs of *Fasciola* groups by optical microscope. *J Vet Med Sci* 63(7), pp. 735–742. DOI: 10.1292/jvms.63.735.

40. Meepool, A., Wanichanon, C., Viyanant, V. *et al.* (2006) Development and roles of vitelline cells in eggshell formation in *Fasciola gigantica*. *Invertebr Reprod Dev* 49(1-2), pp. 9–17. DOI: 10.1080/07924259.2006.9652189.

41. Hanna, R. E. B., Fairweather, I. & Robinson, M. W. (2021) 4 The reproductive system of *Fasciola hepatica*. In: J. P. Dalton (ed). Fasciolosis, 2nd ed. pp. 112–144. *CABI, Wallingford, UK*. DOI: 10.1079/9781789246162.0000.

42. Kazakova, M.: Coloring page with structure of reproductive system of sheep liver fluke (*Fasciola hepatica*) isolated on white background. #484973139, Adobe Stock. Standard License (14.11.2024).

43. Sangster, N. C., Martínez-Moreno, A. & Pérez, J. (2021) 5 Pathology, pathophysiology and clinical aspects. In: J. P. Dalton (ed). Fasciolosis, 2nd ed. *CABI, Wallingford, UK*. DOI: 10.1079/9781789246162.0000.

44. Cullen, J. M. & Stalke, M. J. (2016) 2 Liver and biliary system. In: M. G. Maxie (ed). Jubb, Kennedy, and Palmer's pathology of domestic animals, 6th ed., Vol. 2. pp. 258–352. *Elsevier, St. Louis, MO*. DOI: 10.1016/B978-0-7020-5318-4.00008-5.

45. Lalor, R., Cwiklinski, K., Calvani, N. E. D. *et al.* (2021) Pathogenicity and virulence of the liver flukes *Fasciola hepatica* and *Fasciola gigantica* that cause the zoonosis Fasciolosis. *Virulence* 12(1), pp. 2839–2867. DOI: 10.1080/21505594.2021.1996520.

46. Kahl, A., Samson-Himmelstjerna, G. von, Helm, C. *et al.* (2023) Efficacy of flukicides against *Fasciola hepatica* and first report of triclabendazole resistance on German sheep farms. *Int J Parasitol Drugs Drug Resist* 23, pp. 94–105. DOI: 10.1016/j.ijpddr.2023.11.001.

47. Valero, M. A., Marcos, M. D., Fons, R. *et al.* (1998) *Fasciola hepatica* development in the experimentally infected black rat *Rattus rattus*. *Parasitol Res* 84(3), pp. 188–194. DOI: 10.1007/s004360050381.

48. Chapman, C. B. & Mitchell, G. F. (1982) *Fasciola hepatica*: comparative studies on fascioliasis in rats and mice. *Int J Parasitol* 12(1), pp. 81–91. DOI: 10.1016/0020-7519(82)90099-6.

49. Rajasekariah, G. R. & Howell, M. J. (1977) The fate of *Fasciola hepatica* metacercariae following challenge infection of immune rats. *J Helminthol* 51(4), pp. 289–294. DOI: 10.1017/s0022149x00007616.

50. Boyce, W. M., Courtney, C. H. & Thibideau, M. (1986) Heterologous resistance to *Fasciola hepatica* conferred upon rats by passive transfer of serum from different breeds of sheep. *Vet Parasitol* 22(3-4), pp. 259–266. DOI: 10.1016/0304-4017(86)90113-5.

51. Spithill, T. W., Toet, H., Rathinasamy, V. *et al.* (2021) 12 Vaccines for *Fasciola*: New thinking for an old problem. In: J. P. Dalton (ed). Fasciolosis, 2nd ed. pp. 379–422. *CABI, Wallingford, UK*. DOI: 10.1079/9781789246162.0000.

52. Boray, J. C. (1985) Flukes of domestic animals. In: S. M. Gaafar, W. E. Howard & R. E. Marsh (eds). Parasites, pests, and predators. pp. 179–218. *Elsevier Scientific Pub. Co, Amsterdam, NL.* ISBN: 9780444421753.

53. FAO (1994) Diseases of domestic animals caused by flukes: epidemiologyy, diagnosis and control of *Fasciola*, paramphistome, *Dicrocoelium, Eurytrema* and schistosome infections of ruminants in developing countries. *FAO, Rome, IT*.

54. Spithill T, Smooker P & Copeman D. (1999) 15 *Fasciola gigantica*: epidemiology, control, immunology and molecular biology. In: J. P. Dalton (ed). Fasciolosis. pp. 465–525. *CABI, Wallingford, UK.* ISBN: 9780851992600.

55. Charlier, J., Rinaldi, L., Musella, V. *et al.* (2020) Initial assessment of the economic burden of major parasitic helminth infections to the ruminant livestock industry in Europe. *Prev Vet Med* 182:105103. DOI: 10.1016/j.prevetmed.2020.105103.

56. Fanke, J., Charlier, J., Steppin, T. *et al.* (2017) Economic assessment of *Ostertagia ostertagi* and *Fasciola hepatica* infections in dairy cattle herds in Germany using Paracalc®. *Vet Parasitol* 240, pp. 39–48. DOI: 10.1016/j.vetpar.2017.03.018.

57. Gethmann, J., Probst, C. & Conraths, F. J. (2020) Economic impact of a Bluetongue serotype 8 epidemic in Germany. *Front Vet Sci* 7:65. DOI: 10.3389/fvets.2020.00065.

58. Ubeira, F. M., Martínez-Sernández, V., González-Warleta, M. *et al.* (2021) 10 Diagnostics for animal and human fasciolosis. In: J. P. Dalton (ed). Fasciolosis, 2nd ed. pp. 308–337. *CABI, Wallingford, UK*. DOI: 10.1079/9781789246162.0000.

59. Mas-Coma, S., Bargues, M. D. & Valero, M. A. (2014) Diagnosis of human fascioliasis by stool and blood techniques: update for the present global scenario. *Parasitology* 141(14), pp. 1918–1946. DOI: 10.1017/S0031182014000869.

60. Alvarez, L., Lanusse, C. E., Williams, D. J. L. *et al.* (2021) 7 Flukicidal drugs: Pharmacotherapeutics and drug resistance. In: J. P. Dalton (ed). Fasciolosis, 2nd ed. pp. 211–255. *CABI, Wallingford, UK*. DOI: 10.1079/9781789246162.0000.

61. VETIDATA - Veterinärmedizinischer Informationsdienst für Arzneimittelanwendung, Toxikologie und Arzneimittelrecht. Anthelminthika gegen Trematoden (Fasziolizide). Available at https://vetidata.de/public/details/wirkstgrp_details.php?params=113,74,65,74,139,131,74,67,74,50,123,117,137,50,75,131,74,67,74,50,65,71,67,50,75,141 (23.01.2025).

62. Boray, J. C., Crowfoot, P. D., Strong, M. B. *et al.* (1983) Treatment of immature and mature *Fasciola hepatica* infections in sheep with triclabendazole. *Vet Rec* 113(14), pp. 315–317. DOI: 10.1136/vr.113.14.315.

63. Fairweather, I. & Boray, J. C. (1999) Fasciolicides: efficacy, actions, resistance and its management. *Vet J* 158(2), pp. 81–112. DOI: 10.1053/tvjl.1999.0377.

64. WHO (2020) Ending the neglect to attain the sustainable development goals. A road map for neglected tropical diseases 2021-2030. *WHO, Geneva, CH.* ISBN: ISBN: 978-92-4-001035-2.

65. Molina-Hernández, V., Mulcahy, G., Pérez, J. *et al.* (2015) *Fasciola hepatica* vaccine: we may not be there yet but we're on the right road. *Vet Parasitol* 208(1-2), pp. 101–111. DOI: 10.1016/j.vetpar.2015.01.004.

66. Stitt, A. W. & Fairweather, I. (1993) *Fasciola hepatica*: tegumental surface changes in adult and juvenile flukes following treatment *in vitro* with the sulphoxide metabolite of triclabendazole (Fasinex). *Parasitol Res* 79(7), pp. 529–536. DOI: 10.1007/BF00932235.

67. Stitt, A. W. & Fairweather, I. (1994) The effect of the sulphoxide metabolite of triclabendazole ('Fasinex') on the tegument of mature and immature stages of the liver fluke, *Fasciola hepatica*. *Parasitology* 108, pp. 555–567. DOI: 10.1017/s0031182000077428.

68. Stitt, A. W. & Fairweather, I. (1992) Spermatogenesis in *Fasciola hepatica*: an ultrastructural comparison of the effects of the anthelmintic, thiabendazole ("Fasinex") and the microtubule inhibitor, tubulozole. *Invertebr Reprod Dev* 22(1-3), pp. 139–150. DOI: 10.1080/07924259.1992.9672266.

69. Stitt, A. W. & Fairweather, I. (1996) *Fasciola hepatica*: disruption of the vitelline cells *in vitro* by the sulphoxide metabolite of triclabendazole. *Parasitol Res* 82(4), pp. 333–339. DOI: 10.1007/s004360050122.

70. Robinson, M. W., Trudgett, A., Hoey, E. M. *et al.* (2002) Triclabendazole-resistant *Fasciola hepatica*: beta-tubulin and response to *in vitro* treatment with triclabendazole. *Parasitology* 124(Pt 3), pp. 325–338. DOI: 10.1017/s003118200100124x.

71. Lacey, E. (1988) The role of the cytoskeletal protein, tubulin, in the mode of action and mechanism of drug resistance to benzimidazoles. *Int J Parasitol* 18(7), pp. 885–936. DOI: 10.1016/0020-7519(88)90175-0.

72. Fairweather, I. (2005) Triclabendazole: new skills to unravel an old(ish) enigma. *J Helminthol* 79(3), pp. 227–234. DOI: 10.1079/joh2005298.

73. Lipkowitz, K. B. & McCracken, R. O. (1991) A molecular modeling approach to *in vivo* efficacy of triclabendazole. *J Parasitol* 77(6), pp. 998–1005. DOI: 10.2307/3282756.

74. Ryan, L. A., Hoey, E., Trudgett, A. *et al.* (2008) *Fasciola hepatica* expresses multiple alpha- and beta-tubulin isotypes. *Mol Biochem Parasitol* 159(1), pp. 73–78. DOI: 10.1016/j.molbiopara.2008.02.001.

75. Kwa, M. S., Veenstra, J. G. & Roos, M. H. (1994) Benzimidazole resistance in *Haemonchus contortus* is correlated with a conserved mutation at amino acid 200 in beta-tubulin isotype 1. *Mol Biochem Parasitol* 63(2), pp. 299–303. DOI: 10.1016/0166-6851(94)90066-3.

76. Robinson, M. W. (2004) A possible model of benzimidazole binding to b-tubulin disclosed by invoking an inter-domain movement. *J Mol Graph Model* 23(3), pp. 275–284. DOI: 10.1016/j.jmgm.2004.08.001.

77. Sanabria, R., Ceballos, L., Moreno, L. *et al.* (2013) Identification of a field isolate of *Fasciola hepatica* resistant to albendazole and susceptible to triclabendazole. *Vet Parasitol* 193(1-3), pp. 105–110. DOI: 10.1016/j.vetpar.2012.11.033.

78. Coles, G. C. & Stafford, K. A. (2001) Activity of oxyclozanide, nitroxynil, clorsulon and albendazole against adult triclabendazole-resistant *Fasciola hepatica*. *Vet Rec* 148(23), pp. 723–724. DOI: 10.1136/vr.148.23.723.

79. Ranjan, P., Kumar, S. P., Kari, V. *et al.* (2017) Exploration of interaction zones of β-tubulin colchicine binding domain of helminths and binding mechanism of anthelmintics. *Comput Biol Chem* 68, pp. 78–91. DOI: 10.1016/j.compbiolchem.2017.02.008.

80. Olivares-Ferretti, P., Beltrán, J. F., Salazar, L. A. *et al.* (2023) Protein modelling and molecular docking analysis of *Fasciola hepatica* β-tubulin's interaction sites, with triclabendazole, triclabendazole sulphoxide and triclabendazole sulphone. *Acta Parasitol* 68(3), pp. 535–547. DOI: 10.1007/s11686-023-00692-z.

81. Overend, D. J. & Bowen, F. L. (1995) Resistance of *Fasciola hepatica* to triclabendazole. *Aust Vet J* 72(7), pp. 275–276. DOI: 10.1111/j.1751-0813.1995.tb03546.x.

82. Fairweather, I., Brennan, G. P., Hanna, R. E. B. *et al.* (2020) Drug resistance in liver flukes. *Int J Parasitol Drugs Drug Resist* 12, pp. 39–59. DOI: 10.1016/j.ijpddr.2019.11.003.

83. Martínez-Valladares, M., Cordero-Pérez, C. & Rojo-Vázquez, F. A. (2014) Efficacy of an anthelmintic combination in sheep infected with *Fasciola hepatica* resistant to albendazole and clorsulon. *Exp Parasitol* 136, pp. 59–62. DOI: 10.1016/j.exppara.2013.10.010.

84. Novobilský, A. & Höglund, J. (2015) First report of closantel treatment failure against *Fasciola hepatica* in cattle. *Int J Parasitol Drugs Drug Resist* 5(3), pp. 172–177. DOI: 10.1016/j.ijpddr.2015.07.003.

85. Robles-Pérez, D., Martínez-Pérez, J. M., Rojo-Vázquez, F. A. *et al.* (2013) The diagnosis of fasciolosis in feces of sheep by means of a PCR and its application in the detection of anthelmintic resistance in sheep flocks naturally infected. *Vet Parasitol* 197(1-2), pp. 277–282. DOI: 10.1016/j.vetpar.2013.05.006.

86. Samson-Himmelstjerna, G. von, Blackhall, W. J., McCarthy, J. S. *et al.* (2007) Single nucleotide polymorphism (SNP) markers for benzimidazole resistance in veterinary nematodes. *Parasitology* 134(8), pp. 1077–1086. DOI: 10.1017/S0031182007000054.

87. Fuchs, M.-A., Ryan, L. A., Chambers, E. L. *et al.* (2013) Differential expression of liver fluke β-tubulin isotypes at selected life cycle stages. *Int J Parasitol* 43(14), pp. 1133–1139. DOI: 10.1016/j.ijpara.2013.08.007.

88. Chemale, G., Perally, S., LaCourse, E. J. *et al.* (2010) Comparative proteomic analysis of triclabendazole response in the liver fluke *Fasciola hepatica*. *J Proteome Res* 9(10), pp. 4940–4951. DOI: 10.1021/pr1000785.

89. Alvarez, L., H. D. Solana, M. L. Mottier *et al.* (2005) Altered drug influx/efflux and enhanced metabolic activity in triclabendazole-resistant liver flukes. *Parasitology* 131(4), pp. 501–510. DOI: 10.1017/S0031182005007997.

90. Mottier, L., Alvarez, L., Fairweather, I. *et al.* (2006) Resistance-induced changes in triclabendazole transport in *Fasciola hepatica*: ivermectin reversal effect. *J Parasitol* 92(6), pp. 1355–1360. DOI: 10.1645/GE-922R.1.

91. Robey, R. W., Pluchino, K. M., Hall, M. D. *et al.* (2018) Revisiting the role of ABC transporters in multidrug-resistant cancer. *Nat Rev Cancer* 18(7), pp. 452–464. DOI: 10.1038/s41568-018-0005-8.

92. Raza, A., Williams, A. R. & Abeer, M. M. (2023) Importance of ABC transporters in the survival of parasitic nematodes and the prospect for the development of novel control strategies. *Pathogens* 12(6):755. DOI: 10.3390/pathogens12060755.

93. David, M. A., Orlowski, S., Prichard, R. K. *et al.* (2016) *In silico* analysis of the binding of anthelmintics to *Caenorhabditis elegans* P-glycoprotein 1. *Int J Parasitol Drugs Drug Resist* 6(3), pp. 299–313. DOI: 10.1016/j.ijpddr.2016.09.001.

94. Dupuy, J., Alvinerie, M., Ménez, C. *et al.* (2010) Interaction of anthelmintic drugs with P-glycoprotein in recombinant LLC-PK1-mdr1a cells. *Chem Biol Interact* 186(3), pp. 280–286. DOI: 10.1016/j.cbi.2010.05.013.

95. Meaney, M., Savage, J., Brennan, G. P. *et al.* (2013) Increased susceptibility of a triclabendazole (TCBZ)-resistant isolate of *Fasciola hepatica* to TCBZ following co-incubation *in vitro* with the P-glycoprotein inhibitor, R(+)-verapamil. *Parasitology* 140(10), pp. 1287–1303. DOI: 10.1017/S0031182013000759.

96. Savage, J., Meaney, M., Brennan, G. P. *et al.* (2013) Effect of the P-glycoprotein inhibitor, R(+)-verapamil on the drug susceptibility of a triclabendazole-resistant isolate of *Fasciola hepatica*. *Vet Parasitol* 195(1-2), pp. 72–86. DOI: 10.1016/j.vetpar.2013.03.007.

97. Robinson, M. W., Lawson, J., Trudgett, A. *et al.* (2004) The comparative metabolism of triclabendazole sulphoxide by triclabendazole-susceptible and triclabendazole-resistant *Fasciola hepatica*. *Parasitol Res* 92(3), pp. 205–210. DOI: 10.1007/s00436-003-1003-6.

98. Scarcella, S., Lamenza, P., Virkel, G. *et al.* (2012) Expression differential of microsomal and cytosolic glutathione-S-transferases in *Fasciola hepatica* resistant at triclabendazole. *Mol Biochem Parasitol* 181(1), pp. 37–39. DOI: 10.1016/j.molbiopara.2011.09.011.

99. Fernández, V., Ortiz, P., Solana, M. V. *et al.* (2014) Differential activities of glutathione S-transferase isoenzymes in strains of *Fasciola hepatica* susceptible and resistant to triclabendazole. *Am J Anim Vet Sci* 9(4), pp. 177–181. DOI: 10.3844/ajavsp.2014.177.181.

100. Devine, C., Brennan, G. P., Lanusse, C. E. *et al.* (2009) Effect of the metabolic inhibitor, methimazole on the drug susceptibility of a triclabendazole-resistant isolate of *Fasciola hepatica*. *Parasitology* 136(2), pp. 183–192. DOI: 10.1017/S0031182008005222.

101. Devine, C., Brennan, G. P., Lanusse, C. E. *et al.* (2011) Inhibition of triclabendazole metabolism *in vitro* by ketoconazole increases disruption to the tegument of a triclabendazole-resistant isolate of *Fasciola hepatica*. *Parasitol Res* 109(4), pp. 981–995. DOI: 10.1007/s00436-011-2304-9.

102. Beesley, N. J., Cwiklinski, K., Allen, K. *et al.* (2023) A major locus confers triclabendazole resistance in *Fasciola hepatica* and shows dominant inheritance. *PLOS Pathog* 19(1):e1011081. DOI: 10.1371/journal.ppat.1011081.

103. Robb, E., McCammick, E. M., Wells, D. *et al.* (2022) Transcriptomic analysis supports a role for the nervous system in regulating growth and development of *Fasciola hepatica* juveniles. *PLOS Neg Trop Dis* 16(11):e0010854. DOI: 10.1371/journal.pntd.0010854.

104. Krasky, A., Rohwer, A., Marhoefer, R. J. *et al.* (2009) Bioinformatics and chemoinformatics: key technologies in the drug discovery process. In: P. M. Selzer (ed). Antiparasitic and Antibacterial Drug Discovery. *Wiley-VCH, Weinheim, DE*. DOI: 10.1002/9783527626816.

105. Wolfand, C. & Gunkel, N. (2009) Target identification and validation in antiparasitic drug discovery. In: P. M. Selzer (ed). Antiparasitic and Antibacterial Drug Discovery. *Wiley-VCH, Weinheim, DE*. DOI: 10.1002/9783527626816.

106. Selzer, P. M. & Epe, C. (2021) Antiparasitics in animal health: quo vadis? *Trends Parasitol* 37(1), pp. 77–89. DOI: 10.1016/j.pt.2020.09.004.

107. Machicado, C., Soto, M. P., Timoteo, O. *et al.* (2019) Screening the pathogen box for identification of new chemical agents with anti-*Fasciola hepatica* activity. *Antimicrob Agents Chemother* 63(3):e02373-18. DOI: 10.1128/AAC.02373-18.

108. Alvarez-Mercado, J. M., Ibarra-Velarde, F., Alonso-Díaz, M. Á. *et al.* (2015) *In vitro* antihelmintic effect of fifteen tropical plant extracts on excysted flukes of *Fasciola hepatica*. *BMC Vet Res* 11:45. DOI: 10.1186/s12917-015-0362-4.

109. Cwiklinski, K. & Dalton, J. P. (2022) Omics tools enabling vaccine discovery against fasciolosis. *Trends Parasitol* 38(12), pp. 1068–1079. DOI: 10.1016/j.pt.2022.09.009.

110. Sharma, K. R., Colvis, C. M., Rodgers, G. P. *et al.* (2024) Illuminating the druggable genome: pathways to progress. *Drug Discov Today* 29(3), pp. 103805. DOI: 10.1016/j.drudis.2023.103805.

111. Valderas-García, E., Castilla-Gómez de Agüero, V., Del González Palacio, L. *et al.* (2024) New benzimidazole derivative compounds with *in vitro* fasciolicidal properties. *Parasit Vectors* 17(1):173. DOI: 10.1186/s13071-024-06224-6.

112. McConville, M., Hanna, R. E. B., Brennan, G. P. *et al.* (2012) Impact of compound alpha treatment *in vivo* on egg production by the liver fluke, *Fasciola hepatica*. *Vet Parasitol* 187(1-2), pp. 183–195. DOI: 10.1016/j.vetpar.2011.12.028.

113. Park, S.-K., Friedrich, L., Yahya, N. A. *et al.* (2021) Mechanism of praziquantel action at a parasitic flatworm ion channel. *Sci Transl Med* 13(625):eabj5832. DOI: 10.1126/scitranslmed.abj5832.

114. Sprague, D. J., Park, S.-K., Gramberg, S. *et al.* (2024) Target-based discovery of a broad-spectrum flukicide. *Nat Struct Mol Biol* 31(9), pp. 1386–1393. DOI: 10.1038/s41594-024-01298-3.

115. Morawietz, C. M., Houhou, H., Puckelwaldt, O. *et al.* (2020) Targeting kinases in *Fasciola hepatica*: anthelminthic effects and tissue distribution of selected kinase inhibitors. *Front Vet Sci* 7:611270. DOI: 10.3389/fvets.2020.611270.

116. Beckmann, S. & Grevelding, C. G. (2010) Imatinib has a fatal impact on morphology, pairing stability and survival of adult *Schistosoma mansoni in vitro*. *Int J Parasitol* 40(5), pp. 521–526. DOI: 10.1016/j.ijpara.2010.01.007.

117. Pereira Moreira, B., Weber, M. H. W., Haeberlein, S. *et al.* (2022) Drug repurposing and *de novo* drug discovery of protein kinase inhibitors as new drugs against schistosomiasis. *Molecules* 27(4):1414. DOI: 10.3390/molecules27041414.

118. Toet, H., Piedrafita, D. M. & Spithill, T. W. (2014) Liver fluke vaccines in ruminants: strategies, progress and future opportunities. *Int J Parasitol* 44(12), pp. 915–927. DOI: 10.1016/j.ijpara.2014.07.011.

119. Piacenza, L., Acosta, D., Basmadjian, I. *et al.* (1999) Vaccination with cathepsin L proteinases and with leucine aminopeptidase induces high levels of protection against fascioliasis in sheep. *Infect Immun* 67(4), pp. 1954–1961. DOI: 10.1128/iai.67.4.1954-1961.1999.

120. Maggioli, G., Acosta, D., Silveira, F. *et al.* (2011) The recombinant gut-associated M17 leucine aminopeptidase in combination with different adjuvants confers a high level of protection against *Fasciola hepatica* infection in sheep. *Vaccine* 29(48), pp. 9057–9063. DOI: 10.1016/j.vaccine.2011.09.020.

121. Hasin, Y., Seldin, M. & Lusis, A. (2017) Multi-omics approaches to disease. *Genome Biol* 18(1):83. DOI: 10.1186/s13059-017-1215-1.

122. Cwiklinski, K. & Dalton, J. P. (2018) Advances in *Fasciola hepatica* research using 'omics' technologies. *Int J Parasitol* 48(5), pp. 321–331. DOI: 10.1016/j.ijpara.2017.12.001.

123. Cwiklinski, K., Dalton, J. P., Dufresne, P. J. *et al.* (2015) The *Fasciola hepatica* genome: gene duplication and polymorphism reveals adaptation to the host environment and the capacity for rapid evolution. *Genome Biol* 16(1):71. DOI: 10.1186/s13059-015-0632-2.

124. McNulty, S. N., Tort, J. F., Rinaldi, G. *et al.* (2017) Genomes of *Fasciola hepatica* from the Americas reveal colonization with *Neorickettsia* endobacteria related to the agents of Potomac horse and human Sennetsu fevers. *PLOS Genet* 13(1):e1006537. DOI: 10.1371/journal.pgen.1006537.

125. Cwiklinski, K., Marco Verissimo, C. de, McVeigh, P. *et al.* (2021) 11 Applying 'omics' technologies to understand *Fasciola* spp. biology. In: J. P. Dalton (ed). Fasciolosis, 2nd ed. pp. 336–378. *CABI, Wallingford, UK*. DOI: 10.1079/9781789246162.0000.

126. Beesley, N. J., Williams, D. J. L., Paterson, S. *et al.* (2017) *Fasciola hepatica* demonstrates high levels of genetic diversity, a lack of population structure and high gene flow: possible implications for drug resistance. *Int J Parasitol* 47(1), pp. 11–20. DOI: 10.1016/j.ijpara.2016.09.007.

127. Cwiklinski, K., Robinson, M. W., Donnelly, S. *et al.* (2021) Complementary transcriptomic and proteomic analyses reveal the cellular and molecular processes that drive growth and development of *Fasciola hepatica* in the host liver. *BMC Genomics* 22(1):46. DOI: 10.1186/s12864-020-07326-y.

128. Fontenla, S., Langleib, M., La Torre-Escudero, E. de *et al.* (2021) Role of *Fasciola hepatica* small RNAs in the interaction with the mammalian host. *Front Cell Infect Microbiol* 11:812141. DOI: 10.3389/fcimb.2021.812141.

129. Herron, C. M., O'Connor, A., Robb, E. *et al.* (2022) Developmental regulation and functional prediction of microRNAs in an expanded *Fasciola hepatica* miRNome. *Front Cell Infect Microbiol* 12:811123. DOI: 10.3389/fcimb.2022.811123.

130. Ricafrente, A., Cwiklinski, K., Nguyen, H. *et al.* (2022) Stage-specific miRNAs regulate gene expression associated with growth, development and parasite-host interaction during the intra-mammalian migration of the zoonotic helminth parasite *Fasciola hepatica*. *BMC Genomics* 23(1):419. DOI: 10.1186/s12864-022-08644-z.

131. McCusker, P., Clarke, N. G., Gardiner, E. *et al.* (2024) Neoblast-like stem cells of *Fasciola hepatica*. *PLOS Pathog* 20(5):e1011903. DOI: 10.1371/journal.ppat.1011903.

132. Cwiklinski, K., Jewhurst, H., McVeigh, P. *et al.* (2018) Infection by the helminth parasite *Fasciola hepatica* requires rapid regulation of metabolic, virulence, and invasive factors to adjust to its mammalian host. *Mol Cell Proteom* 17(4), pp. 792–809. DOI: 10.1074/mcp.RA117.000445.

133. Haçarız, O., Baykal, A. T., Akgün, M. *et al.* (2014) Generating a detailed protein profile of *Fasciola hepatica* during the chronic stage of infection in cattle. *Proteomics* 14(12), pp. 1519–1530. DOI: 10.1002/pmic.201400012.

134. Di Maggio, L. S., Tirloni, L., Pinto, A. F. M. *et al.* (2016) Across intra-mammalian stages of the liver fluke *Fasciola hepatica*: a proteomic study. *Sci Rep* 6(1):32796. DOI: 10.1038/srep32796.

135. Bennett, A. P. S., La Torre-Escudero, E. de, Dermott, S. S. E. *et al.* (2022) *Fasciola hepatica g*astrodermal cells selectively release extracellular vesicles via a novel atypical secretory mechanism. *Int J Mol Sci* 23(10):5525. DOI: 10.3390/ijms23105525.

136. Wilson, R. A., Wright, J. M., Castro-Borges, W. de *et al.* (2011) Exploring the *Fasciola hepatica* tegument proteome. *Int J Parasitol* 41(13-14), pp. 1347–1359. DOI: 10.1016/j.ijpara.2011.08.003.

137. Cwiklinski, K., La Torre-Escudero, E. de, Trelis, M. *et al.* (2015) The extracellular vesicles of the helminth pathogen, *Fasciola hepatica*: Biogenesis pathways and cargo molecules involved in parasite pathogenesis. *Mol Cell Proteom* 14(12), pp. 3258–3273. DOI: 10.1074/mcp.M115.053934.

138. Murphy, A., Cwiklinski, K., Lalor, R. *et al.* (2020) *Fasciola hepatica* extracellular vesicles isolated from excretory-secretory products using a gravity flow method modulate dendritic cell phenotype and activity. *PLOS Neg Trop Dis* 14(9):e0008626. DOI: 10.1371/journal.pntd.0008626.

139. Trelis, M., Sánchez-López, C. M., Sánchez-Palencia, L. F. *et al.* (2022) Proteomic analysis of extracellular vesicles from *Fasciola hepatica* hatching eggs and juveniles in culture. *Front Cell Infect Microbiol* 12:903602. DOI: 10.3389/fcimb.2022.903602.

140. Marco Verissimo, C. de, Cwiklinski, K., Nilsson, J. *et al.* (2023) Glycan complexity and heterogeneity of glycoproteins in somatic extracts and secretome of the infective stage of the helminth *Fasciola hepatica*. *Mol Cell Proteom* 22(12):100684. DOI: 10.1016/j.mcpro.2023.100684.

141. Yue, L., Liu, F., Hu, J. *et al.* (2023) A guidebook of spatial transcriptomic technologies, data resources and analysis approaches. *Comput Struct Biotechnol J* 21, pp. 940–955. DOI: 10.1016/j.csbj.2023.01.016.

142. Duan, H., Cheng, T. & Cheng, H. (2023) Spatially resolved transcriptomics: advances and applications. *Blood Sci* 5(1), pp. 1–14. DOI: 10.1097/BS9.0000000000000141.

143. Jovic, D., Liang, X., Zeng, H. *et al.* (2022) Single-cell RNA sequencing technologies and applications: a brief overview. *Clin Transl Med* 12(3):e694. DOI: 10.1002/ctm2.694.

144. Britton, C., Laing, R., McNeilly, T. N. *et al.* (2023) New technologies to study helminth development and host-parasite interactions. *Int J Parasitol* 53(8), pp. 393–403. DOI: 10.1016/j.ijpara.2022.11.012.

145. Diaz Soria, C. L., Lee, J., Chong, T. *et al.* (2020) Single-cell atlas of the first intra-mammalian developmental stage of the human parasite *Schistosoma mansoni*. *Nat Commun* 11(1):6411. DOI: 10.1038/s41467-020-20092-5.

146. Wendt, G., Zhao, L., Chen, R. *et al.* (2020) A single-cell RNA-seq atlas of *Schistosoma mansoni* identifies a key regulator of blood feeding. *Science* 369(6511), pp. 1644–1649. DOI: 10.1126/science.abb7709.

147. Henthorn, C. R., Airs, P. M., Neumann, E. K. *et al.* (2023) Resolving the origins of secretory products and anthelmintic responses in a human parasitic nematode at single-cell resolution. *eLife* 12:e83100. DOI: 10.7554/eLife.83100.

148. Puckelwaldt, O., Gramberg, S., Ajmera, S. *et al.* (2024) Single-cell transcriptomics identifies a p21-activated kinase important for survival of the zoonotic parasite *Fasciola hepatica*. *bioRxiv*. DOI: 10.1101/2024.03.26.586785.

149. Puckelwaldt, O. (2024) Uncovering the cellular diversity of *Fasciola hepatica* utilizing single-cell transcriptomics. Doctoral thesis. Institute of Parasitology, JLU Giessen. DOI: 10.22029/jlupub-19504.

150. Williams, C. G., Lee, H. J., Asatsuma, T. *et al.* (2022) An introduction to spatial transcriptomics for biomedical research. *Genome Med* 14(1):68. DOI: 10.1186/s13073-022-01075-1.

151. Ståhl, P. L., Salmén, F., Vickovic, S. *et al.* (2016) Visualization and analysis of gene expression in tissue sections by spatial transcriptomics. *Science* 353(6294), pp. 78–82. DOI: 10.1126/science.aaf2403.

152. Rao, A., Barkley, D., França, G. S. *et al.* (2021) Exploring tissue architecture using spatial transcriptomics. *Nature* 596(7871), pp. 211–220. DOI: 10.1038/s41586-021-03634-9.

153. Wang, Y., Liu, B., Zhao, G. *et al.* (2023) Spatial transcriptomics: technologies, applications and experimental considerations. *Genomics* 115(5):110671. DOI: 10.1016/j.ygeno.2023.110671.

154. Moses, L. & Pachter, L. (2022) Museum of spatial transcriptomics. *Nat Methods* 19(5), pp. 534–546. DOI: 10.1038/s41592-022-01409-2.

155. Piwecka, M., Rajewsky, N. & Rybak-Wolf, A. (2023) Single-cell and spatial transcriptomics: deciphering brain complexity in health and disease. *Nat Rev Neurol* 19(6), pp. 346–362. DOI: 10.1038/s41582-023-00809-y.

156. Wang, M., Hu, Q., Lv, T. *et al.* (2022) High-resolution 3D spatiotemporal transcriptomic maps of developing *Drosophila* embryos and larvae. *Dev Cell* 57(10), pp. 1271–1283. DOI: 10.1016/j.devcel.2022.04.006.

157. Liu, C., Leng, J., Li, Y. *et al.* (2022) A spatiotemporal atlas of organogenesis in the development of orchid flowers. *Nucleic Acids Res* 50(17), pp. 9724–9737. DOI: 10.1093/nar/gkac773.

158. Lim, H. J., Wang, Y., Buzdin, A. *et al.* (2025) A practical guide for choosing an optimal spatial transcriptomics technology from seven major commercially available options. *BMC genomics* 26(1):47. DOI: 10.1186/s12864-025-11235-3.

159. Asp, M., Bergenstråhle, J. & Lundeberg, J. (2020) Spatially resolved transcriptomes - next generation tools for tissue exploration. *BioEssays* 42(10):e1900221. DOI: 10.1002/bies.201900221.

160. Liao, J., Lu, X., Shao, X. *et al.* (2021) Uncovering an organ's molecular architecture at single-cell resolution by spatially resolved transcriptomics. *Trends Biotechnol* 39(1), pp. 43–58. DOI: 10.1016/j.tibtech.2020.05.006.

161. Merritt, C. R., Ong, G. T., Church, S. E. *et al.* (2020) Multiplex digital spatial profiling of proteins and RNA in fixed tissue. *Nat Biotechnol* 38(5), pp. 586–599. DOI: 10.1038/s41587-020-0472-9.

162. Rodriques, S. G., Stickels, R. R., Goeva, A. *et al.* (2019) Slide-seq: A scalable technology for measuring genome-wide expression at high spatial resolution. *Science* 363(6434), pp. 1463–1467. DOI: 10.1126/science.aaw1219.

163. Stickels, R. R., Murray, E., Kumar, P. *et al.* (2021) Highly sensitive spatial transcriptomics at near-cellular resolution with Slide-seqV2. *Nat Biotechnol* 39(3), pp. 313–319. DOI: 10.1038/s41587-020-0739-1.

164. Oliveira, M. F., Romero, J. P., Chung, M. *et al.* (2024) Characterization of immune cell populations in the tumor microenvironment of colorectal cancer using high definition spatial profiling. *bioRxiv*. DOI: 10.1101/2024.06.04.597233.

165. Chen, A., Liao, S., Cheng, M. *et al.* (2022) Spatiotemporal transcriptomic atlas of mouse organogenesis using DNA nanoball-patterned arrays. *Cell* 185(10), pp. 1777-1792. DOI: 10.1016/j.cell.2022.04.003.

166. Chen, K. H., Boettiger, A. N., Moffitt, J. R. *et al.* (2015) RNA imaging. Spatially resolved, highly multiplexed RNA profiling in single cells. *Science* 348(6233):aaa6090. DOI: 10.1126/science.aaa6090.

167. Janesick, A., Shelansky, R., Gottscho, A. D. *et al.* (2023) High resolution mapping of the tumor microenvironment using integrated single-cell, spatial and *in situ* analysis. *Nat Commun* 14(1):8353. DOI: 10.1038/s41467-023-43458-x.

168. He, S., Bhatt, R., Brown, C. *et al.* (2022) High-plex imaging of RNA and proteins at subcellular resolution in fixed tissue by spatial molecular imaging. *Nat Biotechnol* 40(12), pp. 1794–1806. DOI: 10.1038/s41587-022-01483-z.

169. Jung, N. & Kim, T.-K. (2023) Spatial transcriptomics in neuroscience. *Exp Mol Med* 55(10), pp. 2105–2115. DOI: 10.1038/s12276-023-01093-y.

170. 10x Genomics: Visium Spatial Gene Expression Reagent Kits for FFPE. User Guide. CG000407, RevE. Available at https://cdn.10xgenomics.com/image/upload/v1695417748/support-documents/CG000407_VisiumSpatialGeneExpressionforFFPE_UserGuide_RevE.pdf (13.02.2025).

171. STOmics: Stereo-seq Transcriptomics Set for FFPE. User Manual. STUM-TT004, Vers. A. Available at https://enfile.stomics.tech/STUM-TT004%20Stereo-seq%20Transcriptomics%20Set%20for%20FFPE%20User%20Manual%20ver%20A.pdf (13.02.2025).

172. You, Y., Fu, Y., Li, L. *et al.* (2024) Systematic comparison of sequencing-based spatial transcriptomic methods. *Nat Methods* 21(9), pp. 1743–1754. DOI: 10.1038/s41592-024-02325-3.

173. Habern, O.: Your introduction to Visium HD: Spatial biology in high definition. Available at https://www.10xgenomics.com/blog/your-introduction-to-visium-hd-spatial-biology-in-high-definition (16.02.2025).

174. STOmics: Stereo-seq Analysis Workflow. Q&A. Vers. A3. Available at https://enfile.stomics.tech/Stereo-seq%20SAW%20FAQ%20version%20A3.pdf (16.02.2025).

175. Bruker Spatial Biology: GeoMx DSP Instrument. User Manual. MAN-10152-06. Available at https://university.nanostring.com/geomx-dsp-instrument-user-manual/1163226 (16.02.2025).

176. Xia, C., Fan, J., Emanuel, G. *et al.* (2019) Spatial transcriptome profiling by MERFISH reveals subcellular RNA compartmentalization and cell cycle-dependent gene expression. *PNAS* 116(39), pp. 19490–19499. DOI: 10.1073/pnas.1912459116.

177. Beechem, J., Khafizov, R., Rane, T. *et al.* (2024) Spatial single-cell whole transcriptome imaging in tissue and fixed cells using CosMx spatial molecular imaging. Available at https://nanostring.com/wp-content/uploads/2024/02/AGBT-2024_PST-638-Beechem_Poster_CosMx_WTx_Final.pdf (16.02.2025).

178. 10x Genomics: Xenium Prime 5K Gene Expression Workflow, Analysis & Data Highlights. Technical Note. CG000775, RevA. Available at https://cdn.10xgenomics.com/image/upload/v1721078232/support-documents/CG000775_Prime5K_DataHighlightsTN_RevA.pdf (16.02.2025).

179. 10x Genomics: Benchmarking comparisons: Highlighting spatial imaging comparison studies. Independent technology comparisons. Available at https://pages.10xgenomics.com/WEB-2024-04-WEBSITE-PAGE-XEN-HIGHLIGHTING-SPATIAL-IMAGING-COMP-STUDY_LP.html (16.02.2025).

180. NanoString: CosMx™ SMI vs. Xenium: Superior *in situ* single-cell performance study. Available at https://nanostring.com/resources/cosmx-smi-vs-xenium-superior-in-situ-single-cell-performance-study/ (13.02.2025).

181. Wang, H., Huang, R., Nelson, J. *et al.* (2023) Systematic benchmarking of imaging spatial transcriptomics platforms in FFPE tissues. *bioRxiv*. DOI: 10.1101/2023.12.07.570603.

182. Rademacher, A., Huseynov, A., Bortolomeazzi, M. *et al.* (2024) Comparison of spatial transcriptomics technologies using tumor cryosections. *bioRxiv*. DOI: 10.1101/2024.04.03.586404.

183. Hartman, A. & Satija, R. (2024) Comparative analysis of multiplexed *in situ* gene expression profiling technologies. *bioRxiv*. DOI: 10.1101/2024.01.11.575135.

184. Cook, D. P., Jensen, K. B., Wise, K. *et al.* (2023) A comparative analysis of imaging-based spatial transcriptomics platforms. *bioRxiv*. DOI: 10.1101/2023.12.13.571385.

185. Zhu, P., Wu, K., Zhang, C. *et al.* (2023) Advances in new target molecules against schistosomiasis: a comprehensive discussion of physiological structure and nutrient intake. *PLOS Pathog* 19(7):e1011498. DOI: 10.1371/journal.ppat.1011498.

186. Mansour, T. E. & Mansour, J. M. (2002) Chemotherapeutic targets in parasites. Contemporary strategies. 8 - Targets in the tegument of flatworms pp. 189–214. *Cambridge University Press, Cambridge, UK*. DOI: 10.1017/CBO9780511546440.

187. Pawlak, M., Lefebvre, P. & Staels, B. (2012) General molecular biology and architecture of nuclear receptors. *Curr Top Med Chem* 12(6), pp. 486–504. DOI: 10.2174/156802612799436641.

188. Robinson-Rechavi, M., Escriva Garcia, H. & Laudet, V. (2003) The nuclear receptor superfamily. *J Cell Sci* 116(4), pp. 585–586. DOI: 10.1242/jcs.00247.

189. Sluder, A. E., Mathews, S. W., Hough, D. *et al.* (1999) The nuclear receptor superfamily has undergone extensive proliferation and diversification in nematodes. *Genome Res* 9(2), pp. 103–120.

190. Wu, W. & LoVerde, P. T. (2021) Identification and evolution of nuclear receptors in Platyhelminths. *PLOS One* 16(8):e0250750. DOI: 10.1371/journal.pone.0250750.

191. Weikum, E. R., Liu, X. & Ortlund, E. A. (2018) The nuclear receptor superfamily: a structural perspective. *Protein Sci* 27(11), pp. 1876–1892. DOI: 10.1002/pro.3496.

192. Sar, P. (2023) Chapter Ten - Nuclear receptor: structure and function. In: I. Mani & V. Singh (eds). Progress in molecular biology and translational science: receptor endocytosis and signalling in health and disease - Part B, Vol. 196. pp. 209–227. *Academic Press, Cambridge, MA, US*. DOI: 10.1016/bs.pmbts.2022.07.014. ISBN: 1877-1173.

193. Wu, W. & LoVerde, P. T. (2019) Nuclear hormone receptors in parasitic Platyhelminths. *Mol Biochem Parasitol* 233:111218. DOI: 10.1016/j.molbiopara.2019.111218.

194. Zeitlinger, J. (2020) Seven myths of how transcription factors read the cis-regulatory code. *Curr Opin Syst Biol* 23, pp. 22–31. DOI: 10.1016/j.coisb.2020.08.002.

195. Xu, P. (2023) Nuclear receptors in health and diseases. *Int J Mol Sci* 24(11):9153. DOI: 10.3390/ijms24119153.

196. Sever, R. & Glass, C. K. (2013) Signaling by nuclear receptors. *Cold Spring Harb Perspect Biol* 5(3):a016709. DOI: 10.1101/cshperspect.a016709.

197. Kues, W. A. & Köckritz-Blickwede, M. von (eds.) (2020) Biochemie für die Tiermedizin. 1st ed. *Thieme, Stuttgart, DE*. DOI: 10.1055/b-005-145219.

198. Dubois, V., Staels, B., Lefebvre, P. *et al.* (2020) Control of cell identity by the nuclear receptor HNF4 in organ pathophysiology. *Cells* 9(10):2185. DOI: 10.3390/cells9102185.

199. Sladek, F. M. (2011) What are nuclear receptor ligands? *Mol Cell Endocrinol* 334(1-2), pp. 3–13. DOI: 10.1016/j.mce.2010.06.018.

200. Bridgham, J. T., Eick, G. N., Larroux, C. *et al.* (2010) Protein evolution by molecular tinkering: diversification of the nuclear receptor superfamily from a ligand-dependent ancestor. *PLOS Biol* 8(10):e1000497. DOI: 10.1371/journal.pbio.1000497.

201. Yuan, X., Ta, T. C., Lin, M. *et al.* (2009) Identification of an endogenous ligand bound to a native orphan nuclear receptor. *PLOS One* 4(5):e5609. DOI: 10.1371/journal.pone.0005609.

202. Vemuri, K., Radi, S. H., Sladek, F. M. *et al.* (2023) Multiple roles and regulatory mechanisms of the transcription factor HNF4 in the intestine. *Front Endocrinol* 14:1232569. DOI: 10.3389/fendo.2023.1232569.

203. Beinsteiner, B., Billas, I. M. L. & Moras, D. (2023) Structural insights into the HNF4 biology. *Front Endocrinol* 14:1197063. DOI: 10.3389/fendo.2023.1197063.

204. Chen, L., Luo, S., Dupre, A. *et al.* (2021) The nuclear receptor HNF4 drives a brush border gene program conserved across murine intestine, kidney, and embryonic yolk sac. *Nat Commun* 12(1):2886. DOI: 10.1038/s41467-021-22761-5.

205. Bolotin, E., Liao, H., Ta, T. C. *et al.* (2010) Integrated approach for the identification of human hepatocyte nuclear factor 4alpha target genes using protein binding microarrays. *Hepatology* 51(2), pp. 642–653. DOI: 10.1002/hep.23357.

206. Zhong, W., Sladek, F. M. & Darnell, J. E. (1993) The expression pattern of a *Drosophila* homolog to the mouse transcription factor HNF-4 suggests a determinative role in gut formation. *EMBO J* 12(2), pp. 537–544. DOI: 10.1002/j.1460-2075.1993.tb05685.x.

207. Palanker, L., Tennessen, J. M., Lam, G. *et al.* (2009) *Drosophila* HNF4 regulates lipid mobilization and beta-oxidation. *Cell Metab* 9(3), pp. 228–239. DOI: 10.1016/j.cmet.2009.01.009.

208. Vonolfen, M. C., Meyer Zu Altenschildesche, F. L., Nam, H.-J. *et al.* (2024) *Drosophila* HNF4 acts in distinct tissues to direct a switch between lipid storage and export in the gut. *Cell Rep* 43(9):114693. DOI: 10.1016/j.celrep.2024.114693.

209. Scimone, M. L., Kravarik, K. M., Lapan, S. W. *et al.* (2014) Neoblast specialization in regeneration of the planarian *Schmidtea mediterranea*. *Stem Cell Reports* 3(2), pp. 339–352. DOI: 10.1016/j.stemcr.2014.06.001.

210. Wagner, D. E., Wang, I. E. & Reddien, P. W. (2011) Clonogenic neoblasts are pluripotent adult stem cells that underlie planarian regeneration. *Science* 332(6031), pp. 811–816. DOI: 10.1126/science.1203983.

211. Gramberg, S., Puckelwaldt, O., Schmitt, T. *et al.* (2024) Spatial transcriptomics of a parasitic flatworm provides a molecular map of drug targets and drug resistance genes. *Nat Commun* 15(1):8918. DOI: 10.1038/s41467-024-53215-3.

212. Gramberg, S., Puckelwaldt, O., Schmitt, T. *et al.* (2023) Spatial transcriptomics of a parasitic flatworm provides a molecular map of vaccine candidates, drug targets and drug resistance genes. *bioRxiv*. DOI: 10.1101/2023.12.11.571084.

213. Han, H. (2018) RNA interference to knock down gene expression. In: J. K. DiStefano (ed). Disease gene identification. Methods and protocols, Vol. 1706. pp. 293–302. Springer protocols. *Humana, New York, NY*. DOI: 10.1007/978-1-4939-7471-9_16.

214. McVeigh, P., McCammick, E. M., McCusker, P. *et al.* (2014) RNAi dynamics in juvenile *Fasciola* spp. liver flukes reveals the persistence of gene silencing *in vitro*. *PLOS Neg Trop Dis* 8(9):e3185. DOI: 10.1371/journal.pntd.0003185.

215. McCusker, P., Hussain, W., McVeigh, P. *et al.* (2020) RNA interference dynamics in juvenile *Fasciola hepatica* are altered during *in vitro* growth and development. *Int J Parasitol Drugs Drug Resist* 14, pp. 46–55. DOI: 10.1016/j.ijpddr.2020.08.004.

216. Howe, K. L., Bolt, B. J., Shafie, M. *et al.* (2017) WormBase ParaSite - a comprehensive resource for helminth genomics. *Mol Biochem Parasitol* 215, pp. 2–10. DOI: 10.1016/j.molbiopara.2016.11.005.

217. Gruber, A. R., Lorenz, R., Bernhart, S. H. *et al.* (2008) The Vienna RNA websuite. *Nucleic Acids Res* 36(Web Server issue), pp. W70-W74. DOI: 10.1093/nar/gkn188.

218. Lück, S., Kreszies, T., Strickert, M. *et al.* (2019) siRNA-Finder (si-Fi) software for RNAi-target design and off-target prediction. *Front Plant Sci* 10:1023. DOI: 10.3389/fpls.2019.01023.

219. Kibbe, W. A. (2007) OligoCalc: an online oligonucleotide properties calculator. *Nucleic Acids Res* 35(Web Server issue), pp. W43-46. DOI: 10.1093/nar/gkm234.

220. Collins, J. J., Hou, X., Romanova, E. V. *et al.* (2010) Genome-wide analyses reveal a role for peptide hormones in planarian germline development. *PLOS Biol* 8(10):e1000509. DOI: 10.1371/journal.pbio.1000509.

221. Benchling (2025) Benchling Biology Software. Available at https://benchling.com.

222. Kiselyuk, A., Lee, S.-H., Farber-Katz, S. *et al.* (2012) HNF4α antagonists discovered by a high-throughput screen for modulators of the human insulin promoter. *Chem Biol* 19(7), pp. 806–818. DOI: 10.1016/j.chembiol.2012.05.014.

223. Bauer, L. (2023) Molecular and functional characterization of cell type and tissue specific genes in the liver fluke *Fasciola hepatica*. Master's thesis. Institute of Parasitology, JLU Giessen.

224. Tang, S., Xiao, V., Wei, L. *et al.* (2008) Protein kinase C isozymes and their selectivity towards ruboxistaurin. *Proteins: Struct, Funct, Bioinf* 72(1), pp. 447–460. DOI: 10.1002/prot.21942.

225. Dorak, M. T. (ed.) (2006) Real-time PCR. 1st ed. *Taylor & Francis, London*. DOI: 10.4324/9780203967317.

226. Pfaffl, M. W. (2001) A new mathematical model for relative quantification in real-time RT-PCR. *Nucleic Acids Res* 29(9):e45. DOI: 10.1093/nar/29.9.e45.

227. Livak, K. J. & Schmittgen, T. D. (2001) Analysis of relative gene expression data using real-time quantitative PCR and the 2(-delta delta C(T)) method. *Methods* 25(4), pp. 402–408. DOI: 10.1006/meth.2001.1262.

228. Houhou, H., Puckelwaldt, O., Strube, C. *et al.* (2019) Reference gene analysis and its use for kinase expression profiling in *Fasciola hepatica*. *Sci Rep* 9(1):15867. DOI: 10.1038/s41598-019-52416-x.

229. Tegni Sontia, P. (2023) Bioinformatic characterization of the function of the transcription factor HNF4 in the parasite *F. hepatica*. Master's thesis. Institute of Parasitology, JLU Giessen.

230. Blumenkamp, P., Pfister, M., Diedrich, S. *et al.* (2024) Curare and GenExVis: a versatile toolkit for analyzing and visualizing RNA-Seq data. *BMC Bioinformatics* 25(1):138. DOI: 10.1186/s12859-024-05761-2.

231. Posit team (2024) RStudio. Integrated development environment for R. *Posit Software, PBC*. Available at http://www.posit.com/.

232. R Core Team (2024) R. A language and environment for statistical computing. *R Foundation for Statistical Computing*. Available at https://www.R-project.org/.

233. Love, M. I., Huber, W. & Anders, S. (2014) Moderated estimation of fold change and dispersion for RNA-seq data with DESeq2. *Genome Biol* 15(12):550. DOI: 10.1186/s13059-014-0550-8.

234. Love, M. I., Anders, S. & Huber, W. (2024) Analyzing RNA-seq data with DESeq2. R package. *Bioconductor*. Available at https://bioconductor.org/packages/release/bioc/vignettes/DESeq2/inst/doc/DESeq2.html.

235. Warnes, G. R., Bolker, B., Bonebakker, L. *et al.* (2024) gplots: various R programming tools for plotting data. R package. *CRAN*. Available at https://CRAN.R-project.org/package=gplots.

236. Blighe, K., Rana, S. & Lewis, M. (2024) EnhancedVolcano. Publication-ready volcano plots with enhanced colouring and labeling. R package. *Bioconductor*. Available at https://bioconductor.org/packages/EnhancedVolcano.

237. Ashburner, M., Ball, C. A., Blake, J. A. *et al.* (2000) Gene ontology: tool for the unification of biology. The Gene Ontology Consortium. *Nat Genet* 25(1), pp. 25–29. DOI: 10.1038/75556.

238. Kramer, F. & Beißbarth, T. (2017) Working with ontologies. *Methods Mol Biol* 1525, pp. 123–135. DOI: 10.1007/978-1-4939-6622-6_6.

239. Jones, P., Binns, D., Chang, H.-Y. *et al.* (2014) InterProScan 5: genome-scale protein function classification. *Bioinformatics* 30(9), pp. 1236–1240. DOI: 10.1093/bioinformatics/btu031.

240. Alexa, A. & Rahnenfuhrer, J. (2021) topGO: Enrichment analysis for Gene Ontology. R package. *Bioconductor*. Available at https://bioconductor.org/packages/topGO.

241. Chen, H. (2022) VennDiagram. Generate high-resolution Venn and Euler Plots. R package. *CRAN*. Available at https://CRAN.R-project.org/package=VennDiagram.

242. Gu, Z., Eils, R. & Schlesner, M. (2016) Complex heatmaps reveal patterns and correlations in multidimensional genomic data. *Bioinformatics* 32(18), pp. 2847–2849. DOI: 10.1093/bioinformatics/btw313.

243. 10x Genomics: Methanol Fixation, H&E Staining & Imaging for Visium Spatial Protocols. Demonstrated Protocol. CG000160, RevB. Available at https://cdn.10xgenomics.com/image/upload/v1695417730/support-documents/CG000160_DemonstratedProtocol_MethanolFixation andHEStaining_RevD.pdf (updated version) (09.04.2021).

244. Gramberg, S. & Puckelwaldt, O. (2024) Analysis and visualization of the *Fasciola hepatica* spatial transcriptomics dataset. *Zenodo*. DOI: 10.5281/zenodo.10245261.

245. Hao, Y., Hao, S., Andersen-Nissen, E. *et al.* (2021) Integrated analysis of multimodal single-cell data. *Cell* 184(13), pp. 3573–3587. DOI: 10.1016/j.cell.2021.04.048.

246. Korsunsky, I., Millard, N., Fan, J. *et al.* (2019) Fast, sensitive and accurate integration of single-cell data with Harmony. *Nat Methods* 16(12), pp. 1289–1296. DOI: 10.1038/s41592-019-0619-0.

247. Dries, R., Zhu, Q., Dong, R. *et al.* (2021) Giotto: a toolbox for integrative analysis and visualization of spatial expression data. *Genome Biol* 22(1):78. DOI: 10.1186/s13059-021-02286-2.

248. Zdrazil, B., Felix, E., Hunter, F. *et al.* (2024) The ChEMBL Database in 2023: a drug discovery platform spanning multiple bioactivity data types and time periods. *Nucleic Acids Res* 52(D1), pp. D1180-D1192. DOI: 10.1093/nar/gkad1004.

249. Camacho, C., Coulouris, G., Avagyan, V. *et al.* (2009) BLAST+: architecture and applications. *BMC Bioinformatics* 10(1):421. DOI: 10.1186/1471-2105-10-421.

250. Letunic, I., Khedkar, S. & Bork, P. (2021) SMART: recent updates, new developments and status in 2020. *Nucleic Acids Res* 49(D1), pp. D458-D460. DOI: 10.1093/nar/gkaa937.

251. Marchler-Bauer, A., Bo, Y., Han, L. *et al.* (2017) CDD/SPARCLE: functional classification of proteins via subfamily domain architectures. *Nucleic Acids Res* 45(D1), pp. D200-D203. DOI: 10.1093/nar/gkw1129.

252. Sayers, E. W., Bolton, E. E., Brister, J. R. *et al.* (2022) Database resources of the national center for biotechnology information. *Nucleic Acids Res* 50(D1), pp. D20-D26. DOI: 10.1093/nar/gkab1112.

253. Madeira, F., Pearce, M., Tivey, A. R. N. *et al.* (2022) Search and sequence analysis tools services from EMBL-EBI in 2022. *Nucleic Acids Res* 50(W1), pp. W276-W279. DOI: 10.1093/nar/gkac240.

254. Kumar, S., Stecher, G., Li, M. *et al.* (2018) MEGA X: Molecular evolutionary genetics analysis across computing platforms. *Mol Biol Evol* 35(6), pp. 1547–1549. DOI: 10.1093/molbev/msy096.

255. Szklarczyk, D., Gable, A. L., Lyon, D. *et al.* (2019) STRING v11: protein-protein association networks with increased coverage, supporting functional discovery in genome-wide experimental datasets. *Nucleic Acids Res* 47(D1), pp. D607-D613. DOI: 10.1093/nar/gky1131.

256. Fang, B., Mane-Padros, D., Bolotin, E. *et al.* (2012) Identification of a binding motif specific to HNF4 by comparative analysis of multiple nuclear receptors. *Nucleic Acids Res* 40(12), pp. 5343–5356. DOI: 10.1093/nar/gks190.

257. Rauluseviciute, I., Riudavets-Puig, R., Blanc-Mathieu, R. *et al.* (2024) JASPAR 2024: 20th anniversary of the open-access database of transcription factor binding profiles. *Nucleic Acids Res* 52(D1), pp. D174-D182. DOI: 10.1093/nar/gkad1059.

258. Kulakovskiy, I. V., Vorontsov, I. E., Yevshin, I. S. *et al.* (2018) HOCOMOCO: towards a complete collection of transcription factor binding models for human and mouse via large-scale ChIP-Seq analysis. *Nucleic Acids Res* 46(D1), pp. D252-D259. DOI: 10.1093/nar/gkx1106.

259. Jensen, E. (2014) Technical review: *in situ* hybridization. *Anat Rec* 297(8), pp. 1349–1353. DOI: 10.1002/ar.22944.

260. Castillo, E. & Koziol, U. (2020) Analysis of gene expression in *Fasciola hepatica* juveniles and adults by *in situ* hybridization. In: M. Cancela & G. Maggioli (eds). *Fasciola hepatica:* Methods and protocols. Methods in Molecular Biology Vol. 2137. pp. 93–105. *Humana, New York, NY*. DOI: 10.1007/978-1-0716-0475-5_7.

261. Dapson, R. W. (2007) The history, chemistry and modes of action of carmine and related dyes. *Biotech Histochem* 82(4-5), pp. 173–187. DOI: 10.1080/10520290701704188.

262. Machado-Silva, J. R., Pelajo-Machado, M., Lenzi, H. L. *et al.* (1998) Morphological study of adult male worms of *Schistosoma mansoni* Sambon, 1907 by confocal laser scanning microscopy. *Mem Inst Oswaldo Cruz* 93 Suppl 1, pp. 303–307. DOI: 10.1590/S0074-02761998000700060.

263. Langeron, M. (1913) Précis de microscopie: technique, expérimentation, diagnostic. 1st ed. *Masson, Paris, FR*.

264. McCusker, P., McVeigh, P., Rathinasamy, V. *et al.* (2016) Stimulating neoblast-like cell proliferation in juvenile *Fasciola hepatica s*upports growth and progression towards the adult phenotype *in vitro*. *PLOS Neg Trop Dis* 10(9):e0004994. DOI: 10.1371/journal.pntd.0004994.

265. Salic, A. & Mitchison, T. J. (2008) A chemical method for fast and sensitive detection of DNA synthesis *in vivo*. *PNAS* 105(7), pp. 2415–2420. DOI: 10.1073/pnas.0712168105.

266. Wendt, G. R., Collins, J. N., Pei, J. *et al.* (2018) Flatworm-specific transcriptional regulators promote the specification of tegumental progenitors in *Schistosoma mansoni*. *eLife* 7:e33221. DOI: 10.7554/eLife.33221.

267. Guerrero-Hernández, C., Doddihal, V., Mann, F. G. *et al.* (2024) A powerful and versatile new fixation protocol for immunostaining and *in situ* hybridization that preserves delicate tissues. *BMC Biol* 22(1):252. DOI: 10.1186/s12915-024-02052-3.

268. Kunkely, H. & Vogler, A. (2011) Absorption and luminescence spectra of cochineal. *Anorg Chem Commun* 14(7), pp. 1153–1155. DOI: 10.1016/j.inoche.2011.04.011.

269. Osorio, D. & Cai, J. J. (2021) Systematic determination of the mitochondrial proportion in human and mice tissues for single-cell RNA-sequencing data quality control. *Bioinformatics* 37(7), pp. 963–967. DOI: 10.1093/bioinformatics/btaa751.

270. Bohr, T., Ashley, G., Eggleston, E. *et al.* (2016) Synaptonemal complex components are required for meiotic checkpoint function in *Caenorhabditis elegans*. *Genetics* 204(3), pp. 987–997. DOI: 10.1534/genetics.116.191494.

271. Souquet, B., Abby, E., Hervé, R. *et al.* (2013) MEIOB targets single-strand DNA and is necessary for meiotic recombination. *PLOS Genet* 9(9):e1003784. DOI: 10.1371/journal.pgen.1003784.

272. Fu, M. & Blackshear, P. J. (2017) RNA-binding proteins in immune regulation: a focus on CCCH zinc finger proteins. *Nat Rev Immunol* 17(2), pp. 130–143. DOI: 10.1038/nri.2016.129.

273. Robinson, G. & Threadgold, L. T. (1975) Electron microscope studies of *Fasciola hepatica.* XII. The fine structure of the gastrodermis. *Exp Parasitol* 37(1), pp. 20–36. DOI: 10.1016/0014-4894(75)90050-8.

274. Espino, A. M. & Hillyer, G. V. (2003) Molecular cloning of a member of the *Fasciola hepatica* saposin-like protein family. *J Parasitol* 89(3), pp. 545–552. DOI: 10.1645/GE-3113.

275. Robinson, M. W., Dalton, J. P. & Donnelly, S. (2008) Helminth pathogen cathepsin proteases: it's a family affair. *Trends Biochem Sci* 33(12), pp. 601–608. DOI: 10.1016/j.tibs.2008.09.001.

276. Cancela, M., Corvo, I., Da Silva, E. *et al.* (2017) Functional characterization of single-domain cystatin-like cysteine proteinase inhibitors expressed by the trematode *Fasciola hepatica*. *Parasitology* 144(13), pp. 1695–1707. DOI: 10.1017/S0031182017001093.

277. Lu, Y., Su, F., Li, Q. *et al.* (2020) Pattern recognition receptors in *Drosophila* immune responses. *Dev Comp Immunol* 102:103468. DOI: 10.1016/j.dci.2019.103468.

278. 10x Genomics: Visium Spatial Gene Expression Solution. Product Sheet. LIT000059, RevE. Available at https://pages.10xgenomics.com/rs/446-PBO-704/images/10x_LIT059_Product Sheet_VisiumSpatialGeneExpression_Letter_digital.pdf (19.10.2023).

279. Thomas, C. M. & Timson, D. J. (2016) A mysterious family of calcium-binding proteins from parasitic worms. *Biochem Soc Trans* 44(4), pp. 1005–1010. DOI: 10.1042/BST20150270.

280. Sarrazin, S., Lamanna, W. C. & Esko, J. D. (2011) Heparan sulfate proteoglycans. *Cold Spring Harb Perspect Biol* 3(7):a004952. DOI: 10.1101/cshperspect.a004952.

281. Cervi, L., Rossi, G. & Masih, D. T. (1999) Potential role for excretory-secretory forms of glutathione-S-transferase (GST) in *Fasciola hepatica*. *Parasitology* 119(6), pp. 627–633. DOI: 10.1017/s003118209900517x.

282. Thivierge, K., Cotton, S., Schaefer, D. A. *et al.* (2013) Cathelicidin-like helminth defence molecules (HDMs): absence of cytotoxic, anti-microbial and anti-protozoan activities imply a specific adaptation to immune modulation. *PLOS Neg Trop Dis* 7(7), pp. e2307. DOI: 10.1371/journal.pntd.0002307.

283. Pankao, V., Sirisriro, A., Grams, R. *et al.* (2006) Classification of the parenchymal cells in *Fasciola gigantica* based on ultrastructure and their expression of fatty acid binding proteins (FABPs). *Vet Parasitol* 142(3-4), pp. 281–292. DOI: 10.1016/j.vetpar.2006.07.009.

284. Nebert, D. W. & Vasiliou, V. (2004) Analysis of the glutathione S-transferase (GST) gene family. *Hum Genomics* 1(6), pp. 460–464. DOI: 10.1186/1479-7364-1-6-460.

285. Chemale, G., Morphew, R., Moxon, J. V. *et al.* (2006) Proteomic analysis of glutathione transferases from the liver fluke parasite, *Fasciola hepatica*. *Proteomics* 6(23), pp. 6263–6273. DOI: 10.1002/pmic.200600499.

286. Morphew, R. M., Eccleston, N., Wilkinson, T. J. *et al.* (2012) Proteomics and *in silico* approaches to extend understanding of the glutathione transferase superfamily of the tropical liver fluke *Fasciola gigantica*. *J Proteome Res* 11(12), pp. 5876–5889. DOI: 10.1021/pr300654w.

287. Stuart, R. B., Zwaanswijk, S., MacKintosh, N. D. *et al.* (2021) The soluble glutathione transferase superfamily: role of Mu class in triclabendazole sulphoxide challenge in *Fasciola hepatica*. *Parasitol Res* 120(3), pp. 979–991. DOI: 10.1007/s00436-021-07055-5.

288. Davey, S. D., Chalmers, I. W., Fernandez-Fuentes, N. *et al.* (2022) *In silico* characterisation of the complete Ly6 protein family in *Fasciola gigantica* supported through transcriptomics of the newly-excysted juveniles. *Mol Omics* 18(1), pp. 45–56. DOI: 10.1039/D1MO00254F.

289. Bodian, D. L., Davis, S. J., Morgan, B. P. *et al.* (1997) Mutational analysis of the active site and antibody epitopes of the complement-inhibitory glycoprotein, CD59. *J Exp Med* 185(3), pp. 507–516. DOI: 10.1084/jem.185.3.507.

290. Cai, X., Hou, L., Su, N. *et al.* (2010) Systematic identification of conserved motif modules in the human genome. *BMC Genomics* 11(1):567. DOI: 10.1186/1471-2164-11-567.

291. Braschi, S., Curwen, R. S., Ashton, P. D. *et al.* (2006) The tegument surface membranes of the human blood parasite *Schistosoma mansoni*: a proteomic analysis after differential extraction. *Proteomics* 6(5), pp. 1471–1482. DOI: 10.1002/pmic.200500368.

292. Hahnel, S., Lu, Z., Wilson, R. A. *et al.* (2013) Whole-organ isolation approach as a basis for tissue-specific analyses in *Schistosoma mansoni*. *PLOS Neg Trop Dis* 7(7):e2336. DOI: 10.1371/journal.pntd.0002336.

293. Airs, P. M., Vaccaro, K., Gallo, K. J. *et al.* (2022) Spatial transcriptomics reveals antiparasitic targets associated with essential behaviors in the human parasite *Brugia malayi*. *PLOS Pathog* 18(4):e1010399. DOI: 10.1371/journal.ppat.1010399.

294. Gobert, G. N., McManus, D. P., Nawaratna, S. *et al.* (2009) Tissue specific profiling of females of *Schistosoma japonicum* by integrated laser microdissection microscopy and microarray analysis. *PLOS Neg Trop Dis* 3(6):e469. DOI: 10.1371/journal.pntd.0000469.

295. Chen, T.-Y., You, L., Hardillo, J. A. U. *et al.* (2023) Spatial transcriptomic technologies. *Cells* 12(16):2042. DOI: 10.3390/cells12162042.

296. Sounart, H., Voronin, D., Masarapu, Y. *et al.* (2023) Miniature spatial transcriptomics for studying parasite-endosymbiont relationships at the micro scale. *Nat Commun* 14(1):6500. DOI: 10.1038/s41467-023-42237-y.

297. Cui, G., Dong, K., Zhou, J.-Y. *et al.* (2023) Spatiotemporal transcriptomic atlas reveals the dynamic characteristics and key regulators of planarian regeneration. *Nat Commun* 14(1):3205. DOI: 10.1038/s41467-023-39016-0.

298. Schroeder, A., Mueller, O., Stocker, S. *et al.* (2006) The RIN: an RNA integrity number for assigning integrity values to RNA measurements. *BMC Mol Biol* 7(1):3. DOI: 10.1186/1471-2199-7-3.

299. Haçarız, O. & Sayers, G. (2013) *Fasciola hepatica* - where is 28S ribosomal RNA? *Exp Parasitol* 135(2), pp. 426–429. DOI: 10.1016/j.exppara.2013.07.026.

300. 10x Genomics: Visium Spatial Tissue Optimization User Guide. User Guide. CG000238, RevD. Available at https://cdn.10xgenomics.com/image/upload/v1660261286/support-documents/CG000238_VisiumSpatialTissueOptimizationUserGuide_RevE.pdf (updated version) (13.04.2021).

301. Lopez, M. E. (2014) Combined *in situ* hybridization/immunohistochemistry (ISH/IH) on free-floating vibratome tissue sections. *Bio Protoc* 4(18):e1243. DOI: 10.21769/bioprotoc.1243.

302. Smith, A. M., Dowd, A. J., Heffernan, M. *et al.* (1993) *Fasciola hepatica*: A secreted cathepsin L-like proteinase cleaves host immunoglobulin. *Int J Parasitol* 23(8), pp. 977–983. DOI: 10.1016/0020-7519(93)90117-h.

303. Changklungmoa, N., Chaithirayanon, K., Kueakhai, P. *et al.* (2012) Molecular cloning and characterization of leucine aminopeptidase from *Fasciola gigantica*. *Exp Parasitol* 131(3), pp. 283–291. DOI: 10.1016/j.exppara.2012.04.008.

304. Adisakwattana, P., Viyanant, V., Chaicumpa, W. *et al.* (2007) Comparative molecular analysis of two asparaginyl endopeptidases and encoding genes from *Fasciola gigantica*. *Mol Biochem Parasitol* 156(2), pp. 102–116. DOI: 10.1016/j.molbiopara.2007.07.006.

305. Cabán-Hernández, K. & Espino, A. M. (2013) Differential expression and localization of saposin-like protein 2 of *Fasciola hepatica*. *Acta Trop* 128(3), pp. 591–597. DOI: 10.1016/j.actatropica.2013.08.012.

306. Vichasri-Grams, S., Subpipattana, P., Sobhon, P. *et al.* (2006) An analysis of the calcium-binding protein 1 of *Fasciola gigantica* with a comparison to its homologs in the phylum Platyhelminthes. *Mol Biochem Parasitol* 146(1), pp. 10–23. DOI: 10.1016/j.molbiopara.2005.10.012.

307. Rice-Ficht, A. C., Dusek, K. A., Kochevar, G. J. *et al.* (1992) Eggshell precursor proteins of *Fasciola hepatica*, I. Structure and expression of vitelline protein B. *Mol Biochem Parasitol* 54(2), pp. 129–141. DOI: 10.1016/0166-6851(92)90106-T.

308. Luo, M., Yang, F., Leu, N. A. *et al.* (2013) MEIOB exhibits single-stranded DNA-binding and exonuclease activities and is essential for meiotic recombination. *Nat Commun* 4(1):2788. DOI: 10.1038/ncomms3788.

309. Wang, Y., Liu, L., Tan, C. *et al.* (2022) Novel MEIOB variants cause primary ovarian insufficiency and non-obstructive azoospermia. *Front Genet* 13:936264. DOI: 10.3389/fgene.2022.936264.

310. Moescheid, M. F., Lu, Z., Soria, C. D. *et al.* (2025) The retinoic acid family-like nuclear receptor SmRAR identified by single-cell transcriptomics of ovarian cells controls oocyte differentiation in *Schistosoma mansoni*. *Nucleic Acids Res* 53(4):gkae1228. DOI: 10.1093/nar/gkae1228.

311. Cassandri, M., Smirnov, A., Novelli, F. *et al.* (2017) Zinc-finger proteins in health and disease. *Cell Death Discov* 3(1):17071. DOI: 10.1038/cddiscovery.2017.71.

312. Ling, A. S., Trotter, J. R. & Hendriks, E. F. (2011) A zinc finger protein, TbZC3H20, stabilizes two developmentally regulated mRNAs in trypanosomes. *J Biol Chem* 286(23), pp. 20152–20162. DOI: 10.1074/jbc.M110.139261.

313. Lai, W. S., Carballo, E., Thorn, J. M. *et al.* (2000) Interactions of CCCH zinc finger proteins with mRNA. Binding of tristetraprolin-related zinc finger proteins to AU-rich elements and destabilization of mRNA. *J Biol Chem* 275(23), pp. 17827–17837. DOI: 10.1074/jbc.M001696200.

314. Taylor, G. A., Carballo, E., Lee, D. M. *et al.* (1996) A pathogenetic role for TNF alpha in the syndrome of cachexia, arthritis, and autoimmunity resulting from tristetraprolin (TTP) deficiency. *Immunity* 4(5), pp. 445–454. DOI: 10.1016/s1074-7613(00)80411-2.

315. Bell, S. E., Sanchez, M. J., Spasic-Boskovic, O. *et al.* (2006) The RNA binding protein Zfp36l1 is required for normal vascularisation and post-transcriptionally regulates VEGF expression. *Dev Dyn* 235(11), pp. 3144–3155. DOI: 10.1002/dvdy.20949.

316. Stumpo, D. J., Broxmeyer, H. E., Ward, T. *et al.* (2009) Targeted disruption of Zfp36l2, encoding a CCCH tandem zinc finger RNA-binding protein, results in defective hematopoiesis. *Blood* 114(12), pp. 2401–2410. DOI: 10.1182/blood-2009-04-214619.

317. De, J., Lai, W. S., Thorn, J. M. *et al.* (1999) Identification of four CCCH zinc finger proteins in *Xenopus*, including a novel vertebrate protein with four zinc fingers and severely restricted expression. *Gene* 228(1-2), pp. 133–145. DOI: 10.1016/s0378-1119(98)00617-9.

318. Belloc, E. & Méndez, R. (2008) A deadenylation negative feedback mechanism governs meiotic metaphase arrest. *Nature* 452(7190), pp. 1017–1021. DOI: 10.1038/nature06809.

319. Ramos, S. B. V., Stumpo, D. J., Kennington, E. A. *et al.* (2004) The CCCH tandem zinc-finger protein Zfp36l2 is crucial for female fertility and early embryonic development. *Development* 131(19), pp. 4883–4893. DOI: 10.1242/dev.01336.

320. Gasic, I. (2022) Regulation of tubulin gene expression: From isotype identity to functional specialization. *Front Cell Dev Biol* 10:898076. DOI: 10.3389/fcell.2022.898076.

321. Raff, E. C., Fackenthal, J. D., Hutchens, J. A. *et al.* (1997) Microtubule architecture specified by a beta-tubulin isoform. *Science* 275(5296), pp. 70–73. DOI: 10.1126/science.275.5296.70.

322. Ludueña, R. F. (1998) Multiple forms of tubulin: different gene products and covalent modifications. *Int Rev Cytol* 178, pp. 207–275. DOI: 10.1016/s0074-7696(08)62138-5.

323. Vent, J., Wyatt, T. A., Smith, D. D. *et al.* (2005) Direct involvement of the isotype-specific C-terminus of beta tubulin in ciliary beating. *J Cell Sci* 118(19), pp. 4333–4341. DOI: 10.1242/jcs.02550.

324. Smyth, J. D. & Clegg, J. A. (1959) Egg-shell formation in trematodes and cestodes. *Exp Parasitol* 8(3), pp. 286–323. DOI: 10.1016/0014-4894(59)90027-X.

325. Rao, K. H. (1959) Observations on the Mehlis' gland complex in the liver fluke *Fasciola hepatica* L. *J Parasitol* 45(3), pp. 347–351.

326. Gönnert, A. (1962) Histologische Untersuchungen über den Feinbau der Eibildungsstätte (Oogenotop) von *Fasciola hepatica*. *Z Parasitenkd* 12, pp. 475–492. DOI: 10.1007/BF00260252.

327. Wells, K. E. & Cordingley, J. S. (1991) *Schistosoma mansoni:* Eggshell formation is regulated by pH and calcium. *Exp Parasitol* 73(3), pp. 295–311. DOI: 10.1016/0014-4894(91)90101-2.

328. Homma, Y., Hiragi, S. & Fukuda, M. (2021) Rab family of small GTPases: an updated view on their regulation and functions. *FEBS J* 288(1), pp. 36–55. DOI: 10.1111/febs.15453.

329. Takai, Y., Sasaki, T. & Matozaki, T. (2001) Small GTP-binding proteins. *Physiol Rev* 81(1), pp. 153–208. DOI: 10.1152/physrev.2001.81.1.153.

330. Honoré, B. (2009) The rapidly expanding CREC protein family: members, localization, function, and role in disease. *BioEssays* 31(3), pp. 262–277. DOI: 10.1002/bies.200800186.

331. Wang, J. & Collins, J. J. (2016) Identification of new markers for the *Schistosoma mansoni* vitelline lineage. *Int J Parasitol* 46(7), pp. 405–410. DOI: 10.1016/j.ijpara.2016.03.004.

332. Threadgold, L. T. & Irwin, S. (1970) Electron microscope studies of *Fasciola hepatica*. IX. The fine structure of Mehlis' gland. *Z Parasitenkd* 35(1), pp. 16–30. DOI: 10.1007/BF00259527.

333. Verdier, J., Luedde, T. & Sellge, G. (2015) Biliary mucosal barrier and microbiome. *Viszeralmedizin* 31(3), pp. 156–161. DOI: 10.1159/000431071.

334. Gao, L., Han, Y., Deng, H. *et al.* (2017) The role of a novel C-type lectin-like protein from planarian in innate immunity and regeneration. *Dev Comp Immunol* 67, pp. 413–426. DOI: 10.1016/j.dci.2016.08.010.

335. Clancy, S. M., Whitehead, M., Oliver, N. A. M. *et al.* (2025) The *Calicophoron daubneyi* genome provides new insight into mechanisms of feeding, eggshell synthesis and parasite-microbe interactions. *BMC Biol* 23(1):11. DOI: 10.1186/s12915-025-02114-0.

336. Pukkila-Worley, R. & Ausubel, F. M. (2012) Immune defense mechanisms in the *Caenorhabditis elegans* intestinal epithelium. *Curr Opin Immunol* 24(1), pp. 3–9. DOI: 10.1016/j.coi.2011.10.004.

337. Capo, F., Wilson, A. & Di Cara, F. (2019) The intestine of *Drosophila melanogaster*: An emerging versatile model system to study intestinal epithelial homeostasis and host-microbial interactions in humans. *Microorganisms* 7(9):336. DOI: 10.3390/microorganisms7090336.

338. Kangale, L. J., Raoult, D., Fournier, P.-E. *et al.* (2021) Planarians (Platyhelminthes) - An emerging model organism for investigating innate immune mechanisms. *Front Cell Infect Microbiol* 11:619081. DOI: 10.3389/fcimb.2021.619081.

339. Arancibia, S. A., Beltrán, C. J., Aguirre, I. M. *et al.* (2007) Toll-like receptors are key participants in innate immune responses. *Biol Res* 40(2), pp. 97–112. DOI: 10.4067/s0716-97602007000200001.

340. Dziarski, R. & Gupta, D. (2006) The peptidoglycan recognition proteins (PGRPs). *Genome Biol* 7(8):232. DOI: 10.1186/gb-2006-7-8-232.

341. Orlans, J., Vincent-Monegat, C., Rahioui, I. *et al.* (2021) PGRP-LB: An inside view into the mechanism of the amidase reaction. *Int J Mol Sci* 22(9):4957. DOI: 10.3390/ijms22094957.

342. Lu, X., Wang, M., Qi, J. *et al.* (2006) Peptidoglycan recognition proteins are a new class of human bactericidal proteins. *J Biol Chem* 281(9), pp. 5895–5907. DOI: 10.1074/jbc.M511631200.

343. Wang, Q., Ren, M., Liu, X. *et al.* (2019) Peptidoglycan recognition proteins in insect immunity. *Mol Immunol* 106, pp. 69–76. DOI: 10.1016/j.molimm.2018.12.021.

344. Jiang, S., Wang, L., Huang, M. *et al.* (2017) DM9 domain containing protein functions as a pattern recognition receptor with broad microbial recognition spectrum. *Front Immunol* 8:1607. DOI: 10.3389/fimmu.2017.01607.

345. Jia, Z., Jiang, S., Wang, M. *et al.* (2020) Identification of a novel pattern recognition receptor DM9 domain containing protein 4 as a marker for pro-hemocyte of Pacific oyster *Crassostrea gigas*. *Front Immunol* 11:603270. DOI: 10.3389/fimmu.2020.603270.

346. Li, Y., Yang, W., Sun, J. *et al.* (2024) A DM9-containing protein from crab *Eriocheir sinensis* functions as a novel multipotent pattern recognition receptor. *Fish Shellfish Immunol* 145:109356. DOI: 10.1016/j.fsi.2023.109356.

347. Phadungsil, W. & Grams, R. (2021) Agglutination activity of *Fasciola gigantica* DM9-1, a mannose-binding lectin. *Korean J Parasitol* 59(2), pp. 173–178. DOI: 10.3347/kjp.2021.59.2.173.

348. Silva-Caso, W., Carrillo-Ng, H., Aguilar-Luis, M. A. *et al.* (2024) Parasitosis by *Fasciola hepatica* and variations in gut microbiota in school-aged children from Peru. *Microorganisms* 12(2):371. DOI: 10.3390/microorganisms12020371.

349. Brosschot, T. P. & Reynolds, L. A. (2018) The impact of a helminth-modified microbiome on host immunity. *Mucosal Immunol* 11(4), pp. 1039–1046. DOI: 10.1038/s41385-018-0008-5.

350. Dan, W.-Y., Yang, Y.-S., Peng, L.-H. *et al.* (2023) Gastrointestinal microbiome and cholelithiasis: Current status and perspectives. *World J Gastroenterol* 29(10), pp. 1589–1601. DOI: 10.3748/wjg.v29.i10.1589.

351. Ardelli, B. F., Stitt, L. E. & Tompkins, J. B. (2010) Inventory and analysis of ATP-binding cassette (ABC) systems in *Brugia malayi*. *Parasitology* 137(8), pp. 1195–1212. DOI: 10.1017/S0031182010000120.

352. Alam, A. & Locher, K. P. (2023) Structure and mechanism of human ABC transporters. *Annu Rev Biophys* 52, pp. 275–300. DOI: 10.1146/annurev-biophys-111622-091232.

353. Savage, J., Meaney, M., Brennan, G. P. *et al.* (2013) Increased action of triclabendazole (TCBZ) *in vitro* against a TCBZ-resistant isolate of *Fasciola hepatica* following its co-incubation with the P-glycoprotein inhibitor, R(+)-verapamil. *Exp Parasitol* 135(3), pp. 642–653. DOI: 10.1016/j.exppara.2013.09.015.

354. Greenberg, R. M. (2014) Schistosome ABC multidrug transporters: from pharmacology to physiology. *Int J Parasitol Drugs Drug Resist* 4(3), pp. 301–309. DOI: 10.1016/j.ijpddr.2014.09.007.

355. Toner, E., Brennan, G. P., McConvery, F. *et al.* (2010) A transmission electron microscope study on the route of entry of triclabendazole into the liver fluke, *Fasciola hepatica*. *Parasitology* 137(5), pp. 855–870. DOI: 10.1017/S0031182009991247.

356. Morawietz, C. M., Peter Ventura, A. M., Grevelding, C. G. *et al.* (2022) Spatial visualization of drug uptake and distribution in *Fasciola hepatica* using high-resolution AP-SMALDI mass spectrometry imaging. *Parasitol Res* 121(4), pp. 1145–1153. DOI: 10.1007/s00436-021-07388-1.

357. Wilkinson, R., Law, C. J., Hoey, E. M. *et al.* (2012) An amino acid substitution in *Fasciola hepatica* P-glycoprotein from triclabendazole-resistant and triclabendazole-susceptible populations. *Mol Biochem Parasitol* 186(1), pp. 69–72. DOI: 10.1016/j.molbiopara.2012.08.008.

358. Choi, Y.-J., Rosa, B. A., Fernandez-Baca, M. V. *et al.* (2025) Independent origins and non-parallel selection signatures of triclabendazole resistance in *Fasciola hepatica*. *Nat Commun* 16(1), pp. 2996. DOI: 10.1038/s41467-025-57796-5.

359. Howell, M. K. & Board, P.G., Boray, J.C. (1988) Glutathione S-transferases in *Fasciola hepatica*. *J Parasitol* 74(4), pp. 715–718.

360. Wijffels, G. L., Sexton, J. L., Salvatore, L. *et al.* (1992) Primary sequence heterogeneity and tissue expression of glutathione S-transferases of *Fasciola hepatica*. *Exp Parasitol* 74(1), pp. 87–99. DOI: 10.1016/0014-4894(92)90142-W.

361. Creaney, J., Wijffels, G. L., Sexton, J. L. *et al.* (1995) *Fasciola hepatica*: Localisation of glutathione S-transferase isoenzymes in adult and juvenile liver fluke. *Exp Parasitol* 81(1), pp. 106–116. DOI: 10.1006/expr.1995.1098.

362. Ravidà, A., Cwiklinski, K., Aldridge, A. M. *et al.* (2016) *Fasciola hepatica* surface tegument: Glycoproteins at the interface of parasite and host. *Mol Cell Proteom* 15(10), pp. 3139–3153. DOI: 10.1074/mcp.M116.059774.

363. La Torre-Escudero, E. de, Gerlach, J. Q., Bennett, A. P. S. *et al.* (2019) Surface molecules of extracellular vesicles secreted by the helminth pathogen *Fasciola hepatica* direct their internalisation by host cells. *PLOS Neg Trop Dis* 13(1):e0007087. DOI: 10.1371/journal.pntd.0007087.

364. Martin, I., Cabán-Hernández, K., Figueroa-Santiago, O. *et al.* (2015) *Fasciola hepatica* fatty acid binding protein inhibits TLR4 activation and suppresses the inflammatory cytokines induced by lipopolysaccharide *in vitro* and *in vivo*. *J Immunol* 194(8), pp. 3924–3936. DOI: 10.4049/jimmunol.1401182.

365. McCusker, P., Toet, H., Rathinasamy, V. *et al.* (2020) Molecular characterisation and vaccine efficacy of two novel developmentally regulated surface tegument proteins of *Fasciola hepatica*. *Vet Parasitol* 286:109244. DOI: 10.1016/j.vetpar.2020.109244.

366. Das, K. C., Konhar, R. & Biswal, D. K. (2023) *Fasciola gigantica* vaccine construct: an *in silico* approach towards identification and design of a multi-epitope subunit vaccine using calcium binding EF-hand proteins. *BMC Immunol* 24(1):1. DOI: 10.1186/s12865-022-00535-y.

367. Loughner, C. L., Bruford, E. A., McAndrews, M. S. *et al.* (2016) Organization, evolution and functions of the human and mouse Ly6/uPAR family genes. *Hum Genomics* 10:10. DOI: 10.1186/s40246-016-0074-2.

368. Davies, A., Simmons, D. L., Hale, G. *et al.* (1989) CD59, an LY-6-like protein expressed in human lymphoid cells, regulates the action of the complement membrane attack complex on homologous cells. *J Exp Med* 170(3), pp. 637–654. DOI: 10.1084/jem.170.3.637.

369. AlHossiny, M., Luo, L., Frazier, W. R. *et al.* (2016) Ly6E/K signaling to TGFβ promotes breast cancer progression, immune escape, and drug resistance. *Cancer Res* 76(11), pp. 3376–3386. DOI: 10.1158/0008-5472.CAN-15-2654.

370. Hailin, L., Yiting, C., Yue, W. *et al.* (2024) Ly6E on tumor cells impairs anti-tumor T-cell responses: a novel mechanism of tumor-induced immune exclusion. *Cancer Immunol Immunother* 74(1):4. DOI: 10.1007/s00262-024-03851-x.

371. Shi, Y., Toet, H., Rathinasamy, V. *et al.* (2014) First insight into CD59-like molecules of adult *Fasciola hepatica*. *Exp Parasitol* 144, pp. 57–64. DOI: 10.1016/j.exppara.2014.06.012.

372. Farias, L. P., Krautz-Peterson, G., Tararam, C. A. *et al.* (2013) On the three-finger protein domain fold and CD59-like proteins in *Schistosoma mansoni*. *PLOS Neg Trop Dis* 7(10):e2482. DOI: 10.1371/journal.pntd.0002482.

373. Chalmers, I. W., Fitzsimmons, C. M., Brown, M. *et al.* (2015) Human IgG1 responses to surface localised *Schistosoma mansoni* Ly6 family members drop following praziquantel treatment. *PLOS Neg Trop Dis* 9(7):e0003920. DOI: 10.1371/journal.pntd.0003920.

374. Cardoso, F. C., Macedo, G. C., Gava, E. *et al.* (2008) *Schistosoma mansoni* tegument protein Sm29 is able to induce a Th1-type of immune response and protection against parasite infection. *PLOS Neg Trop Dis* 2(10):e308. DOI: 10.1371/journal.pntd.0000308.

375. Graham, M. K., Fairweather, I. & McGeown, J. G. (2000) Second messengers mediating mechanical responses to the FARP GYIRFamide in the fluke *Fasciola hepatica*. *Am J Physiol Regul Integr Comp Physiol* 279(6):R2089-94. DOI: 10.1152/ajpregu.2000.279.6.R2089.

376. Ressurreição, M., Saram, P. de, Kirk, R. S. *et al.* (2014) Protein kinase C and extracellular signal-regulated kinase regulate movement, attachment, pairing and egg release in *Schistosoma mansoni*. *PLOS Neg Trop Dis* 8(6):e2924. DOI: 10.1371/journal.pntd.0002924.

377. Javey, G., Schwartz, S. G., Flynn, H. W. *et al.* (2010) Ruboxistaurin: review of safety and efficacy in the treatment of diabetic retinopathy. *Clin Med Insights Ther* 2. DOI: 10.4137/CMT.S5046.

378. Burkey, J. L., Campanale, K. M., Barbuch, R. *et al.* (2006) Disposition of 14Cruboxistaurin in humans. *Drug Metab Dispos* 34(11), pp. 1909–1917. DOI: 10.1124/dmd.106.009894.

379. Hennessy, D. R., Lacey, E., Steel, J. W. *et al.* (1987) The kinetics of triclabendazole disposition in sheep. *J Vet Pharmacol Ther* 10(1), pp. 64–72. DOI: 10.1111/j.1365-2885.1987.tb00078.x.

380. McGonigle, L., Mousley, A., Marks, N. J. *et al.* (2008) The silencing of cysteine proteases in *Fasciola hepatica* newly excysted juveniles using RNA interference reduces gut penetration. *Int J Parasitol* 38(2), pp. 149–155. DOI: 10.1016/j.ijpara.2007.10.007.

381. Davies, C. & Smyth, J. D. (1978) *In vitro* cultivation of *Fasciola hepatica* metacercariae and of partially developed flukes recovered from mice. *Int J Parasitol* 8(2), pp. 125–131. DOI: 10.1016/0020-7519(78)90006-1.

382. Smith, M. A. & Clegg, J. A. (1981) Improved culture of *Fasciola hepatica in vitro*. *Parasitol Res* 66(1), pp. 9–15. DOI: 10.1007/BF00941940.

383. Ractliffe, L. H., Guevara-Pozo, D. & Lopez-Roman, R. (1969) *In vitro* maintenance of *Fasciola hepatica*: a factorial approach based on egg production. *Exp Parasitol* 26(1), pp. 41–51. DOI: 10.1016/0014-4894(69)90093-9.

384. Nims, R. W. & Harbell, J. W. (2017) Best practices for the use and evaluation of animal serum as a component of cell culture medium. *In Vitro Cell Dev Biol Anim* 53(8), pp. 682–690. DOI: 10.1007/s11626-017-0184-8.

385. Boffito, M., Back, D. J., Flexner, C. *et al.* (2021) Toward consensus on correct interpretation of protein binding in plasma and other biological matrices for COVID-19 therapeutic development. *Clin Pharmacol Ther* 110(1), pp. 64–68. DOI: 10.1002/cpt.2099.

386. Douthart, R. J. & Burgett, S. G. (1978) Enzymatic degradation by the sera of various animal species of *Penicillium chrysogenum* mycophage double-stranded RNA. *Biochem Biophys Res Commun* 84(3), pp. 809–815. DOI: 10.1016/0006-291X(78)90776-3.

387. Huppi, K., Martin, S. E. & Caplen, N. J. (2005) Defining and assaying RNAi in mammalian cells. *Mol Cell* 17(1), pp. 1–10. DOI: 10.1016/j.molcel.2004.12.017.

388. Rinaldi, G., Dell'Oca, N., Castillo, E. *et al.* (2020) Gene silencing in the liver fluke *Fasciola hepatica*: RNA interference. In: M. Cancela & G. Maggioli (eds). *Fasciola hepatica:* Methods and protocols. Methods in Molecular Biology Vol. 2137. pp. 67–92. *Humana, New York, NY*. DOI: 10.1007/978-1-0716-0475-5_6.

389. Beutler, M., Harnischfeger, J., Weber, M. H. W. *et al.* (2023) Identification and characterisation of the tegument-expressed aldehyde dehydrogenase SmALDH_312 of *Schistosoma mansoni*, a target of disulfiram. *Eur J Med Chem* 251:115179. DOI: 10.1016/j.ejmech.2023.115179.

390. Pfarr, K., Heider, U. & Hoerauf, A. (2006) RNAi mediated silencing of actin expression in adult *Litomosoides sigmodontis* is specific, persistent and results in a phenotype. *Int J Parasitol* 36(6), pp. 661–669. DOI: 10.1016/j.ijpara.2006.01.010.

391. Grimm, D., Streetz, K. L., Jopling, C. L. *et al.* (2006) Fatality in mice due to oversaturation of cellular microRNA/short hairpin RNA pathways. *Nature* 441(7092), pp. 537–541. DOI: 10.1038/nature04791.

392. Stefanić, S., Dvořák, J., Horn, M. *et al.* (2010) RNA interference in *Schistosoma mansoni* schistosomula: selectivity, sensitivity and operation for larger-scale screening. *PLOS Neg Trop Dis* 4(10):e850. DOI: 10.1371/journal.pntd.0000850.

393. Garber, K. (2017) Worth the RISC? *Nat Biotechnol* 35(3), pp. 198–202. DOI: 10.1038/nbt.3810.

394. Moescheid, M. F., Puckelwaldt, O., Beutler, M. *et al.* (2023) Defining an optimal control for RNAi experiments with adult *Schistosoma mansoni*. *Sci Rep* 13(1):9766. DOI: 10.1038/s41598-023-36826-6.

395. Gava, S. G., Tavares, N. C., Salim, Anna Christina de Matos *et al.* (2017) *Schistosoma mansoni*: off-target analyses using nonspecific double-stranded RNAs as control for RNAi experiments in schistosomula. *Exp Parasitol* 177, pp. 98–103. DOI: 10.1016/j.exppara.2017.04.011.

396. Collins, J. J., Wang, B., Lambrus, B. G. *et al.* (2013) Adult somatic stem cells in the human parasite *Schistosoma mansoni*. *Nature* 494(7438), pp. 476–479. DOI: 10.1038/nature11924.

397. Chen, L., Toke, N. H., Luo, S. *et al.* (2019) HNF4 factors control chromatin accessibility and are redundantly required for maturation of the fetal intestine. *Development* 146(19):dev179432. DOI: 10.1242/dev.179432.

398. Choi, H. M. T., Beck, V. A. & Pierce, N. A. (2014) Next-generation *in situ* hybridization chain reaction: higher gain, lower cost, greater durability. *ACS Nano* 8(5), pp. 4284–4294. DOI: 10.1021/nn405717p.

399. Reddien, P. W. (2018) The cellular and molecular basis for planarian regeneration. *Cell* 175(2), pp. 327–345. DOI: 10.1016/j.cell.2018.09.021.

400. Barberán, S., Fraguas, S. & Cebrià, F. (2016) The EGFR signaling pathway controls gut progenitor differentiation during planarian regeneration and homeostasis. *Development* 143(12), pp. 2089–2102. DOI: 10.1242/dev.131995.

401. Hanna, R. E. B., Brennan, G. P., Robinson, M. W. *et al.* (2024) *Fasciola gigantica*: ultrastructural localisation of neoblast recruitment in somatic tissues during growth and development in the hepatic parenchyma of experimentally infected mice. *Vet Parasitol* 330:110244. DOI: 10.1016/j.vetpar.2024.110244.

402. Bennett, C. E. (1975) *Fasciola hepatica*: development of caecal epithelium during migration in the mouse. *Exp Parasitol* 37(3), pp. 426–441. DOI: 10.1016/0014-4894(75)90013-2.

403. Rieger, R. M., Legniti, A., Ladurner, P. *et al.* (1999) Ultrastructure of neoblasts in microturbellaria: significance for understanding stem cells in free-living Platyhelminthes. *Invertebr Reprod Dev* 35(2), pp. 127–140. DOI: 10.1080/07924259.1999.9652376.

404. Bode, A., Salvenmoser, W., Nimeth, K. *et al.* (2006) Immunogold-labeled S-phase neoblasts, total neoblast number, their distribution, and evidence for arrested neoblasts in *Macrostomum lignano* (Platyhelminthes, Rhabditophora). *Cell Tissue Res* 325(3), pp. 577–587. DOI: 10.1007/s00441-006-0196-2.

405. Gąsiorowski, L., Chai, C., Rozanski, A. *et al.* (2025) Regeneration in the absence of canonical neoblasts in an early branching flatworm. *Nat Commun* 16(1):1232. DOI: 10.1038/s41467-024-54716-x.

406. Robinson, M. W., Tort, J. F., Lowther, J. *et al.* (2008) Proteomics and phylogenetic analysis of the cathepsin L protease family of the helminth pathogen *Fasciola hepatica*: expansion of a repertoire of virulence-associated factors. *Mol Cell Proteom* 7(6), pp. 1111–1123. DOI: 10.1074/mcp.M700560-MCP200.

407. Irving, J. A., Spithill, T. W., Pike, R. N. *et al.* (2003) The evolution of enzyme specificity in *Fasciola* spp. *J Mol Evol* 57(1), pp. 1–15. DOI: 10.1007/s00239-002-2434-x.

408. Tort, J., Brindley, P. J., Knox, D. *et al.* (1999) Proteinases and associated genes of parasitic helminths. *Adv Parasitol* 43, pp. 161–266. DOI: 10.1016/s0065-308x(08)60243-2.

409. Dalton, J. P., Caffrey, C. R., Sajid, M. *et al.* (2006) Proteases in trematode biology. In: A. G. Maule & N. J. Marks (eds). Parasitic flatworms. Molecular biology, biochemistry, immunology and physiology. pp. 348–368. *CABI, Wallingford, UK*. DOI: 10.1079/9780851990279.0348.

410. Morris, G. P. (1968) Fine structure of the gut epithelium of *Schistosoma mansoni*. *Experientia* 24(5), pp. 480–482. DOI: 10.1007/BF02144405.

411. Friedman, J. R. & Kaestner, K. H. (2006) The Foxa family of transcription factors in development and metabolism. *Cell Mol Life Sci* 63(19-20), pp. 2317–2328. DOI: 10.1007/s00018-006-6095-6.

412. Liu, N., Wang, A., Xue, M. *et al.* (2024) FOXA1 and FOXA2: the regulatory mechanisms and therapeutic implications in cancer. *Cell Death Discov* 10(1):172. DOI: 10.1038/s41420-024-01936-1.

413. Adler, C. E., Seidel, C. W., McKinney, S. A. *et al.* (2014) Selective amputation of the pharynx identifies a FoxA-dependent regeneration program in planaria. *eLife* 3:e02238. DOI: 10.7554/eLife.02238.

414. Lee, J., Chong, T. & Newmark, P. A. (2020) The esophageal gland mediates host immune evasion by the human parasite *Schistosoma mansoni*. *PNAS* 117(32), pp. 19299–19309. DOI: 10.1073/pnas.2006553117.

415. Reizel, Y., Morgan, A., Gao, L. *et al.* (2020) Collapse of the hepatic gene regulatory network in the absence of FoxA factors. *Genes Dev* 34(15-16), pp. 1039–1050. DOI: 10.1101/gad.337691.120.

416. Horisawa, K., Udono, M., Ueno, K. *et al.* (2020) The dynamics of transcriptional activation by hepatic reprogramming factors. *Mol Cell* 79(4), pp. 660-676. DOI: 10.1016/j.molcel.2020.07.012.

417. Gosalia, N., Yang, R., Kerschner, J. L. *et al.* (2015) FOXA2 regulates a network of genes involved in critical functions of human intestinal epithelial cells. *Physiol Genomics* 47(7), pp. 290–297. DOI: 10.1152/physiolgenomics.00024.2015.

418. Poulet, A., Kratkiewicz, A. J., Li, D. *et al.* (2023) Chromatin analysis of adult pluripotent stem cells reveals a unique stemness maintenance strategy. *Sci Adv* 9(40):eadh4887. DOI: 10.1126/sciadv.adh4887.

419. Neiro, J., Sridhar, D., Dattani, A. *et al.* (2022) Identification of putative enhancer-like elements predicts regulatory networks active in planarian adult stem cells. *eLife* 11:e79675. DOI: 10.7554/eLife.79675.

420. Stegmann, A., Hansen, M., Wang, Y. *et al.* (2006) Metabolome, transcriptome, and bioinformatic cis-element analyses point to HNF-4 as a central regulator of gene expression during enterocyte differentiation. *Physiol Genomics* 27(2), pp. 141–155. DOI: 10.1152/physiolgenomics.00314.2005.

421. Li, X., Madison, B. B., Zacharias, W. *et al.* (2007) Deconvoluting the intestine: molecular evidence for a major role of the mesenchyme in the modulation of signaling cross talk. *Physiol Genomics* 29(3), pp. 290–301. DOI: 10.1152/physiolgenomics.00269.2006.

422. Geertz, M. & Maerkl, S. J. (2010) Experimental strategies for studying transcription factor-DNA binding specificities. *Brief Funct Genomics* 9(5-6), pp. 362–373. DOI: 10.1093/bfgp/elq023.

423. Meijer, I., Willems, S., Ni, X. *et al.* (2020) Chemical starting matter for HNF4α ligand discovery and chemogenomics. *Int J Mol Sci* 21(21):7895. DOI: 10.3390/ijms21217895.

424. Sang, L., Wang, X., Bai, W. *et al.* (2022) The role of hepatocyte nuclear factor 4α (HNF4α) in tumorigenesis. *Front Oncol* 12:1011230. DOI: 10.3389/fonc.2022.1011230.

425. Chang, H. R., Nam, S., Kook, M.-C. *et al.* (2016) HNF4α is a therapeutic target that links AMPK to WNT signalling in early-stage gastric cancer. *Gut* 65(1), pp. 19–32. DOI: 10.1136/gutjnl-2014-307918.

426. Hwang-Verslues, W. W. & Sladek, F. M. (2010) HNF4α - role in drug metabolism and potential drug target? *Curr Opin Pharmacol* 10(6), pp. 698–705. DOI: 10.1016/j.coph.2010.08.010.

427. Da'dara, A. A. & Skelly, P. J. (2012) RNA interference as a tool for drug discovery in parasitic flatworms. In: C. R. Caffrey (ed). Parasitic helminths. Targets, screens, drugs and vaccines. pp. 105–119. Drug discovery in infectious diseases. *Wiley-VCH, Weinheim, DE*. DOI: 10.1002/9783527652969.ch7.

428. Zhong, H., Hou, L., Qin, F. *et al.* (2023) Molecular and functional characterization of *Schistosoma japonicum* annexin A13. *Vet Res* 54(1):116. DOI: 10.1186/s13567-023-01244-z.

429. Cheng, G., Li, X., Qin, F. *et al.* (2019) Functional analysis of the Frzb2 gene in *Schistosoma japonicum*. *Vet Res* 50(1):108. DOI: 10.1186/s13567-019-0716-1.

430. Jadhav, V., Vaishnaw, A., Fitzgerald, K. *et al.* (2024) RNA interference in the era of nucleic acid therapeutics. *Nat Biotechnol* 42(3), pp. 394–405. DOI: 10.1038/s41587-023-02105-y.

431. Sehgal, I., Eells, K. & Hudson, I. (2024) A comparison of currently approved small interfering RNA (siRNA) medications to alternative treatments by costs, indications, and medicaid coverage. *Pharmacy* 12(2). DOI: 10.3390/pharmacy12020058.

432. Rio, D. C. (2013) Expression and purification of active recombinant T7 RNA polymerase from *E. coli*. *Cold Spring Harb Protoc* 2013(11):pdb.prot078527. DOI: 10.1101/pdb.prot078527.

433. Li, X., Weth, O., Haeberlein, S. *et al.* (2023) Molecular characterization of Smtdc-1 and Smddc-1 discloses roles as male-competence factors for the sexual maturation of *Schistosoma mansoni* females. *Front Cell Infect Microbiol* 13:1173557. DOI: 10.3389/fcimb.2023.1173557.

434. Kelley, L. A., Mezulis, S., Yates, C. M. *et al.* (2015) The Phyre2 web portal for protein modeling, prediction and analysis. *Nat Protoc* 10(6), pp. 845–858. DOI: 10.1038/nprot.2015.053.

435. Schindelin, J., Arganda-Carreras, I., Frise, E. *et al.* (2012) Fiji: an open-source platform for biological-image analysis. *Nat Methods* 9(7), pp. 676–682. DOI: 10.1038/nmeth.2019.

5.2 Language tools

In the preparation of this work, I used the DeepL Translate tool in order to improve the readability and language of selected paragraphs. After using this tool, I reviewed and edited the formulations as needed and take full responsibility for the content.

6. SUPPLEMENT

6.1 List of materials

6.1.1 Experimental models: Organisms and strains

Organisms used in this work can be found in Supplementary Table 1.

Supplementary Table 1 Organisms and strains

SPECIES, STRAIN	SOURCE	IDENTIFIER
Rattus norvegicus, Wistar	Janvier Labs	RjHan:WI
Fasciola hepatica, Italian strain	Ridgeway Research	https://ridgewayresearch.co.uk/parasite-diagnostics-laboratory/available-parasites/

6.1.2 Bacterial strains

Bacterial strains used for cloning can be found in Supplementary Table 2.

Supplementary Table 2 Bacterial strains

STRAIN	SUPPLIER	CAT#
NEB 10-beta Competent *E. coli* (High Efficiency)	New England Biolabs	C3019H
NEB 5-alpha Competent *E. coli* (High Efficiency)	New England Biolabs	C2987H

6.1.3 Reagents and chemicals

Reagents and chemicals used in this work can be found in Supplementary Table 3.

Supplementary Table 3 Reagents and chemicals

CHEMICAL	SUPPLIER	CAT#	APPLICATION
Acetic acid	Carl Roth	3738.5	ST (H&E staining), Carmine staining
Agarose	Carl Roth	2267.3	Gel electrophoresis
Agar-Agar	Carl Roth	5210.2	Cloning (Agar plates)
BCIP	Roche	11383221001	CISH
BI6015	Sigma-Aldrich	375240	HNF4 inhibitor
Blocking reagent	Roche	11096176001	ISH
Bovine serum albumin (BSA)	Sigma-Aldrich	A7906	ISH
Carmine (C.I.75470)	Sigma-Aldrich	104175	Carmine staining
Denhardt's solution	Carl Roth	HP33.1	ISH
Dextran sulfate	Carl Roth	5956.4	ISH
Dextran (mini-Ruby)	Invitrogen	D3312	Tegument labelling
Diethyl pyrocarbonate (DEPC)	Carl Roth	K028.1	Preparation of RNase-free water
Digoxigenin-11-UTP	Roche	11209256910	ISH-probe synthesis
Dimethyl sulfoxide (DMSO)	Sigma-Aldrich	D4540	Solvent for compounds

Disodium hydrogen phosphate (Na2HPO4)	Carl Roth	P030.1	Buffer preparation
Dithiothreitol (DTT)	Carl Roth	6908.1	dsRNA synthesis
dNTPs	Solis Biodyne	02-21-0001S	PCR
Eosin Y	Sigma-Aldrich	318906	ST (H&E staining)
Ethanol	Carl Roth	9065.4	ST, Probe & dsRNA synthesis
EDTA	Carl Roth	8043.2	Buffer preparation
EGTA	Sigma Aldrich	M9397	NA/FA fixation
Ethylene glycol	Merck	109621	PCR
Euparal	Carl Roth	7356.1	Carmine staining (Mounting)
Formaldehyde	Carl Roth	4979.1	Fixation
Formamide	Carl Roth	6749.2	ISH
Formamide, deionized	Carl Roth	P040.2	ISH
Formic acid	Thermo Fisher Scientific	270480250	NA/FA fixation
GelRed nucleic acid stain	Biotium	41003	Gel electrophoresis
Glutaraldehyde	Carl Roth	4157.2	TEM
Glycerol	Carl Roth	7530.1	ST & CISH (Mounting), Cloning (Glycerol stock), Loading dye preparation
Haema quick stain (Diff Quick)	Labor + Technik E. Lehmann GmbH	LT 001	Quick staining of cryosections
HEPES	Carl Roth	9105.4	Buffer preparation
Hoechst 33342	Sigma-Aldrich	14533	Fluorescent DNA stain
Hydrochloric acid (HCl)	Carl Roth	9277.1/ T134.1	Buffer preparation
Hydrogen peroxide (H_2O_2)	Carl Roth	8070.2	ISH
Levamisole ((−)-Tetramisole –hydrochloride)	Sigma-Aldrich	L9756	CISH
Lithium chloride (LiCl)	Sigma-Aldrich	L0505	ISH probe & dsRNA synthesis
Magnesium chloride ($MgCl_2$)	Carl Roth	KK36.3	dsRNA synthesis worm immobilization
Magnesium sulfate ($MgSO_4$)	Sigma-Aldrich	M9397	NA/FA fixation
Maleic acid	Sigma-Aldrich	M0375	ISH
Methanol	Carl Roth	4627.1	ST (Fixation), EdU/ dextran staining
NBT	Roche	11383213001	CISH
Nitric acid (HNO_3)	Riedel de Haën	30709	NA/FA fixation
Orange G	Sigma-Aldrich	861286	Gel electrophoresis
Potassium chloride (KCl)	Carl Roth	P017.2	Buffer preparation

Potassium dihydrogen phosphate (KH_2PO_4)	Carl Roth	3904.1	Buffer preparation
Potassium hydroxide (KOH)	Carl Roth	6751.1	Buffer preparation
2-Propanol (Isopropanol)	Carl Roth	7343.1	ST (H&E staining)
RNase AWAY	Thermo Fisher Scientific	7002	RNA work (Decontamination)
ROTIMount FluorCare	Carl Roth	HP19.1	Mounting medium
NTP solution set	New England Biolabs	N0450L	ISH-probe & dsRNA synthesis
Sodium cacodylate	Sigma Aldrich	C0250	TEM
Sodium chloride (NaCl)	Carl Roth	3957.1	Buffer preparation
Sodium hydrogen carbonate ($NaHCO_3$)	Carl Roth	6885.1	Buffer preparation
Sodium hydroxide (NaOH)	Carl Roth	6771.1/ T135.1	Buffer preparation
Sodium hypochlorite	Carl Roth	9062.3	Excystment
Sodium tauroglycocholate	Camlab chemicals	1111693	Excystment
Spermidine	Carl Roth	7161.3	dsRNA synthesis
SPRIselect	Beckmann Coulter	B23317	ST (cDNA cleanup)
D(+)-Saccharose (Sucrose)	Carl Roth	4621.1	Rat infection
Tissue-Tek O.C.T. compound	Sakura Finetek	4583	Worm embedding for cryosectioning
Tri-Sodium citrate 2-hydrate	Carl Roth	3580.1	Buffer preparation
Triclabendazole	Sigma Aldrich	32802	Anthelmintic, positive control
TRIS	Carl Roth	4855.2	Buffer preparation
Triton X-100	Sigma Aldrich	T8787	Buffer preparation
Tween 20	Carl Roth	9127.2	Buffer preparation
Type F Immersion liquid	Leica Microsystems	11513859	CLSM
Yeast RNA	Roche	10109223001	ISH
Water, doubly distilled	Carl Roth	3478.1	PCR

6.1.4 Buffers and solutions

Buffers and solutions used in this work and their composition can be found in Supplementary Table 4.

Supplementary Table 4 Buffers and solutions

SOLUTION/BUFFER	COMPOSITION	APPLICATION
Acidic ethanol	70% (v/v) EtOH 2.5% (v/v) HCl (37%) in ddH_2O	Carmine staining
AFA	2% (v/v) acetic acid 1.1% (v/v) formaldehyde 66.7% (v/v) EtOH in ddH_2O	Fixation for carmine staining

Antibody blocking solution Store at -20 °C	0.5% (w/v) blocking reagent 1% (w/v) BSA in MAB-T	ISH
Alkaline Phosphatase (AP) buffer	100 mM TRIS-HCl 100 mM NaCl 50 mM $MgCl_2$ in ddH_2O pH = 9.5	CISH
Bluing buffer	0.1% (w/v) NaHCO3 in DEPC H_2O pH = 8.2	H&E staining
Carmine solution	2.5% (w/v) carmine 2.5% (v/v) HCl [37%] 2.5% (v/v) dH_2O 92.5% (v/v) EtOH [90%]	Carmine staining
DEPC H_2O autoclave 2x	0.1% (v/v) DEPC in ddH_2O	RNA work
Developing buffer Prepare freshly	330 µg/ml NBT 165 µg/ml BCIP in AP buffer	CISH
DIG-NTPs Store at -20 °C	10 mM ATP/ CTP/ GTP 7 mM UTP 3.5 mM DIG-UTP in DEPC H_2O	ISH-probe synthesis
dNTPs [10mM] Store at -20 °C	10 mM dATP/ dCTP/ dGTP/ dTTP in PCR H_2O	PCR
Eosin Y working solution	Eosin Y [5wt. %], 1:10 in dH_2O	H&E staining
FA fixation solution Prepare freshly	100 mM HEPES-KOH 4% (v/v) formaldehyde 25 mM EGTA 4.8% (v/v) formic acid in dH_2O	NA/FA fixation
HEPES-KOH	1 M HEPES in dH_2O pH = 7.5, adjust with KOH	NA/FA fixation
Hybridization buffer Store at -20 °C	5x SSC 50% (v/v) formamide deionized 10% (w/v) dextran sulfate 1 mg/ml yeast RNA 1x Denhardt's solution in DEPC H_2O	ISH
Hybridization washing buffer	5x SSC 50% (v/v) formamide 0.1% (v/v) Tween-20 in DEPC H_2O	ISH
Low-TE buffer	10 mM TRIS 0.1 mM EDTA in DEPC H_2O pH = 8.0, adjust with HCl	ST

Maleic acid buffer (MAB-T)	100 mM maleic acid 150 mM NaCl in ddH_2O pH = 7.5, adjust with NaOH add 0.1% (v/v) Tween-20	ISH
NaCl solution Prepare freshly	0.9% (w/v) NaCl 1% (v/v) ABAM in dH_2O	Worm harvest
NA fixation solution Prepare freshly	100 mM HEPES-KOH 4% (v/v) formaldehyde 25 mM EGTA 50 mM $MgSO_4$ 0.525% (v/v) HNO_3 in dH_2O	NA/FA fixation
NTPs [25 mM] Store at -20 °C	25 mM ATP/ CTP/ GTP/ UTP	dsRNA synthesis
PBS [10x]	1.37 mM NaCl 27 mM KCl 65 mM Na_2HPO_4 15 mM KH_2PO_4 in dH_2O pH = 7.0 - 7.2	Multipurpose buffer
PBSTx	1x PBS 0.5% (v/v) Triton X-100	ISH, stainings (Permeabilization)
POD inactivation solution Store at -20 °C	0.03% (v/v) H_2O_2 in 4x SSC	FISH
Orange loading dye [10x] Store at 4 °C	25% (v/v) glycerol 0.2% (w/v) orange G in 1x TAE buffer	Gel electrophoresis
SSC [20x]	3 M NaCl 300 mM tri-sodium citrate in DEPC H_2O pH = 7.0, adjust with HCl	ST, ISH
Sugar water Prepare freshly	0.8 g saccharose in 20 ml dH_2O	Rat infection
T7 reaction buffer [10x] Store at -20 °C	0.4 M TRIS 0.1 M $MgCl_2$ 20 mM spermidine M DTT in DEPC H_2O pH = 8.0	dsRNA synthesis
TAE buffer [50x]	2 M TRIS 50 mM EDTA 5.71% (v/v) acetic acid in dH_2O pH = 8.0	Gel electrophoresis
TRIS-acetic acid buffer	0.45 M TRIS in DEPC H_2O pH = 6.0, adjust with acetic acid	H&E staining

6.1.5 Media and supplements

Media and supplements used in this work can be found in Supplementary Table 5.

Supplementary Table 5 Media and supplements

MEDIA/ SUPPLEMENT	SUPPLIER, CAT#	WORKING CONC./ COMPOSITION	APPLICATION
ABAM [10,000 units/ml penicillin, 10 mg/ml streptomycin, 25 mg/ml amphotericin B]	c-c-pro, Z-18-M	1%	*in vitro* culture
Chicken Serum	Thermo Fisher Scientific, 16110082	5-10%	*in vitro* culture
Kanamycin	Sigma Aldrich, K4000	50 mg/l	Cloning
LB medium	Carl Roth, X964.2	20 g/l in ddH_2O, autoclaved	Cloning
LB selection plates	-	20 g/l LB medium 15 g/l Agar-Agar in ddH_2O autoclaved add 50 mg/l kanamycin	Cloning
RPMI 1640 Medium	Thermo Fisher Scientific, C21875034	1x	*in vitro* culture

6.1.6 Commercial assays and kits

Commercial assays and kits used in this work can be found in Supplementary Table 6.

Supplementary Table 6 Commercial assays and kits

KIT	SUPPLIER	CAT#
Visium Spatial Tissue Optimization Slide and Reagent Kit	10xGenomics	1000193
Visium Spatial Gene Expression Slide and Reagent Kit	10xGenomics	1000187
Visium Accessory Kit	10xGenomics	1000194
TSA Cyanine 3 System 50-150 slides	Akoya	NEL704A001KT
Click-iT Plus EdU Cell Proliferation Kit for Imaging, Alexa Fluor 488 dye	Invitrogen	C10637
Monarch Total RNA Miniprep Kit	New England Biolabs	T2010S
Monarch DNA Gel Extraction Kit	New England Biolabs	T1020L
Monarch PCR & DNA Cleanup Kit (5 µg)	New England Biolabs	T1030L
Monarch Plasmid Miniprep Kit	New England Biolabs	T1010L
Agilent RNA 6000 Nano Kit	Agilent Technologies	5067-1511
Agilent RNA 6000 Pico Kit	Agilent Technologies	5067-1513
Agilent High Sensitivity DNA Kit	Agilent Technologies	5067-4626

6.1.7 Antibodies

Antibodies used in this work can be found in Supplementary Table 7.

Supplementary Table 7 Antibodies

ANTIBODY	SUPPLIER	CAT#
Anti-Digoxigenin-POD, Fab fragments	Roche	11207733910
Anti-Digoxigenin-AP, Fab fragments	Roche	11093274910

6.1.8 PCR reagents and enzymes

PCR reagents and enzymes used in this work can be found in Supplementary Table 8.

Supplementary Table 8 PCR reagents and enzymes

REAGENT or RESOURCE	SUPPLIER	CAT#
Q5 High-Fidelity DNA Polymerase	New England Biolabs	M0491L
AccuPrime Taq DNA Polymerase, High Fidelity	Thermo Fisher Scientific	12346086
FIREPol DNA Polymerase Kit	Solis Biodyne	01-01-KIT-0000S
QuantiTect Reverse Transcription Kit	Qiagen	205313
PerfeCTa SYBR Green SuperMix	Quantabio	95054-02K
KAPA SYBR FAST qPCR Kit Master Mix (2x) Universal	Roche	KK4618
T4 DNA Ligase	New England Biolabs	B0202S
AhdI	New England Biolabs	R0584L
T3 RNA polymerases	Roche	11031163001
SP6 RNA polymerase	Roche	11487671001
T7 RNA polymerase	Produced in house [432]	-
DNase I (RNase-free)	New England Biolabs	M0303L
Proteinase K	Roche	3115801001
Proteinase K	Invitrogen	AM2546
Pyrophosphatase, Inorganic (IPP)	New England Biolabs	M0361L
RNase Inhibitor, Murine	New England Biolabs	M0314L

6.1.9 Molecular weight markers

DNA ladders used for gel electrophoresis can be found in Supplementary Table 9.

Supplementary Table 9 Molecular weight markers

LADDER	SUPPLIER	CAT#
HyperLadder 50 bp	meridian bioscience	BIO-33054
HyperLadder 1kb	meridian bioscience	BIO-33053

6.1.10 Primers

6.1.10.1 For cloning

Primers used for cloning (2.2.2, 2.9.2) can be found in Supplementary Table 10.

Supplementary Table 10 Primers used for cloning

PRIMER NAME	SEQUENCE 5'-3'	DESIGN	APPLICATION/ GENE
pJC53.2_seq_s	TTCTGCGGACTGGCTTTCTAC	Oliver Weth [433]	PJC53.2 seq. primer
pJC53.2_T7_extended primer	CCTAATACGACTCACTATAGGGAG	Oliver Weth [433]	T7 extended primer
71-Fh_EF-hand_ISH_fw	GGAAGCGGACAAATCACTGAG	Tobias Schmitt [211]	ISH, D915_003074
72-Fh_EF-hand_ISH_rev	TCATTCGGGTATTTTCCAAAACAAA		
67-Fh_T-family_ISH_fw	CTTGGATACATCCATGACTTTGT	Tobias Schmitt [211]	ISH, D915_000797
68-Fh_T-family_ISH_rev	AACACAACAATGAGAATGGCAAAAG		
101-Fh_T-alpha_ISH_fw	AAACGCCTACATCTCATGTGCT	Tobias Schmitt [211]	ISH, D915_001685
102-Fh_T-alpha_ISH_rev	CTTGCTTCGCATTTAACCTGAC		
183_Fh_ZF31_Tes_ISH1_fw	TTGGTGTGGTGGATGTCGCT	Svenja Gramberg [211]	ISH, D915_005258
184_Fh_ZF31_Tes_ISH1_rv	GCTCTTCTACTGGTTGCCGA		
189_Fh_RIB43A_Tes_ISH2_fw	CCTCGTGGTCCAAGTAATCC	Svenja Gramberg [211]	ISH, D915_002130
190_Fh_RIB43A_Tes_ISH2_rv	GTGGAACAAGAACAACGCAGAT		
111_Fh_Legumain_ISH-2_fw	TCAAACACAAACATCATGAATCACAT	Svenja Gramberg [211]	ISH, D915_002224
112_Fh_Legumain_ISH-2_rv	GTTGGATGAAAGATACAGCGTC		
107_Fh_SapB_ISH_fw	TCATTGTTTAATCCGACATTTCCAC	Svenja Gramberg, unpublished	ISH, D915_010001
108_Fh_SapB_ISH_rv	ATGCCTACAATTGTATACTCGATG		
41_bmpg_ISH2_fw	CAAGTTCAAGCGCTGGTCGT	Oliver Puckelwaldt [149]	ISH, D915_005862
42_bmpg_ISH2_rev	GGTACGGCAATCCTTTTCTCA		
115_Fh_Phos_ISH-3_fw	ATCTGATTGCGCTCGTGACG	Svenja Gramberg [211]	ISH, D915_005757
116_Fh_Phos_ISH-3_rv	TTAGCCAATACTATCCCAGTGG		
167_Fh_BaseMemP_Par_ISH2_fw	CTGAGTCCAGACACGACCG	Svenja Gramberg [211]	ISH, D915_000229
168_Fh_BaseMemP_Par_ISH2_rv	GTGTGAAGATTGTTCCGACGG		

161_Fh_CathB_Par_ISH1_fw	TTCTGGCGTACCACTTGTCC	Svenja Gramberg [211]	ISH, D915_007096
162_Fh_CathB_Par_ISH1_rv	ATTCCGTCTGCCACTAATGTG		
195_Fh_HypP_Meh_ISH1_fw	TCATGCTCCATAATACGGGTTC	Svenja Gramberg [211]	ISH, D915_000089
196_Fh_HypP_Meh_ISH1_rv	GTCCCACCGGATGAGCG		
216_Fh_HypP_S1_ISH2_fw	GATTGGCTCAAATTCTCTGTCC	Svenja Gramberg [211]	ISH, D915_007782
217_Fh_HypP_S1_ISH2_rv	GTGAAAAAGGCAAATCAAGGCG		
202_Fh_Endorib_S1_ISH1_fw	GTGGACAGGAAATCATTGGTTC	Svenja Gramberg [211]	ISH, D915_007390
203_Fh_Endorib_S1_ISH1_rv	AACAGTAACTAATGCGGGCTTG		
206_Fh_VWFA_S1_ISHA_fw	CAGGCTGCATGTGGATTGCA	Svenja Gramberg [211]	ISH, D915_006655
207_Fh_VWFA_S1_ISHA_rv	TATCCCAACAGGAGACATCTAC		
357_Reticulocalbin_ISH2_fw	GACGATCTAATCTCTAATGGAGC	Oliver Puckelwaldt, unpublished	ISH, D915_009175
358_Reticulocalbin_ISH2_rv	CATTCTTATCCAAATCGGCCGA		
212_Fh_HypP_S2_ISH1_fw	ACCGAATCCACAACGTCGCT	Svenja Gramberg [211]	ISH, D915_006136
213_Fh_HypP_S2_ISH1_rv	TTATTACTCCTGGAGCTGCTTC		
210_Fh_PepInh16_S2_ISH1_fw	GTACCCACAACCAACTTTACG	Svenja Gramberg [211]	ISH, D915_001060
211_Fh_PepInh16_S2_ISH1_rv	GATCGTGGTTTCTCATATATCCTA		
141_Tyrosinase_ISH1_fw	GAGCAACATCACGGTGACC	Oliver Puckelwaldt [149]	ISH, D915_002718
142_Tyrosinase_ISH1_rev	GATCAAGTACTGATAGTCTACATC		
85_actin_ISH2_fw	GTGGTTATTCATTCACGACGAC	Oliver Puckelwaldt, unpublished	ISH, D915_007443
86_actin_ISH2_rev	GTGGTCAATGAGGCCAAAATG		
218_Fh_CathL_gut_ISH_fw	TCACGGAAATTGTGCCACCATC	Svenja Gramberg [211]	ISH, D915_011077
219_Fh_CathL_gut_ISH_rv	CAGGAGTGGTATTTATCAGAGC		
195_Vitteline_B1_ISH2_fw	TCGATATGTATGGAAATGTGAAGG	Rice-Ficht et al. [307]	ISH, D915_010963
196_Vitteline_B1_ISH2_rev	GTAACTGTATTTGTCATATGGAGTC		
Fh hnf4 ISH 4 fw	TGGCCAGCCATGGACGATGA	Svenja Gramberg, unpublished	ISH, dsRNA,
Fh hnf4 ISH 4 rv	TTTGCAACTAGCCAGACAAATGG		D915_003315
18_CathepsinL_ISH2_fw	GTCATTCTCTGAGCAACAACTG	Oliver Puckelwaldt [149]	dsRNA, D915_005527
2_CathepsinL_qPCR1_rev	CAACCGAATGTAACCAGACTC		

6.1.10.2 For dsRNA control generation

Primers used to synthesize double-stranded RNA (dsRNA) against the bacterial kanamycin/neomycin resistance gene contained in pJC53.2 (= dsRNA control for RNA interference, 2.2) can be found in Supplementary Table 11.

Supplementary Table 11 Primers for neomycin dsRNA template generation

PRIMER NAME	SEQUENCE 5'-3'	DESIGN	GENE
76_neomycin_fw	TAATACGACTCACTATAGGGAGAGTGGAGAGGCTATTCGGCT	Hicham Houhou, unpublished	neomycin resistance gene in pJC53.2
77_neomycin_rv	TAATACGACTCACTATAGGGAGACATCCTGATCGACAAGACCG		

6.1.10.3 For qRT-PCR

Primers used for qRT-PCR (2.4) can be found in Supplementary Table 12.

Supplementary Table 12 Primers for qRT-PCR

PRIMER NAME	SEQUENCE 5'-3'	DESIGN	GENE/ ID	EFF
14_0.109_qPCR1_F	TACACCACAACCATCGAGGC	Hicham Houhou [228]	*eprs*, maker-scaffold10x_14_pilon snap-gene-0.109/ D915_002574	NA
14_0.109_qPCR1_R	GTGGTCAATCCCCACGAGTT			
Fh hnf4 qPCR-3 fw	AATAAGCAATCGACCTTTGGCATA	Svenja Gramberg, unpublished	*hnf4*, D915_003315	99%
Fh hnf4 qPCR-3 rv	ACCGTCTGGACCACAGTTC			
57-Fh CathL qPCR-7 fw	GCCTCGTCACCTACAAGTTG	Svenja Gramberg, unpublished	cathepsin L, maker-scaffold10x_819_pilon-augustus-gene-0.18/ D915_010438	92%
58-Fh CathL qPCR-7 rv	GTCACGCCAGTCAATGCTC			

6.2 Plasmids

pJC53.2 [220] (Supplementary Table 13) was used as a backbone for all recombinant plasmids generated in this work.

Supplementary Table 13 Plasmid backbones

PLASMID NAME	SOURCE	IDENTIFIER
pJC53.2	Addgene	26536

Recombinant plasmids generated and used in this work can be found in Supplementary Table 14. BLAST results confirming insert sequences for ISH riboprobes can be found in Supplementary Table 21.

Supplementary Table 14 Recombinant plasmids

PLASMID NAME	INSERT GENE ID	GENERATED BY
SGr2_FhHNF4_PJC53.2	D915_003315	Svenja Gramberg
SGr10_FhTegumentalProtein_PJC53.2	D915_003074	Svenja Gramberg
SGr21_FhTubulinα_PJC53.2	D915_001685	Svenja Gramberg
SGr26_FhSaposinB_PJC53.2	D915_010001	Svenja Gramberg
SGr28_FhLegumain_PJC53.2	D915_002224	Svenja Gramberg
SGr29_FhCtypelectin_PJC53.2	D915_005757	Svenja Gramberg
SGr34_FhCathepsinB_ PJC53.2	D915_007096	Svenja Gramberg
SGr36_FhHSPG_PJC53.2	D915_000229	Svenja Gramberg
SGr43_FhC3H1ZnF31_PJC53.2	D915_005258	Svenja Gramberg
SGr46_FhRIB43A_ PJC53.2	D915_002130	Svenja Gramberg
SGr47_FhSecretedProtein_PJC53.2	D915_000089	Svenja Gramberg
SGr50_FhEndoribonuclease_PJC53.2	D915_007390	Svenja Gramberg
SGr52_FhVWFA_PJC53.2	D915_006655	Svenja Gramberg
SGr54_FhPeptidaseInhibitor16_PJC53.2	D915_001060	Svenja Gramberg
SGr55_FhC3H1dom_PJC53.2	D915_006136	Svenja Gramberg
SGr57_FhSecretedProtein_PJC53.2	D915_007782	Svenja Gramberg
SGr58_FhCathepsinL_PJC53.2	D915_011077	Svenja Gramberg
SGr60_FhTetraspanin_PJC53.2	D915_000797	Svenja Gramberg
OP3_FhCathepsinL_ PJC53.2	D915_005527	Oliver Puckelwaldt
OP14_Fhbmpg_PJC53.2	D915_005862	Oliver Puckelwaldt
OP21_FhTyrosinase_PJC53.2	D915_002718	Oliver Puckelwaldt
OP33_FhVB1_PJC53.2	D915_010963	Oliver Puckelwaldt
OP47_FhReticulocalbin_PJC53.2	D915_009175	Oliver Puckelwaldt
OP48_FhCytoplasmicTypeActin_PJC53.2	D915_007443	Oliver Puckelwaldt

6.3 Genomes

Genomes used in this work can be found in Supplementary Table 15. The *F. hepatica* genome PRJEB25283 [6] was used as a reference genome until summer 2022, when the whole research group switched to the alternative *F. hepatica* genome PRJNA179522 [5], due to an annotation update in WPBS17.

Supplementary Table 15 Genomes

RESOURCE	SOURCE	IDENTIFIER
F. hepatica genome	Cwiklinski et al. [123]	PRJEB25283
F. hepatica genome	McNulty et al. [124]	PRJNA179522

6.5 Online databases and software

Online databases and software used in this work can be found in Supplementary Table 16.

Supplementary Table 16 Online databases and software

RESOURCE	RERFERENCE	LINK
Genome databases		
WormBase ParaSite (v16.0-19.0)	[216]	https://parasite.wormbase.org/index.html
NCBI	[252]	https://www.ncbi.nlm.nih.gov/
Compound database		
ChEMBL (v34)	[248]	https://ftp.ebi.ac.uk/pub/databases/chembl/ChEMBLdb/releases/chembl_34/
Transcription factor databases		
HOCOMOCO (v12)	[258]	https://hocomoco12.autosome.org/
JASPER (v10)	[257]	https://jaspar.elixir.no/
Primer, probe and dsRNA design		
RNAfold Webserver (v2.6.3)	[217]	http://rna.tbi.univie.ac.at/cgi-bin/RNAWebSuite/RNAfold.cgi
OligoCalc (v3.26)	[219]	http://biotools.nubic.northwestern.edu/OligoCalc.html
OligoAnalyzer	IDT	https://eu.idtdna.com/calc/analyzer
si-Fi (v1.2.3)	[218]	https://github.com/snowformatics/siFi21-?tab=readme-ov-file
Benchling	[221]	https://www.benchling.com/
Spatial Transcriptomics analysis and visualization		
Loupe Browser (v6.0.0)	10xGenomics	https://www.10xgenomics.com/support/software/loupe-browser
Space Ranger (v1.3.1)	10xGenomics	https://www.10xgenomics.com/support/software/space-ranger
RStudio (v2024.04.2+764)	[231]	https://posit.co/download/rstudio-desktop/
R (v4.1.2 & 4.4.1)	[232]	https://cran.r-project.org/bin/windows/base/
Seurat (v4.3.0)	[245]	https://satijalab.org/seurat/
Harmony (v0.1.1)	[246]	https://github.com/immunogenomics/harmony
Giotto (v4.1.0)	[247]	https://drieslab.github.io/Giotto_website/
BLAST+ (v2.13.0)	[249]	https://blast.ncbi.nlm.nih.gov/doc/blast-help/downloadblastdata.html#downloadblastdata
Python (3.12)	Python	https://www.python.org/downloads/
GO term enrichment analysis		
topGO (v2.46.0)	[240]	https://bioconductor.org/packages/release/bioc/html/topGO.html

RNAseq data analysis		
DESeq2 (v1.44.0)	[233]	https://bioconductor.org/packages/release/bioc/html/DESeq2.html
gplots (v3.1.3.1)	[235]	https://cran.r-project.org/web/packages/gplots/index.html
EnhancedVolcano (v1.22.0)	[236]	https://bioconductor.org/packages/release/bioc/html/EnhancedVolcano.html
ComplexHeatmap (v2.20.0)	[242]	https://bioconductor.org/packages/release/bioc/html/ComplexHeatmap.html
VennDiagram (v1.7.3)	[241]	https://cran.r-project.org/web/packages/VennDiagram/index.html
Protein analysis		
InterProScan (v5.60.92.19)	[239]	https://ftp.ebi.ac.uk/pub/software/unix/iprscan/5/5.60-92.0/interproscan-5.60-92.0-64-bit.tar.gz
SMART (v9.0)	[250]	http://smart.embl-heidelberg.de/
Conserved Domain Database (v3.21)	[251]	https://www.ncbi.nlm.nih.gov/Structure/cdd/wrpsb.cgi
Phyre2 (v2.0)	[434]	http://www.sbg.bio.ic.ac.uk/~phyre2/html/page.cgi?id=index
STRING (v11.5)	[255]	https://version-11-5.string-db.org/organism/STRG0085JJO
Sequence alignment and phylogenetic tree construction		
Muscle (v3.8)	[253]	https://www.ebi.ac.uk/jdispatcher/msa/muscle?stype=protein
MEGA X (v10.2.4)	[254]	https://www.megasoftware.net/downloads/dload_win_gui
Image processing		
Fiji (ImageJ, v1.54f)	[435]	https://fiji.sc/
Inkscape (v1.4)	Inkscape	www.inkscape.org
Data visualization and statistics		
GraphPad Prism (v10.3.1)	GraphPad	https://www.graphpad.com

6.6 Laboratory equipment

In addition to standard laboratory equipment the following equipment was used:

6.6.1.1 PCR cycler

PCR cycler used in this work can be found in Supplementary Table 17.

Supplementary Table 17 PCR cycler

DEVICE	SUPPLIER	APPLICATION
C1000 Thermal Cycler	Biorad	PCR
GeneExplorer GE-48DG Thermal Cycler	Bioer Technology	PCR
Veriti 96-Well Thermal cycler	Thermo Fisher Scientific	ST
Rotor-Gene Q	Qiagen	qRT-PCR

6.6.1.2 Microscopes and cameras

Microscopes and cameras used in this work can be found in Supplementary Table 18.

Supplementary Table 18 Microscopes and cameras

DEVICE	SUPPLIER	APPLICATION
Microscopes		
DMIL LED Fluo	Leica	Brightfield & fluorescence microscopy
DMi8	Leica	ST (tile scanning)
TL3000 Ergo	Leica	Stereo microscope for worm scoring & imaging
iX81	Olympus	ST (TO), Fluorescence microscopy
TCS SP5 VIS	Leica	CLSM
Cameras		
DFC3000G	Leica	B&W camera for DMIL
DMC2900	Leica	Color camera for DMIL, TL3000 Ergo and DMi8
VisiCam 5 Plus	VWR International	Color camera for DMIL
XM10	Olympus	B&W camera for IX81

6.6.1.3 Other devices

Other devices used in this work can be found in Supplementary Table 19.

Supplementary Table 19 Other devices

DEVICE	SUPPLIER	APPLICATION
Agilent 2100 Bioanalyzer	Agilent Technologies	RNA quality assessment & concentration measurement, ST (cDNA QC)
BioSpectrometer basic	Eppendorf	DNA, RNA concentration measurement
Microm HM525	Thermo Fisher Scientific	Cryosectioning
Epredia CryoStar NX50	Thermo Fisher Scientific	Cryosectioning
Premiere Slides Warmer XH-2002	C&A Scientific	H&E staining
HERACELL VIOS 160i CO2 incubator	Thermo Fisher Scientific	*in vitro* culture
Heraeus T 6060 oven	Thermo Fisher Scientific	ISH
Gel iX20	INTAS Science Imaging Instruments	Agarose gel imaging

6.6.1.4 Small items

Small items used in this work can be found in Supplementary Table 20.

Supplementary Table 20 Small items

DEVICE	SUPPLIER	Cat#	APPLICATION
Pestles	Science Services	E64788-20	RNA isolation
Epredia SuperFrost Plus Adhesion slides	Thermo Fisher Scientific	J1800AMNZ	ISH, EdU staining
Coverslips 1.5H	Carl Roth	LH25.2	Fluorescence microscopy
Tissue-Tek Cryomold	Sakura Finetek	Small: 4565 Medium: 4566 Large: 4557	Worm embedding for cryosectioning
Netwell Inserts (74 µm)	Corning	3477	EdU, Carmine staining
Pointed spring steel tweezers	Roth	AL99.1	*in vitro* culture

6.7 Supplementary Figures

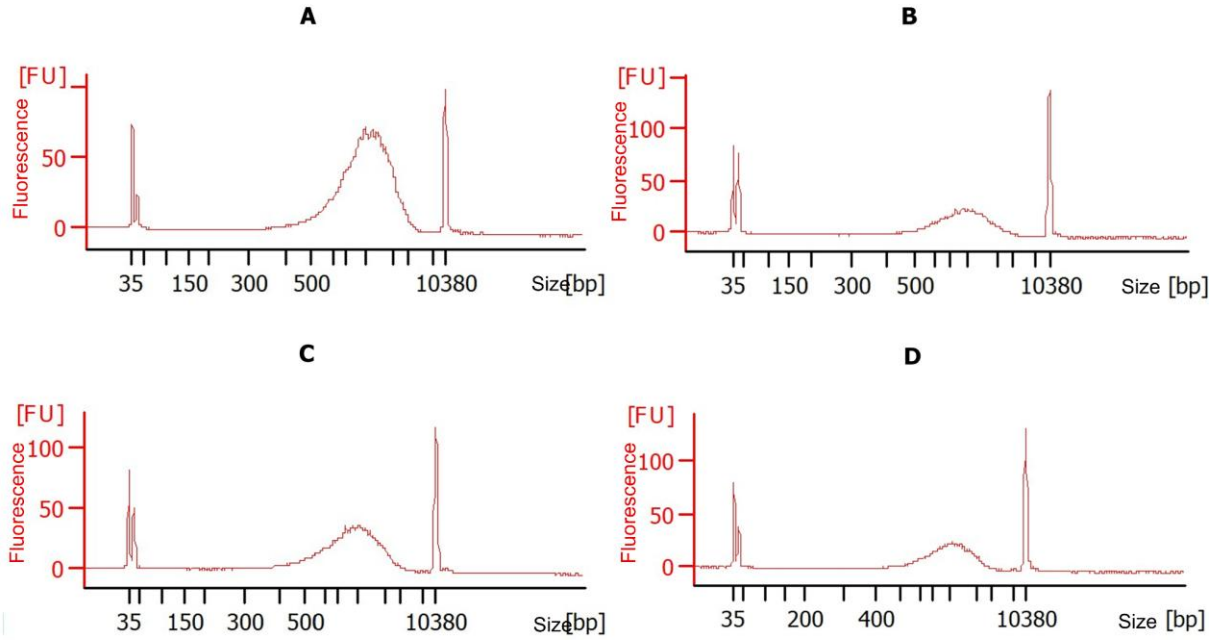

Supplementary Figure 1 Spatial transcriptomics cDNA libraries.
cDNA libraries derived from all four tissue sections used in the spatial transcriptomics experiment (labelled A-D, as shown in Fig. 15). Size distribution was determined using an Agilent Bioanalyzer High Sensitivity DNA assay. [211]

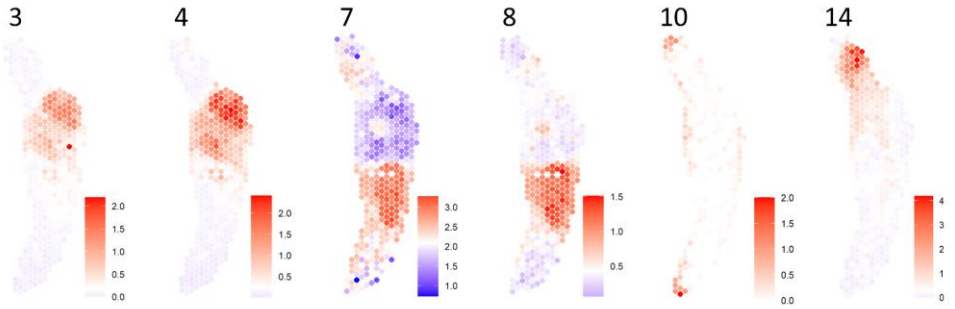

Supplementary Figure 2 Spatial expression of additional Giotto metagenes.
Metagene visualizations for all spatial co-expression modules not shown in Fig. 17. [211]

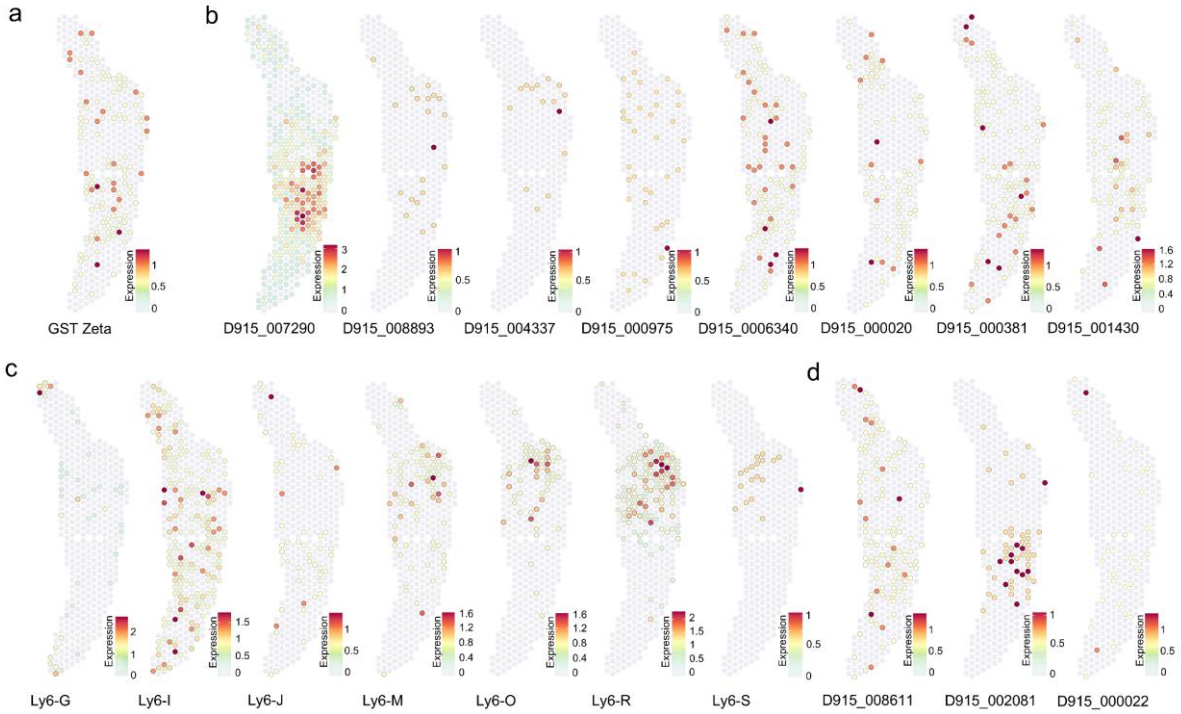

Supplementary Figure 3 Spatial expression patterns of additional GSTs, ABC-B transporters, Ly6 proteins and PKCs.
(**a**) Spatial projection showing the expression pattern of zeta class GST (D915_006391), which was not shown in Fig. 30a. (**b**) Spatial projections showing expression patterns of ABC transporters (subfamily B) not shown in Fig. 30b. (**c**) Spatial projections showing expression patterns of *F. hepatica* Ly6 proteins not shown in Fig. 31b-d: Ly6-G (D915_008997), Ly6-I (D915_002959), Ly6-J (D915_006710), Ly6-M (D915_008952), Ly6-O (D915_000989), Ly6-R (D915_000988), Ly6-S (D915_000991). (**d**) Spatial projections showing expression patterns of PKCs not shown in Fig. 33c. (**a-d**) Expression level encoded by color (grey = low, red = high). [211],[212]

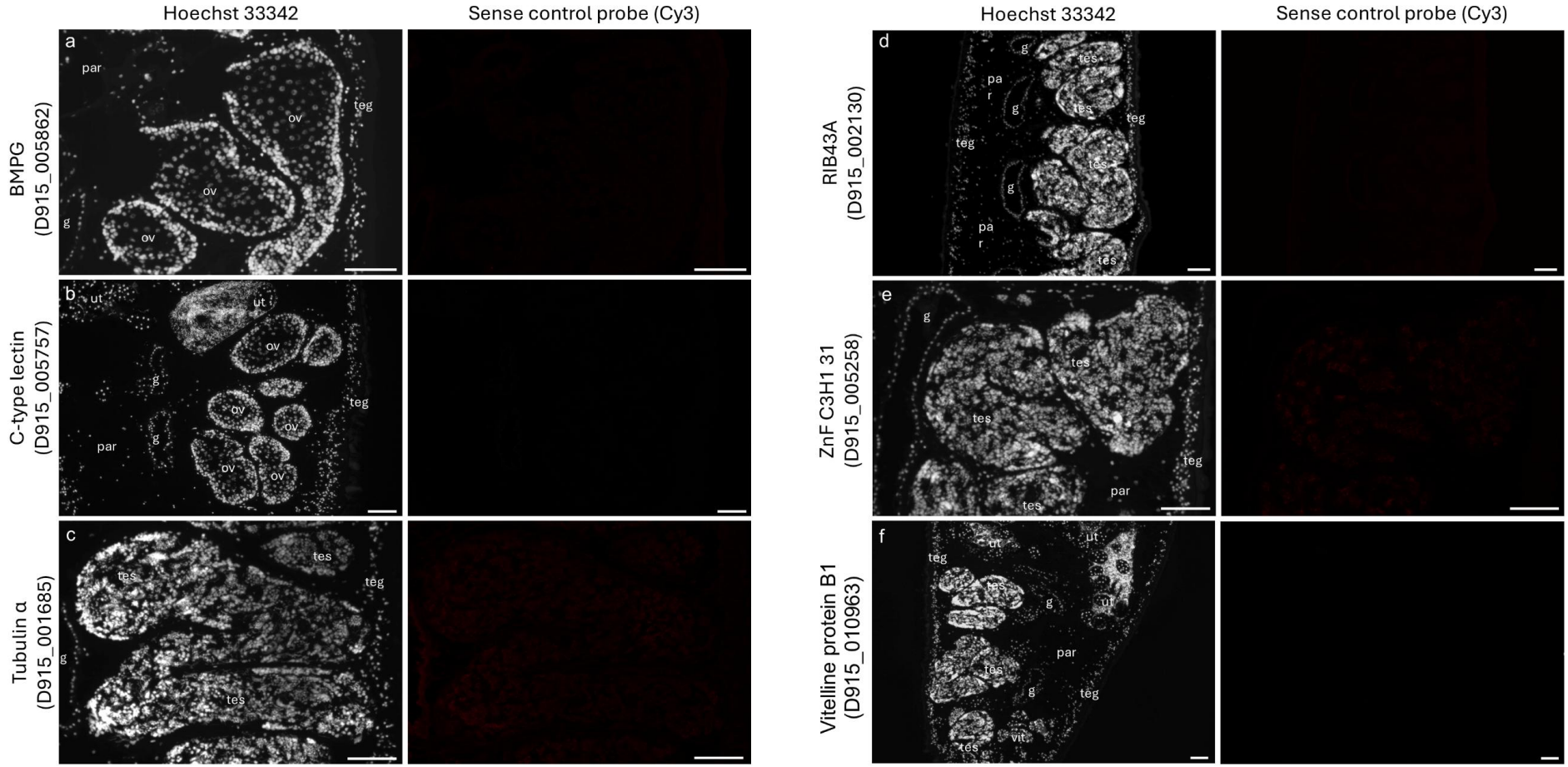

Supplementary Figure 3 (page 1/4)

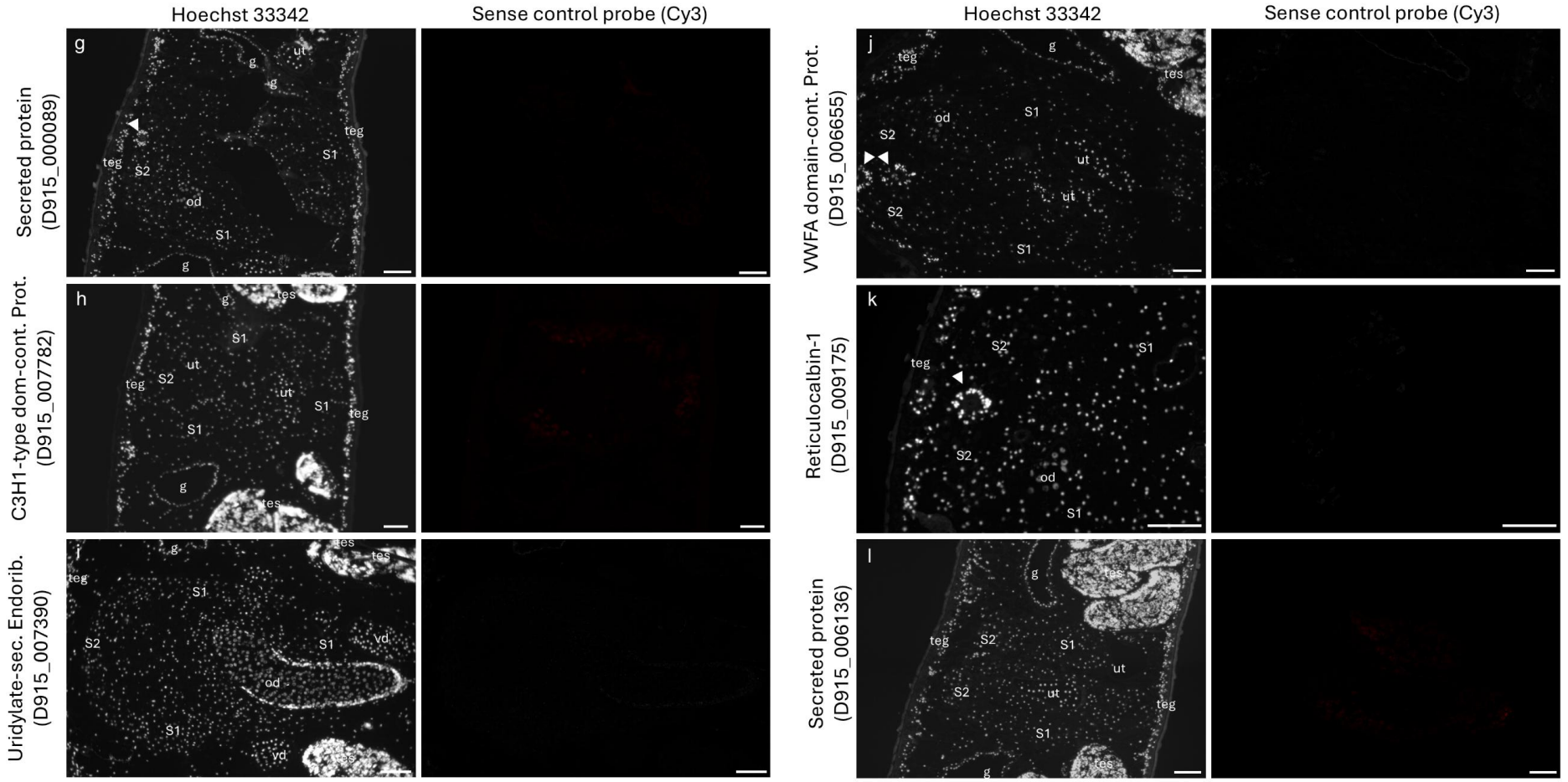

Supplementary Figure 3 (page 2/4)

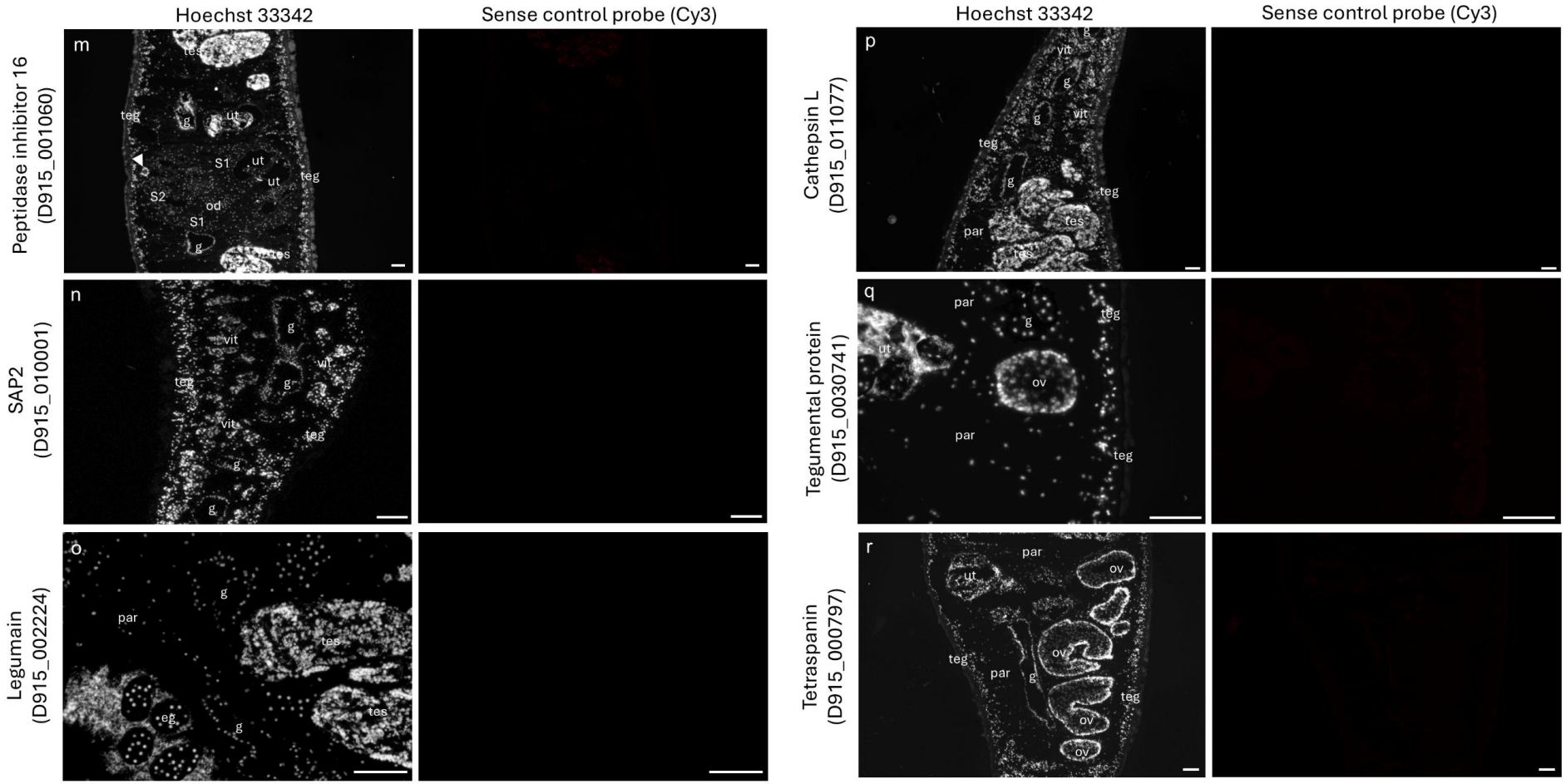

Supplementary Figure 3 (page 3/4)

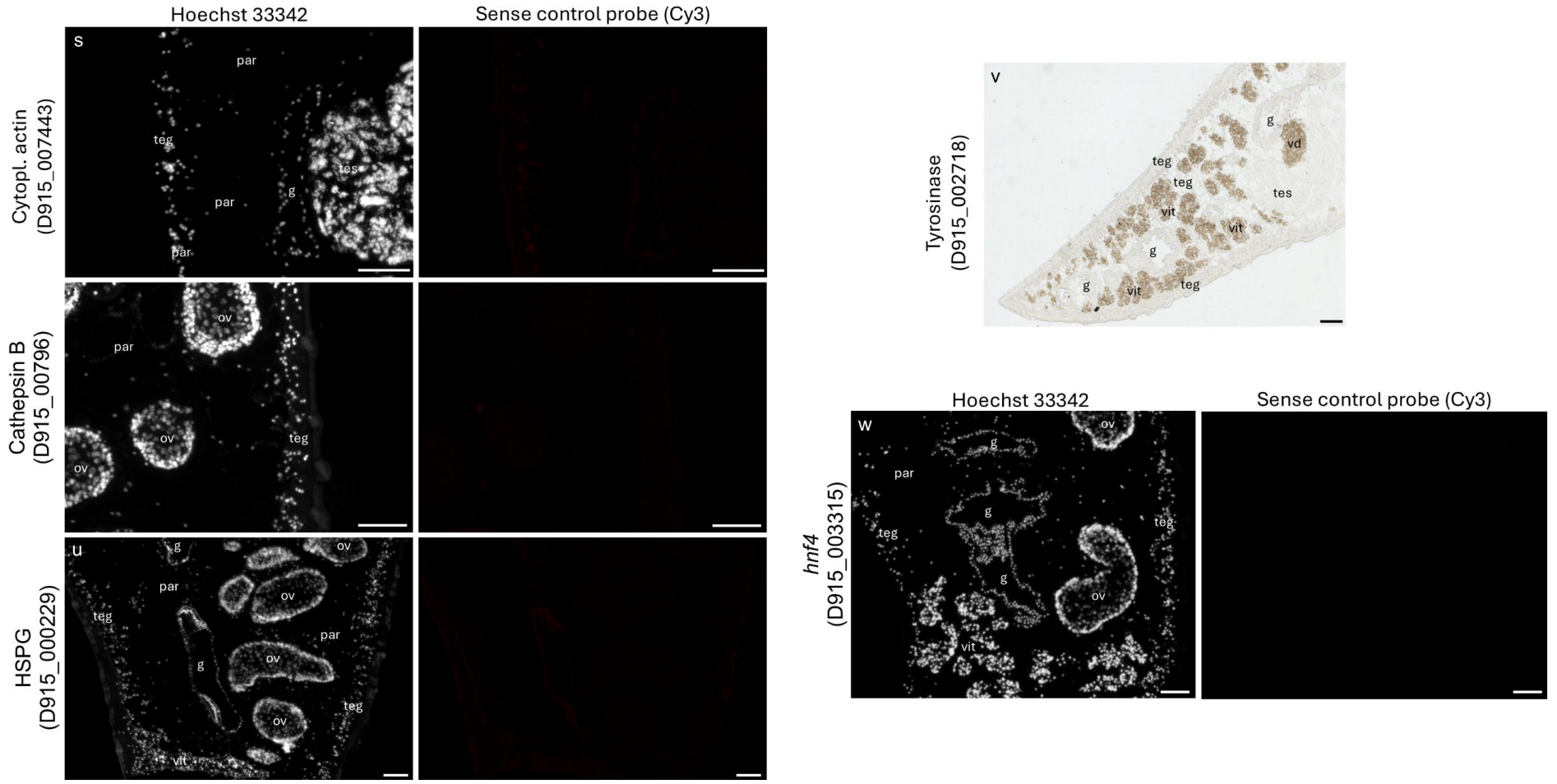

Supplementary Figure 4 Sense probes did not produce signal during *in situ* hybridization.
(**a-w**) Sense controls for *in situ* hybridizations (ISH) of ST cluster markers and *hnf4*. Gene IDs are indicated. Scale = 100 µm. eg: egg, g: gut, od: oviduct, ov: ovary, par: parenchyma, S1: S1 cells, S2: S2 cells, teg: tegument, tes: testis, vd: vitelline duct, ut: uterus, vit: vitellarium. Arrowhead marks Laurer's channel. (**a-u, w**) Nuclei counterstained with Hoechst 33342.

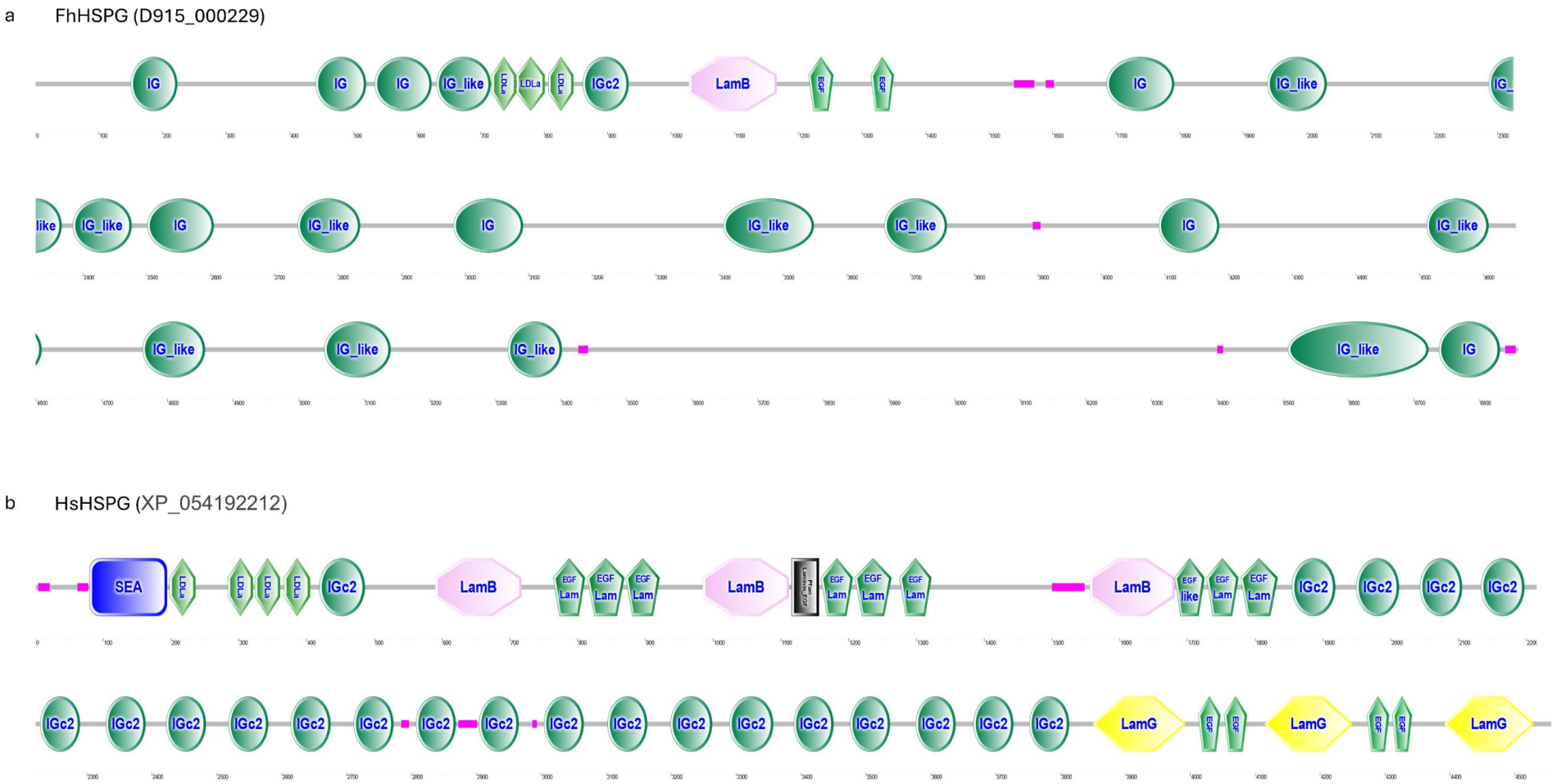

Supplementary Figure 5 Protein domain architecture of liver fluke and human HSPG.
SMART analysis revealed similarities of human and liver fluke HSPG, both consisting of several immunoglobulin-like domains (IG) and one or multiple Laminin B domains (LamB), flanked by low-density lipoprotein receptor domains (LDLa) and epidermal growth factor like domains (EGF). Human HSPG further contained a N-terminal SEA domain (domain found in sea urchin sperm protein, enterokinase, agrin) and three C-terminal Laminin G domains (LamG).

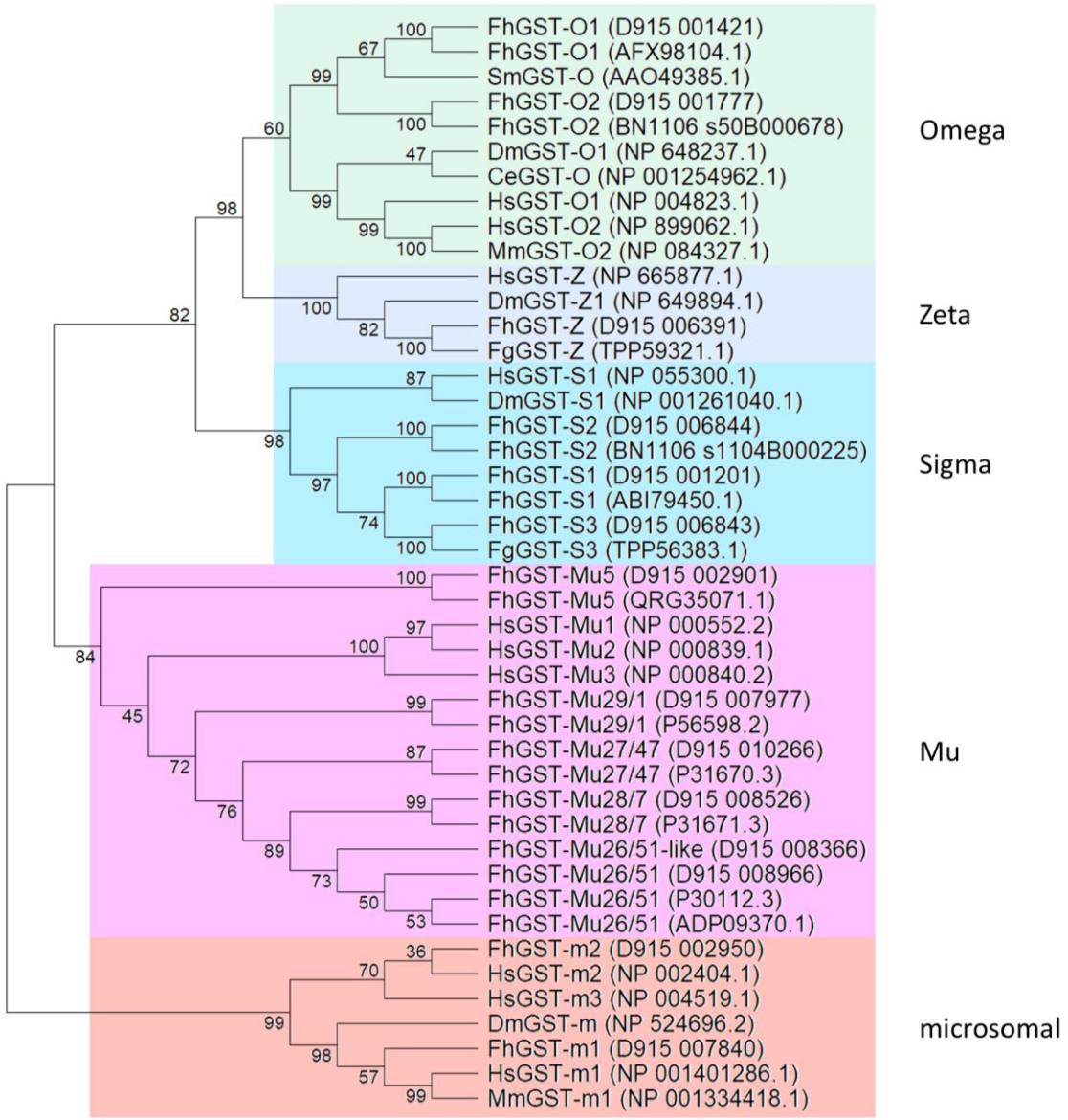

Supplementary Figure 6 GST class assignment by phylogenetic tree construction.
Phylogenetic analysis of *F. hepatica* (Fh) glutathione S-transferases (GSTs). *F. hepatica* GST amino acid sequences found in the liver fluke proteome [124] ("D915"-IDs) were analyzed together with human (Hs), *D. melanogaster* (Dm), *C. elegans* (Ce) and murine (Mm) GST sequences as well as *Fasciola* GST sequences from the literature. The latter were adopted from Stuart et al. [287]. If no *F. hepatica* sequence was available, *F. gigantica* (Fg) sequences were used instead. Maximum likelihood analysis was performed in MegaX to 1,000 bootstraps with JTT substitution. The tree was displayed as "Topology only". [211],[212]

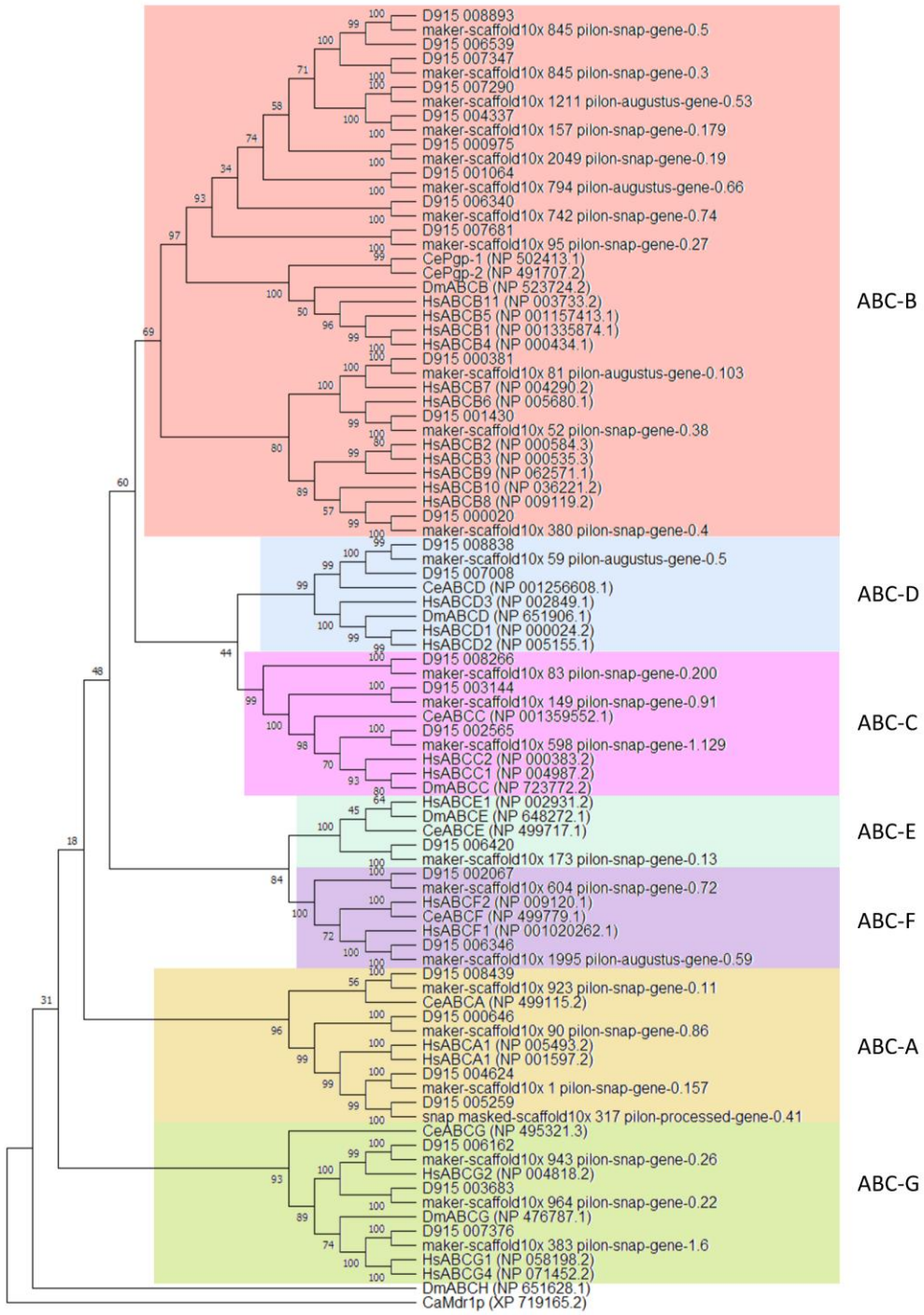

Supplementary Figure 7 ABC transporter subfamily assignment by phylogenetic tree construction.
Phylogenetic analysis of *F. hepatica* ATP-binding cassette (ABC) transporters. ABC transporter amino acid sequences of two *F. hepatica* proteomes [123],[124] (“D915”-IDs & “marker-scaffold”-IDs) were analyzed together with human (Hs), *C. elegans* (Ce) and *D. melanogaster* (Dm) ABC sequences of all subfamilies (A-H). *Candida albicans* (Ca) Mdr1p was used as outgroup. “marker-scaffold” ABC transporter gene IDs were adopted from Beesley et al. [102]. Maximum likelihood analysis was performed in MegaX to 1,000 bootstraps with JTT substitution. The tree was displayed as “Topology only”. [211],[212]

```
CAG46523.1    26 LQCYNCPN-PTADCKTAVNCSSDFDACLITK-AGLQVYNKCWKFEHC---NFNDVTTRLR 80
FhLy6N        22 VKCYHCDNCSE--VTNTTPVRDSCPICAWGLFTPFDTQKKPVVIRHCVNETCTPGNVEIP 79
FhLy6Q        37 LDCYSCSVCRQPFSKKTTDTMTGCTVCSISQ-TWLDGKRVTTT-RGCEN-SCSPADLRIK 93
FhLy6B        22 VQCYSCTSCPIPFVPTTSVIRSSCSQCEISQ-TLVNFQVQSET-RGCVA-VCTPQNNVIR 78
FhLy6F        22 VRCYLCTTCQKPFVPTSSLIRSSCTQCQIAQ-SIFDNEVQSET-RGCVS-ACTPQDNVKF 78
                  : ** *         .:     .   *     : .:          *     .

CAG46523.1    81 ENE-LTYYCCKKDLCNFNEQLENGGTSLSE-KTVLLLVTPFLAAAWSLHP 128
FhLy6N        80 NEGRLEGKCCQRDLCN-----------RALIKRAHFAVMMTVIPLSLLI 117
FhLy6Q        94 GNG-LVKTCCKTDLCN-------GNTNLRWFKSVVLFSGLIVFKLTHI-- 133
FhLy6B        79 GFG-ARTDCCSTHLCN-----EKYNTSNRHSPFNFALIGLITISLLKIQL 122
FhLy6F        79 GNG-GRVACCSTDLCN-----EKYNTSDRRFPSNFALLGLITTSLWKIQL 122
                    **.  ***                    :   :      :
```

Supplementary Figure 8 Tegumental Ly6 proteins lack complement binding residues.
Muscle alignment of amino acid sequences of the four tegumental FhLy6 proteins with that of the human CD59 (CAG46523.1). Signal sequences were excluded. Cysteine residues are highlighted in yellow. The conserved Ly6/CD59 motif is boxed; regions with high sequence identity are shaded in gray. Complement binding residues of HsCD59 are colored (D49, W65, R78 and E81) in red.

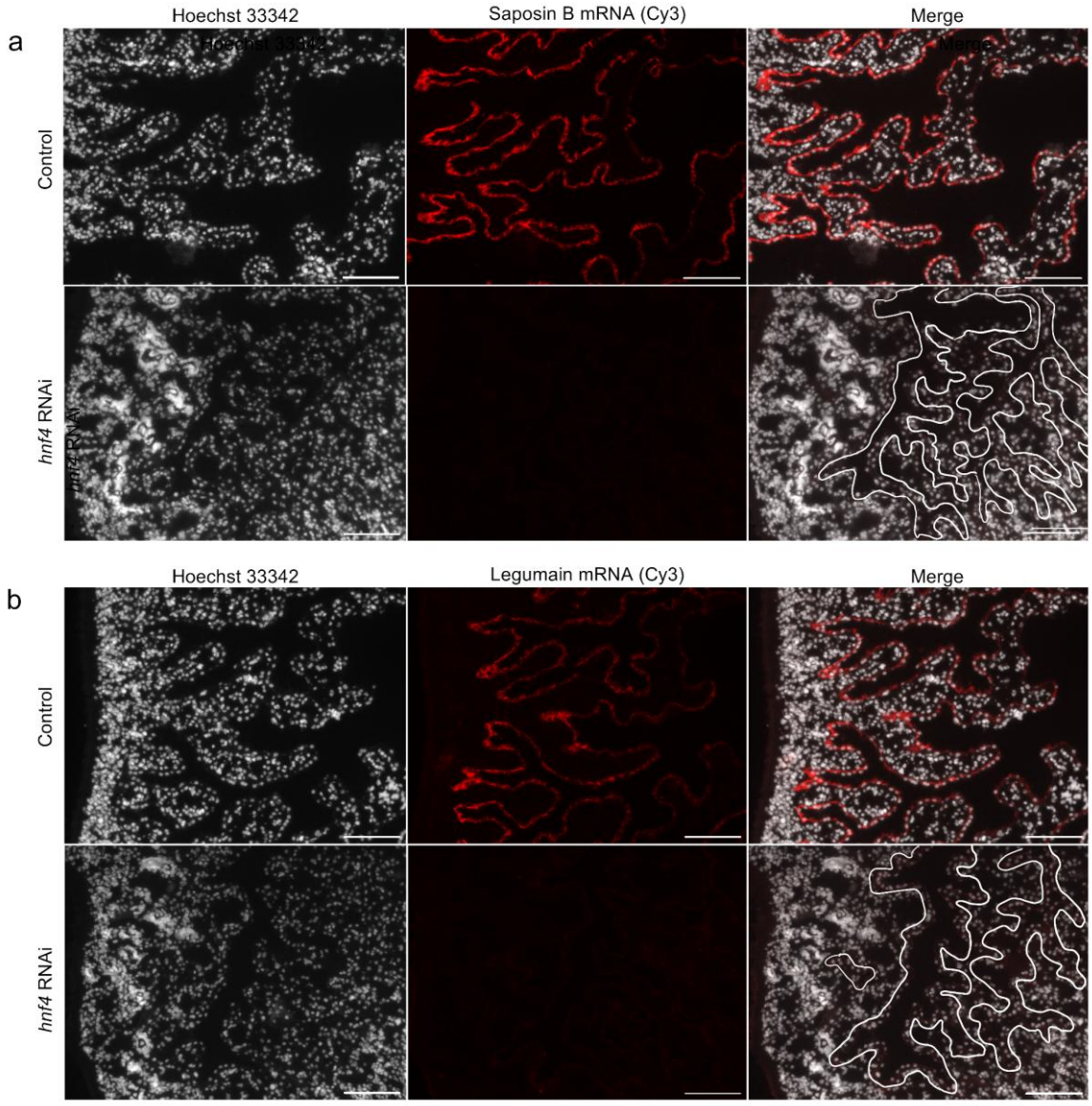

Supplementary Figure 9 Expression of saposin B and legumain was downregulated upon *hnf4* RNAi.
FISH of transcripts encoding (**a**) saposin B (D915_010001) and (**b**) legumain (D915_002224) performed after 15 days of dsRNA treatment. Controls showed fluorescent signal in the gastrodermis. No signal was observed after *hnf4* RNAi. White lining marks the contour of the gastrodermis. Images are representative for 4 out of 5 (Control, saposin B), 3/5 (Control, legumain), and 6/6 (RNAi) biological replicates derived from two independent experiments. Nuclei were counterstained with Hoechst 33342. Scale = 100 µm

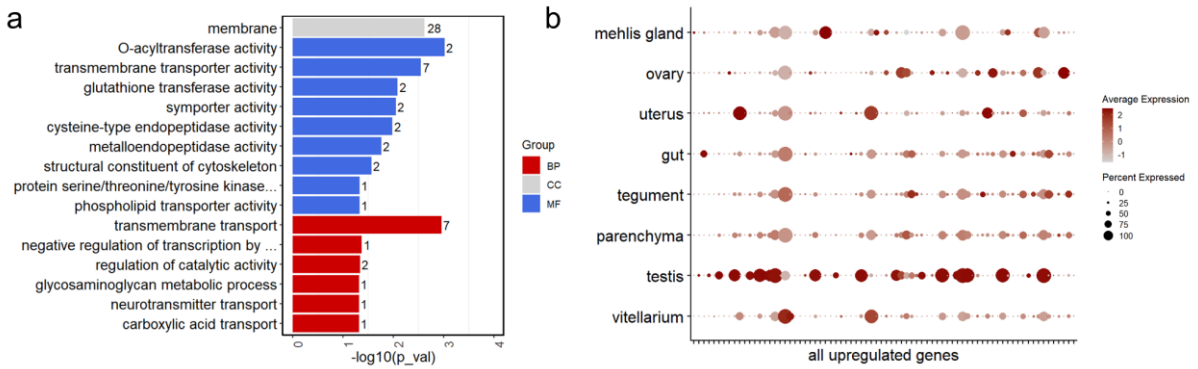

Supplementary Figure 10 GO term analysis and tissue expression of upregulated genes.
(a) Gene ontology analysis of upregulated genes revealed characteristic biological processes (BP), molecular functions (MF) and cellular components (CC) that were enriched among upregulated genes after *hnf4* RNAi. Overrepresented functional terms were identified using a two-sided Fisher's exact test (p-value < 0.05). (b) DotPlot based on a spatial transcriptome of adult parasites, showing tissue expression profiles of all upregulated genes (sorted by log2FC) after *hnf4* RNAi. Dot color encodes the average expression level (Z-score scaled counts) within a tissue-cluster. Dot size encodes the percentage of spots within a cluster that have captured this transcript.

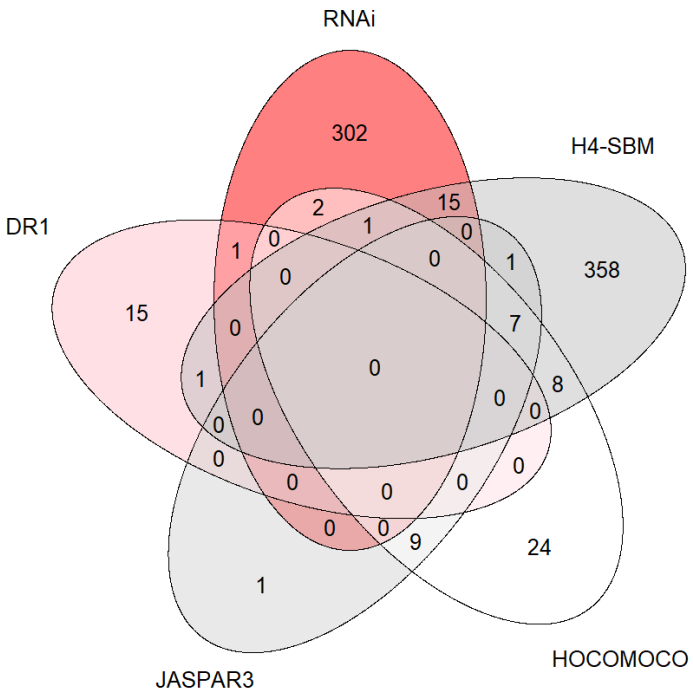

Supplementary Figure 11 Motif search could not explain RNAi effects.
Venn diagram of genes that were significantly regulated after RNAi and genes containing potential HNF4-binding motifs. Four different motif sequences were used (see Table 25).

6.8 Supplementary Tables

Supplementary Table 21 Riboprobes for *in situ* hybridization – BLAST of plasmid sequences and number of independent ISH experiments

				BLAST (Gene ID, Length / E-val / %ID)		number of ISH experiments	
Gene Description	**Gene ID (Design)**	**Plasmid no.**	**Length (Design)**	**Top hit**	**Second highest hit**	**CISH**	**FISH**
Bone marrow proteoglycan	D915_005862	OP14	444 bp	D915_005862 444 / 0.0 / 100.0	D915_006549 18 / 6.4 / 95.5	1	3
C-type lectin	D915_005757	SGr29	500 bp	D915_005757 500 / 0.0 / 99.8	D915_005606 21 / 1.0 / 95.2	0	1
Tubulin alpha	D915_001685	SGr21	509 bp	D915_001685 509 / 0.0 / 99.0	D915_005428 28 / 2.8e-07 / 94.4	1	1
Zinc finger C3H1 31	D915_005258	SGr43	489 bp	D915_005258 489 / 0.0 / 100.0	D915_000955 19 / 0.063 / 92.6	0	2
RIB43A	D915_002130	SGr46	415 bp	D915_002130 415 / 0.0 / 100.0	D915_000217 19 / 0.053 / 100.0	0	2
Tyrosinase	D915_002718	OP21	448 bp	D915_002718 449 / 0.0 / 99.1	D915_002134 22 / 6.5 / 95.5	2	0
Vitelline protein B1	D915_010963	OP33	326 bp	D915_010963 327 / 1.1e-179 / 99.4	D915_008125 244 / 6.4e-135 / 99.2	2	2
Secreted protein	D915_000089	SGr47	472 bp	D915_000089 460 / 0.0 / 99.1	D915_008689 17 /0.92/ 100.0	0	1
C3H1-type dom.-cont. prot.	D915_007782	SGr57	471 bp	D915_007782 471 / 0.0 / 99.4	D915_010853 18 / 0.24 / 100.0	0	1
Poly(U)-specific endoribonuclease	D915_007390	SGr50	423 bp	D915_007390 423 / 0.0 / 100.0	D915_003956 19 / 0.054 / 100.0	0	1
VWFA dom.-cont. prot.	D915_006655	SGr52	510 bp	D915_006655 510 / 0.0 / 98.0	D915_000973 19 / 0.066 / 100.0	0	1
Reticulocalbin-1	D915_009175	OP47	448 bp	D915_009175 448 / 0.0 / 99.777	D915_005611 20 / 1.6 / 95.5	0	1

Secreted protein	D915_006136	SGr55	257 bp	D915_006136 257 / 7.3e-142 / 99.6	D915_005589 18 / 0.13 / 100.0	0	1
Peptidase inhibitor 16	D915_001060	SGr54	447 bp	D915_001060 447 / 0.0 / 100.0	D915_005421 17 / 0.89 / 100.0	2	2
Cathepsin L	D915_011077	SGr58	226 bp	D915_009243 226 / 1e-106 / 96.5	D915_011077 226 / 6.1e-102 / 95.6	0	2
Legumain	D915_002224	SGr28	500 bp	D915_002224 578 / 0.0 / 99.3	D915_006080 17 / 1.2 / 100.0	1	2
Saposin B	D915_010001	SGr26	324 bp	D915_010001 91 / 7.4e-31 / 93.4	D915_010001 31 / 2.2e-9 / 100.0	1	1
Tegumental protein	D915_003074	SGr10	483 bp	D915_003074 483 / 0.0 / 100.0	D915_003713 22 / 0.24 / 95.5	1	2
Tetraspanin	D915_000797	SGr60	526 bp	D915_000797 494 / 0.0 / 100.0	D915_000369 19 / 0.063 / 100.0	0	1
Cytoplasmic type actin 1	D915_007443	OP48	466 bp	D915_007443 455 / 0.0 / 100.0	D915_007442 204 / 1.2e-81 / 99.4	0	1
Basement membrane-specific heparan sulfate proteoglycan core protein	D915_000229	SGr36	478 bp	D915_000229 469 / 0.0 / 99.6	D915_001424 17 / 0.94 / 100.0	0	1
Cathepsin B	D915_007096	SGr34	491 bp	D915_007096 481 / 0.0 / 100.0	D915_010977 20 / 0.016 / 100.0	0	1
HNF4	D915_003315	SGr2	480bp	D915_003315 480 / 0.0 / 99.8	D915_004411 17 / 0.96 / 100.0	1	2

Supplementary Table 22 dsRNA for RNA interference. (Off-)target prediction using SiFi2

Gene Description	Gene ID (Design)	Plasmid no.	Length (Design)	Predicted targets (clone sequence) & no. of hits (siRNA size: 21 bp, 1 mismatch)
Cathepsin L	D915_005572	OP3	551 bp	D915_010438; D915_005527; D915_009243; D915_011077; D915_010977; D915_010675; D915_010874; D915_009772; D915_009795; D915_005615; D915_010422; D915_006264 (all cystein proteases) - 94 to 1 hit(s)
HNF4	D915_003315	SGr2	480 bp	D915_003315 - 460 hits

Supplementary Table 23 List of marker genes of spatial transcriptomics clusters

The top 15 marker genes (sorted by power) per cluster and all marker genes validated by ISH (red) are shown. P = predictive power, indicates how well a marker discriminates different groups, (0 – no classification, 1 – perfect classification), FC = average log2FC between this cluster and the rest of the dataset, Diff = average expression difference between this cluster and the rest of the dataset, Pct.1 = percentage of spots in that cluster and Pct.2 = percentage of spots in the rest where the gene was detected.

No.	Cluster	Gene ID	Gene description	P	Fc	Diff	Pct.1	Pct.2
1	vitellarium	D915_007343	NA	0,89	2,13	1,48	1	0,71
2	vitellarium	D915_006291	Btz domain-containing protein	0,88	2,20	1,53	1	0,54
3	vitellarium	D915_003631	Ferritin	0,88	2,28	1,58	1	0,66
4	vitellarium	D915_003630	Ferritin	0,87	2,32	1,60	1	0,70
5	vitellarium	D915_004535	Trematode Eggshell Synthesis	0,86	2,15	1,49	1	0,58
6	vitellarium	D915_008125	Vitelline protein B2	0,85	2,19	1,52	1	0,60
7	vitellarium	D915_002179	Tyrosinase	0,85	1,87	1,30	0,98	0,38
8	vitellarium	D915_003632	Ferritin	0,84	2,14	1,48	1	0,63
9	vitellarium	D915_003341	Myoglobin 2	0,81	1,83	1,27	1	0,70
10	vitellarium	D915_005807	Ferritin	0,80	1,66	1,15	1	0,58
11	vitellarium	D915_001201	glutathione transferase	0,79	1,59	1,10	1	0,90
12	vitellarium	D915_002718	Tyrosinase	0,78	1,85	1,28	0,95	0,40
13	vitellarium	D915_002380	Ferritin	0,77	1,43	0,99	1	0,60
14	vitellarium	D915_010963	Vitelline protein BI	0,75	1,86	1,29	1	0,50
15	vitellarium	D915_004883	Protein PFC0760c-like	0,75	1,76	1,22	0,91	0,37
1	testis	D915_001685	Tubulin alpha	0,96	2,32	1,61	1	0,58
2	testis	D915_005959/ "alpha-tub5"	Tubulin alpha chain	0,96	2,35	1,63	1	0,58
3	testis	D915_005258	Zinc finger CCCH domain-containing protein 31	0,96	2,36	1,64	1	0,60
4	testis	D915_007453	Leucine-rich repeat-containing protein 23	0,96	2,30	1,59	1	0,65
5	testis	D915_007398/ "beta-tub1"	Tubulin beta chain	0,95	2,18	1,51	1	0,68
6	testis	D915_003952	Solute carrier family 2 facilitated glucose transporter member 3	0,95	2,09	1,45	1	0,73
7	testis	D915_005431	Tubulin alpha chain	0,94	2,07	1,44	1	0,66
8	testis	D915_003393	Venom allergen protein 13	0,94	2,18	1,51	1	0,61
9	testis	D915_002144	ELAV like protein 2/3/4	0,93	2,20	1,52	1	0,59
10	testis	D915_004441	CSD domain-containing protein	0,93	2,04	1,42	1	0,57
11	testis	D915_004663	phosphopyruvate hydratase	0,93	2,06	1,43	1	0,50
12	testis	D915_002130	RIB43A domain with coiled coils 1	0,92	2,00	1,39	1	0,48
13	testis	D915_001137	DUF1907 domain-containing protein	0,92	1,99	1,38	1	0,60
14	testis	D915_003483	Protein HID1	0,91	1,95	1,35	1	0,62
15	testis	D915_001174	Four and A half lim domains protein	0,91	2,01	1,39	1	0,83
1	parenchyma	D915_003368	Fatty acid-binding protein type 2	0,88	1,79	1,24	1	0,96
2	parenchyma	D915_003367	Fatty acid-binding protein Fh15	0,87	1,65	1,14	1	0,95
3	parenchyma	D915_001319	Four and a half LIM domains protein 3	0,81	1,47	1,02	1	0,88

4	parenchyma	D915_007621/ "MF6"	MF6p protein	0,79	1,39	0,97	1	1
5	parenchyma	D915_007977	glutathione transferase	0,75	1,29	0,89	1	0,86
6	parenchyma	D915_008526	Glutathione S-transferase	0,73	1,35	0,93	1	0,77
7	parenchyma	D915_004249	Farnesoic acid o-methyltransferase	0,73	1,22	0,85	0,99	0,69
8	parenchyma	D915_008782	Regulator of microtubule dynamics protein 1	0,71	1,17	0,81	1	0,72
9	parenchyma	D915_008366	glutathione transferase	0,70	1,22	0,84	0,97	0,48
10	parenchyma	D915_010266	glutathione transferase	0,70	1,21	0,84	1	0,83
11	parenchyma	D915_000540	Putative calcium-binding protein	0,67	1,18	0,82	0,99	0,78
12	parenchyma	D915_001097	CD59 protein; CD59-like protein	0,66	1,09	0,76	0,98	0,73
13	parenchyma	D915_003030	UPF0506 domain-containing protein	0,64	1,02	0,71	0,99	0,78
14	parenchyma	D915_008422	Fatty acid binding protein a	0,61	0,92	0,64	1	0,91
15	parenchyma	D915_006972	Secreted protein	0,61	0,96	0,66	0,99	0,79
18	parenchyma	D915_007096	Cathepsin B endopeptidase	0,56	0,93	0,65	0,99	0,81
22	parenchyma	D915_000229	Basement membrane-specific heparan sulfate proteoglycan core protein	0,51	0,82	0,57	0,89	0,56
1	tegument	D915_008604	NA	0,90	3,06	2,12	1,00	0,65
2	tegument	D915_003183	CaBP1; Tegumental calcium-binding EF-hand protein 4	0,85	2,32	1,61	0,99	0,68
3	tegument	D915_009456	Secreted protein	0,84	2,89	2,00	1,00	0,74
4	tegument	D915_007443	Cytoplasmic type actin 1	0,82	2,40	1,66	0,95	0,51
5	tegument	D915_008996	UPAR/Ly6 domain-containing protein	0,81	2,32	1,61	0,95	0,45
6	tegument	D915_008863	UPAR/Ly6 domain-containing protein	0,80	2,28	1,58	0,94	0,45
7	tegument	D915_003074	Tegumental protein	0,78	2,06	1,43	0,93	0,42
8	tegument	D915_008616/ "alpha-tub3"	Tubulin alpha chain	0,78	1,90	1,31	0,94	0,44
9	tegument	D915_005316	Glucose transporter	0,78	2,18	1,51	0,89	0,29
10	tegument	D915_003182/ "22-2"	Calcium-binding protein; Tegumental calcium-binding EF-hand protein 4	0,75	1,76	1,22	0,93	0,47
11	tegument	D915_008443	CaM3	0,75	1,80	1,25	0,92	0,43
12	tegument	D915_000797	Tetraspanin	0,74	1,94	1,34	0,87	0,30
13	tegument	D915_007373	UPAR/Ly6 domain-containing protein	0,73	1,86	1,29	0,91	0,43
14	tegument	D915_006521	CUB domain-containing protein	0,73	1,97	1,37	0,86	0,30
15	tegument	D915_001928	Sodium-coupled neutral amino acid transporter 9	0,72	1,91	1,32	0,87	0,36
1	gut	D915_007743	RING-type domain-containing protein	0,97	3,33	2,31	1	0,74
2	gut	D915_011077	Cathepsin L	0,96	3,59	2,49	1	0,86
3	gut	D915_010675	Putative pre-pro-cysteine proteinase	0,96	3,61	2,50	1	0,90
4	gut	D915_010438	Secreted cathepsin L 1	0,96	3,47	2,41	1	0,82
5	gut	D915_011152	Cathepsin B	0,96	3,20	2,22	1	0,55
6	gut	D915_009243	Cathepsin L	0,96	3,56	2,47	1	0,88
7	gut	D915_008045	Putative cathepsin b endopeptidase ixodes scapularis cathepsin b endopeptidase	0,95	3,05	2,12	0,99	0,47

8	gut	D915_002224	Legumain like	0,95	3,31	2,29	1	0,60
9	gut	D915_005499	Acid sphingomyelinase phosphodiesterase 3a	0,95	3,08	2,13	0,99	0,47
10	gut	D915_007658	Fst	0,95	3,13	2,17	0,99	0,45
11	gut	D915_006213	Dipeptidyl peptidase 2	0,95	2,96	2,05	1	0,68
12	gut	D915_005958	Cathepsin B	0,94	3,20	2,22	0,99	0,55
13	gut	D915_009989	Thioredoxin domain-containing protein 17	0,94	3,04	2,11	0,98	0,45
14	gut	D915_003994	DM9 domain-containing protein	0,94	2,87	1,99	0,99	0,50
15	gut	D915_007020	Cathepsin B	0,94	2,74	1,90	0,99	0,38
20	gut	D915_010001	FHAP protein	0,93	3,57	2,47	0,99	0,63
1	uterus	D915_004614	NA	0,98	3,91	2,71	1	0,66
2	uterus	D915_008554	Secreted protein	0,98	3,75	2,60	1	0,60
3	uterus	D915_002208	Glutamine synthetase	0,97	3,57	2,47	1	0,55
4	uterus	D915_011253	NA	0,93	3,09	2,14	1	0,42
5	uterus	D915_004563	Universal stress protein	0,93	2,65	1,83	0,99	0,40
6	uterus	D915_006749	Putative Multidrug resistance protein 2	0,93	3,23	2,24	1	0,38
7	uterus	D915_011252	NA	0,92	3,12	2,17	0,99	0,53
8	uterus	D915_006412	phenylalanine 4-monooxygenase	0,92	2,44	1,69	0,98	0,31
9	uterus	D915_011254	NA	0,92	3,10	2,15	1	0,41
10	uterus	D915_011251	NA	0,91	2,97	2,06	1	0,50
11	uterus	D915_005807	Ferritin	0,91	2,70	1,87	1	0,61
12	uterus	D915_011255	NA	0,91	2,82	1,96	1	0,48
13	uterus	D915_002380	Ferritin	0,90	2,61	1,81	1	0,63
14	uterus	D915_009087	Kunitz/Bovine pancreatic trypsin inhibitor domain protein	0,88	2,63	1,82	0,95	0,22
15	uterus	D915_011250	NA	0,85	2,33	1,62	0,99	0,42
40	uterus	D915_010963	Vitelline protein BI	0,66	1,56	1,08	0,99	0,54
1	ovary	D915_005757	C-type lectin domain-containing protein	0,99	3,62	2,51	1	0,33
2	ovary	D915_004345	Malate dehydrogenase	0,99	2,31	1,60	1	0,91
3	ovary	D915_004205	phosphoenolpyruvate carboxykinase (GTP)	0,98	3,16	2,19	1	0,51
4	ovary	D915_009802	Ribonucleoside-diphosphate reductase small subunit	0,98	3,71	2,57	1	0,34
5	ovary	D915_000633	Proline-rich protein HaeIII subfamily 1-like	0,98	3,27	2,27	1	0,23
6	ovary	D915_004953	Syntaxin-binding protein 5	0,98	3,39	2,35	1	0,52
7	ovary	D915_008934	Glyceraldehyde-3-phosphate dehydrogenase	0,98	1,71	1,19	1	1
8	ovary	D915_000373	Putative deferrochelatase /peroxidase	0,97	2,25	1,56	1	0,57
9	ovary	D915_004863	60S ribosomal protein L7a	0,97	1,52	1,06	1	0,96
10	ovary	D915_006205	Ubiquinone biosynthesis protein	0,96	2,06	1,43	1	0,34
11	ovary	D915_005060	40S ribosomal protein S23	0,96	1,76	1,22	1	0,93
12	ovary	D915_011031	Prothymosin alpha-like	0,96	1,72	1,19	1	0,96
13	ovary	D915_003451	Major egg antigen	0,95	2,08	1,44	1	0,61
14	ovary	D915_009078	Malate dehydrogenase	0,95	1,37	0,95	1	0,98
15	ovary	D915_006665	Poly(RC)-binding protein 2	0,95	2,26	1,57	0,99	0,24

42	ovary	D915_005862	Bone marrow proteoglycan	0,92	2,13	1,47	0,97	0,14
1	Mehlis' gland	D915_000089	Secreted protein	1,00	5,25	3,64	1	0,22
2	Mehlis' gland	D915_000433	Dynein light intermediate chain 1 cytosolic	0,99	2,39	1,66	1	0,04
3	Mehlis' gland	D915_000193	NA	0,99	5,21	3,61	1	0,23
4	Mehlis' gland	D915_007782	C3H1-type domain-containing protein	0,98	5,96	4,13	1	0,30
5	Mehlis' gland	D915_007390	Uridylate-specific endoribonuclease	0,98	5,45	3,78	1	0,26
6	Mehlis' gland	D915_006404	Signal peptide protein	0,98	5,22	3,62	1	0,25
7	Mehlis' gland	D915_003364	Family M13 unassigned peptidase (M13 family)	0,96	2,41	1,67	0,97	0,06
8	Mehlis' gland	D915_009175	Reticulocalbin-1	0,96	3,76	2,61	1	0,11
9	Mehlis' gland	D915_002627	Anoctamin	0,94	1,81	1,25	0,97	0,13
10	Mehlis' gland	D915_002503	Beta-1 3-galactosyl-O-glycosyl-glycoprotein beta-1 6-N-acetylglucosaminyl-transferase	0,93	2,02	1,40	0,94	0,04
11	Mehlis' gland	D915_006655	VWFA domain-containing protein	0,90	2,62	1,81	0,92	0,05
12	Mehlis' gland	D915_000972	Dysferlin limb girdle muscular dystrophy 2B	0,89	1,54	1,07	0,92	0,04
13	Mehlis' gland	D915_000038	RNA-binding protein fusilli	0,84	1,20	0,83	0,86	0,03
14	Mehlis' gland	D915_004975	TBC1 domain family member 10B	0,83	1,32	0,92	0,97	0,27
15	Mehlis' gland	D915_001250	Rab GDP dissociation inhibitor	0,82	1,16	0,81	0,97	0,44
65	Mehlis' gland	D915_006136	Secreted protein	0,51	3,13	2,17	0,56	0,06
67	Mehlis' gland	D915_001060	Peptidase inhibitor 16	0,50	3,38	2,34	0,56	0,07

Supplementary Table 24 WormBase BLASTp *F. gigantica* against *F. hepatica*

Ly6	Fg Gene ID	*F. hepatica* orthologue*	Best BLAST hit	%ID	Length (aa)	2nd best hit	%ID	Length (aa)
A	FGIG_07282	+	D915_001097	99.1	107	D915_008394	42.1	38
B	FGIG_11580	+	D915_008996	87.7	122	D915_008863	68	122
C	FGIG_07203	+	D915_004900	90.2	132	D915_008997	50	26
D	FGIG_03655	+	D915_006706	99.2	121	D915_007373	29.3	41
E	11274 [288]	+	D915_000675	88.0	100	D915_005931	29.3	82
F	FGIG_10706	+	D915_008863	92.6	122	D915_008996	73	122
G	FGIG_09511	+	D915_008997	91.8	122	D915_008996	60.4	106
H	FGIG_09512	−	D915_005087	46.4	97	D915_011082	54.5	77
I	FGIG_02796	+	D915_002959	96.7	150	D915_006710	40.6	32
J	FGIG_07508	+	D915_006710	97.9	143	D915_000367	41.2	34
K	FGIG_10413	+	D915_009743	100	102	-	-	-
L	FGIG_07116	+	D915_008235	99.3	138	-	-	-
M	FGIG_01443	+	D915_008952	97.4	153	-	-	-
N	FGIG_03657	+	D915_007373	96.7	92	-	-	-
O	FGIG_02025	+	D915_000989	93.4	136	D915_000991	49.3	69
P	FGIG_02999	−	D915_000989	30.0	90	D915_000991	31.6	76
Q	FGIG_08043	+	D915_008394	89.0	100	D915_008863	40.5	74
R	FGIG_02024	+	D915_000988	86.0	121	D915_000991	56.7	30
S	FGIG_02997	+	D915_000991	89.5	143	D915_000989	43.2	44
T	FGIG_08044	−	D915_008996	38.4	73	D915_011082	34.9	86
U	FGIG_10483 (fragment)	+	D915_000333	97.2	71	-	-	-
V	*F. hepatica* only	NA	D915_011082	NA	NA	-	-	-

* > 85% sequence identity over >70 aa with *F. gigantica* sequence at protein level, top BLAST hits were included in the table even if they were below this threshold.

Supplementary Table 25 List of predicted targets and drugs in the *F. hepatica* tegument

Fh gene ID	Gene description	%ID	E-val.	Score	ChEMBL target name	Acc.	Drug name	CP*
D915_008739	Chloride channel protein	29.6	7.07E-48	181	Chloride channel protein 2	P51788	LUBIPROSTONE	4
D915_006415	ornithine aminotransferase	24.3	9.58E-18	84.3	Gamma-amino-N-butyrate transaminase	P80404	VIGABATRIN	4
D915_002343	Serine/threonine kinase	31.1	2.77E-110	377	Rho-associated protein kinase 2	O75116	BELUMOSUDIL	4
D915_008291	Carbonic anhydrase	33.8	5.28E-42	147	Carbonic anhydrase XII	O43570	DICHLORPHENAMIDE	4
							ACETAZOLAMIDE	4
							ACETAZOLAMIDE SODIUM	4
		33.2	9.14E-33	122	Carbonic anhydrase IV	P22748	DICHLORPHENAMIDE	4
							METHAZOLAMIDE	4
							TOPIRAMATE	4
							ACETAZOLAMIDE	4
							ACETAZOLAMIDE SODIUM	4
D915_001973	Cellular tumor antigen p53	26. 9	1.80E-13	71.2	Cellular tumor antigen p53	P04637	EPRENETAPOPT	3
D915_001050	Bcl-2 ous antagonist/killer	31.1	1.06E-06	49.3	Induced myeloid leukemia cell differentiation protein Mcl-1	Q07820	OBATOCLAX MESYLATE	3
D915_008390	Cytidine deaminase	45.3	1.52E-30	106	Cytidine deaminase	P32320	CEDAZURIDINE	4
D915_004146	Filamin-A	40.8	0	1543	Filamin-A	P21333	SIMUFILAM	3
D915_006901	Protein kinase C	62.2	0	721	Protein kinase C beta	P05771	ENZASTAURIN	3
							RUBOXISTAURIN	3
D915_006539	ATP binding cassette subfamily B MDR TAP	41.3	0	919	P-glycoprotein 1	P08183	TARIQUIDAR	3
							ZOSUQUIDAR	3
D915_007347	Multidrug resistance protein 2	40.9	0	913			ENCEQUIDAR	3

*CP = clinical phase

Supplementary Table 26 List of predicted targets and drugs in the *F. hepatica* gut

Fh gene ID	Gene description	%ID	E-val.	Score	ChEMBL target name	Acc.	Drug name	CP*
D915_005050	N-acetylated-alpha-linked acidic dipeptidase 2	25.2	2.25E-60	216	Glutamate carboxypeptidase II	Q04609	LUTETIUM LU 177 VIPIVOTIDE TETRAXETAN	4
D915_004198	Equilibrative nucleoside transporter 1	31.7	2.95E-71	232	Equilibrative nucleoside transporter 1	Q99808	DIPYRIDAMOLE	4
D915_000724	Niemann-Pick C1 protein	33.1	0	623	Niemann-Pick C1-like protein 1	Q9UHC9	EZETIMIBE	4
D915_007426	Arachidonate 5-lipoxygenase	23.9	7.22E-43	164	Arachidonate 5-lipoxygenase	P09917	ZILEUTON	4
							BALSALAZIDE DISODIUM	4
							MECLOFENAMATE SODIUM	4
							MESALAMINE	4
							OLSALAZINE SODIUM	4
							SULFASALAZINE	4
		25.6	3.94E-38	149	Arachidonate 12-lipoxygenase	P18054	BENOXAPROFEN	4
D915_008045	Cathepsin b endopeptidase	32.6	6.24E-37	137	Dipeptidyl peptidase I	P53634	BRENSOCATIB	3
D915_004176	Solute carrier family 10 member 6	28.71	1.98E-28	114	Ileal bile acid transporter	Q12908	MARALIXIBAT CHLORIDE	4
							MARALIXIBAT	4
							LINERIXIBAT	3
							ELOBIXIBAT	3
							ODEVIXIBAT	4
							ODEVIXIBAT SESQUIHYDRATE	4
D915_001479	Subfamily S9B unassigned peptidase (S09 family)	29.6	2.61E-88	296	Dipeptidyl peptidase IV	P27487	VILDAGLIPTIN	4
							ALOGLIPTIN BENZOATE	4
							LINAGLIPTIN	4
							GOSOGLIPTIN	4
							DBPR-108	3
							SITAGLIPTIN PHOSPHATE	4

*CP = clinical phase

							SAXAGLIPTIN HYDROCHLORIDE	4
							EVOGLIPTIN	4
							ANAGLIPTIN	4
							TRELAGLIPTIN SUCCINATE	4
							OMARIGLIPTIN	4
							TENELIGLIPTIN	4
							GEMIGLIPTIN	3
							DUTOGLIPTIN	3
							SITAGLIPTIN FUMARATE	4
D915_001731	Phosphodiesterase-nucleotide pyrophosphatase	26.5	3.50E-43	164	Autotaxin	Q13822	ZIRITAXESTAT	3
D915_004118	Mitogen-activated protein kinase kinase kinase 15	38.2	2.66E-143	474	Mitogen-activated protein kinase kinase kinase 5	Q99683	SELONSERTIB	3
D915_001064	ATP-binding cassette sub-family B	42.0	0	743	P-glycoprotein 1	P08183	TARIQUIDAR	3
							ZOSUQUIDAR	3
							ENCEQUIDAR	3

Supplementary Table 27 BLAST of HNF4 amino acid sequences

Query		Target	1. **& 2. BLAST hit**	Annotation	Score	E-value	%ID	Length	Platform
HNF4 [*S. mansoni*]	Smp_174700	Fh proteome PRJNA179522	D915_003315	Hepatocyte nuclear factor 4-alpha	455	3.50E-54	63.00%	135	WormBase ParaSite
			D915_003315	Hepatocyte nuclear factor 4-alpha	345	4.00E-39	71.70%	106	
HNF4a [*H. sapiens*]	NP_849180	Fh proteome PRJNA179522	D915_003315	Hepatocyte nuclear factor 4-alpha	345	3.50E-40	77.90%	77	WormBase ParaSite
			D915_006508	Retinoic acid receptor RXR	287	4.00E-32	60.80%	79	
HNF4g [*H. sapiens*]	NP_004124	Fh proteome PRJNA179522	D915_003315	Hepatocyte nuclear factor 4-alpha	345	4.50E-40	77.90%	77	WormBase ParaSite
			D915_007001	COUP transcription factor 1	283	1.80E-31	55.60%	81	
HNF4 [*F. hepatica*]	D915_003315	Sm proteome PRJEA36577	Smp_174700	Putative hepatocyte nuclear factor 4-alpha	455	2.60E-54	63.00%	135	WormBase ParaSite
			Smp_174700	Putative hepatocyte nuclear factor 4-alpha	420	1.70E-49	71.70%	106	
HNF4 [*F. hepatica*]	D915_003315	Hs proteome taxid:9606	NP_001245284	hepatocyte nuclear factor 4-alpha isoform 7	213	1.00E-58	46.56%	262	NCBI
			CAA89989.1	hepatocyte nuclear factor 4-alpha	213	1.00E-58	46.56%	262	

Supplementary Table 28 Influence of dsRNA treatment and medium on cathepsin L expression (ANOVA results from qRT-PCR data)

Source of Variation	% of total variation*	P value	Significant?
Treatment	87.66	<0,0001	Yes
Medium	0.5729	0.4552	No
Interaction*	0.9232	0.6295	No

*The calculation takes three sources of variation into account: Treatment effect, medium effect and potential interactions between these two effects (Does the effect of the treatment depend on the medium?). The percentage indicates which parameter has the greatest influence on the total variance in the data set.

Supplementary Table 29 Differentially expressed TFs after *hnf4* RNAi

Gene ID	Gene description	Log2FC	p_adj
D915_005933	NFAT5	1.3315	2.58E-10
D915_001142	DNA-binding protein inhibitor ID-2-A	1.2838	7.34E-35
D915_004441	CSD domain-containing protein	1.0574	0.0442
D915_005261	Early growth response protein	1.0062	0.0205
D915_008198	Putative Zinc finger protein	-1.1656	2.56E-68
D915_000562	PRDM1	-1.1872	4.75E-11
D915_006419	Myoblast determination protein	-1.2013	3.46E-30
D915_003286	Forkhead box protein L1	-1.3097	0.0002
D915_006325	LIM/homeobox protein Lhx1	-1.3361	0.0487
D915_008093	B-cell lymphoma/leukemia 11B	-1.5781	0.0266
D915_001114	Collier protein	-1.5847	0.0023
D915_003315	Hepatocyte nuclear factor 4-alpha	-1.6679	1.17E-32
D915_002667	B-cell lymphoma/leukemia 11B	-1.7811	2.23E-40
D915_002176	Forkhead box protein D3	-2.4185	3.53E-08
D915_003161	Transcription factor glial cells missing	-3.2476	0.0386
D915_003573	Fork head protein	-3.6135	5.16E-07

7. ACKNOWLEDGEMENT/ DANKSAGUNG

Zu guter Letzt gilt es DANKE zu sagen! Danke an alle, die mich in den letzten vier Jahren unterstützt haben und zum Gelingen dieser Arbeit beigetragen haben.

Mein besonderer Dank gilt meiner Betreuerin PD Dr. Simone Häberlein. Ich hätte mir keine bessere Mentorin für diese Doktorarbeit wünschen können! Danke, dass Du mich auf allen erdenklichen Ebenen in die Wissenschaftswelt eingeführt hast - sei es beim experimentellen Arbeiten, beim wissenschaftlichen Schreiben oder beim Networken. Ich habe unfassbar viel von Dir gelernt! Danke, dass Du mich mit Deinen unerschöpflichen Ideen immer wieder neu herausgefordert und an stets das Potenzial des Projektes geglaubt hast. Nicht zuletzt danke ich Dir auch für drei Jahre angenehme Büronachbarschaft, die mir nicht nur durch die kurzen Wege, sondern vor allem auch durch den persönlichen Austausch besonders wertvoll waren.

Mein Dank geht auch an Prof. Dr. Christoph Grevelding, der - obwohl er nicht mein primärer Betreuer war - immer ein eine offene Tür und ein offenes Ohr für mich hatte.

Einen lieben Dank auch an alle meiner anderen Kollegen am Institut für Parasitologie. Allen voran an Oli! Danke, dass Du mir einen Weg durch den *Fasciola*-Transkriptom-Dschungel gebahnt hast! Ohne Deine Vorarbeit und Deinen unermüdlichen Einsatz im Kampf mit Genom-Annotationen und *in situ*-Protokollen wäre das Spatial-Projekt bei weitem nicht so gut gelaufen. Vielen Dank auch an Max, der für jegliche RNA-Fragen immer einen guten Tipp parat hatte und mit dem sich zufällige Begegnungen auf dem Flur oder im Labor schnell in gute Gespräche entwickeln konnten. Danke an Tobi für seine tatkräftige Unterstützung bei Klonierungs-Marathons und *in situ*-Materialschlachten und an Konstantin, mit dem das FGS-Projekt zu einer sehr spannenden und willkommenen Abwechslung wurde. Ich danke auch den beiden Masterstudenten Lisa und Patrice, die mit mir zusammen das HNF4 Projekt bearbeitet haben. Danke besonders an Lisa, die sich trotz unzähliger Fehlschläge und Enttäuschungen nicht unterkriegen lassen hat, sodass aus einem scheinbar verfluchten Projekt am Ende doch noch etwas Gutes geworden ist.

Mein herzlicher Dank gilt auch meiner Familie und Freunden, die nie an mir oder dem Gelingen dieser Arbeit gezweifelt haben. Danke an meine Eltern, die immer für mich da waren. Und Danke an Susanne & Sven, die mir besonders während meines Studiums ein zweites zu Hause gegeben haben.

Auch wenn wir inzwischen getrennte Wege gehen, möchte ich mich bei Markus bedanken, der mich die Hälfte meines Studiums und fast die ganze Doktorandenzeit begleitet hat. Danke, dass Du mich stets mit Frühstück versorgt, den Haushalt geschmissen und so viel Nachsicht gezeigt hast, wenn es mal wieder später wurde. Danke, für unvergessliche Reisen mit dem BiDuBus bei denen ich auch mal auf andere Gedanken kommen konnte. Und Danke dafür, dass Du Fino Flausch in unser Leben geholt hast. Auch wenn er mich oft in den Wahnsinn getrieben hat, hat er mir noch viel öfter ein Lächeln ins Gesicht gezaubert.

Leif, Dir danke ich von Herzen, dafür, dass Du Dich von meinen überarbeitungsbedingten Stimmungsschwankungen beim Tanzen nicht abschrecken lassen hast und nun die letzten Meter dieses scheinbar endlosen Weges an meiner Seite gegangen bist. Da ich kaum in Worte fassen kann, wie viel mir das vergangene Jahr bedeutet, belasse ich es bei einem tief empfundenen: DANKE!

8. DECLARATION/ SELBSTSTÄNDIGKEITSERKLÄRUNG

Ich erkläre: Ich habe die vorgelegte Dissertation selbständig und ohne unerlaubte fremde Hilfe und nur mit den Hilfen angefertigt, die ich in der Dissertation angegeben habe. Alle Textstellen, die wörtlich oder sinngemäß aus veröffentlichten oder nicht veröffentlichten Schriften entnommen sind, und alle Angaben, die auf mündlichen Auskünften beruhen, sind als solche kenntlich gemacht. Bei den von mir durchgeführten und in der Dissertation erwähnten Untersuchungen habe ich die Grundsätze guter wissenschaftlicher Praxis, wie sie in der "Satzung der Justus-Liebig-Universität Gießen zur Sicherung guter wissenschaftlicher Praxis" niedergelegt sind, eingehalten.

Gießen, den 25.09.2025

Svenja Gramberg